Imine Macrocycle Based Crystalline Solids for Gas and Vapour Separations

Donglin He

Department of Chemistry and Materials Innovation Factory,

University of Liverpool

Thesis submitted in accordance with the requirements of the

University of Liverpool for the degree of Doctor of Philosophy

Supervisor: Prof. Andrew I. Cooper

August 2022

Abstract

Although many porous materials have been developed for gas and vapour separations, it remains challenging to create materials with precise cavity shapes and well-defined pore structures for specific and complex separation processes. Imine macrocycles have been used as molecular hosts to bind small molecules from the soil, water, and air. They can be considered supramolecular building blocks for the construction of higher-level assemblies and have promising applications in gas and vapour separations. This thesis investigates molecular crystalline solids assembled using imine macrocycles via non-covalent and coordination bonds for gas and vapour separations. In Chapter 2, guided by crystal structure prediction (CSP), the focus was on a "templating" strategy - solvent direction for constructing selective binding sites in a trianglimine macrocycle crystal for ethyl acetate. The resulting molecular crystals exhibit inherently high selectivity, reasonable adsorption kinetics, good reliability towards ethyl acetate. These properties enabled the trianglimine macrocycle to separate ethyl acetate from azeotropic mixtures with ethanol. In Chapter 3, a heterochiral pairing co-crystallisation strategy was used to create solid state porosity in a formally non-porous chiral isotrianglimine macrocycle. The stable racemic crystal was formed by co-crystallising two macrocycles with opposing chiralities to create a crystal structure containing an interconnected pore network with a Brunauer–Emmett–Teller surface area (SA_{BET}) of 355 m^2g^{-1}. With its increased surface area, the racemic crystals showed higher adsorption kinetic and capacity for separating *para*-xylene from *meta*-xylene. In Chapter 4, the assembly of salen (OH···N=C) macrocycles using zinc ions was used to construct hollow metal-organic cage molecules. Among the cages, a sandwich-like metal-organic cage (**MOC-1**), which was assembled from two calixsalen macrocycles with three zinc(II) ions, was found to contain narrow windows (<3.0 Å). As a result of its narrow pore and local flexibility, **MOC-1** exhibited good D_2 / H_2 selectivity of 2.2 and has a capacity of 1.10 mmol/g for D_2 at 77 K. **MOC-1** is a rare example of a metal-organic cage used for kinetic quantum sieving. The material also had good adsorption selectivity and capacities at temperatures up to 77 K. In Chapter 4, the assembly of four trianglsalen macrocycles with six zinc ions was also used to afford neutral octahedral metal-organic polyhedrons (MOPs). The MOPs were found to have SA_{BET} of up to 745 m^2 g^{-1}. In addition, among the MOP series, **MOP-2** was found to exhibits excellent potential for Xe/Kr separations. Overall, the work carried out in this thesis developed imine macrocycles based crystalline solids for gas and vapour separation, which presented a series of design considerations for future adsorbent materials.

Acknowledgements

Firstly, I extend a great deal of gratitude towards Prof Andy Cooper, Dr Ming Liu and Dr Marc Little for their academic support, particularly for challenging me to be a more patient and creative researcher. Over the past four years, Andy has provided a first-class research environment and many opportunities to discuss my work with many talented researchers. Ming has been a reliable mentor throughout my PhD, especially regarding his help and advice concerning experiment design, organic synthesis, scientific writing, and other things. Marc, who is my research coordinator with great patience and professional knowledge, has tried his best to help me with my project, solve the problems in single crystal X-ray diffraction analysis, and track all the important timelines throughout my PhD. Without their help and guidance in my project, I would not have done impressive work and finished this thesis.

There are many people who I would like to thank for making a significant contribution to this thesis: Prof Graeme Day (University of Southampton), Dr Linjiang Chen, Dr Chengxi Zhao and Dr Tao Liu for their computational simulations, Dr Samantha Y. Chong for powder X-ray diffraction analysis and Le Bail refinement, and Mr Katherine McKie and Mr Mark G. Roper (Hiden Isochema Ltd) for the gravimetric sorption measurement. Dr Linda Zhang and Prof Michael Hirscher from Max Planck Institute for Intelligent Systems for TDS measurement and cryogenic gas adsorption. Rob Clowes is a friendly and reliable man for Cooper Group equipment maintenance.

I have been really fortunate to have friends who provide essential motivation and encouragement to me for surviving the PhD. Thank Aiting Kai, Qiang Zhu, Weiwei Zhang, Xiaowei Zhu, Xue Wang, Xinxin Lin, Yongjie Xu, Zhonghu Pang and Zhiwei Fu for the help in daily life and work. Thank Biyi Chen, Haowei Huang and Mengyao Wang who have gotten me through when I face challenges. Also, a special thanks to Dr. Xiaofeng Wu, who has assisted me with my PhD application.

My family are always the strong support for my growth. Thank my parents for love, support and inspiration. Thank them for telling me ‘you can make it’, which is the origin of my courage for pursuing my PhD.

And lastly, I would like to thank every member of the Cooper Group, past and present for letting me enjoy the time in Liverpool.

List of publications

1) **Donglin He**[‡]; Linda Zhang[‡]*;Tao Liu; Rob Clowes; Marc A. Little*; Ming Liu*; Michael Hirscher; and Andrew I. Cooper*. Hydrogen isotope separation using a metal-organic cage built from macrocycles. ***Angewandte Chemie International Edition***, 2022, e202202450. (Early View)

2) **Donglin He**; Rob Clowes; Marc A. Little*; Ming Liu*; Andrew I. Cooper*. Creating porosity in a trianglimine macrocycle by heterochiral pairing. ***Chemical Communications,*** 2021, 57 (50), 6141-6144.

3) **Donglin He**[‡]; Chengxi Zhao[‡]; Linjiang Chen; Marc Little; Samantha Chong; Rob Clowes; Katherine McKie; Mark Roper; Graeme Day*; Ming Liu*; Andrew I. Cooper*. Inherent Ethyl Acetate Selectivity in a Trianglimine Molecular Solid. ***Chemistry – A European Journal,*** 2021, 27 (41), 10589-10594.

4) Eva Martínez-Ahumada[‡]; **Donglin He**[‡]; Victoria Berryman; Vojtech Jancik; Alfredo López-Olvera; Magali Hernandez; Vladimir Martis; Marco A. Vera; Enrique Lima; Douglas J. Parker; Andrew I. Cooper*; Ilich A. Ibarra*; Ming Liu*. SO_2 Capture using Porous Organic Cages. ***Angewandte Chemie International Edition,*** 2021, 60 (32), 17556-17563.

5) Matthew P. Rivera, Ming Liu, **Donglin He**, Ryan P. Lively. Tuning Material Properties of Porous Organic Cage CC3 with Postsynthetic Dynamic Covalent Chemistry. ***European Journal of Organic Chemistry,*** 2022, 2022 (2), e202101507.

6) Isaiah Borne; **Donglin He**; Stephen J. A. DeWitt; Ming Liu*; Andrew I. Cooper; Christopher W. Jones; and Ryan P. Lively*. Polymeric Fiber Sorbents Embedded with Porous Organic Cages. ***ACS Applied Materials & Interfaces,*** 2021, 13 (39), 47118-47126.

7) Peifa Wei*; Xuan He; Zheng Zheng; **Donglin He**; Qiyao Li; Junyi Gong; Jun Zhang; Herman H. Y. Sung; Ian D. Williams; Jacky W. Y. Lam; Ming Liu*; Ben Zhong Tang*. Robust Supramolecular Nano-Tunnels Built from Molecular Bricks. ***Angewandte Chemie International Edition,*** 2021, 60 (13), 7148-7154.

8) Ming Liu; Linda Zhang; Marc A. Little; Venkat Kapil; Michele Ceriotti; Siyuan Yang; Lifeng Ding; Daniel L. Holden; Rafael Balderas-Xicohténcatl; **Donglin He**; Rob Clowes; Samantha Y. Chong; Gisela Schütz; Linjiang Chen; Michael Hirscher*; Andrew I. Cooper*. Barely porous organic cages for hydrogen isotope separation. ***Science,*** 2019, 366 (6465), 613.

(‡ authors contributed equally)

Abbreviations

BET	Brunauer-Emmett-Teller
CSP	Crystal structure prediction
DOSY	Diffusion ordered spectroscopy
DSC	Differential scanning calorimetry
ES-MS	Electrospray mass spectrometry
FTIR	Fourier-transform infrared
HRMS	High resolution mass spectrometry
IAST	Ideal adsorbed solution theory
IGA	Gravimetric sorption apparatus
KQS	Kinetic quantum sieving
MALDI-TOF-MS	Matrix-assisted laser desorption /ionization time of flight mass spectrometry
NMR	Nuclear magnetic resonance
PXRD	Powder x-ray diffraction
PSD	Pore size distribution
QTOF	Quadrupole time-of-flight
RT	Room temperature
SA_{BET}	BET surface area
SBU	Secondary building unit
SC-XRD	Single crystal x-ray diffraction
TGA	Thermogravimetric analysis

Chemical abbreviations

AC	Activated carbon
$CHCl_3$	Chloroform
COF	Covalent organic framework
DCM	Dichloromethane
DEF	*N*,*N*-diethylformamide
EA	Ethyl acetate
EtOH	Ethanol

CMPs	Conjugated microporous polymers
COFs	Covalent organic frameworks
CTFs	Covalent triazine frameworks
DCM	Dichloromethane
HOFs	Hydrogen bonded organic framework
DACH	Diaminocyclohexane
MeOH	Methanol
MOC	Metal-organic cage
MOFs	Metal organic frameworks
MOP	Metal organic polyhedral
PAFs	Porous aromatic frameworks
PCPs	porous coordination polymers
POC	Porous organic cage
POPs	Porous organic polymers
PIMs	Polymers of intrinsic microporosity
SBU	Secondary building units
THF	Tetrahydrofuran
ZIF	Zeolitic imidazolate framework
ZSM-5	Zeolite Socony Mobil–5

Table of Contents

Chapter 1:

Introduction

"Purifying mixtures without using heat would lower global energy use, emissions and pollution — and open up new routes to resources."

David S. Sholl and Ryan P. Lively, 2016[1]

The rapid increase in energy demand and environmental pollution are worldwide challenges of our time. The separation and purification of critical commodities, such as gases, vapours, fine chemicals and fresh water, account for half of the total energy consumed by the whole industrial sector.[1, 2] Furthermore, energy consumption associated with the separation and purification processes will increase three-fold by 2050 as the global population grows and living standards improve.[2] Distillation is one of the most fundamental ways to separate chemical mixtures because of its simplicity, low capital cost, and reliability.[3] More than 80% of the energy associated with chemical separations is used in distillation and similar processes such as evaporation that rely on phase changes.[4] The key disadvantage of distillation is its high energy cost and low efficiency. Therefore, the development of alternative solutions that can operate under atmospheric conditions with less energy demand, high efficiency and environmental sustainability are being aggressively pursued.

Adsorption, an affinity-based separation technology, emerged as a key gas separation process in industry since the invention of synthetic zeolites in the 1940s.[5] It is a low-energy alternative to distillation because zeolites separation technologies can operate at ambient temperature and pressure, leading to an energy-saving and making some separation processes more sustainable. As a result, various adsorbent materials have been developed to separate gas and vapours.

1.1 Adsorbent materials

1.1.1 Activated carbon

Activated carbon (AC) is a wide range of carbonised materials with high porosity and high surface area. AC is a traditional and widely used class of adsorbent material for removing, retrieving, separating, and modifying various compounds in liquid and gas.[6] AC was widely used for medicinal applications in the olden days (1500 B.C).[7] However, the adsorptive power of AC for gases was discovered in 1773 by Scheele.[7] Subsequently, the AC was firstly applied in the liquid phase for various aqueous solution decolourisation by Lowitz *et al.* in 1785.[7] The global AC market size in 2019 was USD 2,856.7 million. It is projected to reach USD 4,064.7 million by 2027 in the forecast period.[8] The most common sources of AC on a commercial scale are wood, anthracite and bitumen charcoal, lignite, peat shells and coconut.[6] Alternative sources from agricultural residues such as olive corn, biomass, rice rolls, corn stalks, bagasse, fruit stones, hard shells, fruit pulp, bones and coffee beans are also used. [9] Physical activation and chemical activation are two typical methods for AC production.[6] Physical activation involves two steps. The first step is to carbonise raw material. The second step is to activate the material in atmospheric oxidising gases such as steam, carbon dioxide, and nitrogen or air mixtures with increasing temperatures in the range of 800 to 1100 °C.[10] Carbonisation and activation in chemical activation takes place in a single step only.[11] The precursor is mixed with the chemical agent and kept for activation at high temperatures.[12]

ACs have a wide range of pore structures and surface chemistries for the adsorption of gases.[13] This has enabled ACs to be developed for trace impurity removal from a contaminated gas,[14] separations of hydrogen-hydrocarbon mixtures[15] and selective adsorption of trace volatile organic compounds from the air.[16] However, although ACs can be surface modified to optimise the adsorption of different gas and vapour,[17] it's not yet possible to finely tune the pore size to the required sizes for gas and vapour separation applications.

1.1.2 Porous frameworks and networks

1.1.2.1 Zeolite

Zeolites are crystalline, microporous, hydrated aluminosilicates of alkaline or alkaline.[18] The frameworks are composed of TO_4 tetrahedra, where T stands usually for Si and/or Al and can be substituted with P, Fe, and Be.[19] They can both be found in nature as minerals and be made synthetically.[20] The zeolite was firstly reported by Cronstedt in 1756 and was described as "boiling stones"; therefore, the word zeolite originates from the Greek words zeo (to boil) and lithos (stone).[21] The efforts to synthesise zeolites can be traced back to 1862.[22] Milton and Breck at Union Carbide developed the reactive gel crystallisation, which is the most influential early synthesis milestones for zeolites.[21] After the discovery of Al-rich zeolites A and X by the reactive gel crystallisation, the zeolite Y was discovered by Breck in 1964.[21] In 1969, (Zeolite Socony Mobil–5) ZSM-5, a high-silica zeolite, was firstly synthesised by Argauer and Landolt.[23] As the increasing number of novel zeolites with various structures and compositions, the necessity to categorise and group the different zeolite materials appeared. The paper that can be considered to be the forerunner of the first edition of the *Atlas Zeolite Framework Types* was published in 1970 with 27 zeolite framework structures described.[24] The book is the foundation for a systematic description of zeolite framework structures. In order to keep track of discoveries of new framework types, the Structure Commission of the International Zeolite Association (IZA),[24] charged by the International Union of Pure and Applied Chemistry (IUPAC) was established in 1977. The materials with the same topology whose primary building blocks (usually TO_4 tetrahedra) are connected in the same way are a framework type.[21] For example, ZSM-5[25] and silicalite[26] are both belong to the MFI framework type (Figure 1.1), though they are in very different compositions (Si/Al: 2.7 vs ∞).

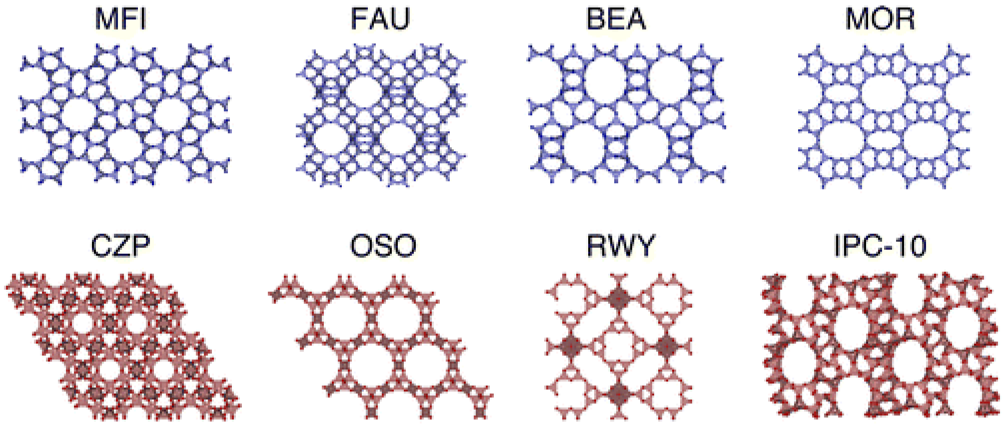

Figure 1.1. Selected zeolite framework structures. Reprinted from *Cryst. Growth Des.*, 2016, 16 (6), 3043-3048.[21] Copyright 2016, with permission from American Chemical Society. Each framework type is given a three-letter code based on the name of the first material possessing the framework type in question. For example, the code MFI is derived from the material ZSM-5 because it stands for "Zeolite Socony Mobil five".[21]

Zeolites, because of high porosity, their microporous architectures for molecular sieving, inherent ability to adsorb polar compounds, and good thermal and chemical stability, are excellent candidate materials for the separation and purification of gases.[27, 28] They have been applied in O_2 production, removal of N_2O from air[29], CO_2 separation from flue gas[30] and others. Currently, zeolites have been used in membrane form for separating gases at industrially relevant conditions.[31] The applications of zeolite membranes include H_2/N_2,[32] CO_2/N_2,[33] and CO_2/CH_4[34] separations. However, the insolubility and high crystallinity of zeolites lead to the brittleness of zeolite membranes, which limits their application in industrialization[35] In addition, limited topologies[36] and less chemically diversity[37] of zeolites make it difficult fine-tune them for technologically challenging separation applications.

1.1.2.2 Metal-organic frameworks (MOFs)

Metal–organic frameworks (MOFs), also known as porous coordination polymers (PCPs) are constructed by connecting metal-containing nodes (also known as secondary building units, or SBUs) to organic linkers.[38] MOFs have various applications, including separation,[5] storage,[39] delivery,[40] and catalysis[41] due to their ultrahigh porosity, high function tenability and crystallinity. As shown in Figure 1.2, this field emerging from coordination chemistry can date back to the early 18th century when "Prussian Blue", an extended coordination compound was found, and a porous coordination polymer $Cu[C(C_6H_4CN)_4]$ was reported in 1999.[42] Then, the construction of a robust MOF with permanent porosity from Zn_4O clusters and linear dicarboxylate linkers was reported by Yaghi and co-workers in 1999.[43] After that, ultra porous MOFs such as MIL-101, ultrastable MOFs such as UiO-66, and flexible MOFs such as MIL-88 were developed.[42, 44-46] Currently, heterarchical, or multivariate MOFs such as PCN-222 and NU-1000 constructed from multiple metal clusters and linkers have attract attention due to [47, 48] their hierarchical porosity and integrated functionalities.

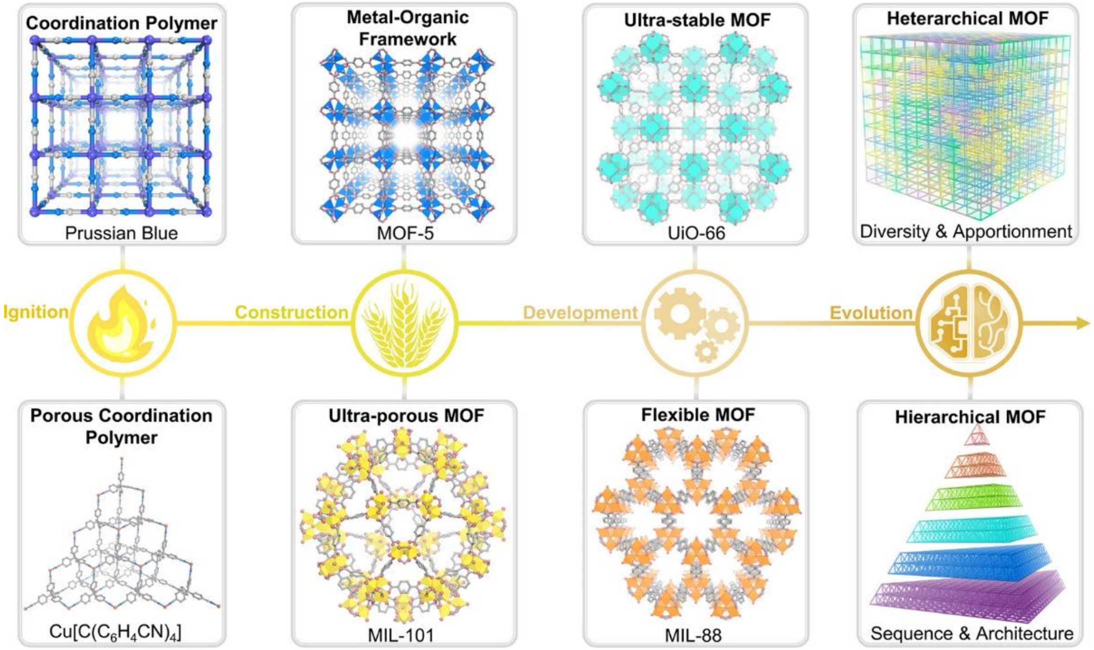

Figure 1.2. Advances in the development of metal-organic frameworks (MOFs). Reprinted from *ACS Cent. Sci.* 2020, 6 (3), 359-367.[42] Copyright 2020, with permission from American Chemical Society.

MOFs, owing to the ultrahigh porosity with surface area ranging from 100 to 10,000 m^2/g, tunable pore sizes of 3 to 100 Å, high thermal stability (up to 500 °C), and even exceptional chemical stability have been are recognised as excellent materials for gas storage and gas separation.[49, 50] As a result, gas separation using MOFs has progressed (Figure 1.3), especially for the industrially significant hydrocarbon separation[51-65], CO_2 capture[66-72], sulfide removal and Xe/Kr separation[73] and H_2/D_2 separation.[51-74] However, MOFs are insoluble frameworks, which limits their processability.[75] In addition, high-cost organic ligands (novel ligands that need to be designed and synthesised) and strict synthetic conditions (such as solvothermal methods) are the challenges for applying MOFs for large-scale applications.[76]

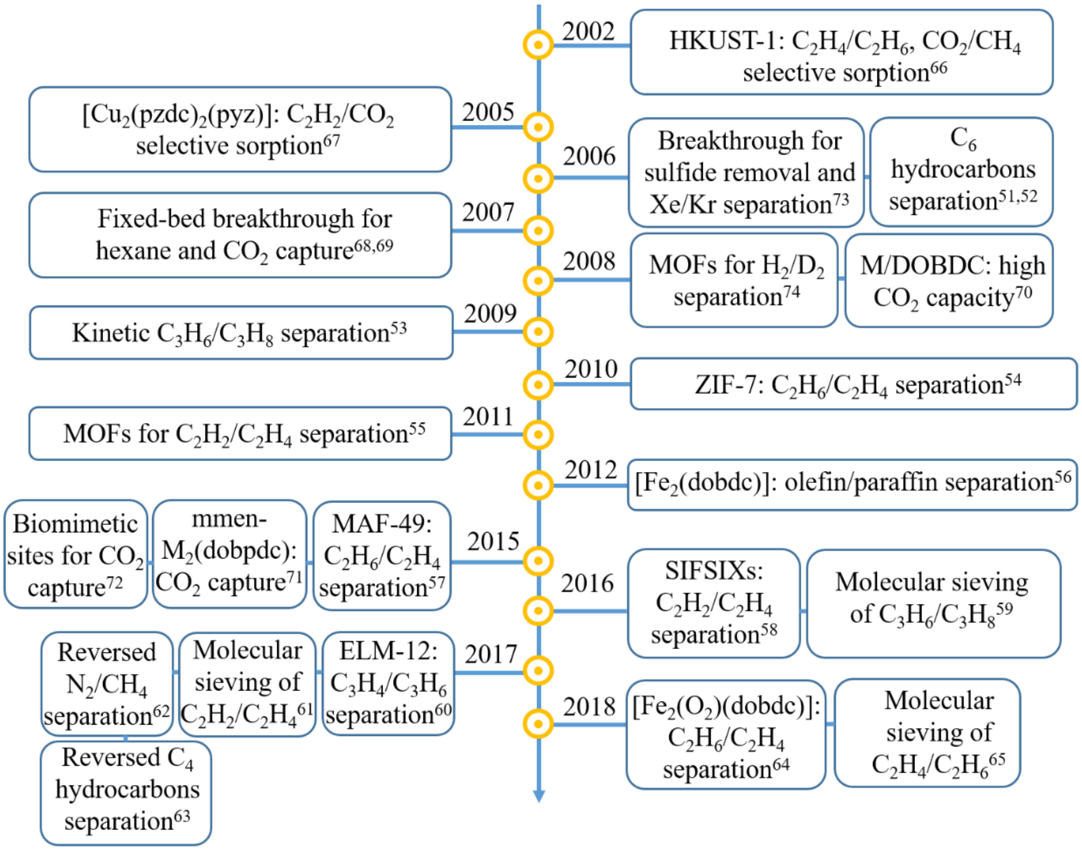

Figure 1.3. Timeline of important breakthroughs in using MOFs for separating representative gases. Regenerated from *EnergyChem*, 2019, 1 (1), 100006.[50] Copyright 2019, with permission from Elsevier.

1.1.2.3 Covalent organic frameworks (COFs)

Covalent organic frameworks (COFs) are crystalline, extended solids in which strong covalent bonds link the building blocks. In 2005, COF-1 and COF-5 were first reported and successfully synthesised by condensation reactions of phenyl diboronic acid and hexahydroxytriphenylene, which opens the field of COFs.[77] Over the past decade, a great variety of COFs including boroxine-linked,[78] boronate ester-linked,[79, 80] imine-linked,[81] imide-linked,[82] β-ketoenamine-linked,[83] azine-linked,[84] triazine-linked,[85] phenazine-linked,[86] hydrazone-linked,[87] and sp^2-carbon linked[88] COFs have been developed. (Figure 1.4) COFs can be also divided into two-dimensional (2D) COFs and three-dimensional (3D) COFs according to the different dimensions of the building unit.[89] Compared to 2D COFs, 3D COFs usually present a higher surface area, though the construction of 3D COFs has been considered a significant challenge due to the limited diversity of tetrahedron-type knots.[90, 91]

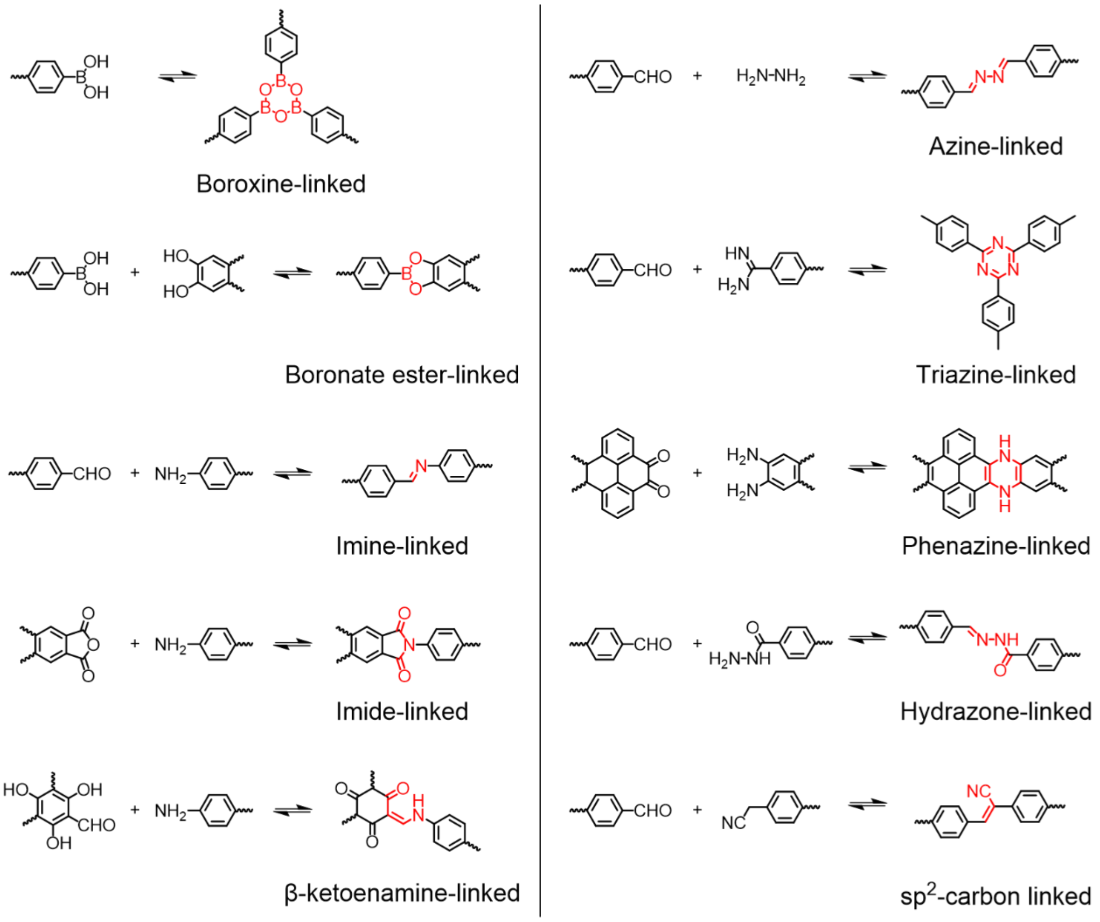

Figure 1.4. Selected reaction types used to synthesise COFs.

Due to their well-defined crystalline structures, low density, good chemical stability, large surface area, and facilely-tailored functionalities,[92] COF materials have great potential in diverse applications, such as catalysis,[93] gas storage and separation,[94, 95] drug delivery,[96] chemical sensors[97] and supercapacitors.[98] Among them, various separation applications, including methane purification,[99] separation of hydrogen isotopes,[100] carbon dioxide/nitrogen separation,[101] hydrogen purification,[102] homologue separation,[103] chiral separation,[104] have been studied with COFs materials due to their ordered pore channels and uniform pore size.[92] Although facile membrane can be formed with COFs for the separation process,[105] COFs are insoluble like MOFs, limiting their processability. In addition, it is much less developed than MOFs,[75] and has no large-scale applications due to the cost and difficulty of synthesis.

1.1.2.4 Hydrogen bonded organic framework (HOF)

Hydrogen bonded organic frameworks (HOFs) are constructed from organic molecules and stabilised by non-covalent hydrogen bonding interactions. HOFs have emerged as a new class of porous crystalline materials.[106] Generally, a scaffold (or backbone) and hydrogen bonding interaction sites (or sticky sides) are two indispensable parts in HOF building motifs.[107] The assemble of adjacent scaffolds through hydrogen binding sites in these scaffolds accomplishes the fabrication of HOFs. Therefore, the structural symmetries of rigid cores and synthetic convenience of scaffolds that affect the hydrogen bonding motif are important considerations in designing HOFs. Since the first HOF structure of 1,3,5-benzenetricarboxylic acid reported in 1969 by Duchamp,[108] (Figure 1.5) hydroxyl or amine groups,[109, 110] carboxylic or pyrazole groups,[111, 112] amide or urea groups,[113, 114] macrocyclic receptors,[115] linear dipeptide,[116] pyridone or UPy groups,[117, 118] DAT or DAP groups[119, 120] and charge-assisted hydrogen bonds[121] have been developed as backbones for the synthesis of HOFs.

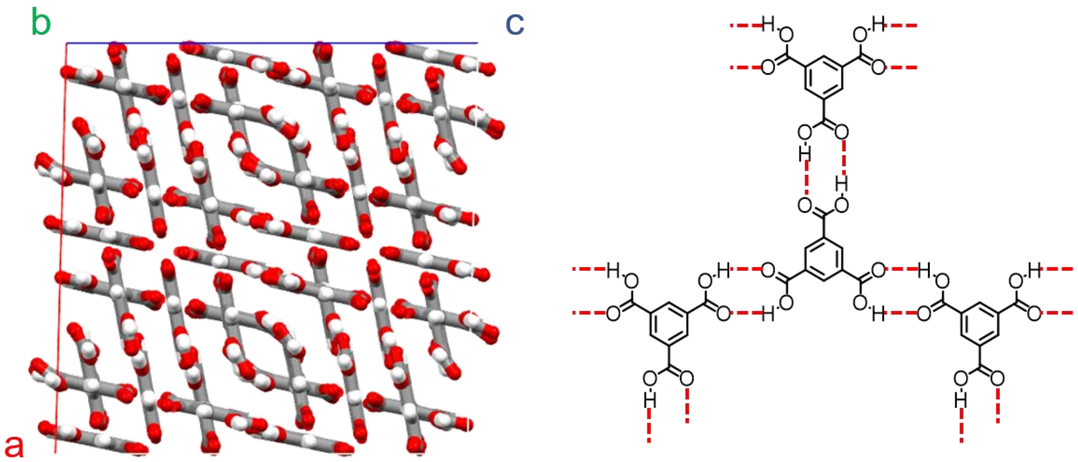

Figure 1.5. The HOF structure viewed down the b axis (left, CCDC 1115589[108]; white, H; red, O; grey, C), 1,3,5-benzenetricarboxylic acid formula (right, hydrogen bonds are labeled by red dash lines).

Although there has been much progress in this field over the last two decades, the development of HOF materials with permanent porosity faces several challenges. The strength of hydrogen bonds is generally weak compared with covalent and ionic bonds.

Consequently, without the structural support of solvent guests through non-covalent intermolecular interactions, such as additional hydrogen bonds and π-π interactions, the supramolecular networks may collapse and lose their porosity.

The first microporous HOF with permanent porosity for highly selective C_2H_2/C_2H_4 separation at ambient temperature was reported by the Chen group in 2011.[122] (Figure 1.6) After that, a series of HOFs with permanent porosity have been synthesised and utilised for gas sorption and separation, such as C_2H_2/CO_2,[123] C_2H_2/C_2H_4,[124] C_2H_4/C_2H_6[125] and C_3H_6/C_3H_8[126] separations.[126] Despite a limited number of HOFs materials with permanent porosity, their advantages in the ease of synthesis, structural elucidation via single-crystal X-ray diffraction, low energy consuming regeneration processes, and good thermal stability attract researchers all over the world. [106] More potential of HOFs in the application of gas storage and separation and catalysis[127] are being developed.

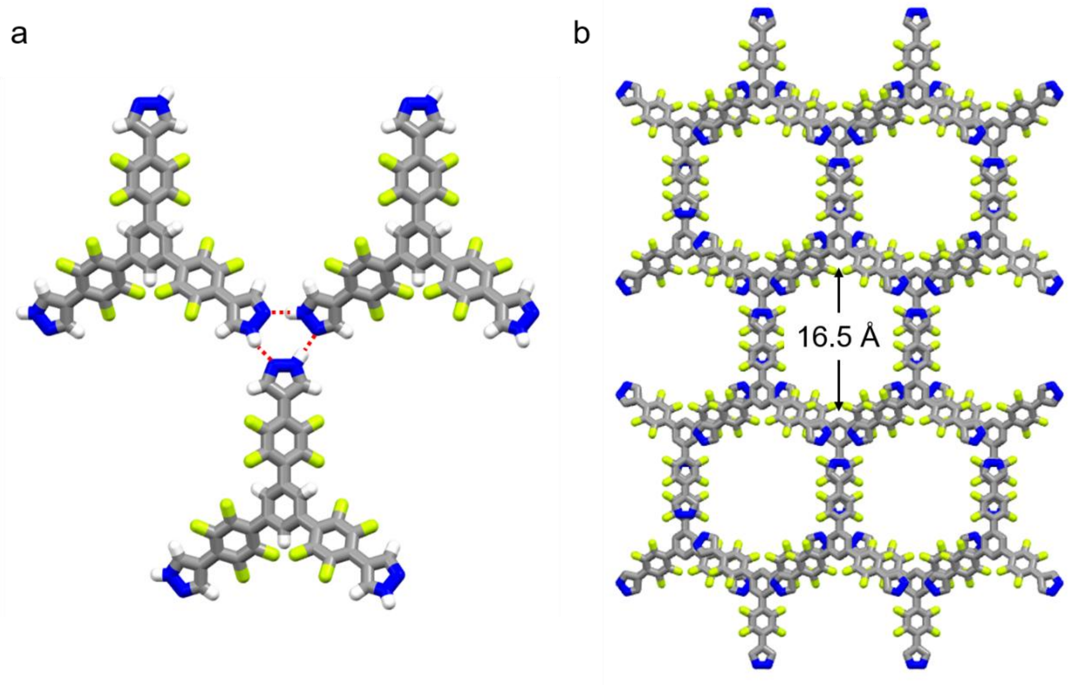

Figure 1.6. The first microporous HOF with permanent porosity: (a) Three pyrazoles come together in each of the layers with triplet of hydrogen bonds, (b) A hexagonal network results, with infinite fluorine-lined channels protruding throughout the structure along the crystallographic c axis, H atoms are omitted for clarity. (CCDC 1004205[122]; white, H; blue, N; green, F; grey, C)

1.1.2.5 Porous organic polymers (POPs)

Porous organic polymers (POPs) composed predominantly of carbon, boron, oxygen, and nitrogen that are connected through strong covalent bonds, are a category of highly crosslinked amorphous polymers with nanopores.[128] Amorphous POPs mainly include conjugated microporous polymers (CMPs),[129] polymers of intrinsic microporosity (PIMs),[130] hyper-crosslinked polymers (HCPs),[131] covalent triazine-based frameworks (CTFs),[132] and porous aromatic frameworks (PAFs).[133] Attributed to their exceptionally high surface area, tunable pores, and intriguing functionalities,[134] POPs have been used in gas separation and storage,[135, 136] catalysis,[137] environmental remediations,[138] and sensing.[139] The gas separation and storage of hydrogen, carbon dioxide, and methane have been widely explored with POPs whose pore environment can be modified by introducing functional units to the wall surface.[134] For example, an ultrahigh-surface-area porous polymer network (PPN-6) grafted with task-specific groups like sulfonic acid, lithium sulfonate, polyamines, or sulfonate ammonium can achieve excellent CO_2 adsorption capacities as well as high CO_2/N_2 selectivity.[140-142] However, the synthesis of such POPs that involve expensive transition-metal-based catalysts and extra purification efforts may limit the scale-up preparation.[143] In addition, it is difficult to design amorphous porous materials for specific applications because there structures are amorphous, and their three-dimensional structures cannot be unambiguously modelled.[75]

1.1.3 Porous molecular solids

Porous molecular solids are discrete molecules held together by weak intermolecular forces.[75, 144] Unlike MOFs, COFs, and POPs, the molecular-scale porosity of the solid derives from the cavity of the molecule and packing between molecules instead of infinitely extended one-, two- or three-dimensional framework structures.[145]

1.1.3.1 Porous organic cages (POCs)

Porous organic cages (POCs) are an emerging class of porous materials composed of discrete, covalently bonded organic molecules with guest-accessible cavities.[146] POCs can be synthesised by forming irreversible or reversible covalent bonds. Among them, reversible chemistry has been widely applied to the preparation of POCs because it generally requires fewer steps and allows error correction for yielding the thermodynamic product with high yields and high purity. As shown in Figure 1.7, imine condensation is the most prevalent reversible route[147]. Other reversible bond-forming chemistry such as boronic ester[148] or boroxine[149] formation and dynamic alkyne metathesis[150] have also been used.[151] Irreversible chemistry is rarer for porous organic cages, but examples have been seen include carbon–carbon bond formation through metal-catalyst-assisted cross-coupling,[152] nucleophilic aromatic substitution,[153] ester condensation,[154] and azide–alkyne Huisgen cycloaddition.[155]

Significant progress has been made in the preparation of POCs with different shapes and sizes, POCs with excellent chemical stability, internal porosity and rich functionalities.[156] This has enabled POCs to be explored for applications including molecular recognition, [157] catalysis[158] and gas storage and separation.[159, 160] Although the research of the solid-state porosity in molecular crystals was not so much as the study in the area of porous frameworks and networks such as MOFs, COFs and POPs. Until recently, POCs have become a real alternative to extended framework materials with high specific surface areas up to 3758 m^2 g^{-1} and a pore diameter of 2.3 nm.[148] Therefore, due to their permanent gas/solvent-accessible channels, POCs have been studied especially for separation of CO_2 from N_2 and CH_4,[161], SF_6 from N_2,[162], noble gases,[160] hydrocarbon isomers,[163] chiral molecules[160] and hydrogen isotope.[164]

The molecular solubility of POCs not only expands their processability but enables tuning of their pore structure by crystal engineering,[151, 165] and the porosity control for the POCs will be discussed in Section 1.3.4.

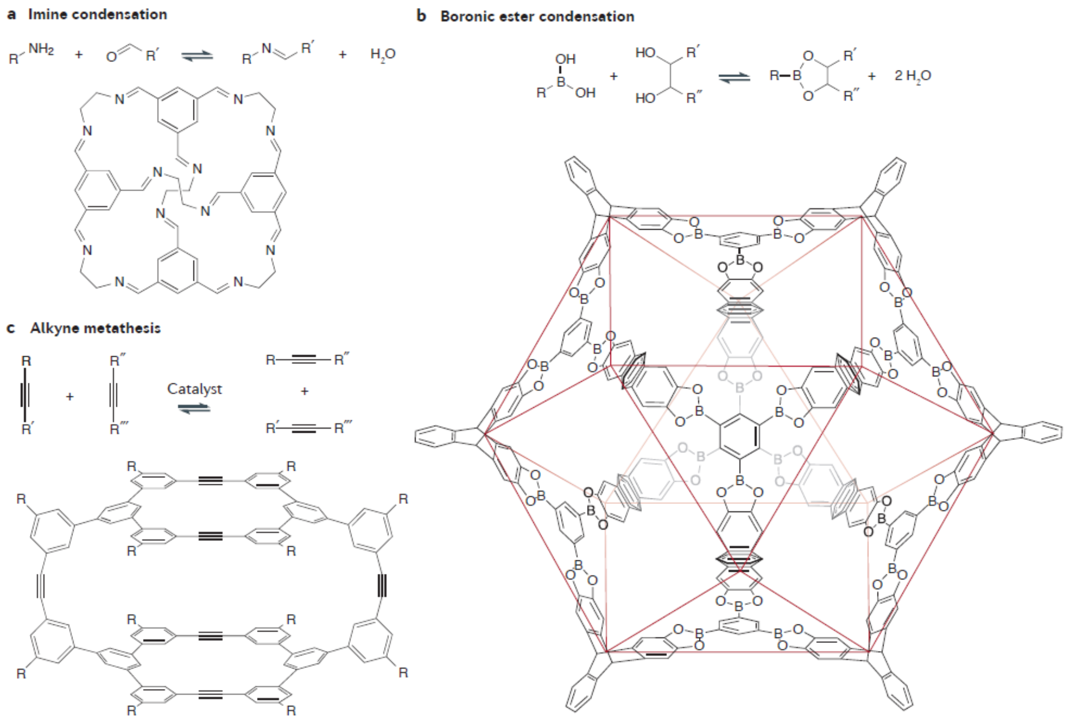

Figure 1.7. Synthetic routes for porous cage formation using reversible chemistry with examples. Reprinted from *Nat. Rev. Mater.*, 2016, 1, 16053.[151] Copyright 2016, with permission from Nature.

1.1.3.2 Macrocycles

IUPAC defines a macrocycle as, "a cyclic macromolecule or a macromolecular cyclic portion of a molecule".[166] Macrocycles have had a profound influence on the establishment of supramolecular chemistry because of their abundant molecular recognition and self-assembly characteristics.[167] The field of macrocycles can trace back to half a century ago, crown ethers and their complexes with metal salts were discovered by Pedersen.[168] Then, cryptands[169] and cryptates[170] were reported in 1969 by Lehn *et al.* who coined the term “supramolecular chemistry” for what is described as “chemistry beyond the molecule”.[171] After that, various of macrocycles including calixarenes,[172] cucurbiturils,[173] pillararenes,[174] cyclodextrins,[175] porphyrins,[176] polyimine macrocycles,[177] and conjugated cyclophanes[178] were reported (Figure 1.8).

Macrocycles have been intensively studied in solution as hosts for binding of various guest molecules, such as metal ions and nucleotides.[179-181] Macrocycles have also been used as host building blocks to construct supramolecular structures, such as host-guest hydrogels, which have adaptive structures and are useful for biomedical applications.[182] With diverse cavity shapes, sizes, and functionalities, they have shown potential as porous media for selective adsorption of gases and vapours. For example, β-Cyclodextrin (β-CD), a macrocycle of seven glucose units, is an attractive VOC capture sorbent because it forms host-guest complexes with a large number of organic compounds.[183-185] Calix-[4]-arene macrocycles with hydrophobic cavities have also been reported selectively adsorb VOCs, such as toluene, benzene, nitrobenzene and phenol.[186] In addition, pillar[n]arenes, have been used for purifying styrene from ethyl benzene, and selectively adsorbing *para*-xylene from its ortho- and meta-isomers.[187, 188] Although certain macrocycles pack to give porous structures,[114, 189-191] some solvent-free macrocycles require particular activation strategies to maintain porosity. This is because solvated molecular crystals tend to transform or collapse when the lattice solvent is removed and this 'virtual porosity' is typically lost during desolvation.[192-194] In order to retain the structures of porous crystal after activation, strategies such introducing hydrogen bonding interaction between organic molecules to form stable HOFs.[195] Therefore, it's possible for the macrocycles to maintain porosity after activation by introducing non-covalent interactions. In addition, macrocycles with large enough inner channels and cavities to accommodate guest molecules; and thus have the potential to be applied for gas and vapour separation, organic pollutants removal, chemical sensing and other environmental remediation application.

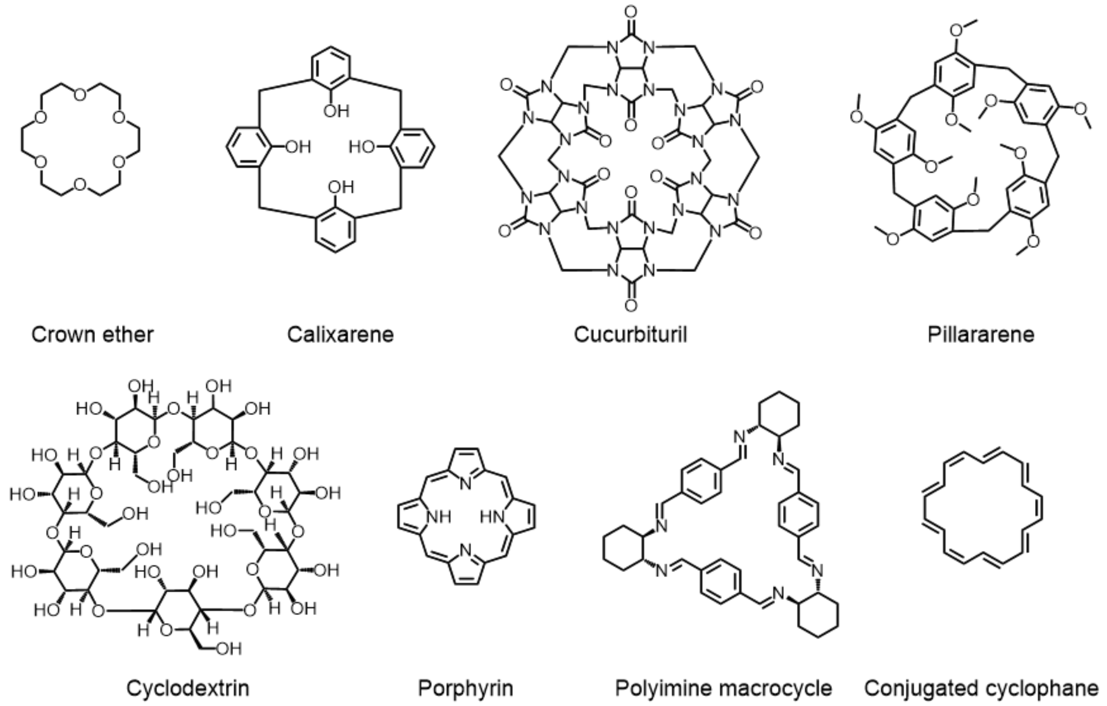

Figure 1.8. Typical examples of organic macrocycles.

1.1.3.3 Metal organic cages (MOCs)

Metal–organic cages (MOCs), also known as metal–organic polygons or polyhedrons (MOPs), are discrete molecular assemblies formed via coordination driven self-assembly of metal cations and organic linkers.[196] MOCs are a relatively new subclass of molecular materials that contains the merits of both POCs and MOFs.[196-200] The early work in this field could date back to three decades ago,[168] a tetranuclear magnesium-based tetrahedron and two palladium cages are subsequently reported by Saalfrank in 1988[201] and Fujita in 1995,[202, 203] respectively. In 2001, the term MOPs was first introduced by Yaghi to describe a cage compound Cu$_{24}$(bdc)$_{24}$ (MOP-1 shown in Figure 1.9), formed by the assembly of Cu$_2$(CO$_2$)$_4$ with polytopic carboxylate linkers.[204] A series of MOCs or MOPs were reported by groups including Raymond,[205] Stang,[206] Cotton,[207] Mirkin,[208] Cook,[209] Nitschke,[210], Bloch,[211] Furukawa,[212] Li,[213] Yuan,[214] and Kitagawa,[215] and others. Similar to their intrinsically porous organic counterparts POCs, MOCs can have good solubility in a range of solvents thus can be processed into different forms to optimise their functions. In addition, crystal structure prediction (CSP),[216] which can predict the packing of the molecular systems and enable their physical properties to be simulated, likewise has the potential to help researchers select the most promising MOC molecule for a given application prior to its synthesis. Furthermore, as the discrete counterparts of MOFs, MOCs can contain open metal sites, which can enhance the gas adsorption affinity.[5, 204, 217] Up to date, MOCs with specific pore sizes have been demonstrated to selectively adsorb CO_2,[218] O_2,[219] CO,[220] NO,[211] and C_3H_8.[221].

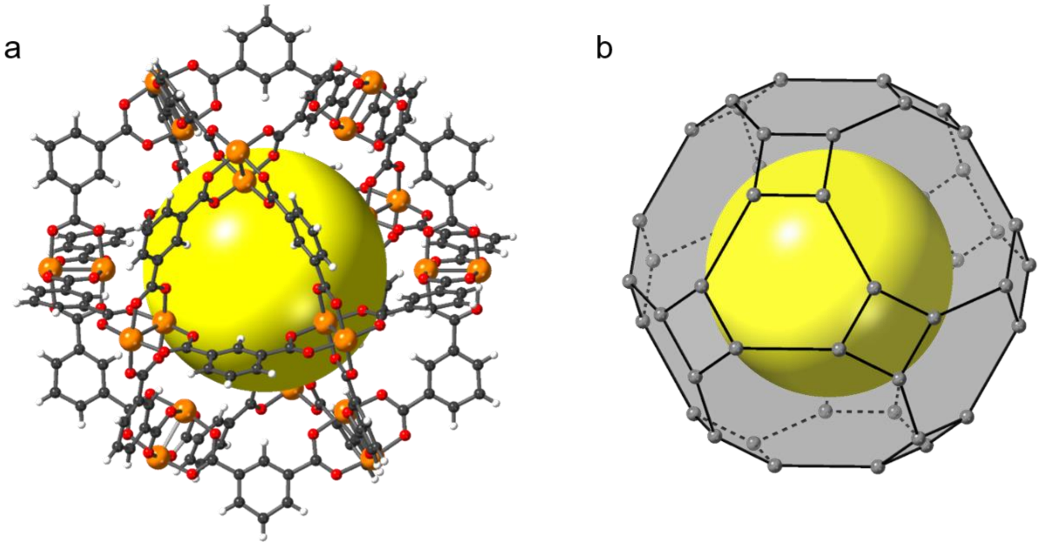

Figure 1.9. The crystal structure of MOP-1 (CCDC 1212282[204]): (a) 12 paddle-wheel units (Cu, orange; O, red, C; grey), (b) large truncated cuboctahedron of 15 Å diameter void (yellow sphere), the grey spheres represent the polyhedron. All terminal ligands pointing in the cavities and away from the surface have been omitted in (a–b). Regenerated from *J. Am. Chem. Soc.* 2001, 123 (18), 4368-4369.[204]

In solids, the porosity of MOCs is affected by a combination of their intrinsic porosity and its accessibility in addition to extrinsic porosity created between the MOCs.[199, 222] The intrinsic porosity of MOCs can be controlled by choosing appropriate organic linkers and metal centers,[223, 224] or post-synthetic modification.[225] While the extrinsic porosity in MOC solids can be controlled using crystal engineering methods.[226, 227] Building units or ligands are the key structural components of MOCs and significantly affect their porosity and flexibility.[211, 228] Although linear or planar organic linkers are the most common building units for MOCs, macrocycles with the intrinsic cavity such as porphyrins[229] calixarene,[211] and calixsalens[230] have recently emerged as building units for the synthesis of shape-persistent MOCs. With their own intrinsic cavities and structural varieties, macrocycles can significantly enrich the functionality and structural diversity of MOCs. Typically, the macrocycles are used as capping units to synthesise MOCs. For example, calixarene-based macrocyclic ligands have been used to cap tetranuclear clusters,[231-233] to form MOCs with surface areas ranging from 26 to 1239 m^2/g.[211] Therefore, expecting the structure of the macrocycles would affect the pore structure of the formed cage molecule, more attention could be paid to using macrocycles as organic linkers to build MOCs.

1.2 Macrocycles formed by imine condensation

Imine-based molecular structures, synthesised from condensation of carbonyl compounds as the acceptor with primary amines as the donor, were discovered by Hugo Schiff in 1864.[234] The reversible nature of the covalent imine bond provides the prevalent formation of the thermodynamically stable structures in solution during the synthesis.[235] Imine formation in organic solvents is generally considered to occur in a stepwise manner. Firstly, the unsaturated carbon of the carbonyl compound is attacked by the nucleophilic amino group and forms a tetrahedral intermediate (the carbinolamine). Subsequently, the C=N linkage is generated from a tetrahedral intermediate with the elimination of water. (Figure 1.10)

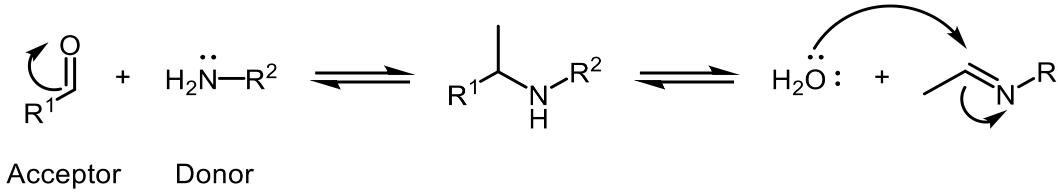

Figure 1.10. Carbinolamine formation and decomposition steps in imine formation reaction. Regenerated from *Org. Biomol. Chem.* 2015, 13 (3), 646-654.[236] Copyright 2015, with permission from Royal Society of Chemistry.

The equilibrium shown in Figure 1.11 can be affected by many external considerations, including solvent, concentration, pH and temperature, as well as steric and electronic factors.[235] For example, water can react with the imine and convert the imine product back to the original compound(s) containing amino and carbonyl groups. (Figure 1.11a - hydrolysis) In addition, the original imine may undergo transamination where the R groups are exchanged upon introduction of a second amine. (Figure 1.11b - exchange) Furthermore, the two imines can undergo a reaction in which the two R groups are exchanged upon the introduction of a second imine. (Figure 1.11c - metathesis)

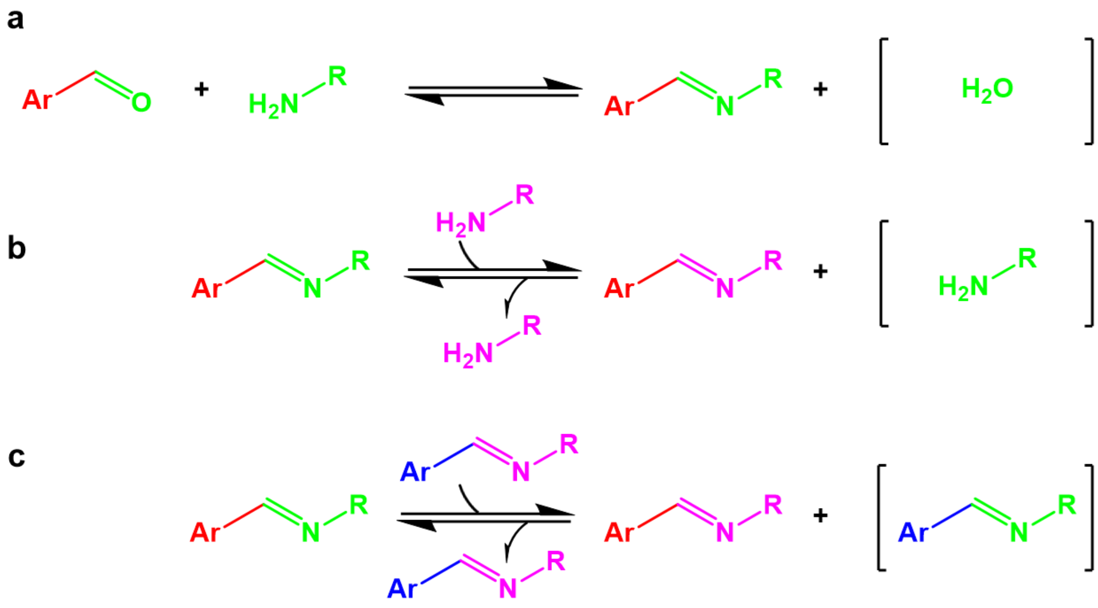

Figure 1.11. The three fates involving imine reactants: (a) imine condensation, (b) exchange and (c) metathesis. Regenerated from *Chem. Soc. Rev.* 2007, 36 (11), 1705-1723.[235] Copyright 2007, with permission from Royal Society of Chemistry.

Macrocyclic Schiff bases can be considered as supramolecular building blocks for the construction of higher-level assemblies and have promising applications in sensors and molecular machines.[237] They have also been used as a molecular host to bind environmental toxins from soil, water and food and remove undesired trace by-products from the bulk manufacturing of fine chemicals. The limited flexibility of diamine is believed to be the important factor for constructing the shape persistent polyimine macrocycles.[238] Therefore, the (1*R*, 2*R*)–diaminocyclohexane (DACH) that has C_2 symmetry, the rigid cyclohexane skeleton and amine groups in the diequatorial position can be a good choice.[239, 240] As shown in Figure 1.12, the chiral polyimine macrocycles formed from chiral DACH can be classified by the structure of dialdehyde.

	Trianglimine	**Isotrianglimine**	**Calixsalen**	**Trianglsalen**
	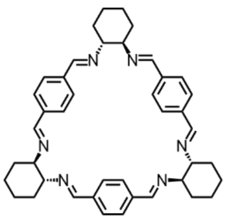	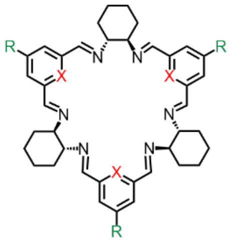	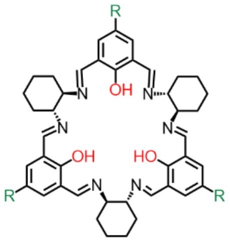	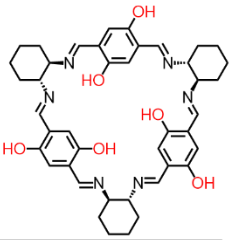
Donor	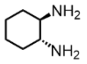			
Acceptor	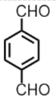	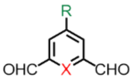	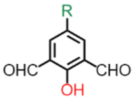	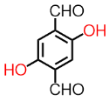
Product preferred	• [3+3] product is strongly preferred	• [2+2], [3+3] and [4+4] products are possible • [2+2] product is thermodynamically favoured	• [3+3] product is strongly preferred	• [3+3] and [4+4] products are possible
Symmetry	• Non-symmetrical aldehyde = non-symmetrical product	• Unusually large conformational liability	• Substituent of R does not affect symmetry of the macrocycle	• Non-symmetrical aldehyde = non-symmetrical product
Advantage	• Easy modification of macrocycle cavity	• High structural diversity	• Structure is stabilized by the hydrogen bonding cascade • Easy modification of the lower rim of the macrocycle • Possibility to formation of various supramolecular assemblies	• Easy modification of macrocycle cavity • Structure is stabilized by the hydrogen bonding cascade • Possibility to formation of various supramolecular assemblies
Weakness	• Difficult to expand the structure up and down	• Difficult to modify the macrocycle cavity	• Difficult to modify the macrocycle cavity	• Poor solubility of the large macrocycle without substituent of R

Figure 1.12. The comparison of the basic structural motifs within polyimine macrocycles. (Regenerated from Marcin K. *et al.*[177])

Gawronski and co-workers reported a series of trianglimine macrocyles (Figure 1.12) in 2000.[241] Diastereomeric structures of the trianglimine macrocycles were subsequently reported by the group of Hodacova.[242] In 2003, Kuhnert and co-workers reported the scope and limitations of the [3 + 3] cyclocondensation between DACH and various aromatic dicarboxaldehydes.[237] Kuhnert and co-workers used a variety of dilithiation strategies to synthesise new aromatic dicarboxaldehydes for forming trianglimine macrocycles, which they used to synthesise enantiomerically pure macrocycles.

Trianglimines macrocycles can be divided into three main categories based on the structure of the dialdehyde linker: (i) terephtaladehyde and its derivatives, (ii) the derivatives in which formyl groups are parallel but not linear due to the shift in the structure of dialdehyde and (iii) 4,4′-diformyldiphenyl and its derivatives with three or more aromatic rings in their structure.[177] (Figure 1.13) The cavity of trianglimine macrocycles is dependent on the linker used, and its size can be easily modified by using dialdehyde linkers with different lengths.

Isotrianglimines macrocycles are synthesised via the condensation of DACH with isophthalaldehyde or its heteroaromatic congeners.[177] (Figure 1.12) From the reaction with isophthaldehyde, the kinetic product is the triangular-shaped [3+3] macrocycles. However, the primarily formed [3+3] isotrianglimines macrocycle can be transformed over time into the thermodynamically more stable and smaller [2+2] products. [243, 244] In addition, a dynamic library of [2+2], [3+3] and [4+4] products was reported via the condensation of DACH with pyridine-2,6-dicarboxaldehyde without any visible preference for a product under template-free conditions.[245]

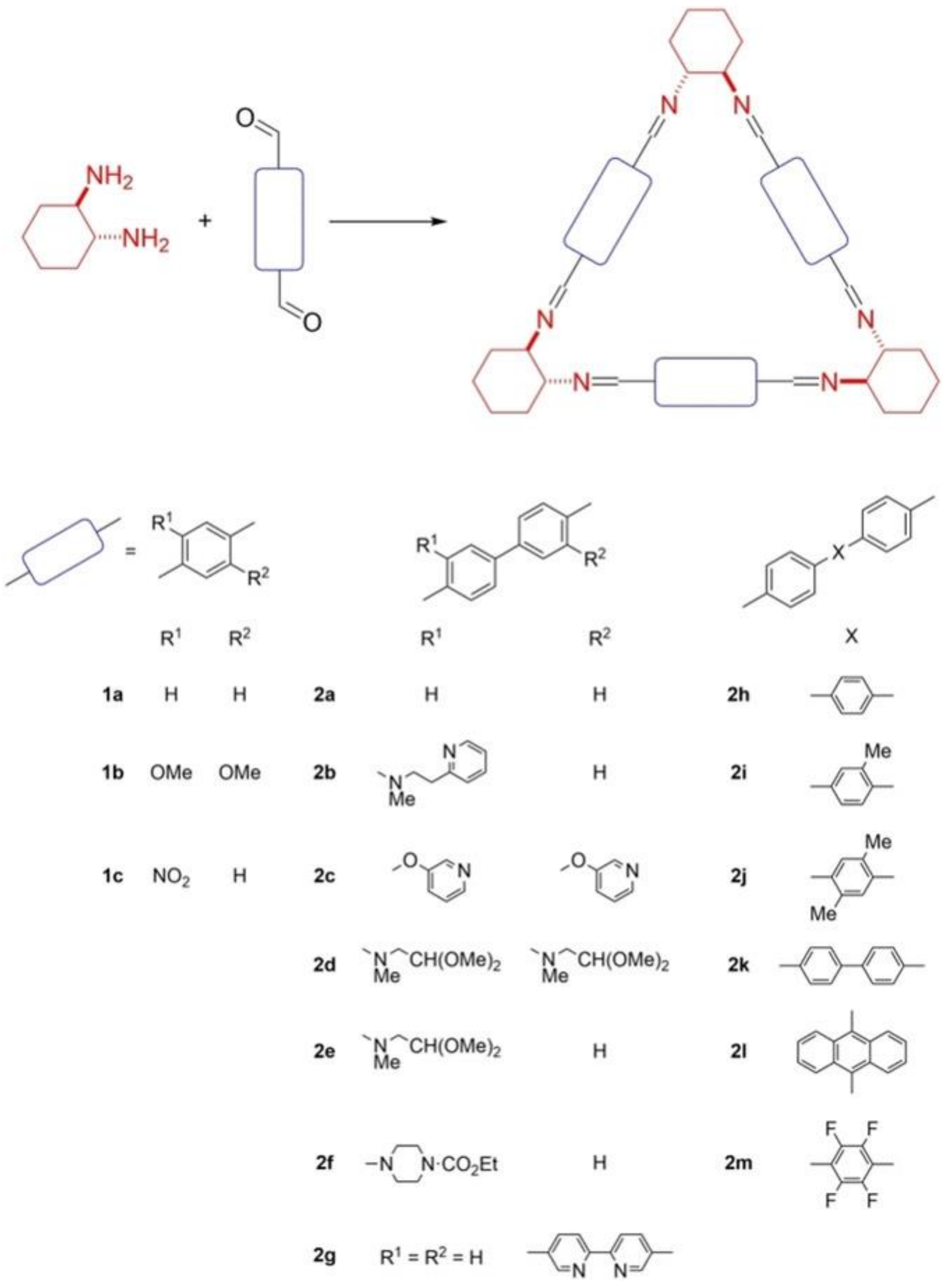

Figure 1.13 Synthesis of representative trianglimines. Regenerated from *Chem. Rec.*, 2019, 19 (2-3), 213-237.[177] Copyright 2019, with permission from Wiley Online Library.

Calixsalens were first reported in 1999 by Jablonski *et al.*, who condensed 2-hydroxyisophthalaldehyde derivatives with (1*R*, 2*R*)-DACH.[246, 247] Calixsalens have a bowl-like shape and small intrinsic cavity with salen unit in each vertex of the macrocycle.[248] As shown in Figure 1.14, the calixsalen skeleton consists of two rims.

One rim (head) consists of the cyclohexane rings, and halves of the arene rings with the hydroxyl and imine substituents, another rim (tail) is composed of the remaining parts of the arene rings with the substituents in the C5 positions.[249] The *s-trans* conformation of C=N imine groups and the structure of the macrocycle are stabilised by the OH···N=C hydrogen bonding between the hydroxyl groups and their adjacent imine functionalities. The presence of the salen unit has also been utilised in the coordination chemistry to form metal complexes with or without ring contraction.[230] Furthermore, the form of supramolecules or dimers can be controlled by the substituent at the C5 position.[249] Calixsalens substituted by small and/or polar groups such as hydrogen, bromine and methyl group tend to form tail-to-tail dimers by mutual insertion of one aromatic moiety of each monomer into the internal macrocyclic cavity of a partner. (Figures 1.14b)[250] By contrast, the calixsalens substituted by tert-butyl or trityl groups can form as head-to-head dimers (the capsules) with hollow spaces allowed the solvent entrapments. (Figures 1.14c)[250, 251] However, calixsalens with hydroxyl groups in the C5 positions is an exception, and they can form an hourglass structure by bounding each macrocycles via hydrogen bonds between OH groups at their lower rims.[252] (Figure 1.14d)

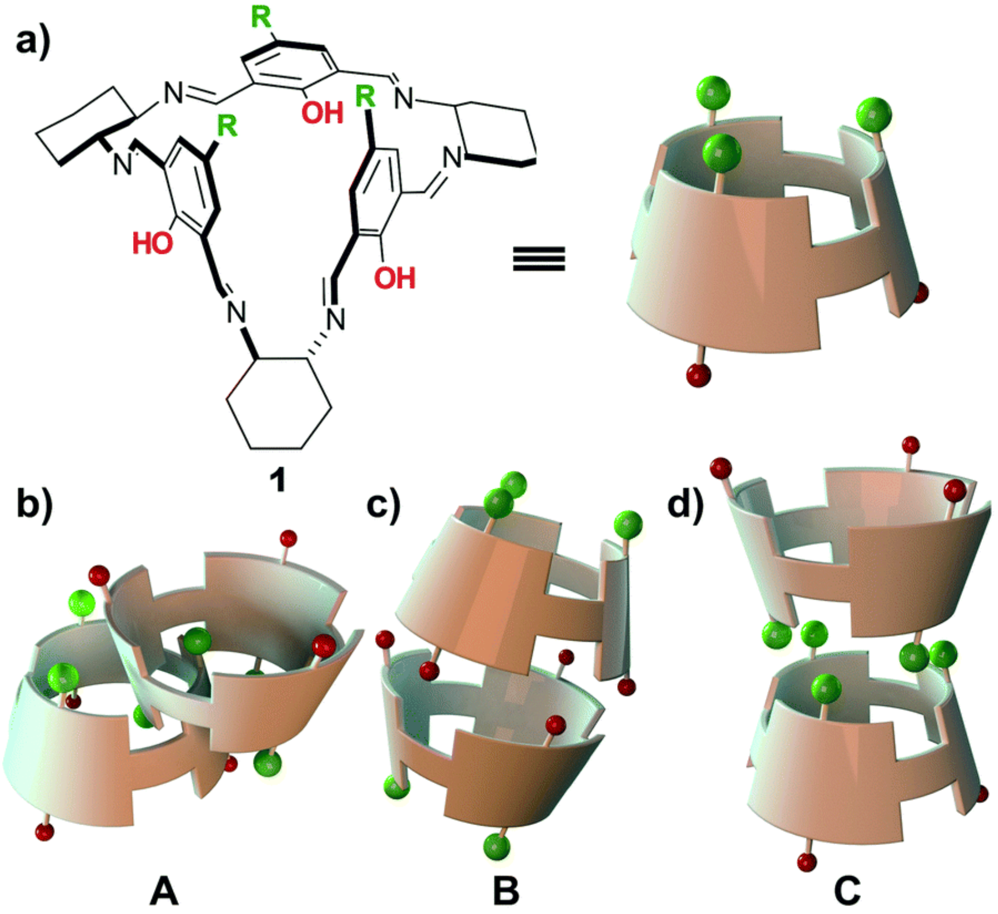

Figure 1.14 (a) General structure of calixsalen and (b–d) possible types of host packing in calixsalen crystals: tail-to-tail dimer (A), capsule (B) and putative structure of an hourglass dimer (C). Reprinted from *CrystEngComm* 2017, 19 (39), 5825-5829.[252] with permission from The Royal Society of Chemistry.

Trianglsalens, which are also called the oxygenated trianglimines, have taken their name from the structurally closest class of unsubstituted trianglimines by adding the suffix “salen”.[177] (Figure 1.12) Trianglsalens often have one or two OH groups on each aromatic ring of the macrocycle.[253, 254] Similar to the trianglimines, the chiral large-ring triangular salen macrocycle can be formed by using linearly connected bis-salicylaldehydes with three or more aromatic rings.[255] This means that their cavity can be easily modified by choosing suitable linearly connected bis-salicylaldehydes. These salen-type macrocycles also have the merit of calixsalens. For example, the triangular structure can be stabilised by the hydrogen bonding. In addition, the formation of supramolecular assemblies can be accomplished by enantioselective self-recognition.[254] Furthermore, trianglsalens have potential for the synthesis of multicenter metal complexes due to the salen units in the structure.

1.3. Assembly of molecular systems by non-covalent bonds

The spontaneous and reversible organization of molecular units into ordered structures are referred as non-covalent assembly or self-assembly, which is mainly derived by weak or non-covalent directional intermolecular interactions such as hydrogen bonding, hydrophobic interactions, aromatic interactions, and electrostatic interactions.[256] For example, hydrogen bonds and coordination bonds are utilised to control assembly to form functional nanostructures in the solid-state using supramolecular chemistry. This is because these two interactions are strong enough to direct the assembly of the precursors but weak enough to allow reversibility and enable self-sorting to occur during the reactions.[256] Although hydrogen bonds are more frequently used in nature, coordination bonds can achieve a higher modularity in their bond strengths and angles.[256] In addition, solvent direction and modular co-crystallisation have been used to direct the assembly of molecular system by using a combination of intermolecular interactions, such as van der Waals forces and electrostatic hydrogen-bonding interactions coupled with the design of molecules with rigid or awkward shapes.[199] Then, self-assembly using hydrogen-bonded assemblies, coordination bonds, solvent templating, and modular co-crystallisation will be introduced.

1.3.1 Hydrogen-bonded assemblies

Hydrogen bonding is primarily an electrostatic force of attraction between a hydrogen atom and more electronegative atoms or groups (hydrogen bond donor, nitrogen, oxygen, or fluorine) and the other hydrogen bond acceptors (hydrogen bond acceptor). The energy of a hydrogen bond can vary between 1 and 40 kcal/mol based on the bonding geometry, the environment, and the nature of the specific donor and acceptor atoms.[257] Hydrogen bond interaction can be somewhat stronger than a van der Waals interaction (0.4 and 4 kJ/mol), but weaker than coordination bonds (90 – 350 kJ/mol) or covalent (300-600 kJ/mol).[258] The intramolecular hydrogen bond interaction, occurring among parts of the same molecule, can help stabilise the molecule's construction. And the intermolecular hydrogen bond interaction, occurring between separate molecules, creates the potential for forming porous molecular materials such as HOFs mentioned in Section 1.1.2.4 and other capsule-like molecules[259] by the self-assembly.

1.3.2 Coordination assemblies

Coordination-driven self-assembly of organic building blocks with metal ions or clusters based on the metal-ligand coordination bond has produced many topologically complex structures, such as rings, helicates, cages, and capsules,[223, 260, 261] as well as knots and links.[262, 263] These assemblies have been used for a number of applications such as optical[264] and electronic devices,[265] catalysis[266, 267] and molecular recognition systems.[213] However, the widespread application of these supramolecular structures has some challenges in synthetic methodology or even industrial production. The first reason is the starting materials, such as some complex organic linkers and metal clusters, are expensive. In addition, the production of defect-free supramolecular assemblies require highly controlled reaction conditions. They can, therefore, be difficult to produce at scale, as the desired assembly may not be accessible via larger synthetic routes.

1.3.3 Solvent direction

A distinguishing difference between molecular solids and frameworks is their solubility. Most molecular solids can be dissolved in common solvents allowing processing options unavailable for insoluble frameworks.[268] New opportunities in molecular solids design have been presented by solvent direction. For example, on–off porosity switching in POCs can be achieved in response to a specific chemical stimulus.[269, 270] For example, different packing methods in POCs are induced from different solvents, and their activated solid have different porosity and selectivity for gases. In addition, the solvent guest incorporation control has been used for tuning porosity in other molecular crystals built by C–H···N-bonded[271] and hydrogen-bonded.[272]

1.3.4 Modular co-crystallisation

The solubility of molecular material is advantageous because it makes it possible to engineer long-range ordered hierarchical structures via supramolecular self-assembly driven by non-covalent forces, such as van der Waals and dipole-dipole interactions, etc.[151, 165] For example, the molecular pores in soluble POCs can be combined via ‘mix-and-match’ strategies (Figure 1.15) using favourable interaction between cages of opposite chirality. Such strategies have been shown to markedly lower the solubility of the racemic POC mixture racemate for similar-sized tetrahedral cages, thus driving co-crystallisation (Figure 1.15b).[273] Using this strategy and mixing two POC enantiomers in solution has made it possible to control size and shape of porous POC co-crystals crystals down to the nanoscale size (Figure 1.15c).[274] This strategy has also been extended to ternary cage co-crystals, as shown in Figure 1.15d, by combining three cage modules, CC1, CC3-R and CC4-R, which is analogous to the concept of multivariate MOFs.[275] Furthermore, the introduction of ‘gating cages’ into a porous co-crystal, by choosing a second cage to exclude a competitive guest, can achieve high guest selectivity.[151] Overall, modular co-crystallisation is a good method to achieve molecular diversity in size, geometry, stereochemistry, electronic properties and other functionalities. This method adjusting the interaction between host and gust could be extended to selectivity capturing certain organic pollutants.

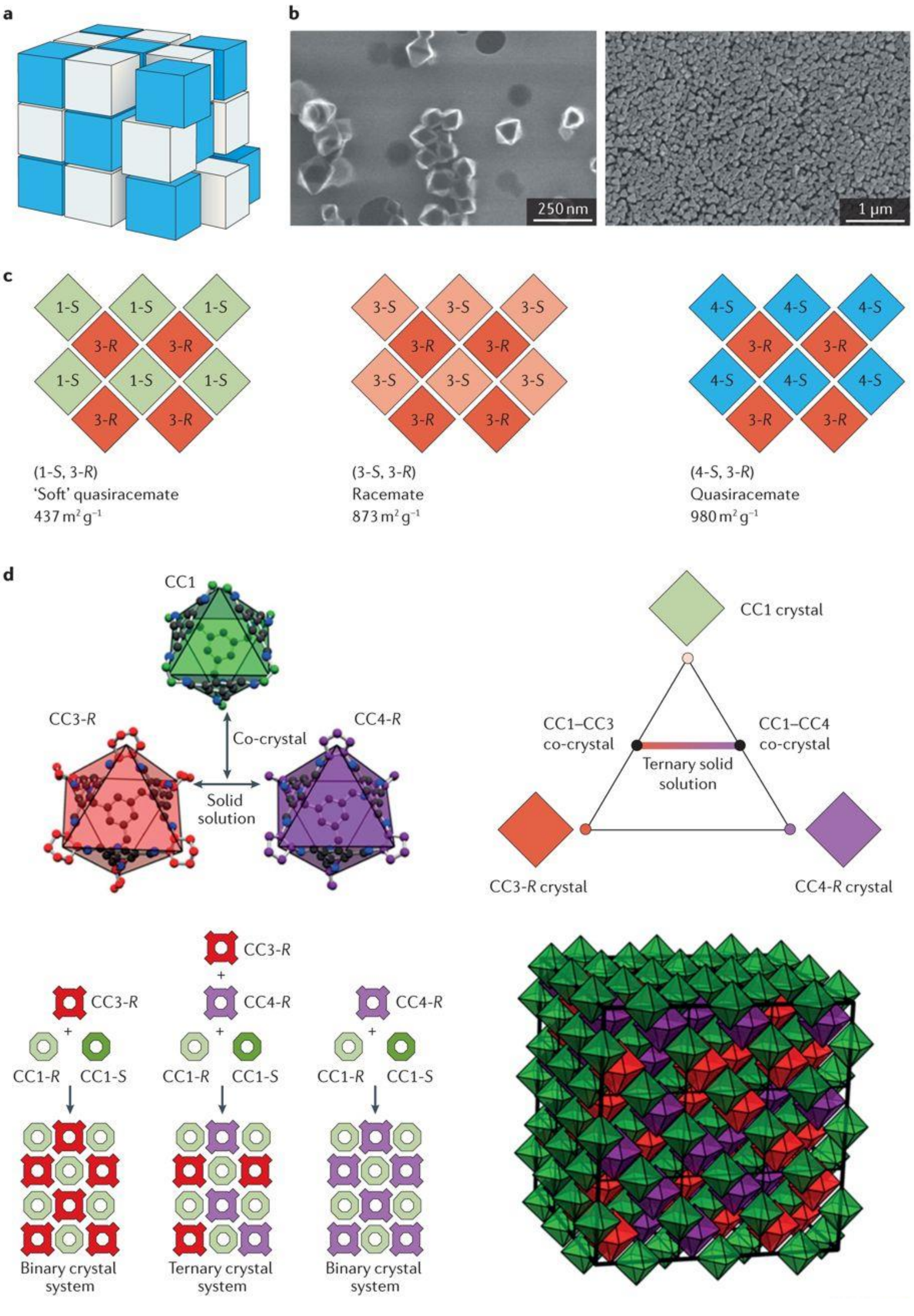

Figure 1.15 Modular co-crystallisation of porous organic cages: (a) a schematic illustration of molecular cage assembly, (b) scanning electron micrographs of the resultant porous nanocrystals, (c) cages with opposing chirality can be combined to make binary co-crystals, (d) the formation of a ternary cage co-crystal using three different cage modules. Reprinted from *Nat. Rev. Mater.*, 2016, 1, 16053.[151] Copyright 2019, with permission from Nature.

1.4 Aims of the project

Although many porous materials have been developed for the gas and vapour separation. It is challenging to develop the materials with highly specific cavity shapes and well defined pore structures for specific and difficult separation process. Macrocycles with molecular recognition and self-assembly characteristics can be the units for the construction of materials that have high selectivity for the specific vapour or gas. Therefore, the aim of this thesis is to develop the molecular crystalline solids based on the assembly of imine macrocycles via non-covalent bonds for the gas and vapour separation.

This idea is from our Cooper Group's work of imine cages for the gas and vapour separation. Through synthetic modification of both the trialdehyde and diamine precursors, the pore structure and affinity of imine cages can be finely-tuned, resulting in enhanced properties with respect to both gas storage and selectivity. Although the synthesis of new imine macrocycles by using different dialdehyde will be discussed in this thesis. The main attention will be paid on designing and synthesising sorbents by the assembly of imine macrocycles.

Chapter 2, *Solvent direction in the assembly of imine macrocycles,* presents a "templating" strategy to construct selective binding sites in a trianglimine macrocycle crystal for ethyl acetate, an important chemical raw material and solvent. X-ray diffraction along with crystal structure prediction is used to understand the structure and the stability of the inclusion complex of the macrocycle with ethyl acetate. The adsorption and breakthrough experiments are used to prove the inherently high selectivity of the guest-free macrocycle towards ethyl acetate, and hence can separate ethyl acetate from azeotropic mixtures with ethanol.

Chapter 3, *Chiral recognition in the assembly of imine macrocycles*, presents a modular assembly – the heterochiral pairing strategy to create porosity in a non-porous trianglimine macrocycles for gas/vapour adsorption. The racemic cocrystal can be obtained by mixing an equal molar ratio of the opposite chirality trianglimines in solvent. Then, X-ray diffraction is used to understand the size of pore and interconnected channel in the crystal. Furthermore, gas adsorption-desorption and vapour adsorption experiments are used to investigate the performance of racemic cocrystal compared with the chiral one.

Chapter 4, *Assembly of imine macrocycles by coordination with metal ion*, presents hollow metal – organic molecules assembled from the enantiopure [3+3] phenolic imine macrocycles with zinc ions. X-ray diffraction is used to understand the structure of the metal organic cages or metal organic polyhedrons. Gas isotherms and separations including the D_2/H_2 separation by quantum sieving is used to explore the potential application of these assemblies.

1.5 References

1. David S Sholl; Ryan P Lively, Seven chemical separations to change the world. *Nature* **2016,** *532* (7600), 435-437.

2. K. Adil, *et al.*, Gas/vapour separation using ultra-microporous metal-organic frameworks: insights into the structure/separation relationship. *Chem. Soc. Rev.* **2017,** *46* (11), 3402-3430.

3. Yu Huang, *et al.*, Low-Energy Distillation-Membrane Separation Process. *Ind. Eng. Chem. Res.* **2010,** *49* (8), 3760-3768.

4. Ryan P. Lively; David S. Sholl, From water to organics in membrane separations. *Nat. Mater.* **2017,** *16* (3), 276-279.

5. Jian-Rong Li, *et al.*, Selective gas adsorption and separation in metal–organic frameworks. *Chem. Soc. Rev.* **2009,** *38* (5), 1477-1504.

6. Zoha Heidarinejad, *et al.*, Methods for preparation and activation of activated carbon: a review. *Environ. Chem. Lett.* **2020,** *18* (2), 393-415.

7. Sadashiv Bubanale; M Shivashankar, History, method of production, structure and applications of activated carbon. *Int. J. Eng. Res.* **2017,** *6*, 495-498.

8. Activated Carbon Market Size, Trends and Report [2021-2028]. https://www.fortunebusinessinsights.com/activated-carbon-market-102175.

9. Wolfgang Heschel; Erhard Klose, On the suitability of agricultural by-products for the manufacture of granular activated carbon. *Fuel* **1995,** *74* (12), 1786-1791.

10. Chafia Bouchelta, *et al.*, Preparation and characterization of activated carbon from date stones by physical activation with steam. *J. Anal. Appl. Pyrolysis* **2008,** *82* (1), 70-77.

11. Mohd Adib Yahya, *et al.*, Agricultural bio-waste materials as potential sustainable precursors used for activated carbon production: A review. *Renew. Sustain. Energy Rev.* **2015,** *46*, 218-235.

12. V. O. Njoku, *et al.*, Preparation of activated carbons from rambutan (Nephelium lappaceum) peel by microwave-induced KOH activation for acid yellow 17 dye adsorption. *Chem. Eng. J.* **2014,** *250*, 198-204.

13. S. Sircar, *et al.*, Activated carbon for gas separation and storage. *Carbon* **1996,** *34* (1), 1-12.

14. Ho-Chul Shin, *et al.*, Removal characteristics of trace compounds of landfill gas by activated carbon adsorption. *Environ. Pollut.* **2002,** *119* (2), 227-236.

15. Javad Keypour, *et al.*, Synthesis of hybrid nano-adsorbent for separation of hydrogen from methane. *Chem. Eng. J.* **2012,** *183*, 510-514.

16. Tănase Dobre, *et al.*, Volatile Organic Compounds Removal from Gas Streams by Adsorption onto Activated Carbon. *Ind. Eng. Chem. Res.* **2014,** *53* (9), 3622-3628.

17. Mohammad Saleh Shafeeyan, *et al.*, A review on surface modification of activated carbon for carbon dioxide adsorption. *J. Anal. Appl. Pyrolysis* **2010,** *89* (2), 143-151.

18. Ivan Petrov; Todor Michalev, Synthesis of zeolite A: a review. *Научни трудове на русенския университет* **2012,** *51*, 30-35.

19. Pramatha Payra, *et al.*, Handbook of zeolite science and technology. *Ohio, USA* **2003**.

20. Edith M Flanigen, *et al.*, Zeolites in industrial separation and catalysis. *Chapter* **2010,** *1*, 1-26.

21. Nils E. R. Zimmermann; Maciej Haranczyk, History and Utility of Zeolite Framework-Type Discovery from a Data-Science Perspective. *Cryst. Growth Des.* **2016,** *16* (6), 3043-3048.

22. Mark E Davis; Raul F Lobo, Zeolite and molecular sieve synthesis. *Chem. Mater.* **1992,** *4* (4), 756-768.

23. Robert J Argauer; George R Landolt, Crystalline zeolite ZSM-5 and method of preparing the same. Google Patents: 1972.

24. Ch Baerlocher, *et al.*, *Atlas of zeolite framework types*. Elsevier: 2007.

25. GT Kokotailo, *et al.*, Structure of synthetic zeolite ZSM-5. *Nature* **1978,** *272* (5652), 437-438.

26. Eo M Flanigen, *et al.*, Silicalite, a new hydrophobic crystalline silica molecular sieve. *Nature* **1978,** *271* (5645), 512-516.

27. Veronique Van Speybroeck, *et al.*, Advances in theory and their application within the field of zeolite chemistry. *Chem. Soc. Rev.* **2015,** *44* (20), 7044-7111.

28. Mark W. Ackley, *et al.*, Application of natural zeolites in the purification and separation of gases. *Microporous Mesoporous Mater.* **2003,** *61* (1), 25-42.

29. G. Centi, *et al.*, Removal of N_2O from Industrial Gaseous Streams by Selective Adsorption over Metal-Exchanged Zeolites. *Ind. Eng. Chem. Res.* **2000,** *39* (1), 131-137.

30. Ocean Cheung; Niklas Hedin, Zeolites and related sorbents with narrow pores for CO_2 separation from flue gas. *RSC Adv.* **2014,** *4* (28), 14480-14494.

31. Nikolay Kosinov, *et al.*, Recent developments in zeolite membranes for gas separation. *J. Membr. Sci.* **2016,** *499*, 65-79.

32. Takao Masuda, *et al.*, Modification of pore size of MFI-type zeolite by catalytic cracking of silane and application to preparation of H_2-separating zeolite membrane. *Microporous Mesoporous Mater.* **2001,** *48* (1-3), 239-245.

33. Katsuki Kusakabe, *et al.*, Formation of a Y-type zeolite membrane on a porous α-alumina tube for gas separation. *Ind. Eng. Chem. Res.* **1997,** *36* (3), 649-655.

34. Jonas Lindmark; Jonas Hedlund, Modification of MFI membranes with amine groups for enhanced CO_2 selectivity. *J. Mater. Chem.* **2010,** *20* (11), 2219-2225.

35. J. Caro, *et al.*, Zeolite membranes – state of their development and perspective. *Microporous Mesoporous Mater.* **2000,** *38* (1), 3-24.

36. Zoey R. Herm, *et al.*, Separation of Hexane Isomers in a Metal-Organic Framework with Triangular Channels. *Science* **2013,** *340* (6135), 960-964.

37. Galo J. de A. A. Soler-Illia, *et al.*, Chemical Strategies To Design Textured Materials: from Microporous and Mesoporous Oxides to Nanonetworks and Hierarchical Structures. *Chem. Rev.* **2002,** *102* (11), 4093-4138.

38. Hong-Cai "Joe" Zhou; Susumu Kitagawa, Metal–Organic Frameworks (MOFs). *Chem. Soc. Rev.* **2014,** *43* (16), 5415-5418.

39. Hiroyasu Furukawa; Omar M Yaghi, Storage of hydrogen, methane, and carbon dioxide in highly porous covalent organic frameworks for clean energy applications. *J. Am. Chem. Soc.* **2009,** *131* (25), 8875-8883.

40. Joseph Della Rocca, *et al.*, Nanoscale metal–organic frameworks for biomedical imaging and drug delivery. *Acc. Chem. Res.* **2011,** *44* (10), 957-968.

41. JeongYong Lee, *et al.*, Metal–organic framework materials as catalysts. *Chem. Soc. Rev.* **2009,** *38* (5), 1450-1459.

42. Liang Feng, *et al.*, Hierarchy in Metal–Organic Frameworks. *ACS Cent. Sci.* **2020,** *6* (3), 359-367.

43. Hailian Li, *et al.*, Design and synthesis of an exceptionally stable and highly porous metal-organic framework. *Nature* **1999,** *402* (6759), 276-279.

44. CMDC Serre, *et al.*, Role of solvent-host interactions that lead to very large swelling of hybrid frameworks. *Science* **2007,** *315* (5820), 1828-1831.

45. Jasmina Hafizovic Cavka, *et al.*, A new zirconium inorganic building brick forming metal organic frameworks with exceptional stability. *J. Am. Chem. Soc.* **2008,** *130* (42), 13850-13851.

46. Gerard Férey, *et al.*, A chromium terephthalate-based solid with unusually large pore volumes and surface area. *Science* **2005,** *309* (5743), 2040-2042.

47. Joseph E. Mondloch, *et al.*, Vapor-Phase Metalation by Atomic Layer Deposition in a Metal–Organic Framework. *J. Am. Chem. Soc.* **2013,** *135* (28), 10294-10297.

48. Dawei Feng, *et al.*, Zirconium-Metalloporphyrin PCN-222: Mesoporous Metal–Organic Frameworks with Ultrahigh Stability as Biomimetic Catalysts. *Angew. Chem. Int. Ed.* **2012,** *51* (41), 10307-10310.

49. Hiroyasu Furukawa, *et al.*, The chemistry and applications of metal-organic frameworks. *Science* **2013,** *341* (6149).

50. Hao Li, *et al.*, Porous metal-organic frameworks for gas storage and separation: Status and challenges. *EnergyChem* **2019,** *1* (1), 100006.

51. Banglin Chen, *et al.*, A microporous metal–organic framework for gas-chromatographic separation of alkanes. *Angew. Chem. Int. Ed.* **2006,** *45* (9), 1390-1393.

52. Long Pan, *et al.*, Separation of hydrocarbons with a microporous metal–organic framework. *Angew. Chem. Int. Ed.* **2006,** *45* (4), 616-619.

53. Kunhao Li, *et al.*, Zeolitic imidazolate frameworks for kinetic separation of propane and propene. *J. Am. Chem. Soc.* **2009,** *131* (30), 10368-10369.

54. Canan Gucuyener, *et al.*, Ethane/ethene separation turned on its head: selective ethane adsorption on the metal− organic framework ZIF-7 through a gate-opening mechanism. *J. Am. Chem. Soc.* **2010,** *132* (50), 17704-17706.

55. Sheng-Chang Xiang, *et al.*, Rationally tuned micropores within enantiopure metal-organic frameworks for highly selective separation of acetylene and ethylene. *Nat. Commun.* **2011,** *2* (1), 1-7.

56. Eric D Bloch, *et al.*, Hydrocarbon separations in a metal-organic framework with open iron (II) coordination sites. *Science* **2012,** *335* (6076), 1606-1610.

57. Pei-Qin Liao, *et al.*, Efficient purification of ethene by an ethane-trapping metal-organic framework. *Nat. Commun.* **2015,** *6* (1), 1-9.

58. Xili Cui, *et al.*, Pore chemistry and size control in hybrid porous materials for acetylene capture from ethylene. *Science* **2016,** *353* (6295), 141-144.

59. Amandine Cadiau, *et al.*, A metal-organic framework–based splitter for separating propylene from propane. *Science* **2016,** *353* (6295), 137-140.

60. Libo Li, *et al.*, Flexible–robust metal–organic framework for efficient removal of propyne from propylene. *J. Am. Chem. Soc.* **2017,** *139* (23), 7733-7736.

61. Bin Li, *et al.*, An ideal molecular sieve for acetylene removal from ethylene with record selectivity and productivity. *Adv. Mater.* **2017,** *29* (47), 1704210.

62. Ji Woong Yoon, *et al.*, Selective nitrogen capture by porous hybrid materials containing accessible transition metal ion sites. *Nat. Mater.* **2017,** *16* (5), 526-531.

63. Pei-Qin Liao, *et al.*, Controlling guest conformation for efficient purification of butadiene. *Science* **2017,** *356* (6343), 1193-1196.

64. Libo Li, *et al.*, Ethane/ethylene separation in a metal-organic framework with iron-peroxo sites. *Science* **2018,** *362* (6413), 443-446.

65. Rui-Biao Lin, *et al.*, Molecular sieving of ethylene from ethane using a rigid metal–organic framework. *Nat. Mater.* **2018,** *17* (12), 1128-1133.

66. Qing Min Wang, *et al.*, Metallo-organic molecular sieve for gas separation and purification. *Microporous Mesoporous Mater.* **2002,** *55* (2), 217-230.

67. Ryotaro Matsuda, *et al.*, Highly controlled acetylene accommodation in a metal–organic microporous material. *Nature* **2005,** *436* (7048), 238-241.

68. Patrick S Bárcia, *et al.*, Kinetic separation of hexane isomers by fixed-bed adsorption with a microporous metal− organic framework. *J. Phys. Chem. B* **2007,** *111* (22), 6101-6103.

69. Hideki Hayashi, *et al.*, Zeolite A imidazolate frameworks. *Nat. Mater.* **2007,** *6* (7), 501-506.

70. Stephen R Caskey, *et al.*, Dramatic tuning of carbon dioxide uptake via metal substitution in a coordination polymer with cylindrical pores. *J. Am. Chem. Soc.* **2008,** *130* (33), 10870-10871.

71. Thomas M McDonald, *et al.*, Cooperative insertion of CO_2 in diamine-appended metal-organic frameworks. *Nature* **2015,** *519* (7543), 303-308.

72. Pei-Qin Liao, *et al.*, Monodentate hydroxide as a super strong yet reversible active site for CO_2 capture from high-humidity flue gas. *Energy Environ. Sci.* **2015,** *8* (3), 1011-1016.

73. U Mueller, *et al.*, Metal–organic frameworks—prospective industrial applications. *J. Mater. Chem.* **2006,** *16* (7), 626-636.

74. Banglin Chen, *et al.*, Surface interactions and quantum kinetic molecular sieving for H_2 and D_2 adsorption on a mixed metal− organic framework material. *J. Am. Chem. Soc.* **2008,** *130* (20), 6411-6423.

75. Anna G. Slater; Andrew I. Cooper, Function-led design of new porous materials. *Science* **2015,** *348* (6238).

76. Jian-Rong Li, *et al.*, Metal–Organic Frameworks for Separations. *Chem. Rev.* **2012,** *112* (2), 869-932.

77. Adrien P. Côté, *et al.*, Porous, Crystalline, Covalent Organic Frameworks. *Science* **2005,** *310* (5751), 1166-1170.

78. Adrien P. Côté, *et al.*, Reticular Synthesis of Microporous and Mesoporous 2D Covalent Organic Frameworks. *J. Am. Chem. Soc.* **2007,** *129* (43), 12914-12915.

79. Brian T. Koo, *et al.*, A classification scheme for the stacking of two-dimensional boronate ester-linked covalent organic frameworks. *J. Mater. Chem.* **2012,** *22* (34), 17460-17469.

80. Shun Wan, *et al.*, A Photoconductive Covalent Organic Framework: Self-Condensed Arene Cubes Composed of Eclipsed 2D Polypyrene Sheets for Photocurrent Generation. *Angew. Chem. Int. Ed.* **2009,** *48* (30), 5439-5442.

81. Fernando J. Uribe-Romo, *et al.*, A Crystalline Imine-Linked 3-D Porous Covalent Organic Framework. *J. Am. Chem. Soc.* **2009,** *131* (13), 4570-4571.

82. Qianrong Fang, *et al.*, Designed synthesis of large-pore crystalline polyimide covalent organic frameworks. *Nat. Commun.* **2014,** *5* (1), 4503.

83. Shan Wang, *et al.*, Exfoliation of Covalent Organic Frameworks into Few-Layer Redox-Active Nanosheets as Cathode Materials for Lithium-Ion Batteries. *J. Am. Chem. Soc.* **2017,** *139* (12), 4258-4261.

84. Sasanka Dalapati, *et al.*, An Azine-Linked Covalent Organic Framework. *J. Am. Chem. Soc.* **2013,** *135* (46), 17310-17313.

85. Manying Liu, *et al.*, Crystalline covalent triazine frameworks by in situ oxidation of alcohols to aldehyde monomers. *Angew. Chem. Int. Ed.* **2018,** *57* (37), 11968-11972.

86. Jia Guo, *et al.*, Conjugated organic framework with three-dimensionally ordered stable structure and delocalized π clouds. *Nat. Commun.* **2013,** *4* (1), 2736.

87. Fernando J. Uribe-Romo, *et al.*, Crystalline Covalent Organic Frameworks with Hydrazone Linkages. *J. Am. Chem. Soc.* **2011,** *133* (30), 11478-11481.

88. Enquan Jin, *et al.*, Two-dimensional sp^2 carbon–conjugated covalent organic frameworks. *Science* **2017,** *357* (6352), 673-676.

89. Xiao Feng, *et al.*, Covalent organic frameworks. *Chem. Soc. Rev.* **2012,** *41* (18), 6010-6022.

90. Jianlong Wang; Shuting Zhuang, Covalent organic frameworks (COFs) for environmental applications. *Coord. Chem. Rev.* **2019,** *400*, 213046.

91. Yi Meng, *et al.*, 2D and 3D porphyrinic covalent organic frameworks: the influence of dimensionality on functionality. *Angew. Chem.* **2020,** *132* (9), 3653-3658.

92. Xiaoxue Kou, *et al.*, Recent advances of covalent organic frameworks and their application in sample preparation of biological analysis. *TrAC, Trends Anal. Chem.* **2021,** *136*, 116182.

93. Chun‐Yu Lin, *et al.*, Design principles for covalent organic frameworks as efficient electrocatalysts in clean energy conversion and green oxidizer production. *Adv. Mater.* **2017,** *29* (17), 1606635.

94. Zhifang Wang, *et al.*, Covalent organic frameworks for separation applications. *Chem. Soc. Rev.* **2020,** *49* (3), 708-735.

95. Bishnu P. Biswal, *et al.*, Chemically Stable Covalent Organic Framework (COF)-Polybenzimidazole Hybrid Membranes: Enhanced Gas Separation through Pore Modulation. *Chem. Eur. J.* **2016,** *22* (14), 4695-4699.

96. Vijay S Vyas, *et al.*, Exploiting noncovalent interactions in an imine‐based covalent organic framework for quercetin delivery. *Adv. Mater.* **2016,** *28* (39), 8749-8754.

97. W Karl Haug, *et al.*, The luminescent and photophysical properties of covalent organic frameworks. *Chem. Soc. Rev.* **2020,** *49* (3), 839-864.

98. Jie Li, *et al.*, Bulk COFs and COF nanosheets for electrochemical energy storage and conversion. *Chem. Soc. Rev.* **2020,** *49* (11), 3565-3604.

99. Heping Ma, *et al.*, A 3D microporous covalent organic framework with exceedingly high C_3H_8/CH_4 and C2 hydrocarbon/CH_4 selectivity. *Chem. Commun.* **2013,** *49* (84), 9773-9775.

100. Hyunchul Oh, *et al.*, A Cryogenically Flexible Covalent Organic Framework for Efficient Hydrogen Isotope Separation by Quantum Sieving. *Angew. Chem. Int. Ed.* **2013,** *52* (50), 13219-13222.

101. Zhongping Li, *et al.*, A 2D azine-linked covalent organic framework for gas storage applications. *Chem. Commun.* **2014,** *50* (89), 13825-13828.

102. Jingru Fu, *et al.*, Fabrication of COF-MOF Composite Membranes and Their Highly Selective Separation of H_2/CO_2. *J. Am. Chem. Soc.* **2016,** *138* (24), 7673-7680.

103. Cheng-Xiong Yang, *et al.*, Facile room-temperature solution-phase synthesis of a spherical covalent organic framework for high-resolution chromatographic separation. *Chem. Commun.* **2015,** *51* (61), 12254-12257.

104. Hai-Long Qian, *et al.*, Bottom-up synthesis of chiral covalent organic frameworks and their bound capillaries for chiral separation. *Nat. Commun.* **2016,** *7* (1), 12104.

105. Shushan Yuan, *et al.*, Covalent organic frameworks for membrane separation. *Chem. Soc. Rev.* **2019,** *48* (10), 2665-2681.

106. Avishek Karmakar, *et al.*, Hydrogen-Bonded Organic Frameworks (HOFs): A New Class of Porous Crystalline Proton-Conducting Materials. *Angew. Chem. Int. Ed.* **2016,** *55* (36), 10667-10671.

107. Yi-Fei Han, *et al.*, Porous Hydrogen-Bonded Organic Frameworks. *Molecules* **2017,** *22* (2), 266.

108. David J Duchamp; RICHARD E Marsh, The crystal structure of trimesic acid (benzene-1, 3, 5-tricarboxylic acid). *Acta Crystallogr., Sect. B: Struct. Crystallogr. Cryst. Chem.* **1969,** *25* (1), 5-19.

109. Jean-Hugues Fournier, *et al.*, Molecular Tectonics. Hydrogen-Bonded Networks Built from Tetraphenols Derived from Tetraphenylmethane and Tetraphenylsilane. *Cryst. Growth Des.* **2003,** *3* (4), 535-540.

110. Dominic Laliberté, *et al.*, Molecular Tectonics. Porous Hydrogen-Bonded Networks Built from Derivatives of Pentaerythrityl Tetraphenyl Ether. *J. Org. Chem.* **2004,** *69* (6), 1776-1787.

111. Ichiro Hisaki, *et al.*, A Series of Layered Assemblies of Hydrogen-Bonded, Hexagonal Networks of C3-Symmetric π-Conjugated Molecules: A Potential Motif of Porous Organic Materials. *J. Am. Chem. Soc.* **2016,** *138* (20), 6617-6628.

112. Teng-Hao Chen, *et al.*, Thermally robust and porous noncovalent organic framework with high affinity for fluorocarbons and CFCs. *Nat. Commun.* **2014,** *5* (1), 5131.

113. Michael Mastalerz; Iris M. Oppel, Rational Construction of an Extrinsic Porous Molecular Crystal with an Extraordinary High Specific Surface Area. *Angew. Chem. Int. Ed.* **2012,** *51* (21), 5252-5255.

114. Linda S. Shimizu, *et al.*, Self-Assembled Nanotubes that Reversibly Bind Acetic Acid Guests. *J. Am. Chem. Soc.* **2003,** *125* (49), 14972-14973.

115. Li-Li Tan, *et al.*, Pillar[5]arene-Based Supramolecular Organic Frameworks for Highly Selective CO_2-Capture at Ambient Conditions. *Adv. Mater.* **2014,** *26* (41), 7027-7031.

116. Carl Henrik Görbitz, Microporous organic materials from hydrophobic dipeptides. *Chem. Eur. J.* **2007,** *13* (4), 1022-1031.

117. Nadia Malek, *et al.*, Molecular Tectonics: Porous Cleavable Networks Constructed by Dipole-Directed Stacking of Hydrogen-Bonded Sheets. *Angew. Chem. Int. Ed.* **2005,** *44* (26), 4021-4025.

118. Xue Huang, *et al.*, Supramolecular organic network assembled from quadruple hydrogen-bonding motifs. *Chem. Commun.* **2016,** *52* (39), 6597-6600.

119. Fatima Helzy, *et al.*, Engineering Hydrogen-Bonded Hexagonal Networks Built from Flexible 1,3,5-Trisubstituted Derivatives of Benzene. *J. Org. Chem.* **2016,** *81* (8), 3076-3086.

120. Peng Li, *et al.*, Solvent Dependent Structures of Hydrogen-Bonded Organic Frameworks of 2,6-Diaminopurine. *Cryst. Growth Des.* **2014,** *14* (7), 3634-3638.

121. Sharon Lie, *et al.*, Molecular Networks Created by Charge-Assisted Hydrogen Bonding in Phosphonate, Phosphate, and Sulfonate Salts of Bis(amidines). *Cryst. Growth Des.* **2014,** *14* (7), 3658-3666.

122. Yabing He, *et al.*, A Microporous Hydrogen-Bonded Organic Framework for Highly Selective C_2H_2/C_2H_4 Separation at Ambient Temperature. *J. Am. Chem. Soc.* **2011,** *133* (37), 14570-14573.

123. Peng Li, *et al.*, A rod‐packing microporous hydrogen‐bonded organic framework for highly selective separation of C_2H_2/CO_2 at room temperature. *Angew. Chem. Int. Ed.* **2015,** *54* (2), 574-577.

124. Zongbi Bao, *et al.*, Fine Tuning and Specific Binding Sites with a Porous Hydrogen-Bonded Metal-Complex Framework for Gas Selective Separations. *J. Am. Chem. Soc.* **2018,** *140* (13), 4596-4603.

125. Xu Zhang, *et al.*, Selective ethane/ethylene separation in a robust microporous hydrogen-bonded organic framework. *J. Am. Chem. Soc.* **2019,** *142* (1), 633-640.

126. J. Gao, *et al.*, A Microporous Hydrogen-Bonded Organic Framework for the Efficient Capture and Purification of Propylene. *Angew. Chem. Int. Ed. Engl.* **2021,** *60* (37), 20400-20406.

127. Catherine M. Aitchison, *et al.*, Photocatalytic proton reduction by a computationally identified, molecular hydrogen-bonded framework. *J. Mater. Chem.* **2020,** *8* (15), 7158-7170.

128. Yugen Zhang; Siti Nurhanna Riduan, Functional porous organic polymers for heterogeneous catalysis. *Chem. Soc. Rev.* **2012,** *41* (6), 2083-2094.

129. Xiaoyan Wang, *et al.*, Nitrogen-rich conjugated microporous polymers: impact of building blocks on porosity and gas adsorption. *J. Mater. Chem.* **2015,** *3* (42), 21185-21193.

130. Neil B. McKeown, *et al.*, Towards Polymer-Based Hydrogen Storage Materials: Engineering Ultramicroporous Cavities within Polymers of Intrinsic Microporosity. *Angew. Chem. Int. Ed.* **2006,** *45* (11), 1804-1807.

131. Jun-Young Lee, *et al.*, Hydrogen adsorption in microporous hypercrosslinked polymers. *Chem. Commun.* **2006,** (25), 2670-2672.

132. Pierre Kuhn, *et al.*, Porous, covalent triazine-based frameworks prepared by ionothermal synthesis. *Angew. Chem. Int. Ed.* **2008,** *47* (18), 3450-3453.

133. Hao Ren, *et al.*, Targeted synthesis of a 3D porous aromatic framework for selective sorption of benzene. *Chem. Commun.* **2010,** *46* (2), 291-293.

134. Weijie Zhang, *et al.*, Retracted Article: Potential applications of functional porous organic polymer materials. *J. Mater. Chem.* **2017,** *5* (19), 8795-8824.

135. Xiang Zhu, *et al.*, In Situ Doping Strategy for the Preparation of Conjugated Triazine Frameworks Displaying Efficient CO_2 Capture Performance. *J. Am. Chem. Soc.* **2016,** *138* (36), 11497-11500.

136. Trevor A. Makal, *et al.*, Methane storage in advanced porous materials. *Chem. Soc. Rev.* **2012,** *41* (23), 7761-7779.

137. Ryan K. Totten, *et al.*, Catalytic Solvolytic and Hydrolytic Degradation of Toxic Methyl Paraoxon with La(catecholate)-Functionalized Porous Organic Polymers. *ACS Catal.* **2013,** *3* (7), 1454-1459.

138. Xi-Sen Wang, *et al.*, A porous covalent porphyrin framework with exceptional uptake capacity of saturated hydrocarbons for oil spill cleanup. *Chem. Commun.* **2013,** *49* (15), 1533-1535.

139. Baltasar Bonillo, *et al.*, Tuning Photophysical Properties in Conjugated Microporous Polymers by Comonomer Doping Strategies. *Chem. Mater.* **2016,** *28* (10), 3469-3480.

140. Weigang Lu, *et al.*, Building multiple adsorption sites in porous polymer networks for carbon capture applications. *Energy Environ. Sci.* **2013,** *6* (12), 3559-3564.

141. Weigang Lu, *et al.*, Polyamine-Tethered Porous Polymer Networks for Carbon Dioxide Capture from Flue Gas. *Angew. Chem. Int. Ed.* **2012,** *51* (30), 7480-7484.

142. Weigang Lu, *et al.*, Sulfonate-Grafted Porous Polymer Networks for Preferential CO_2 Adsorption at Low Pressure. *J. Am. Chem. Soc.* **2011,** *133* (45), 18126-18129.

143. Xiang Zhu, *et al.*, Efficient CO_2 capture by a task-specific porous organic polymer bifunctionalized with carbazole and triazine groups. *Chem. Commun.* **2014,** *50* (59), 7933-7936.

144. J. R. Holst, *et al.*, Porous organic molecules. *Nat. Chem.* **2010,** *2* (11), 915-20.

145. Elena Sanna, *et al.*, Macrocyclic Tetraimines: Synthesis and Reversible Uptake of Diethyl Phthalate by a Porous Macrocycle. *J. Org. Chem.* **2016,** *81* (12), 5173-5180.

146. Kongzhao Su, *et al.*, Reticular Chemistry in the Construction of Porous Organic Cages. *J. Am. Chem. Soc.* **2020,** *142* (42), 18060-18072.

147. Tomokazu Tozawa, *et al.*, Porous organic cages. *Nat. Mater.* **2009,** *8* (12), 973.

148. Gang Zhang, *et al.*, A permanent mesoporous organic cage with an exceptionally high surface area. *Angew. Chem. Int. Ed.* **2014,** *53* (6), 1516-1520.

149. Steven D Bull, *et al.*, Exploiting the reversible covalent bonding of boronic acids: recognition, sensing, and assembly. *Acc. Chem. Res.* **2012,** *46* (2), 312-326.

150. Qi Wang, *et al.*, Solution - Phase Dynamic Assembly of Permanently Interlocked Aryleneethynylene Cages through Alkyne Metathesis. *Angew. Chem. Int. Ed.* **2015,** *54* (26), 7550-7554.

151. Tom Hasell; Andrew I. Cooper, Porous organic cages: soluble, modular and molecular pores. *Nat. Rev. Mater.* **2016,** *1*, 16053.

152. Antonio Avellaneda, *et al.*, Kinetically controlled porosity in a robust organic cage material. *Angew. Chem. Int. Ed.* **2013,** *52* (13), 3746-3749.

153. Chun Zhang, *et al.*, A porous tricyclooxacalixarene cage based on tetraphenylethylene. *Angew. Chem. Int. Ed.* **2015,** *54* (32), 9244-9248.

154. Kosuke Ono, *et al.*, Self-assembly of nanometer-sized boroxine cages from diboronic acids. *J. Am. Chem. Soc.* **2015,** *137* (22), 7015-7018.

155. Jianhong Zhang, *et al.*, A smart porphyrin cage for recognizing azide anions. *Chem. Commun.* **2012,** *48* (30), 3602-3604.

156. Hailong Wang, *et al.*, Post-synthetic modification of porous organic cages. *Chem. Soc. Rev.* **2021**.

157. Malte Brutschy, *et al.*, Porous Organic Cage Compounds as Highly Potent Affinity Materials for Sensing by Quartz Crystal Microbalances. *Adv. Mater.* **2012,** *24* (45), 6049-6052.

158. Xinchun Yang, *et al.*, Encapsulating highly catalytically active metal nanoclusters inside porous organic cages. *Nat. Catal.* **2018,** *1* (3), 214-220.

159. Michael Mastalerz, *et al.*, A Salicylbisimine Cage Compound with High Surface Area and Selective CO_2/CH_4 Adsorption. *Angew. Chem. Int. Ed.* **2011,** *50* (5), 1046-1051.

160. Linjiang Chen, *et al.*, Separation of rare gases and chiral molecules by selective binding in porous organic cages. *Nat. Mater.* **2014,** *13*, 954.

161. Chao Liu, *et al.*, Porous organic cages for efficient gas selective separation and iodine capture. *Chem. Eng. J.* **2022,** *428*, 131129.

162. Tom Hasell, *et al.*, Porous Organic Cages for Sulfur Hexafluoride Separation. *J. Am. Chem. Soc.* **2016,** *138* (5), 1653-1659.

163. Adam Kewley, *et al.*, Porous Organic Cages for Gas Chromatography Separations. *Chem. Mater.* **2015,** *27* (9), 3207-3210.

164. Ming Liu, *et al.*, Barely porous organic cages for hydrogen isotope separation. *Science* **2019,** *366* (6465), 613-620.

165. Mingming Hua, *et al.*, Hierarchically Porous Organic Cages. *Angew. Chem. Int. Ed.* **2021,** *60* (22), 12490-12497.

166. Alan D McNaught; Andrew Wilkinson, *Compendium of chemical terminology*. Blackwell Science Oxford: 1997; Vol. 1669.

167. Yu Wang, *et al.*, Molecular Triangles: A New Class of Macrocycles. *Acc. Chem. Res.* **2021,** *54* (8), 2027-2039.

168. Charles J Pedersen, Cyclic polyethers and their complexes with metal salts. *J. Am. Chem. Soc.* **1967,** *89* (26), 7017-7036.

169. B Dietrich, *et al.*, Diaza-polyoxa-macrocycles et macrobicycles. *Tetrahedron Lett.* **1969,** *10* (34), 2885-2888.

170. B Dietrich, *et al.*, Les cryptates. *Tetrahedron Lett.* **1969,** *10* (34), 2889-2892.

171. Jean-Marie Lehn, Supramolecular Chemistry: Receptors, Catalysts, and Carriers. *Science* **1985,** *227* (4689), 849-856.

172. C. David Gutsche, Calixarenes. *Acc. Chem. Res.* **1983,** *16* (5), 161-170.

173. Neng-yang Shih. Host-guest chemistry of cucurbituril. University of Illinois at Chicago, 1981.

174. Tomoki Ogoshi, *et al., para*-Bridged symmetrical pillar [5] arenes: their Lewis acid catalyzed synthesis and host–guest property. *J. Am. Chem. Soc.* **2008,** *130* (15), 5022-5023.

175. Mikhail V Rekharsky; Yoshihisa Inoue, Complexation thermodynamics of cyclodextrins. *Chem. Rev.* **1998,** *98* (5), 1875-1918.

176. Walter Jentzen, *et al.*, Conservation of the Conformation of the Porphyrin Macrocycle in Hemoproteins. *Biophys. J.* **1998,** *74* (2), 753-763.

177. Marcin Kwit, *et al.*, One-Step Construction of the Shape Persistent, Chiral But Symmetrical Polyimine Macrocycles. *The Chemical Record* **2019,** *19* (2-3), 213-237.

178. James R Dobscha, *et al.*, Sequence-defined macrocycles for understanding and controlling the build-up of hierarchical order in self-assembled 2D arrays. *J. Am. Chem. Soc.* **2019,** *141* (44), 17588-17600.

179. Andrew Hamilton, *et al.*, Coreceptor molecules. Synthesis of metalloreceptors containing porphyrin subunits and formation of mixed substrate supermolecules by binding of organic substrates and of metal ions. *J. Am. Chem. Soc.* **1986,** *108* (17), 5158-67.

180. Rosaria Schettini, *et al.*, Macrocyclic Hosts in Asymmetric Phase-Transfer Catalyzed Reactions. *Synthesis* **2018,** *50* (24), 4777-4795.

181. Alamgir Hossain, *et al.* In *Supramolecular complexes of nucleotides with a macrocycle-based molecular host*, American Chemical Society: 2018; pp INOR-705.

182. Chiara M. A. Gangemi, *et al.*, Supramolecular complexes for nanomedicine. *Bioorg. Med. Chem. Lett.* **2018,** *28* (20), 3290-3301.

183. R Peila, *et al.*, Different methods for β-cyclodextrin/triclosan complexation as antibacterial treatment of cellulose substrates. *Cellulose* **2013,** *20* (4), 2115-2123.

184. N. Szaniszlo, *et al.*, Structure-stability study of cyclodextrin complexes with selected volatile hydrocarbon contaminants of soils. *J Incl Phenom Macro* **2005,** *53* (3-4), 241-248.

185. Diego M. Alzate-Sánchez, *et al.*, Cotton Fabric Functionalized with a β-Cyclodextrin Polymer Captures Organic Pollutants from Contaminated Air and Water. *Chem. Mater.* **2016,** *28* (22), 8340-8346.

186. Alexander Katz, *et al.* In *The Design and Synthesis of Immobilized Calix-[4]-arene Materials for the Specific Adsorption of Organic Molecules from Aqueous Solution*, American Chemical Society: 2002; pp IEC-051.

187. Kecheng Jie, *et al.*, Near-Ideal Xylene Selectivity in Adaptive Molecular Pillar[n]arene Crystals. *J. Am. Chem. Soc.* **2018,** *140* (22), 6921-6930.

188. Kecheng Jie, *et al.*, Styrene Purification by Guest-Induced Restructuring of Pillar[6]arene. *J. Am. Chem. Soc.* **2017,** *139* (8), 2908-2911.

189. Qing Ji, *et al.*, Cyclotetrabenzoin: Facile Synthesis of a Shape‐Persistent Molecular Square and Its Assembly into Hydrogen‐Bonded Nanotubes. *Chem. Eur. J.* **2015,** *21* (48), 17205-17209.

190. Merry K Smith; Ognjen Š Miljanić, Arylene ethynylene macrocycles: from molecular hosts to components of high-performance supramolecular architectures. *Org. Biomol. Chem.* **2015,** *13* (29), 7841-7845.

191. Elena Sanna, *et al.*, A crystalline sponge based on dispersive forces suitable for X-ray structure determination of included molecular guests. *Chem. Sci.* **2015,** *6* (10), 5466-5472.

192. Kenneth E. Maly, Assembly of nanoporous organic materials from molecular building blocks. *J. Mater. Chem.* **2009,** *19* (13), 1781-1787.

193. Arne Thomas, *et al.*, Hard templates for soft materials: Creating nanostructured organic material. *Chem. Mater.* **2008,** *20* (3), 738-755.

194. Jens Weber, *et al.*, Mesoporous poly(benzimidazole) networks via solvent mediated templating of hard spheres. *Macromolecules* **2007,** *40* (4), 1299-1304.

195. I. Hisaki, *et al.*, Designing Hydrogen-Bonded Organic Frameworks (HOFs) with Permanent Porosity. *Angew. Chem. Int. Ed. Engl.* **2019,** *58* (33), 11160-11170.

196. Omar Barreda, *et al.*, Ligand-Based Phase Control in Porous Molecular Assemblies. *ACS Appl. Mater. Interfaces* **2018,** *10* (14), 11420-11424.

197. Timothy R. Cook; Peter J. Stang, Recent Developments in the Preparation and Chemistry of Metallacycles and Metallacages via Coordination. *Chem. Rev.* **2015,** *115* (15), 7001-7045.

198. Mei Pan, *et al.*, Chiral metal–organic cages/containers (MOCs): From structural and stereochemical design to applications. *Coord. Chem. Rev.* **2019,** *378,* 333-349.

199. Marc A. Little; Andrew I. Cooper, The Chemistry of Porous Organic Molecular Materials. *Adv. Funct. Mater.* **2020,** *30* (41), 1909842.

200. Dawei Zhang, *et al.*, Metal–organic cages for molecular separations. *Nat. Rev. Chem.* **2021**.

201. Rolf W. Saalfrank, *et al.*, The First “Adamantoid” Alkaline Earth Metal Chelate Complex: Synthesis, Structure, and Reactivity. *Angew. Chem. Int. Ed.* **1988,** *27* (6), 851-853.

202. Makoto Fujita, *et al.*, Guest-Induced Organization of a Three-Dimensional Palladium(II) Cagelike Complex. A Prototype for "Induced-Fit" Molecular Recognition. *J. Am. Chem. Soc.* **1995,** *117* (5), 1649-1650.

203. Makoto Fujita, *et al.*, Self-assembly of ten molecules into nanometre-sized organic host frameworks. *Nature* **1995,** *378* (6556), 469-471.

204. M. Eddaoudi, *et al.*, Porous Metal−Organic Polyhedra: 25 Å Cuboctahedron Constructed from 12 $Cu_2(CO_2)_4$ Paddle-Wheel Building Blocks. *J. Am. Chem. Soc.* **2001,** *123* (18), 4368-4369.

205. Michel Meyer, *et al.*, Rearrangement Reactions in Dinuclear Triple Helicates1. *Inorg. Chem.* **1997,** *36* (23), 5179-5191.

206. Bogdan Olenyuk, *et al.*, Self-assembly of nanoscale cuboctahedra by coordination chemistry. *Nature* **1999,** *398* (6730), 796-799.

207. F. Albert Cotton, *et al.*, Supramolecular Arrays Based on Dimetal Building Units. *Acc. Chem. Res.* **2001,** *34* (10), 759-771.

208. Christopher G. Oliveri, *et al.*, Heteroligated Supramolecular Coordination Complexes Formed via the Halide-Induced Ligand Rearrangement Reaction. *Acc. Chem. Res.* **2008,** *41* (12), 1618-1629.

209. Yuzhen Zhang, *et al.*, Phosphorescent Decanuclear Bimetallic Pt_6M_4 (M = Zn, Fe) Tetrahedral Cages. *Inorg. Chem.* **2017,** *56* (8), 4258-4262.

210. Edmundo G. Percástegui, *et al.*, Waterproof architectures through subcomponent self-assembly. *Chem. Sci.* **2019,** *10* (7), 2006-2018.

211. Aeri J. Gosselin, *et al.*, Permanently Microporous Metal–Organic Polyhedra. *Chem. Rev.* **2020,** *120* (16), 8987-9014.

212. Gavin A. Craig, *et al.*, Hysteresis in the gas sorption isotherms of metal–organic cages accompanied by subtle changes in molecular packing. *Chem. Commun.* **2020,** *56* (25), 3689-3692.

213. Zhi-Yin Zhang, *et al.*, Guest-boosted phosphorescence efficiency of a supramolecular cage. *Inorg. Chem. Front.* **2021,** *8* (9), 2299-2304.

214. Chunqing Ji, *et al.*, A high-efficiency dye-sensitized Pt(II) decorated metal-organic cage for visible-light-driven hydrogen production. *Appl. Catal. B* **2021,** *285*, 119782.

215. Nobuhiko Hosono, *et al.*, Metal–Organic Polyhedral Core as a Versatile Scaffold for Divergent and Convergent Star Polymer Synthesis. *J. Am. Chem. Soc.* **2016,** *138* (20), 6525-6531.

216. Graeme M. Day; Andrew I. Cooper, Energy–Structure–Function Maps: Cartography for Materials Discovery. *Adv. Mater.* **2018,** *30* (37), 1704944.

217. Jesse M. Teo, *et al.*, Hetero-bimetallic metal–organic polyhedra. *Chem. Commun.* **2016,** *52* (2), 276-279.

218. A. W. Augustyniak, *et al.*, A vanadium(iv) pyrazolate metal–organic polyhedron with permanent porosity and adsorption selectivity. *Chem. Commun.* **2015,** *51* (79), 14724-14727.

219. Gregory R. Lorzing, *et al.*, Selective Gas Adsorption in Highly Porous Chromium(II)-Based Metal–Organic Polyhedra. *Chem. Mater.* **2017,** *29* (20), 8583-8587.

220. Jinhee Park, *et al.*, Chromium(II) Metal–Organic Polyhedra as Highly Porous Materials. *ACS Appl. Mater. Interfaces* **2017,** *9* (33), 28064-28068.

221. Xinxin Hang, *et al.*, Discrete {Ni_{40}} Coordination Cage: A Calixarene-Based Johnson-Type (J_{17}) Hexadecahedron. *J. Am. Chem. Soc.* **2016,** *138* (9), 2969-2972.

222. Stephen P. Argent, *et al.*, Porous Metal–Organic Polyhedra: Morphology, Porosity, and Guest Binding. *Inorg. Chem.* **2020,** *59* (21), 15646-15658.

223. David J. Tranchemontagne, *et al.*, Reticular Chemistry of Metal–Organic Polyhedra. *Angew. Chem. Int. Ed.* **2008,** *47* (28), 5136-5147.

224. Sara Pasquale, *et al.*, Giant regular polyhedra from calixarene carboxylates and uranyl. *Nat. Commun.* **2012,** *3* (1), 785.

225. Guoliang Liu, *et al.*, Process-Tracing Study on the Postassembly Modification of Highly Stable Zirconium Metal–Organic Cages. *J. Am. Chem. Soc.* **2018,** *140* (20), 6231-6234.

226. Feng-Rong Dai, *et al.*, Synthetic Supercontainers Exhibit Distinct Solution versus Solid State Guest-Binding Behavior. *J. Am. Chem. Soc.* **2014,** *136* (20), 7480-7491.

227. Michael J. Bojdys, *et al.*, Supramolecular Engineering of Intrinsic and Extrinsic Porosity in Covalent Organic Cages. *J. Am. Chem. Soc.* **2011,** *133* (41), 16566-16571.

228. Andrés E. Martín Díaz; James E. M. Lewis, Structural Flexibility in Metal-Organic Cages. *Front. Chem.* **2021,** *9* (456).

229. Edmundo G. Percástegui; Vojtech Jancik, Coordination-driven assemblies based on meso-substituted porphyrins: Metal-organic cages and a new type of meso-metallaporphyrin macrocycles. *Coord. Chem. Rev.* **2020,** *407*, 213165.

230. Aleksandra Sarnicka, *et al.*, Controlling the macrocycle size by the stoichiometry of the applied template ion. *Chem. Commun.* **2012,** *48* (16), 2237-2239.

231. Feng-Rong Dai; Zhenqiang Wang, Modular Assembly of Metal–Organic Supercontainers Incorporating Sulfonylcalixarenes. *J. Am. Chem. Soc.* **2012,** *134* (19), 8002-8005.

232. Shangchao Du, *et al.*, A giant coordination cage based on sulfonylcalix[4]arenes. *Chem. Commun.* **2012,** *48* (73), 9177-9179.

233. Mei Liu, *et al.*, Calixarene-Based Nanoscale Coordination Cages. *Angew. Chem. Int. Ed.* **2012,** *51* (7), 1585-1588.

234. Hugo Schiff, Sur quelques dérivés phéniques des aldéhydes. *Anal. Chim.* **1864,** *131*, 118.

235. Cari D Meyer, *et al.*, Template-directed synthesis employing reversible imine bond formation. *Chem. Soc. Rev.* **2007,** *36* (11), 1705-1723.

236. Maria Ciaccia; Stefano Di Stefano, Mechanisms of imine exchange reactions in organic solvents. *Org. Biomol. Chem.* **2015,** *13* (3), 646-654.

237. Nikolai Kuhnert, *et al.*, The synthesis of trianglimines: On the scope and limitations of the [3 + 3] cyclocondensation reaction between (1*R*,2*R*)-diaminocyclohexane and aromatic dicarboxaldehydes. *Org. Biomol. Chem.* **2003,** *1* (7), 1157-1170.

238. Marcin Kwit, *et al.*, Chiral Macrocyclic Aliphatic Oligoimines Derived from trans-1,2-Diaminocyclohexane. *Chem. Eur. J.* **2007,** *13* (31), 8688-8695.

239. Stuart J Rowan, *et al.*, Dynamic covalent chemistry. *Angew. Chem. Int. Ed.* **2002,** *41* (6), 898-952.

240. Ignacio Alfonso, Chiral Molecular Receptors Based on Trans-Cyclohexane-1,2-diamine. *Curr. Org. Synth.* **2010,** *7* (1), 1-23.

241. J. Gawroński, *et al.*, Designing large triangular chiral macrocycles: efficient [3 + 3] diamine−dialdehyde condensations based on conformational bias. *J. Org. Chem.* **2000,** *65* (18), 5768-5773.

242. Martin Chadim, *et al.*, (3+3)-Cyclocondensation of the enantiopure and racemic forms of trans-1,2-diaminocyclohexane with terephthaldehyde. Formation of diastereomeric molecular triangles and their stereoselective solid-state stacking into microporous chiral columns. *Tetrahedron: Asymmetry* **2001,** *12* (1), 127-133.

243. Janusz Gregoliński, *et al.*, New 2+ 2, 3+ 3 and 4+ 4 macrocycles derived from 1, 2-diaminocyclohexane and 2, 6-diformylpyridine. *Org. Biomol. Chem.* **2005,** *3* (17), 3161-3166.

244. Hany F. Nour, *et al.*, Probing the mechanism and dynamic reversibility of trianglimine formation using real-time electrospray ionization time-of-flight mass spectrometry. *Rapid Commun. Mass Spectrom.* **2012,** *26* (9), 1070-1080.

245. Nikolai Kuhnert, *et al.*, The synthesis and conformation of oxygenated trianglimine macrocycles. *Org. Biomol. Chem.* **2005,** *3* (3), 524-537.

246. Zengmin Li; Chet Jablonski, Synthesis and characterization of 'calixsalens': a new class of macrocyclic chiral ligands. *Chem. Commun.* **1999,** (16), 1531-1532.

247. Agnieszka Janiak, *et al.*, An unexpected relationship between solvent inclusion and gas sorption properties of chiral calixsalen solids. *Supramol. Chem.* **2018,** *30* (5-6), 479-487.

248. Marcin Kwit, *et al.*, Synthesis, structure, and contrasting chiroptical properties of large trianglimine macrocycles. *Chirality* **2005,** *17* (Suppl.), S93-S100.

249. Marcin Kwit, *et al.*, One-Step Construction of the Shape Persistent, Chiral But Symmetrical Polyimine Macrocycles. *Chem Rec* **2019,** *19* (2-3), 213-237.

250. Agnieszka Janiak, *et al.*, Readily prepared inclusion forming chiral calixsalens. *Org. Biomol. Chem.* **2016,** *14* (2), 669-673.

251. M. Kwit; J. Gawronski, Chiral calixsalen-type macrocycles from trans-1,2-diaminocyclohexane. *Tetrahedron: Asymmetry* **2003,** *14* (10), 1303-1308.

252. Małgorzata Petryk, *et al.*, Unexpected formation of a tubular architecture by optically active pure organic calixsalen. *CrystEngComm* **2017,** *19* (39), 5825-5829.

253. Joanna Szymkowiak; Marcin Kwit, Electronic and vibrational exciton coupling in oxidized trianglimines. *Chirality* **2018,** *30* (2), 117-130.

254. Joanna Szymkowiak, *et al.*, Consistent supramolecular assembly arising from a mixture of components – self-sorting and solid solutions of chiral oxygenated trianglimines. *CrystEngComm* **2018,** *20* (35), 5200-5208.

255. Marcin Kwit, *et al.*, Synthesis of chiral large-ring triangular salen ligands and structural characterization of their complexes. *Dalton Trans.* **2009,** (34), 6783-6789.

256. Jean-Pierre Sauvage; Pierre Gaspard, *From non-covalent assemblies to molecular machines*. John Wiley & Sons: 2011.

257. Thomas Steiner, The Hydrogen Bond in the Solid State. *Angew. Chem. Int. Ed.* **2002,** *41* (1), 48-76.

258. Juncong Jiang, *et al.*, Covalent Chemistry beyond Molecules. *J. Am. Chem. Soc.* **2016,** *138* (10), 3255-3265.

259. Kenji Kobayashi; Masamichi Yamanaka, Self-assembled capsules based on tetrafunctionalized calix[4]resorcinarene cavitands. *Chem. Soc. Rev.* **2015,** *44* (2), 449-466.

260. M. Jaya Prakash; Myoung Soo Lah, Metal–organic macrocycles, metal–organic polyhedra and metal–organic frameworks. *Chem. Commun.* **2009,** (23), 3326-3341.

261. Scott J Dalgarno, *et al.*, Metallo-supramolecular capsules. *Coord. Chem. Rev.* **2008,** *252* (8-9), 825-841.

262. Ross S. Forgan, *et al.*, Chemical Topology: Complex Molecular Knots, Links, and Entanglements. *Chem. Rev.* **2011,** *111* (9), 5434-5464.

263. Jonathon E. Beves, *et al.*, Strategies and Tactics for the Metal-Directed Synthesis of Rotaxanes, Knots, Catenanes, and Higher Order Links. *Angew. Chem. Int. Ed.* **2011,** *50* (40), 9260-9327.

264. A. Prasanna de Silva*, et al.*, Newer optical-based molecular devices from older coordination chemistry. *Dalton Trans.* **2003,** (10), 1902-1913.

265. Li-Ping Sun, *et al.*, Crystal structure and surface photovoltage of a series of Ni(II) coordination supramolecular polymer. *Inorg. Chem. Commun.* **2006,** *9* (7), 679-682.

266. Nathan C. Gianneschi, *et al.*, A Supramolecular Approach to an Allosteric Catalyst. *J. Am. Chem. Soc.* **2003,** *125* (35), 10508-10509.

267. Zi-Ye Chen, *et al.*, Cobalt-Based Metal–Organic Cages for Visible-Light-Driven Water Oxidation. *Inorg. Chem.* **2021,** *60* (14), 10380-10386.

268. T. Hasell, *et al.*, Controlling the crystallization of porous organic cages: molecular analogs of isoreticular frameworks using shape-specific directing solvents. *J. Am. Chem. Soc.* **2014,** *136* (4), 1438-48.

269. James T. A. Jones, *et al.*, On–Off Porosity Switching in a Molecular Organic Solid. *Angew. Chem. Int. Ed.* **2011,** *50* (3), 749-753.

270. S. Bera, *et al.*, Porosity Switching in Polymorphic Porous Organic Cages with Exceptional Chemical Stability. *Angew. Chem. Int. Ed.* **2019,** *58* (13), 4243-4247.

271. Hiroshi Yamagishi, *et al.*, Self-assembly of lattices with high structural complexity from a geometrically simple molecule. *Science* **2018,** *361* (6408), 1242-1246.

272. You-Gui Huang, *et al.*, Superior thermoelasticity and shape-memory nanopores in a porous supramolecular organic framework. *Nat. Commun.* **2016,** *7* (1), 11564.

273. James T. A. Jones, *et al.*, Modular and predictable assembly of porous organic molecular crystals. *Nature* **2011,** *474*, 367.

274. T. Hasell, *et al.*, Porous organic cage nanocrystals by solution mixing. *J. Am. Chem. Soc.* **2012,** *134* (1), 588-98.

275. Hexiang Deng, *et al.*, Multiple functional groups of varying ratios in metal-organic frameworks. *Science* **2010,** *327* (5967), 846-850.

Chapter 2:

Solvent direction in the assembly of imine macrocycles

2.1 Contributions to this chapter

The work reported in Chapter 2 is published in Donglin He[‡]; Chengxi Zhao[‡]; Linjiang Chen; Marc Little; Samantha Chong; Rob Clowes; Katherine McKie; Mark Roper; Graeme Day*; Ming Liu*; Andrew I. Cooper*. *Chemistry - A European Journal*, 2021, 27 (41), 10589-10594. (‡ authors contributed equally)

Author Contributions: Dr Ming Liu, Prof Andy I. Cooper, and Donglin He conceived and designed the project. Donglin He synthesised and characterised the compounds. Dr Marc A. Little collected and refined the data of single crystal structures. Dr Samantha Y. Chong performed the high-resolution variable temperature PXRD measurements. Rob Clowes assisted with gas isotherms measurements. Prof Graeme M. Day performed and supervised crystal structure prediction (CSP) calculation. Dr Chengxi Zhao performed the electrostatic surface potential (ESP), NCI, and CSP calculations. Dr Linjiang Chen performed the ideal adsorbed solution theory (IAST) calculations. Katherine McKie and Mark G. Roper performed vapour sorption experiments. Donglin He drafted the manuscript and all authors provided critical feedback and helped shape the manuscript.

2.2 Introduction

2.2.1 Selective adsorption of ethyl acetate

Ethyl acetate (EA) is an important solvent for the chemical industry. It is also a key volatile organic compound (VOC) that can determine the flavour and quality of beers or wines.[1] EA is also a biomarker for the early diagnosis of lung cancer.[2-4] Fisher esterification of ethanol (EtOH) is the primary industrial process for synthesising EA. The subsequent separation of EA from EtOH is difficult because they have similar boiling points (78.5 °C and 77.1 °C, respectively); EA and EtOH can also form azeotropic mixtures.[5] Current purification techniques include extractive distillation,[6] azeotropic distillation using ionic liquids,[7] and membrane separation,[8] but these can be inefficient and energy-intensive. There is potential to find alternative separation processes based on selective adsorption using microporous materials that can operate under atmospheric conditions. In addition to separations, porous materials with high selectivity for EA might be used as sorbents in thermal desorption techniques[9] to quantify trace level (ppm) EA from a gas mixture.

2.2.2 Trianglimine macrocycle (TAMC)

The trianglimine macrocycle (**TAMC**) shown in Figure 2.1 is formed from the condensation of terephthalaldehyde and (1*R*,2*R*)-diaminocyclohexane, and was first reported in 2000.[10] The amine form of **TAMC** was reported to be a good host for tricarboxylic acids or anions in solution.[11, 12] Most recently, **TAMC** was shown to form supramolecular organic frameworks with intrinsic porosity, which show good selectivity for CO_2 over CH_4.[13] In this chapter, "templating" strategy is used to construct selective binding sites in **TAMC** crystals for ethyl acetate. X-ray diffraction and crystal structure predictions are used to understand the structure and the stability of the inclusion complex of the macrocycle with ethyl acetate. The adsorption and breakthrough experiments are used to prove the inherently high selectivity of the guest-free macrocycle towards EA. They can therefore separate ethyl acetate from azeotropic mixtures with ethanol.

2.2.3 Crystal structure prediction (CSP)

Reliable methods of predicting the crystal structure of a compound, based only on its composition, is important in academic and industrial science, particularly for pharmaceuticals where polymorphism is beneficial.[14, 15] The crystal structure prediction (CSP) aims typically to search for the minimum-energy arrangement of the molecule's constituent atoms in space. CSP has been successfully applied in large but relatively rigid systems, such as porous organic cages,[16] pillar[n]arene[17] and hydrogen-bonded organic framework.[18] However, it remains difficult to predict all the possible putative polymorphs for flexible systems, starting from the chemical diagram only.

In this chapter, to investigate how the macrocycle's flexibility contributes to the adsorption process, CSP is used to calculate the landscapes of the possible 1:1 EA:**TAMC** co-crystal structures available to both the conformation that was extracted from the experiment for EA@**TAMC** crystal structure the calculated gas phase minimum conformer from a conformational search. In addition, CSP calculations were performed on guest-free **TAMC** using the gas phase conformer, followed by DFT re-optimisation of the predicted structures.

2.3 TMAC synthesis and characterisation

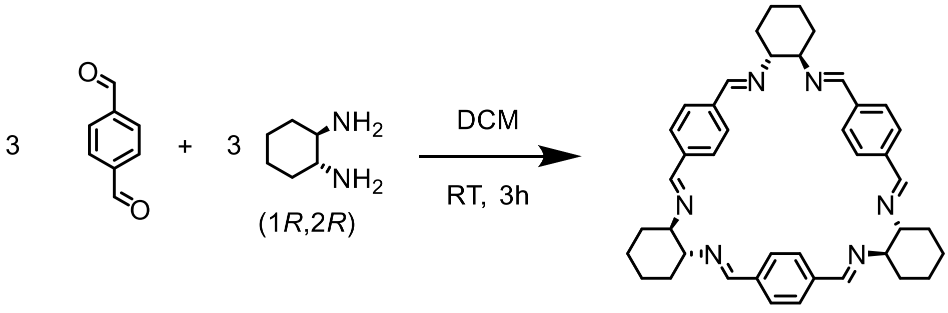

TAMC

Figure 2.1. Scheme of the synthesis of **TAMC.**

TAMC was synthesised as described previously.[10] Terephthaldehyde (1.34 g, 10 mmol) in dichloromethane (8.3 ml) was added to a solution of (1*R*,2*R*)-diaminocyclohexane (1.14 g, 10 mmol) in dichloromethane (5 ml). The mixture was stirred at room temperature for 3 h. The solvent was evaporated under vacuum, to afford the crude compound as a white powder. It should be noted that (1*S*,2*S*)-diaminocyclohexane can be used to synthesise the opposite enantiomer of **TAMC**, but only the 1*R*,2R enantiomer shown in Figure 2.1 was used in this study. After synthesis, **TAMC** was recrystallised from EA to afford a crystal structure named EA@**TAMC** as colourless needles. Unexpectedly, we found that one molecule of EA per **TAMC** molecule remained in the structure after the **TAMC** crystals were activated under a high vacuum at room temperature; this was deduced initially from thermogravimetric analysis (TGA, Figure 2.2a) and ^{1}H NMR data (Figure 2.2b). We found that these residual EA molecules were bound strongly, and they could only be removed from the solvated crystals by heating at temperatures above 70 °C under a high vacuum for about 12h to afford the guest free polymorph named *α*-**TAMC** (Figure 2.2c).

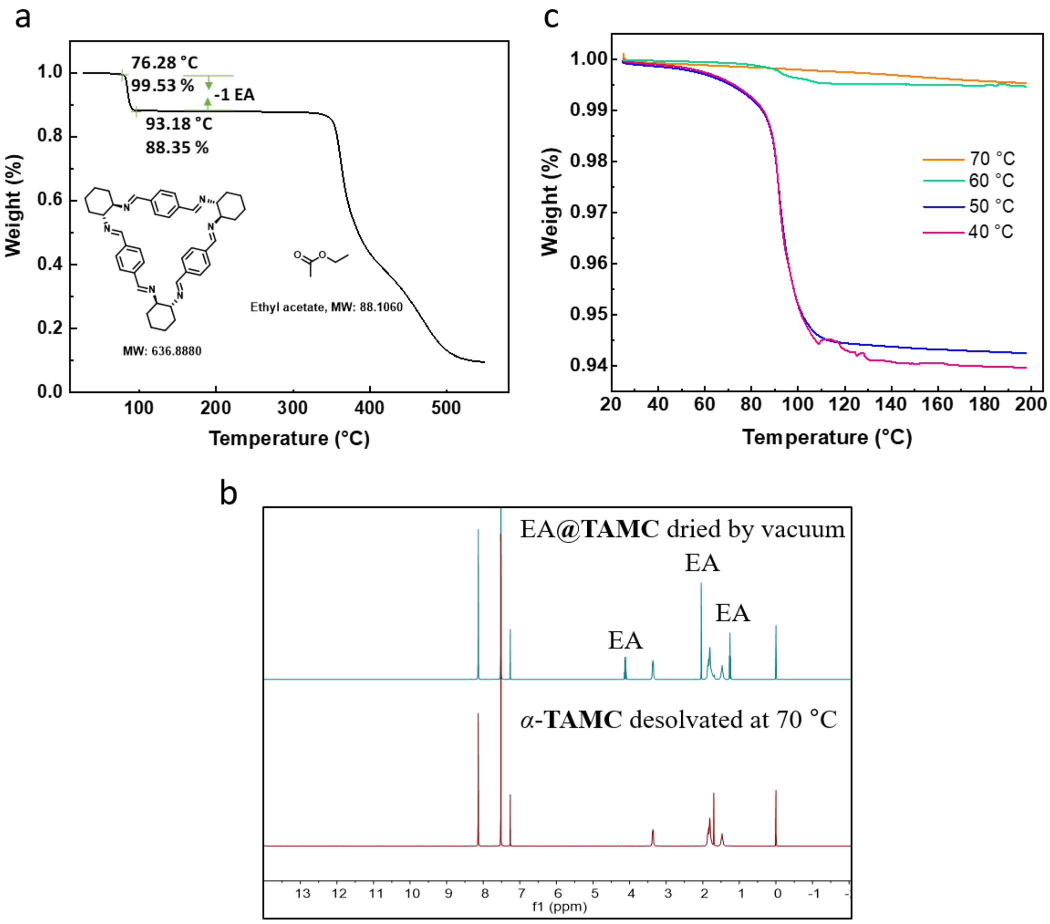

Figure 2.2. (a) Thermogravimetric analysis of EA@**TAMC** crystal. (b) ^{1}H NMR spectrum (400 MHz, $CDCl_3$, 293 K) of EA@**TAMC** and guest-free *α*-**TAMC** desolvated at 70 °C. (c) Thermogravimetric analysis of EA@**TAMC** samples that were heated at different temperatures (40–70 °C) under vacuum.

2.4 Structural analysis of TAMC

The single crystal structure for EA@**TAMC** confirmed the 1:1 **TAMC**: EA molar ratio, with the ethyl group of each EA molecule being located in the centre of the **TAMC** cavity, interacting with **TAMC** via three of C–H···π interactions (Figure 2.3a). The acetate ester group of EA is located in an extrinsic void created between three **TAMC** molecules. There is also a hydrogen bond interaction between the carbonyl oxygen atom of EA and the cyclohexane group of a second **TAMC** molecule.

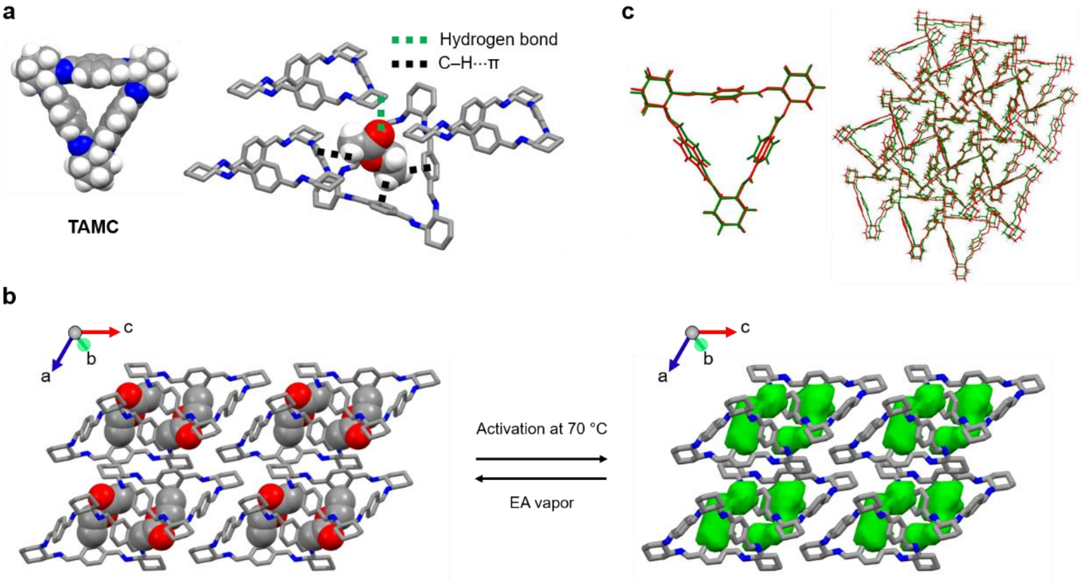

Figure 2.3. Single-crystal structures: (a) EA@**TAMC** showing hydrogen bonding and C–H···π interactions between **TAMC** and EA; (b) crystal packings for EA@**TAMC** (left) and α-**TAMC** (right) with EA-selective voids coloured in green. Hydrogen atoms are omitted for clarity. (c) Crystal packing overlay for EA@**TAMC** (green) and *α*-**TAMC** (red), as generated using the crystal packing similarity tool in *Mercury*.

After thermally removing the EA solvent from EA@**TAMC** at 70 °C, we found that the structure of the activated crystals, *α*-**TAMC**, was closely related to EA@**TAMC**, based on similarities between their single crystal structures (Figure 2.3b) and PXRD patterns (Figure 2.4). After activation, the unit cell volume decreased by 5.4%, which is mainly due to a structural contraction of 0.5 Å along the *b*-axis (Figure 2.3b). However, the packing of **TAMC** molecules in EA@**TAMC** and desolvated *α*-**TAMC** is essentially isostructural (Figure 2.3b). However, the packing of **TAMC** molecules in EA@**TAMC** and desolvated *α*-**TAMC** is essentially isostructural (Figure 2.3 b–c,

Table 2.1). Hence, near-perfect voids for adsorbing EA are retained in *α*-**TAMC**. PXRD data collected during in situ heating (273–393 K, then cooled to 295 K) for EA@**TAMC** (Figure 2.4b) show that the bulk material also undergoes limited rearrangement when the solvent is removed. The unit cell (Table 2.1) indicates a reduced symmetry structure with lattice dimensions and molecular volume for the macrocycle close to that of EA@**TAMC**.

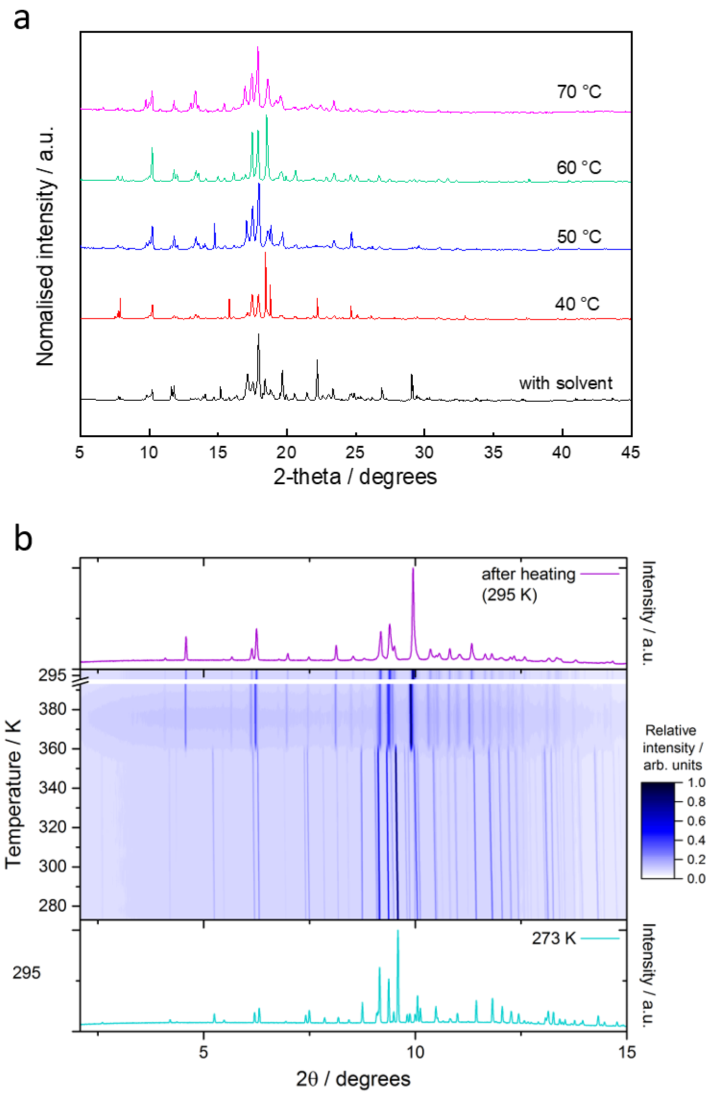

Figure 2.4. (a) PXRD patterns of EA@**TAMC** samples that were activated at different temperatures (40–70 °C) under vacuum. (b) PXRD patterns were collected during in situ heating (273 – 393 K, then cooled to 295 K) for a sample of EA@**TAMC** contained in a borosilicate glass capillary (diameter = 0.5 mm).

Table 2.1. SC-XRD data for **TAMC**.

Molecule	EA@**TAMC**[a]	*α*-**TAMC**
Collection Temperature	100 K	100 K
Formula	$C_{46}H_{56}N_6O_2$	$C_{42}H_{48}N_6$
Mr [g mol^{-1}]	724.96	636.86
Crystal Size [mm]	0.152×0.313×0.533	0.026×0.022×0.019
Crystal System	Monoclinic	Monoclinic
Space Group	*P*21	*P*21
a [Å]	11.4675(10)	11.685(2)
b [Å]	10.2584(8)	9.759(2)
c [Å]	18.5370(16)	18.239(4)
α [°]	90	90
β [°]	105.090(2)	106.755(18)
γ [°]	90	90
V [Å3]	2105.5(3)	1991.6(8)
Z	2	2
Dcalcd [g cm^{-3}]	1.143	1.062
μ [mm^{-1}]	0.071	0.060
F(000)	780.0	684
2θ range [°]	1.89 – 30.033	2.295 – 24.999
Reflections collected	30809	13154
Independent reflections, R_{int}	9838, 0.0427	4048,0.1702
Obs. Data [I > 2σ(I)]	9221	2203
Data /restraints /parameters	9838/1/489	4048/379/397
Final R_1 values ($I > 2\sigma(I)$)	0.0366	0.0687
Final R_1 values (all data)	0.0394	0.1118
Final $wR(F^2)$ values (all data)	0.0943	0.1665
Goodness-of-fit on F^2	1.051	0.913
Largest difference peak and hole [e.A^{-3}]	0.350/-0.173	0.248/-0.136
CCDC	2049238	2049237

[a] X-ray data for EA@**TAMC** is comparable to the reported X-ray crystal of XAGXUY reported in the Crystal Structure Database.[8]

2.5 Ethyl acetate vapour-phase adsorption studies

Inspired by the potentially EA-selective voids in α-**TAMC**, the adsorption of EA and EtOH as a single pure component and a mixture was investigated. (Figure 2.5)

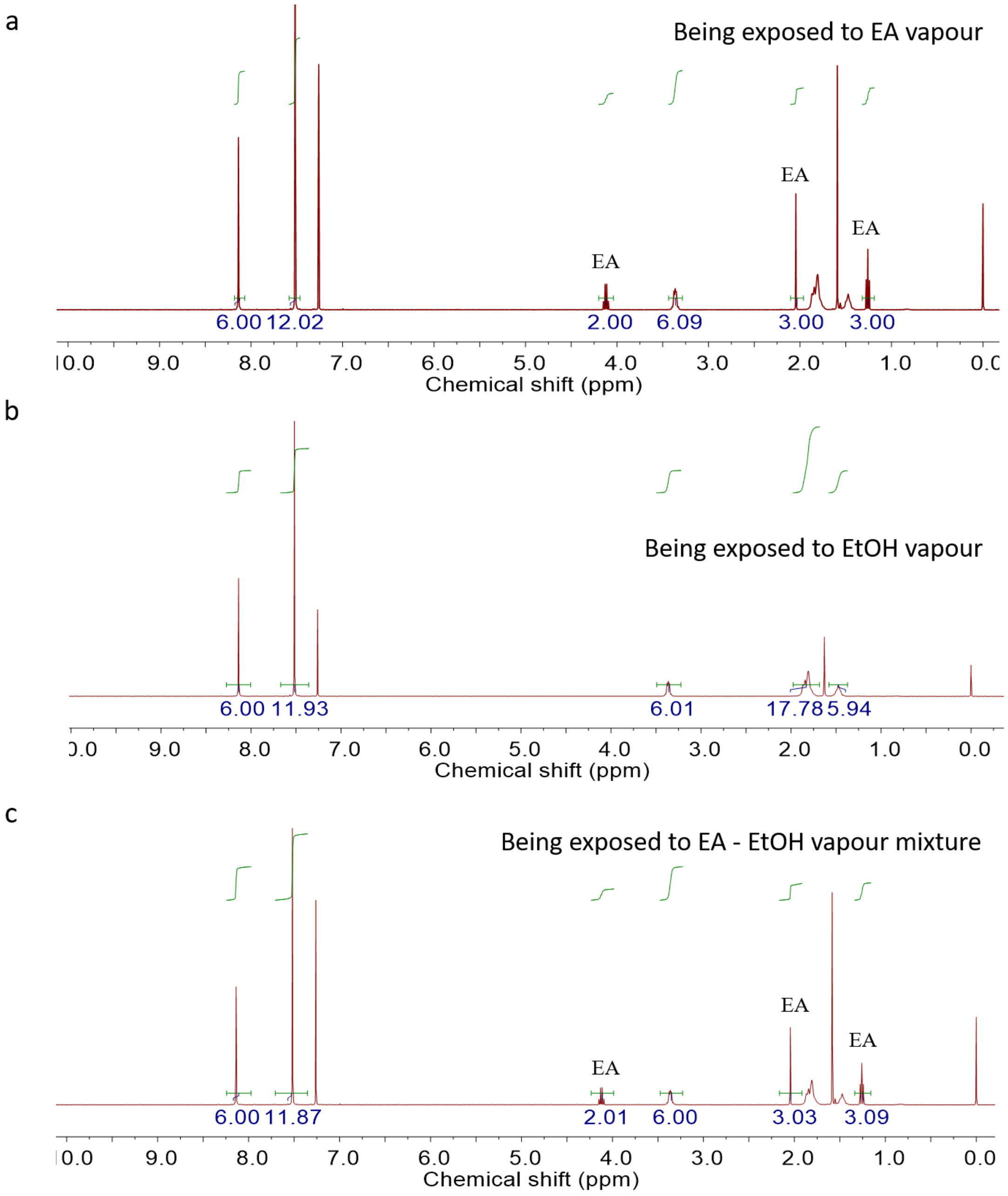

Figure 2.5. ^{1}H NMR spectrum (400 MHz, $CDCl_3$, 293 K) of **TAMC** (a) after being exposed to EA vapour for 13 h, (b) after being exposed to EtOH vapour for 23 h and (c) after being exposed to EA-EtOH vapour mixture for 14 h.

After being exposed to EA vapour, α-**TAMC** adsorbs EA at 1:1 molar ratio, as confirmed by NMR (Figure 2.5 a), which agrees with the molar ratio observed in the EA@**TAMC** crystal structure. In contrast, no EtOH is detected by ^{1}H NMR in **TAMC** after being exposed to EtOH vapour. (Figure 2.5 b) In addition, after 14 h exposure to the EA-EtOH vapour mixture, no EtOH could be detected in the 1H NMR spectrum of the dissolved crystals (Figure 2.5 c) and the EA uptake saturated at 1 mol/mol EA/**TAMC** (1.57 mmol/g).

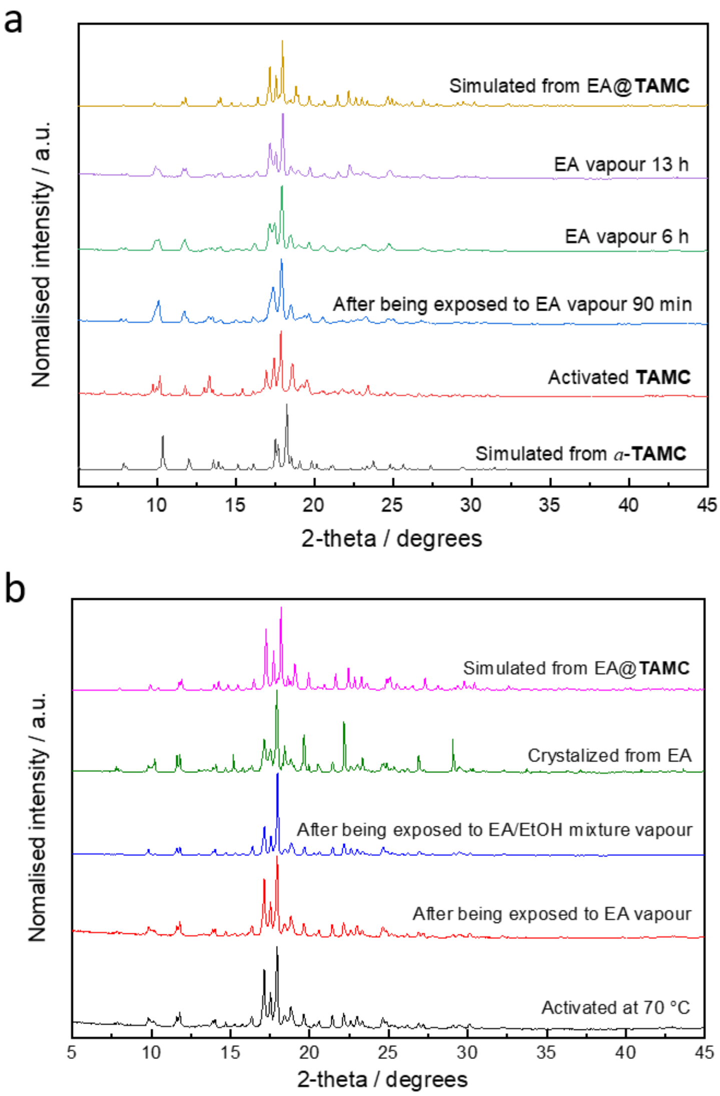

Figure 2.6. (a) Time-dependent PXRD patterns of activated **TAMC** solid after being exposed to EA vapour. (b) PXRD patterns of **TAMC** at different conditions. From bottom to top: **TAMC** activated at 70 °C; after being exposed to EA vapour for 16 h; after being exposed to EA-EtOH vapour for 6 h; **TAMC** crystalised from EA (EA@**TAMC**); simulated from crystal structure EA@**TAMC**.

Furthermore, the PXRD patterns of *α*-**TAMC** after exposure to both EA vapour and EA-EtOH vapour mixtures are shown in Figure 2.6. As shown in Figure 2.6a, the PXRD pattern of *α*-**TAMC** is turned gradually to be similar to the EA@**TAMC** after exposure to EA vapour for 90 min to 13 h. Similarly, the PXRD pattern of *α*-**TAMC** after exposure to EA-EtOH vapour mixtures are very similar to EA@**TAMC**. (Figure 2.6b) These PXRD results are consistent with the 1H NMR spectrums (Figure 2.5), suggesting that *α*-**TAMC** is more affiliative to EA and can form the EA@**TAMC** crystal both in EA vapour and in EA-EtOH vapour mixtures.

The single-component EtOH and EA vapour isotherms for *α*-**TAMC** were measured by gravimetric sorption apparatus (IGA-002, Hiden Isochma) at 25 °C (Figure 2.7a). In the EA isotherm, a steep rise was observed in uptake in the low relative pressure region ($P/P_0 < 0.00975$). A second, less steep rise was then observed in the relative pressure range 0.01–0.3, before the isotherm reached the expected 1 mol/mol saturation point at $P/P_0 \sim 0.5$. The desorption isotherm for EA shows that the material is still saturated with EA at P/P_0 at 0.15. This hysteresis behaviour is consist with the TGA results (Figure 2.2c) that the EA molecules bounded strongly by **TAMC** and difficultly removed even in high vacuum at room temperature (RT). This can be attributed to the strong guest – host interactions in EA@**TAMC** as shown in Figure 2.3a and the further discussion will be in Section 2.10. By contrast, the EtOH adsorption isotherm is completely different: there is a linear uptake in the low relative pressure region (Figure. 2.7a). The EtOH desorption isotherm also shows some hysteresis, but it is far less pronounced than for EA. The single-component isotherms indicate that *α*-**TAMC** has a stronger affinity for EA than EtOH, and the EA uptake is much higher than for EtOH in the low relative pressure region ($P/P_0 < 0.3$).

The EA-EtOH binary mixture adsorption selectivity was then predicted using ideal adsorption solution theory (IAST) based on the single-component isotherms shown in Figure 2.7a.[19] The IAST-predicted selectivity is shown in Figure 2.7b for binary mixtures of EA-EtOH with compositions of 50:50 and 5:95 at 298 K. For equimolar mixtures, the initially predicted selectivity was 39.4, and then gradually decreased to 10.6 at 0.1 bar; this is much higher than the selectivity reported for ZIF-8 (1.7–8.3) under the same conditions calculated by the same method.[5] Even for the 5:95 EA-

EtOH binary mixture, EA is still predicted to be preferentially captured by **TAMC** with high selectivity from 45.9 to 16.8. (Figure 2.7b)

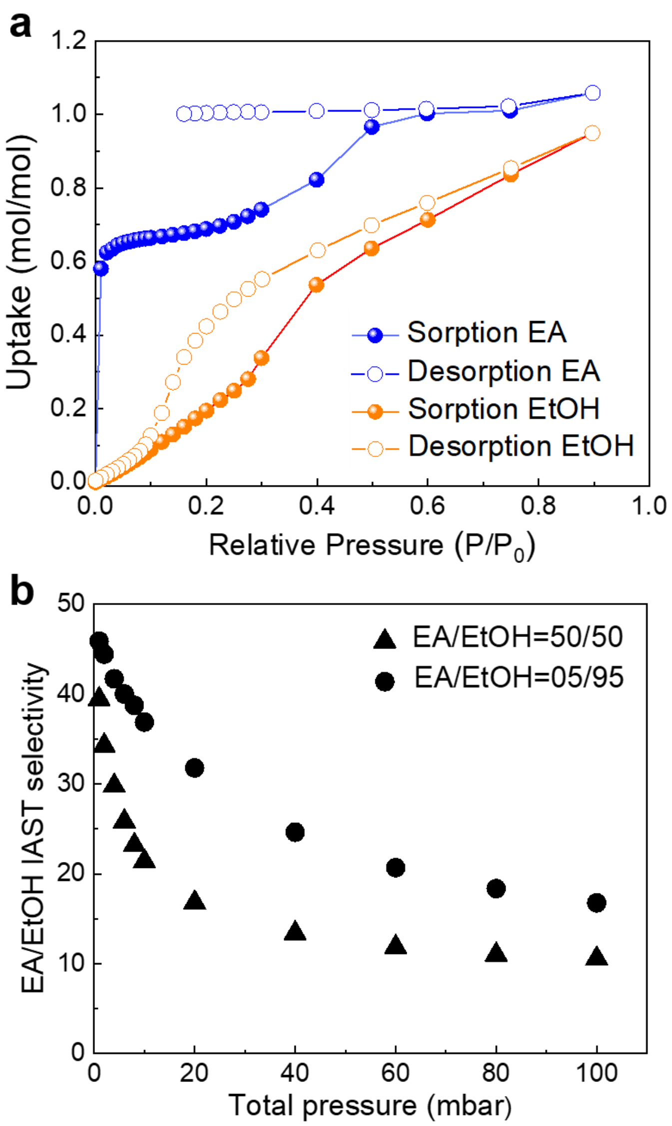

Figure 2.7. (a) EtOH (P_0= 7.95 kPa) and EA (P_0= 13.33 kPa) vapour sorption isotherms for *α*-**TAMC** at 298 K. (b) IAST selectivity of EA-EtOH mixtures for *α*-**TAMC** at 298 K as calculated from these pure component vapour sorption isotherms.

2.6 Static separation of EA-EtOH mixture vapour

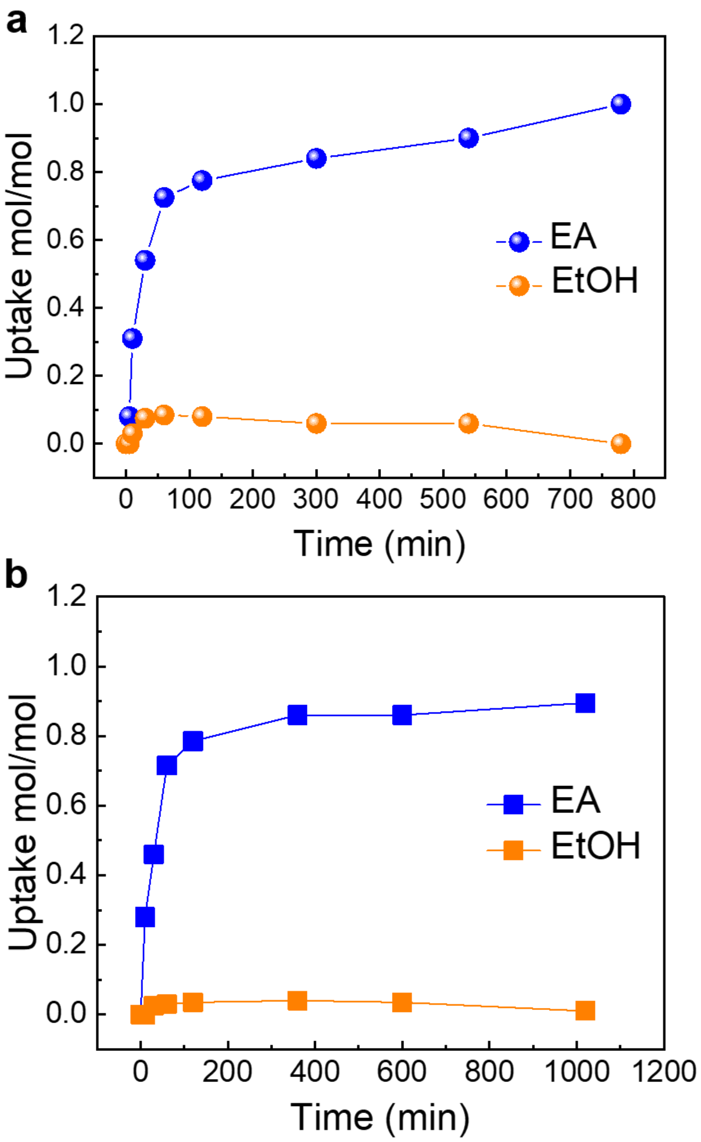

Figure 2.8. Time-dependent **TAMC** solid−vapour sorption plot for (a) the 1:1 v/v EA-EtOH mixture vapour at 25 °C. (b) the EA/EtOH azeotropic mixture vapour (30:70 wt.%, 72 °C).

To determine if *α*-**TAMC** selectively adsorbed EA from actual EA-EtOH vapour mixtures, time-dependent static solid-vapour sorption experiments using a EA-EtOH (1:1 v/v) mixture at room temperature were carried out. The uptake of EA and EtOH by *α*-**TAMC** was determined by 1H NMR after dissolving the crystals in $CDCl_3$. As shown in Figure 2.8a, the EA uptake increased sharply to ~0.80 mol/**TAMC** after 120 mins. By contrast, the EtOH uptake was much lower (0.17 mol/**TAMC**) after the same time period. The EtOH uptake decreased slowly after this time, suggesting that adsorbed EtOH molecules might be replaced by EA molecules in the structure over time as the system equilibrates. Indeed, after 14 h exposure to the EA-EtOH vapour mixture for 14 h, no EtOH could be detected in the 1H NMR spectrum of the dissolved crystals (Figure 2.5c) and the EA uptake saturated at 1 mol/mol EA/**TAMC** (1.57 mmol/g, Figure2.8a), consistent with TGA, X-ray diffraction, and vapour isotherm data. This suggests that the initial EtOH adsorption at shorter times is a kinetic process. Likewise, **TAMC** captures EA selectively from an EA-EtOH azeotropic mixture vapour (30:70 wt.%, 72 °C), which is a mixture that is difficult to separate in the industrial Fisher esterification process. As shown in Figure 2.8b, the EA uptake increased sharply to ~0.78 mol/**TAMC** after 120 mins. After that, the EA uptake equilibrated at 0.86 – 0.90 mol/**TAMC.** By contrast, the EtOH uptake remained much lower around 0.01 – 0.03 mol/**TAMC** in the same period, which further confirm that **TMAC** adsorbs EA but effectively rejects EtOH.

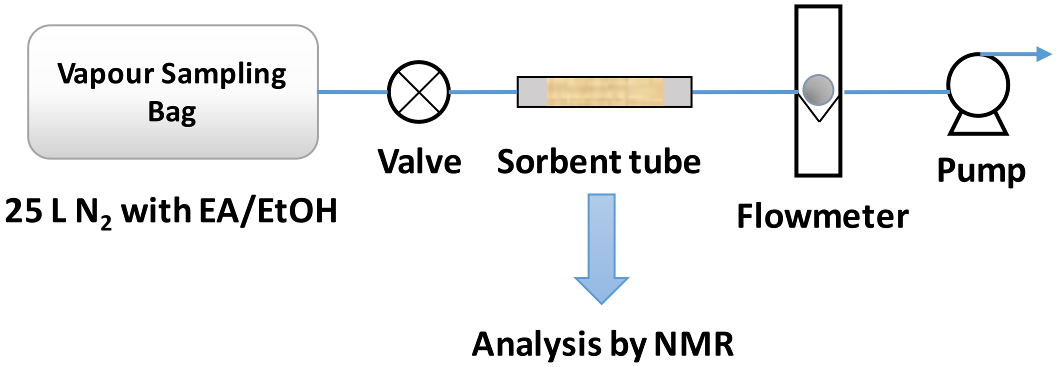

Figure 2.9. Schematic representation of the method to measure the selective uptake from a low concentration of EA-EtOH mixture in **TAMC**.

The EA selectivity of *α*-**TAMC** at low EA concentrations was also investigated. As shown in Figure. 2.9, activated *α*-**TAMC** solid (30 mg) was packed into empty thermal desorption tubes (I.D. × O.D. × L 4 mm × 6 mm × 4.5 in. made by *Dynatherm*) and plugged with a small amount of quartz wool. This was attached to a 25 L *Tedlar* bag containing the required EtOH-EA vapour mixture by using a short piece of silicone tubing. The EtOH-EA vapour mixture was generated by injecting a liquid mixture (8 to 25 μL) with a ratio of 50:50 v/v into the *Tedlar* bag. The pump with a flowmeter was attached to the other end of the tube, again using silicone tubing. The feed flow rate is 0.2 L/min. Uptake in the **TAMC** crystals was measured after 20 min exposure by completely dissolving the crystals in $CDCl_3$ and measuring the ratio of EA or EtOH to **TAMC** (mol/mol) by ^{1}H NMR, respectively. All the adsorption processes were carried out at room temperature.

When dry N_2 containing EA (100–500 ppm, a range that EA can be detected in wine) and EtOH (200–800 ppm) was passed through a column packed with *α*-**TAMC** at a flow rate of 0.2 L/min for 20 minutes, we found that only EA was adsorbed by *α*-**TAMC**, as confirmed by NMR (Table 2.2).

Table. 2.2. The selective uptake from a low concentration of EA-EtOH mixture in **TAMC**

Maximum vapour concentration in Tedlar bag		Uptake of vapour	
EA (ppm)	EtOH (ppm)	EA (mol/mol)	EtOH (mol/mol)
124	210	0.015	0
254	425	0.025	0
508	850	0.04	0

2.7 Dynamic separation of EA-EtOH mixture via breakthrough experiment

To evaluate the performance of *α*-**TAMC** for the dynamic separation of EA-EtOH mixtures under N_2 flow, we performed breakthrough measurements using an adsorption column packed with activated *α*-**TAMC** (ABR automated breakthrough analyser manufactured by Hiden Isochema). Breakthrough profiles for a 1:1 v/v EA-EtOH vapour mixture at 25 °C are shown in Figure 2.10.

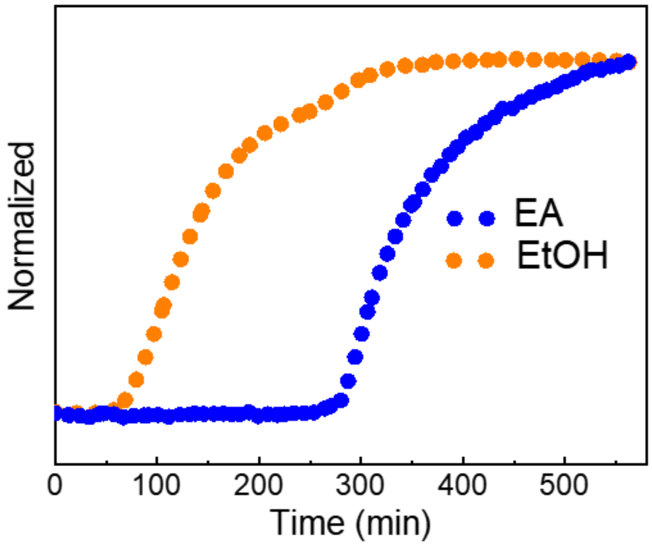

Figure 2.10. Breakthrough profiles for a 1:1 v/v EA-EtOH vapour mixture at 25 °C (sorbate rate: 1.5 mL/min; total flow rates: 5 mL/min with a carrier gas of N_2).

Both EA and EtOH were retained in the *α*-**TAMC** column at the beginning of the experiment at a carrier gas flow rate of 1.5 mL/min. (Figure 2.10) The EtOH then broke through in the period 50–300 min. By contrast, EA was retained until 300 mins, and did not break through until almost all of the EtOH had eluted. Then the EA signal increased gradually until the feed concentration was reached after about 500 mins. This breakthrough experiment confirms the potential of *α*-**TAMC** to separate EA and EtOH in real flow processes cleanly.

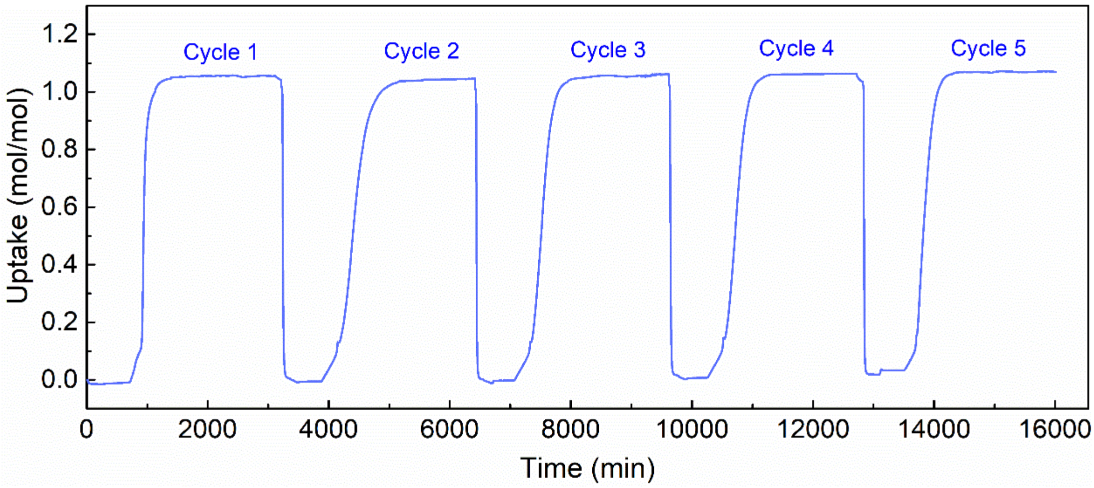

Figure 2.11. Adsorption–desorption cycles for pure EA vapour (P_0= 13.33 kPa) at 25 °C (degas temperature at 70 °C) recorded by a gravimetric sorption analyser.

Repeated EA sorption-desorption cycles were performed using a gravimetric sorption apparatus. In contrast to many crystalline framework materials, which tend to lose performance because of a progressive decrease in crystallinity during repeat sorption cycles, there was no drop in the adsorption performance of the α-**TAMC** material after 5 cycles (Figure 2.11). This suggests that α-**TAMC** could be suitable for actual separation applications in the future.

2.8 Gas sorption result of TAMC

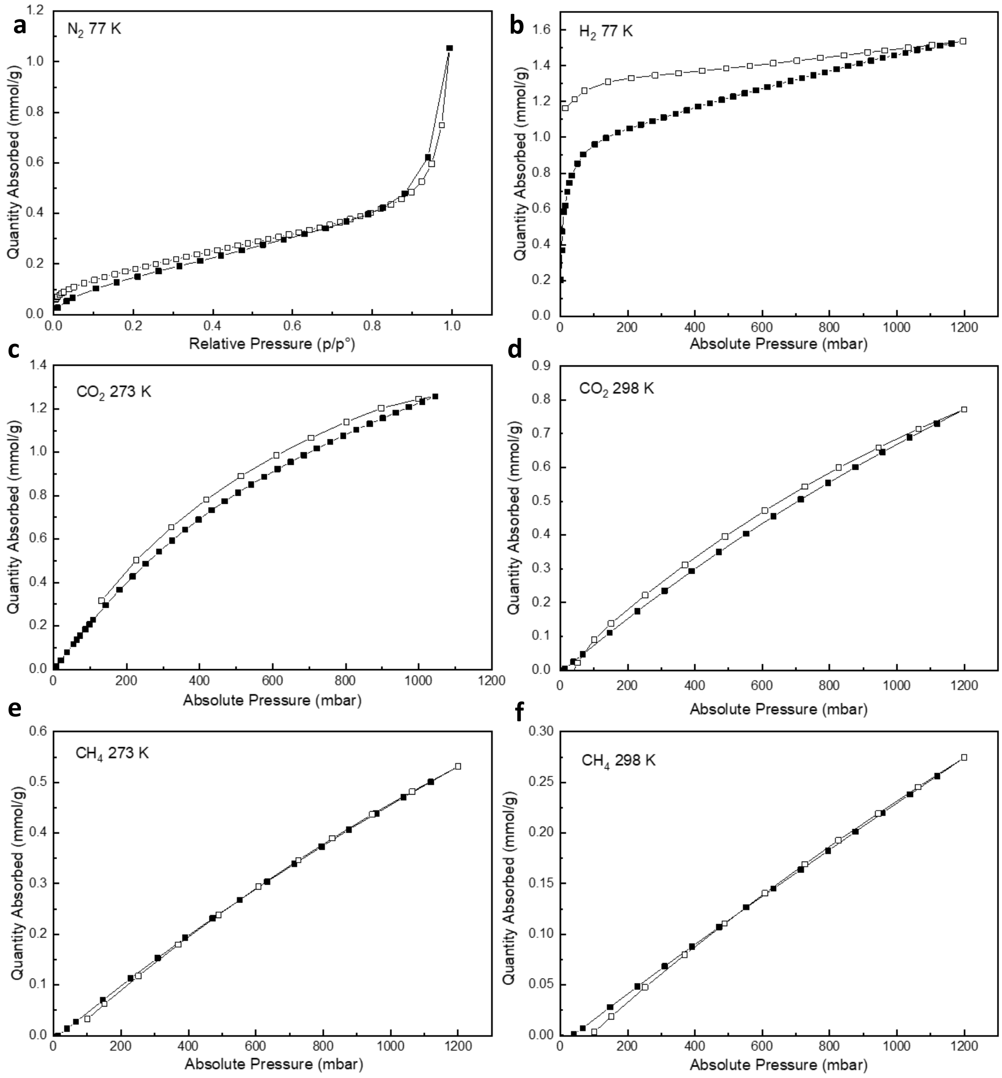

Figure 2.12. Gas adsorption / desorption isotherms for α-**TAMC**. (a) Nitrogen isotherms at 77 K. (b) Hydrogen at 77 K. (c) Carbon dioxide at 273 K. (d) Carbon dioxide at 298 K. (e) Methane at 273 K. (e) Methane at 298 K. Adsorption (filled symbols), desorption (hollow symbols).

As shown in Figure 2.12, *α*-**TAMC** has lower uptakes for CO_2 (0.8 mmol/g) and CH_4 (0.3 mmol/g) than for EA (1.6 mmol/g) at comparable temperatures (298 K). Both EA and EtOH have much larger kinetic diameters than H_2, N_2, CO_2 and CH_4.[20] Therefore, we exclude molecular sieving as the cause for the EA/EtOH selectivity and believe instead that **TAMC** adsorbs more EA vapour because of the stronger host-guest interaction between **TAMC** and EA. That is, the separation is driven by thermodynamics, not kinetics, which is consistent with the result of time-dependent static solid-vapour sorption experiments. (Figure 2.8).

2.9 Polymorph screening for TAMC

Table 2.3. Solvents for crystallisation

Solvent	Boiling Point (°C)	Solvent	Boiling Point (°C)
Acetone	56.3	Methanol	64.7
Acetonitrile	81.6	*iso*-Propanol	82.3
Chloroform	61.2	*n*-Propanol	97.2
Cyclohexane	80.7	Tetrahydrofuran	66.0
Dichloromethane	39.8	Toluene	110.6
1,4-Dioxane	101.0	Triethyl orthoformate	148.2
1,4-Difluorobenzene	88-89	Water	100.0
Ethanol	78.3	*o*-Xylene	144.4
Heptane	98.4	*m*-Xylene	139.1
n-Hexane	68.7	*p*-Xylene	138.5

TAMC has been reported to have more than two polymorphs[21, 22]. In order to screen polymorphs of **TAMC**, various organic solvents listed in Table 2.3 were used to recrystallise **TAMC.** 1 mL of the organic solvents were added to 10 mg **TAMC** in separate glass sample vials. The solvents were then allowed to evaporate from the vials at room temperature, which took between 2–15 days, and the crystals were collected.

The PXRD patterns of **TAMC** obtained from good solvents that can dissolve it, the PXRD are shown in Figure 2.13. Among them, the PXRD patterns of samples evaporating from chloroform, propan-1 ol, propan-2 ol are very similar but with significant difference in main peaks compared with the α-**TAMC.** The obvious change is also found in the PXRD patterns of samples evaporating from THF and DCM.

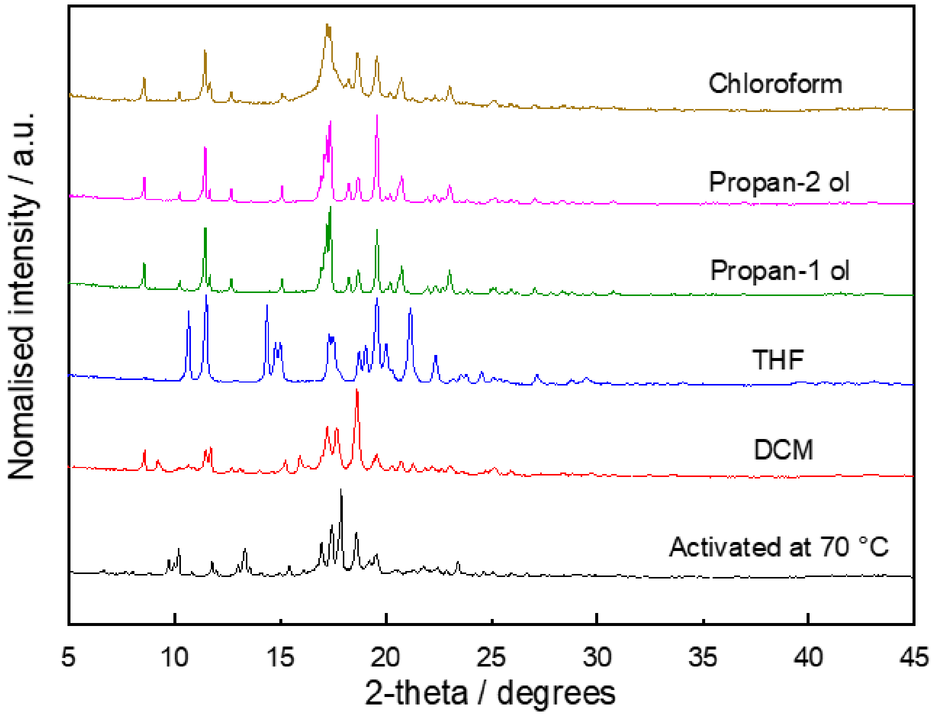

Figure 2.13. PXRD patterns of **TAMC** samples obtained from solvents that can dissolve **TAMC**.

In addition, the PXRD patterns after evaporating from these bad solvents that cannot dissolve it **TAMC** are shown in Figure 2.14. As shown in Figure 2.14a, after evaporating from xylenes, 1,4-difluorobenzene and toluene, **TAMC** undergoes some changes in PXRD patterns. The PXRD patterns of samples evaporating from triethyl orthoformate, heptane, hexane and acetone are very similar (Figure 2.14b), and have a slight shift around 17.5 (2-theta degrees) compared with the α-**TAMC**. Similarly, **TAMC** after evaporating from acetonitrile, cyclohexane, methanol and 1,4-dioxane, undergoes slight changes in PXRD patterns.

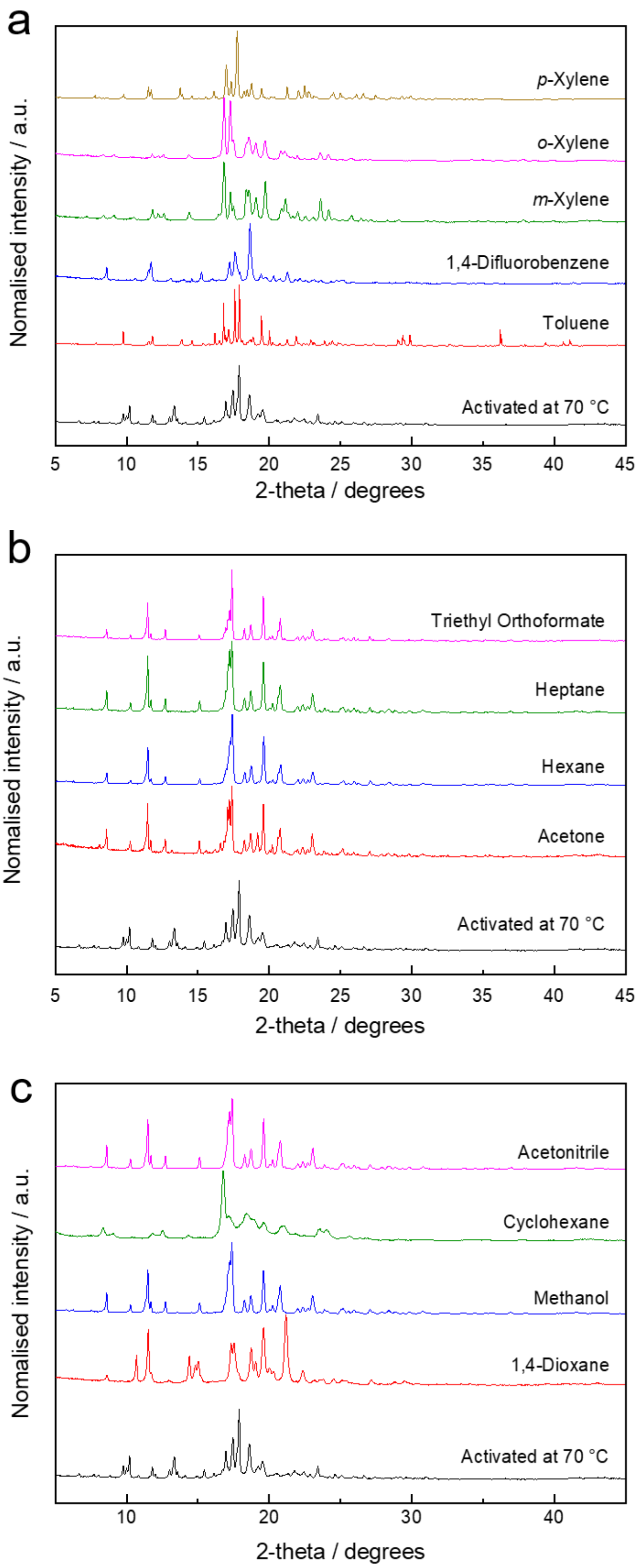

Figure 2.14. PXRD patterns of **TAMC** obtained from solvents that cannot dissolve it **TAMC**.

Interestingly, the PXRD patterns of the **TAMC** samples obtained from EtOH and H_2O are similar to *α*-**TAMC**. (Figure 2.15) This indicates that being exposed to EtOH and H_2O will not lead the rearrangement of structure of **TAMC**. In other words, **TAMC** is hydrophobic and resistant to EtOH.

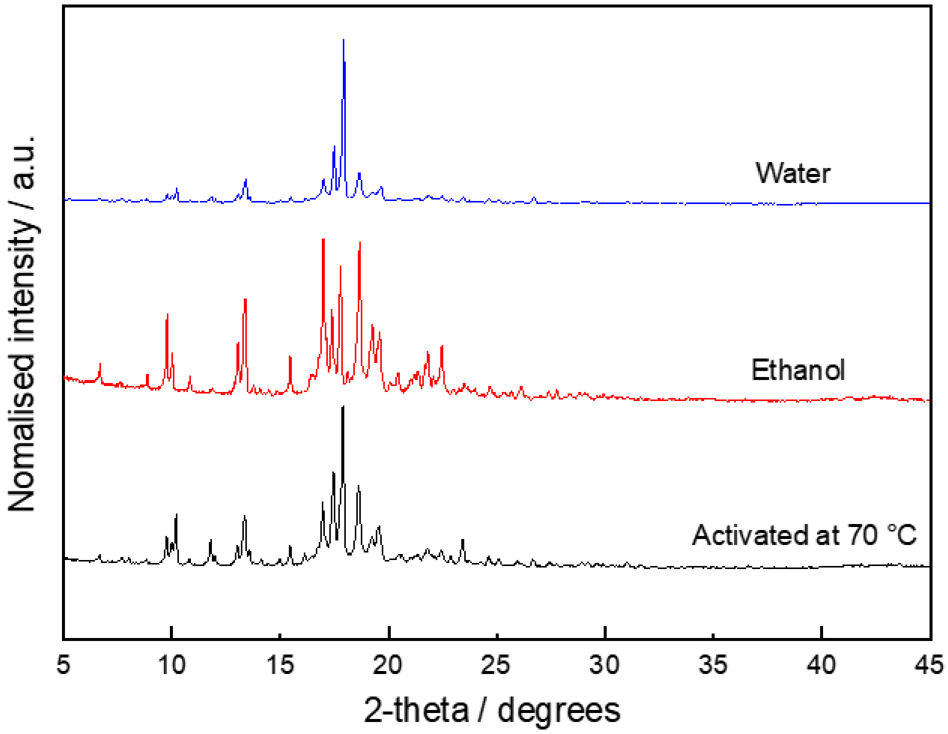

Figure 2.15. PXRD patterns of **TAMC** sample obtained from EtOH and H_2O.

These other polymorphs of **TAMC** can also selectively adsorb EA via a structural transformation process. As shown in Figure 2.16a, when **TAMC** was crystallised from dichloromethane (DCM) and then exposed to EA or a mixed EA-EtOH vapour, the structure gradually transformed into the EA solvate structure, EA@**TAMC**. However, the kinetics of this transformation was slower, taking over 16 hours to transform into EA@**TAMC**. In addition, the time-dependent vapour sorption plot for EA/EtOH mixture vapour shows that the polymorph from DCM has the slower EA uptake and reaches 0.47 mol/mol (EA/**TAMC)** compared with the *α*-**TAMC** that its EA uptake can achieve 0.80 mol/**TAMC** after 120 mins. (Figure 2.16b)

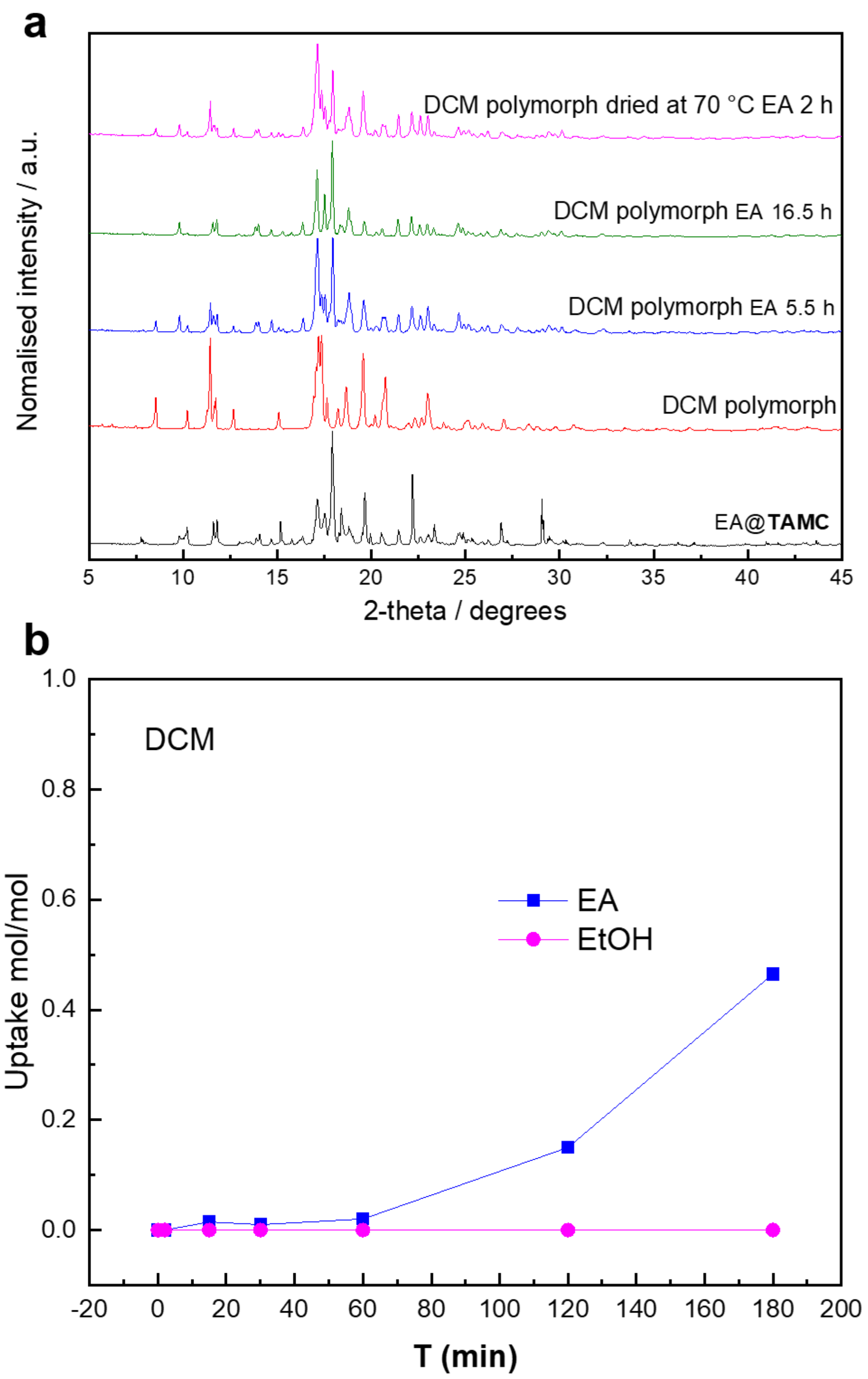

Figure 2.16. (a) PXRD patterns of **TAMC** polymorph from DCM after being exposed different vapour conditions. (b) Time-dependent vapour sorption plot for EA/EtOH mixture vapour at 298 K for the **TAMC** polymorph by using DCM.

A similar experimental result was also found for a different polymorph crystallised from acetone. As shown in Figure 2.17, **TAMC** from acetone can selectively adsorb EA with slower kinetics compared with the *α*-**TAMC** and even the polymorph from DCM. After being exposed in EA/EtOH mixture vapour for 180 min, only 0.11 mol/**TAMC** of EA was absorbed.

These results show that **TAMC** can selectively adsorb EA by adaptation to EA@**TAMC** structure, even if it does not start with the *α*-**TAMC** phase, albeit at the expense of slower kinetics. This means that the selectivity of **TAMC** for EA is inherent, and EA "templating" can improve the kinetic for EA adsorption.

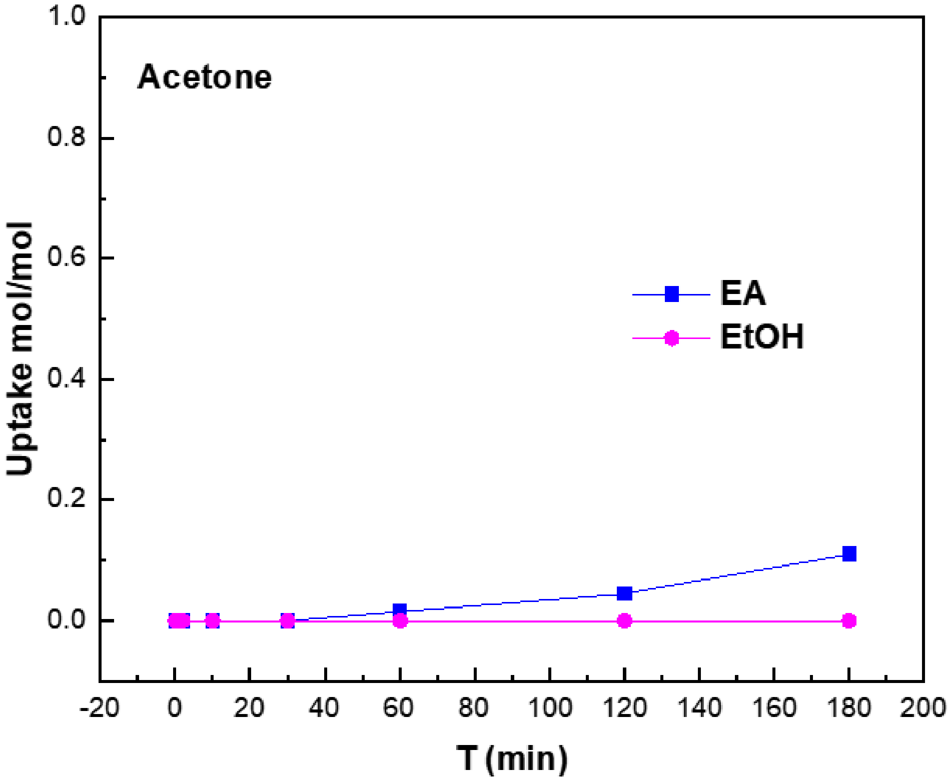

Figure 2.17. Time-dependent vapour sorption plot for EA/EtOH mixture vapour at 298 K for the **TAMC** polymorph induced using acetone.

Solvated molecular crystals often transform to another phase or collapse when the adsorbed solvent is removed, and any extrinsic porosity between molecules is commonly lost during desolvation.[23-26] Various strategies have been developed[27] to retain porous structures in molecular crystals after activation, such as introducing hydrogen bonding interactions between building blocks or a second molecule that matches the size and shape of the unstable voids.[23] Surprisingly, **TAMC** can retain its original packing essentially after losing 11.2 wt.% from the solvated structure when the EA is removed, without any obvious strong and directional intermolecular interactions between **TAMC** molecules, such as hydrogen bonding.

2.10 Crystal structure prediction and electrostatic surface potential analysis

To probe the stability of EA@**TAMC**, the host-guest chemistry of **TAMC** with EA was investigated by CSP. Lattice energy searching for theoretical low-energy crystal forms is used in CSP. The stability of the crystal can be related to its lattice energy, the lower lattice energy means that the crystal is more stable under assumed conditions.[28] It should be noted that Chengxi Zhao led the generation of the CSP landscapes, and the results were used to quantify the experimental results.

To investigate how the macrocycle's flexibility contributes to the adsorption process, the energy landscapes of the possible 1:1 EA:**TAMC** co-crystal structures were calculated from a available conformation that was extracted from the experiment for EA@**TAMC** crystal structure (Figure 2.18a) and the lowest energy gas phase conformer calculated in a conformational search (Figure 2.18b). The conformational search for calculating gas phase minimum conformer is shown in Figure 2.18d, the top two rows show the 8 unique conformers after DFT re-optimisation, showing two views per conformer. Energies are relative to the lowest energy conformer, taken from the DFT calculation. The bottom row shows an overlay of the 8 conformers from three views. In addition, the structural difference between gas phase minimum conformer (red) and the conformer from experiment EA@**TAMC** structure (blue) are shown in Figure 2.18c.

These two **TAMC** conformers were then used for the CSP calculations. Each point in Figure 2.18a-b corresponds to a predicted crystal structure on the lattice energy surface. The colour-coding of structures is given by the positioning of the EA molecule relative to the **TAMC** cavity. Red dots represent structures in which the methyl end of EA sits inside **TAMC** cavity, blue dots are structures where the ethyl end of EA is inside the **TAMC** cavity, and black dots are structures where EA is outside the **TAMC** cavity. In EA@**TAMC**, the ethyl group of EA sits inside the **TAMC** cavity, with its methyl group forming three C–H···π hydrogen bonds with the three phenyl rings of **TAMC**. An additional hydrogen bond is formed between the carbonyl of EA and another **TAMC**.

Although the molecular geometry in the observed EA@**TAMC** crystal structure and the gas phase optimised conformation differ only by small rotations of the phenyl rings, this modest difference has a large impact on the **TAMC**'s ability to adsorb EA. The observed behaviour is reproduced in the crystal structure landscape derived from the observed molecular conformation: most low-energy structures are densely packed with either the methyl or ethyl group of the EA molecule located inside the **TAMC** cavity. The lowest energy predicted structures have the ethyl group of EA located in this cavity (Figure 2.18a). The lowest energy structure accurately reproduces the experimental crystal structure, EA@**TAMC** (Figure 2.18a). By contrast, EA remains outside the **TAMC** cavity in the majority of the predicted crystal structures when the gas phase conformer is used (Figure 2.18b); none has the methyl end inside the cavity and only high-energy predicted structures (more than 35 kJ/mol above the global minimum) have the ethyl end inside the **TAMC** cavity.

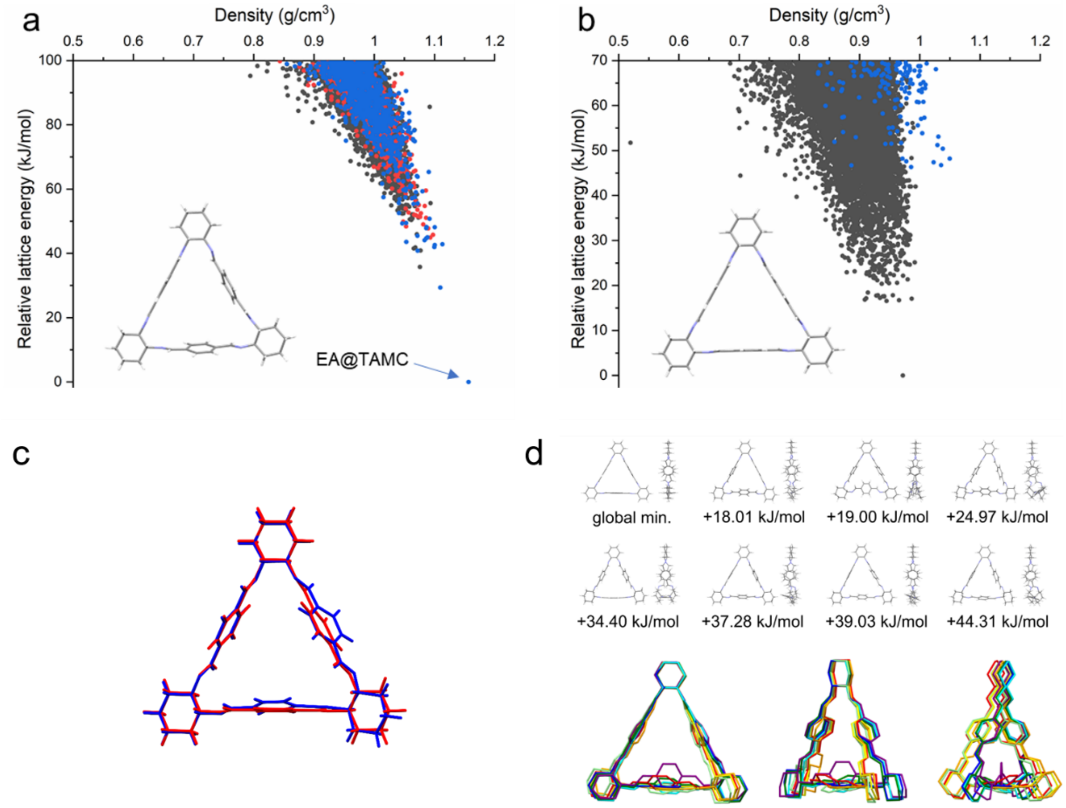

Figure 2.18. Crystal structure prediction (CSP) landscapes for a 1:1 composition of EA:**TAMC** in 6 common space groups (a) using the conformation from the experimentally determined EA@**TAMC** crystal structure; (b) using the calculated gas phase minimum conformer from a conformational search (Figure 2.18d). Red dots represent structures in which the methyl end of EA sits inside **TAMC** cavity, blue dots are structures where the ethyl end of EA is inside the **TAMC** cavity, and black dots are structures where EA is outside the **TAMC** cavity. Note that there are no red dots in (b). (c) Difference in molecular geometry of gas phase minimum conformer (red) and the conformer from experiment EA@**TAMC** structure (blue). (d) Unique conformers for the isolated **TAMC** molecule.

These results demonstrate the importance of flexibility in guest adsorption.[17] The rigid backbone of **TAMC** retains the inherent pore in the structure after activation. At the same time, the subtle flexibility associated with rotation of the phenyl rings allows the macrocycle cavity to adapt for the ethyl group in EA, thus explaining both the adaptability and the stability of EA@**TAMC** crystal.

In addition, a more complete CSP search in an expanded set of space groups was performed with the gas phase molecular geometry, each point in Figure 2.19a corresponds to a predicted crystal structure that is a local minimum on the lattice energy surface. The colour-coded is given by the positioning of the EA molecule relative to the **TAMC** cavity. Blue dots for the ethyl end of EA inside **TAMC** and black dots for EA outside **TAMC**. There are no predicted structures with the methyl end of EA inside **TAMC**, confirming that EA does not fit within the cavity without distortion of the macrocycle.

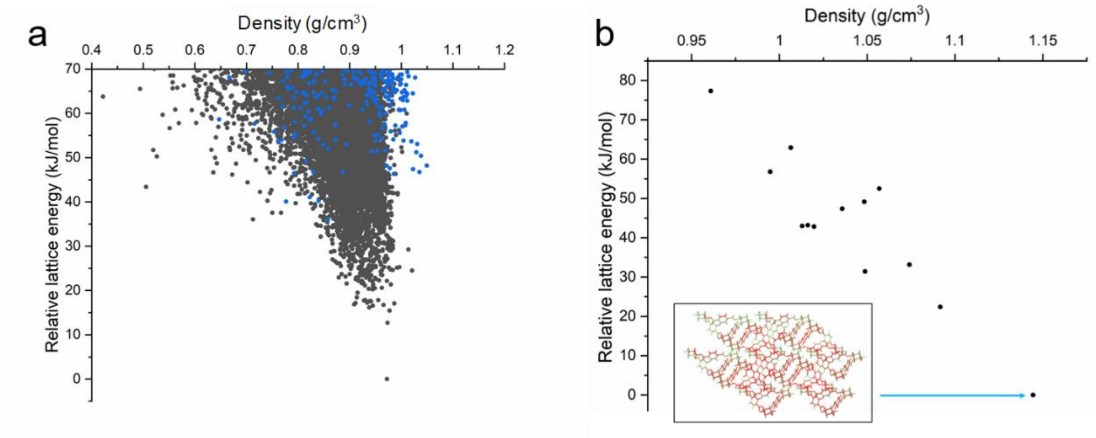

Figure 2.19. (a) CSP landscape for a 1:1 composition of EA:**TAMC** using the gas phase minimum conformer with a 70 kJ/mol relative lattice energy window (13 Sohncke space groups). (b) CSP landscape for a 1:1 composition of EA:**TAMC** after density functional theory (DFT) re-optimisation with no geometry restrictions. The colour-coded is given by the positioning of the EA molecule relative to the **TAMC** cavity. Blue dots for the ethyl end of EA inside **TAMC** and black dots for EA outside **TAMC**.

To verify the energy ranking, the predicted structures from the lowest 20 kJ/mol in both landscapes were re-optimised with solid state density functional theory (DFT) with no geometry constraints (Chapter 5, Section 5.3.5 for details). Each point in Figure 2.19b corresponds to a predicted crystal structure that is a local minimum on the DFT lattice energy surface. The experimental result is predicted as the global minimal packing structure. The inset shows a crystal packing similarity match between the experimental structure (red) and the simulated structure (green). These more accurate calculations find the observed EA@**TAMC** structure 22 kJ/mol lower in energy than other predicted alternatives. This result further confirms that the experimental EA@**TAMC** structure is the global minimal packing structure.

CSP calculations were also performed on guest-free **TAMC** using the gas phase conformer, followed by DFT re-optimisation of the predicted structures. The observed experimental structure was located among the predicted structures, 50 kJ/mol above the lowest energy predicted structure. This energy gap is comparable to other desolvated, porous molecular crystals that can be accessed experimentally.[29, 30] It seems that the EA interactions with the host **TAMC** structure stabilise the observed EA@**TAMC** phase during crystallisation, and that this structure occupies a sufficiently deep energy basin such that α-**TAMC** does not rearrange after desolvation. At least on the experimental timescales investigated here, even though we estimate that there are packings available to this macrocycle that are around 50 kJ/mol more stable. Hence, we only observe a subtle structural difference between the packing of **TAMC** molecules in EA@**TAMC** and α-**TAMC**. This has practical importance because while other **TAMC** polymorphs can transform to EA@**TAMC**, and hence show EA selectivity (see discussion above), the kinetics are significantly slower than for α-**TAMC**. As such, the structural ‘imprint’ of EA in α-**TAMC** improves the prospects for practical separation processes.

Furthermore, the electrostatic surface potential (ESP) of EA and EtOH with the most positive ESP (Vs,max) and most negative ESP (Vs,min) are presented in Figure 2.20a,b. To give a deep insight into the intermolecular interaction model, the non-covalent index (NCI)[31] theory was adopted to provide a more global description of the interaction between hosts and guests. As shown in Figure 2.20c, there is a strong C-H···O hydrogen bonding interaction between the carbonyl group on EA and cyclohexane ring on the second **TAMC**. One **TAMC** captured the methyl group of one EA molecule with each benzene ring forming a C–H···π interaction with one methyl group C-H, leading to this methyl end being captured in the centre of the **TAMC** cavity. With EA extended in the space, the other end of EA interacts with the benzene ring on another **TAMC**, as shown by the green iso-surface on the NCI plot. According to these first principles calculations, the interaction energy between **TAMC** and EtOH (-0.62 eV) is weaker than the interaction energy between **TAMC** and EA (-0.91 eV). This can be attributed to both the weak $V_{s,max}$ of hydrogen bond sites and loss of C–H···π interaction on the hydroxyl end of EtOH.

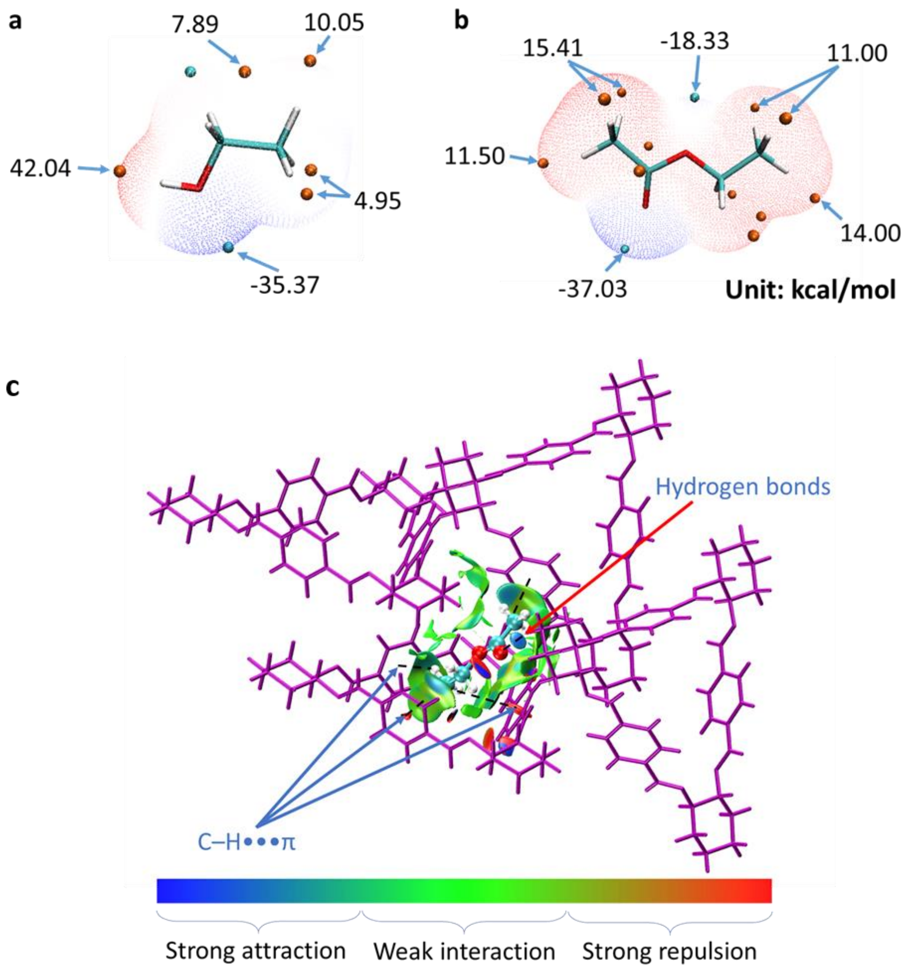

Figure 2.20. Electrostatic surface potential (ESP) of the (**a**): EA; (**b**): EtOH, the blue point represents most negative ESP ($V_{s,min}$), and the red point represents most positive ESP ($V_{s,max}$). Values are given in kcal/mol. The $V_{s,max}$ appear along the extension of the C-H bonds. In contrast, the C=O in the ester group shows the most negative **ESP**, attributed to the unpaired electrons on this atom. EA with these extreme point sites interacting with **TAMC** could form stable co-crystal. (c) Non-covalent interactions index iso-surface of EA@**TAMC**.

2.11 Conclusion

In this chapter, a known macrocycle molecule, **TAMC**, has been found to selectively adsorb EA, forming a stable EA@**TAMC** complex in the solid state. State-of-the-art crystal structure prediction, using solid state electronic structure calculations, shows that this solvate is the lowest energy EA:**TAMC** solvate structure; *i.e.*, its formation is thermodynamically driven. Crucially, it is also found that the same **TAMC** packing when EA is removed corresponds to a stable, albeit high energy, structure on the predicted landscape of **TAMC**. Thus, desolvation leaves an ‘imprinted’, near-perfect selective binding cavity after solvent removal. As a result of this inherently high selectivity, α-**TAMC** shows great promise for the static separation and dynamic separation of EA from EA-EtOH (azeotropic) mixtures, as confirmed by vial trials and breakthrough experiments, respectively. The selectivity of **TAMC** for EA on equimolar mixtures is about 5~6 times higher than the selectivity of the reported benchmark porous material (ZIF-8) under the same conditions for breakthrough experiments.[5] It has been also demonstrated that **TAMC** can selectively adsorb EA at a low concentration (100–500 ppm), a range that EA can be detected in wine. In conculsion, **TAMC** is readily synthesised from inexpensive starting materials, shows good reliability after multiple adsorption cycles, and holds strong promise for practical separation or detection applications in the future. More generally, the concept of solvent-imprinted molecular crystals, stabilised because they occupy deep energy basins on their structure landscapes, might be extended to other molecular separations in the future.

2.12 References

1. Margaret A. Cliff; Gary J. Pickering, Determination of odour detection thresholds for acetic acid and ethyl acetate in ice wine. *J. Wine Res.* **2006,** *17* (1), 45-52.

2. Catarina L. Silva, *et al.*, Volatile metabolomic signature of human breast cancer cell lines. *Sci. Rep.* **2017,** *7* (1), 43969.

3. J. Rudnicka, *et al.*, Determination of volatile organic compounds as potential markers of lung cancer by gas chromatography-mass spectrometry versus trained dogs. *Sens. Actuators B Chem.* **2014,** *202*, 615-621.

4. Joanna Rudnicka, *et al.*, Determination of volatile organic compounds as biomarkers of lung cancer by SPME–GC–TOF/MS and chemometrics. *J. Chromatogr. B* **2011,** *879* (30), 3360-3366.

5. Thomas Virdis, *et al.*, Nonideality in the Adsorption of Ethanol/Ethyl Acetate/Water Mixtures On ZIF-8 Metal Organic Framework. *Ind. Eng. Chem. Res.* **2018,** *57* (20), 7040-7047.

6. L. Berg, *et al.*, The Recovery of Ethyl-Acetate by Extractive Distillation. *Chem. Eng. Commun.* **1985,** *39* (1-6), 193-199.

7. Alfonsina E. Andreatta, *et al.*, Using Ionic Liquids To Break the Ethanol–Ethyl Acetate Azeotrope. *ACS Sustainable Chem. Eng.* **2015,** *3* (12), 3435-3444.

8. A. Hasanoğlu, *et al.*, Pervaporation separation of ethyl acetate–ethanol binary mixtures using polydimethylsiloxane membranes. *Chem. Eng. Process.* **2005,** *44* (3), 375-381.

9. Olga A. Pogodina, *et al.*, Combination of Sorption Tube Sampling and Thermal Desorption with Hollow Waveguide FT-IR Spectroscopy for Atmospheric Trace Gas Analysis: Determination of Atmospheric Ethene at the Lower ppb Level. *Anal. Chem.* **2004,** *76* (2), 464-468.

10. J. Gawroński, *et al.*, Designing Large Triangular Chiral Macrocycles: Efficient [3 + 3] Diamine−Dialdehyde Condensations Based on Conformational Bias. *J. Org. Chem.* **2000,** *65* (18), 5768-5773.

11. Jana Hodacova, *et al.*, Shape-Complementarity in the Recognition of Tricarboxylic Acids by a [3+3] Polyazacyclophane Receptor. *J. Org. Chem.* **2005,** *70* (6), 2042-2047.

12. Nikolai Kuhnert, *et al.*, The application of quasi-enantiomeric trianglamine macrocycles as chiral probes for anion recognition in ion trap ESI mass spectrometry. *Tetrahedron: Asymmetry* **2007,** *18* (14), 1648-1654.

13. Arnaud Chaix, *et al.*, Trianglamine-Based Supramolecular Organic Framework with Permanent Intrinsic Porosity and Tunable Selectivity. *J. Am. Chem. Soc.* **2018,** *140* (44), 14571-14575.

14. Luca Iuzzolino, *et al.*, Crystal structure prediction of flexible pharmaceutical-like molecules: density functional tight-binding as an intermediate optimisation method and for free energy estimation. *Faraday Discuss.* **2018,** *211* (0), 275-296.

15. M. A. Neumann, *et al.*, Combined crystal structure prediction and high-pressure crystallization in rational pharmaceutical polymorph screening. *Nat. Commun.* **2015,** *6* (1), 7793.

16. James T. A. Jones, *et al.*, Modular and predictable assembly of porous organic molecular crystals. *Nature* **2011,** *474* (7351), 367-371.

17. Kecheng Jie, *et al.*, Near-Ideal Xylene Selectivity in Adaptive Molecular Pillar[n]arene Crystals. *J. Am. Chem. Soc.* **2018,** *140* (22), 6921-6930.

18. Peng Cui, *et al.*, An Expandable Hydrogen-Bonded Organic Framework Characterised by Three-Dimensional Electron Diffraction. *J. Am. Chem. Soc.* **2020,** *142* (29), 12743-12750.

19. David W. Hand, *et al.*, Prediction of multicomponent adsorption equilibria using ideal adsorbed solution theory. *Environ. Sci. Technol.* **1985,** *19* (11), 1037-1043.

20. M. Thommes, *et al.*, Physisorption of gases, with special reference to the evaluation of surface area and pore size distribution (IUPAC Technical Report). *Pure Appl. Chem.* **2015,** *87* (9-10), 1051-1069.

21. Martin Chadim, *et al.*, (3+3)-Cyclocondensation of the enantiopure and racemic forms of trans-1,2-diaminocyclohexane with terephthaldehyde. Formation of diastereomeric molecular triangles and their stereoselective solid-state stacking into microporous chiral columns. *Tetrahedron: Asymmetry* **2001,** *12* (1), 127-133.

22. Agnieszka Janiak, *et al.*, A thermo-responsive structural switch and colossal anisotropic thermal expansion in a chiral organic solid. *Chem. Commun.* **2018,** *54* (30), 3727-3730.

23. Marc A. Little, *et al.*, Trapping virtual pores by crystal retro-engineering. *Nat. Chem.* **2015,** *7* (2), 153-159.

24. Kenneth E. Maly, Assembly of nanoporous organic materials from molecular building blocks. *J. Mater. Chem.* **2009,** *19* (13), 1781-1787.

25. Arne Thomas, *et al.*, Hard templates for soft materials: Creating nanostructured organic material. *Chem. Mater.* **2008,** *20* (3), 738-755.

26. Jens Weber, *et al.*, Mesoporous poly(benzimidazole) networks via solvent mediated templating of hard spheres. *Macromolecules* **2007,** *40* (4), 1299-1304.

27. I. Hisaki, *et al.*, Designing Hydrogen-Bonded Organic Frameworks (HOFs) with Permanent Porosity. *Angew. Chem. Int. Ed. Engl.* **2019,** *58* (33), 11160-11170.

28. Graeme M. Day, *et al.*, An Assessment of Lattice Energy Minimization for the Prediction of Molecular Organic Crystal Structures. *Cryst. Growth Des.* **2004,** *4* (6), 1327-1340.

29. Angeles Pulido, *et al.*, Functional materials discovery using energy–structure–function maps. *Nature* **2017,** *543* (7647), 657-664.

30. Catherine M. Aitchison, *et al.*, Photocatalytic proton reduction by a computationally identified, molecular hydrogen-bonded framework. *J. Mater. Chem.* **2020,** *8* (15), 7158-7170.

31. E. R. Johnson, *et al.*, Revealing noncovalent interactions. *J. Am. Chem. Soc.* **2010,** *132* (18), 6498-506.

Chapter 3:

Chiral recognition in the assembly of imine macrocycles

3.1 Contributions to this chapter

The work reported in Chapter 3 is published in Donglin He; Rob Clowes; Marc A. Little*; Ming Liu*; Andrew I. Cooper*. *Chemical Communications*, 2021, 57 (50), 6141-6144.

Donglin He synthesised and characterised the compounds, and conducted the structural study of the compounds. Dr. Marc A. Little assisted with the refinement of the single crystal structures. Rob Clowes assisted with gas isotherms measurements. Donglin He drafted the manuscript and all authors provided critical feedback and helped shape the manuscript.

3.2 Introduction

3.2.1 Porous molecular solids

Porous materials are widely useful in applications such as gas storage, molecular separations, and sensing of gases or vapours[1-4]. Synthetic control over pore structure and topology has been achieved for extended framework materials such as zeolites[5], MOFs[6] and COFs[7]. There is also a growing interest in porous molecular solids; one such example is POCs[8-10], where solid state function can be intrinsic to the molecular building units. Porous molecular crystals have some potential advantages compared with their extended framework cousins, such as their improved processibility.[11, 12] In general, however, it is also more challenging to design structure and hence function for porous molecular solids because their crystal packing is often dictated by the sum of a variety of relatively weak and often non-directional intermolecular forces.

3.2.2 Gas/vapour separation with macrocycles

Macrocycles, whose solution-phase host-guest chemistry has been studied extensively,[13] have been explored recently for a range of molecular separations using the macrocycles in the solid, crystalline state. For example, Janiak and co-workers reported a trianglamine macrocycle crystal with 1-D channels that absorbed ethanol.[14] In Chapter 2, it was shown that a trianglimine macrocycle crystal can separate ethyl acetate from its azeotropic mixture with ethanol.[15] Eddaoudi and co-workers reported a triangleamine-based supramolecular organic framework that showed permanent porosity and high affinity for CO_2.[16] It has also been shown that formally non-porous pillar[*n*]arenes that do not adsorb gasses can selectively adsorb styrene from ethylbenzene[17] and *para*-xylene from its structural isomers.[18] However, a challenge to the practical use of macrocycles as adsorbents for separations is their limited adsorption capacities and (often) slow adsorption kinetics. One strategy to solve these kinetic and capacity problems is to increase the porosity in the molecular system. For example, 3-D POCs, with larger cavities can exhibit Brunauer-Emmett-Teller surface areas (SA_{BET}) as high as 3758 $m^2\ g^{-1}$.[19, 20] It is more challenging to introduce significant porosity into macrocycles. This is because macrocycles have lower dimensional intrinsic porosity; they are also prone to close packing, minimizing any void space in the solid state.[21, 22] Hence, unlike POCs with 3-D intrinsic connected pores in the solid state, macrocycle solids rarely have interconnected pore networks that facilitate the rapid diffusion of guest molecules. To date, examples of macrocycles that have been reported with a specific surface area higher than 100 m^2/g are still rare.[18, 23] While high surface areas are catered for by numerous other existing porous solids, there is potential benefit in accessing porous macrocycle crystals with porosity levels that are high enough to permit good diffusion kinetics while retaining the small and size/shape-specific cavity of the macrocycle.

3.2.3 Approaches for creating porosity in macrocycles

One approach to create porosity in macrocycle structures is to introduce "extrinsic" pores that connect to the small intrinsic macrocycle pores.[24] Modular co-crystallization strategies have proven to be effective here.[22] For example, the modular assembly of POCs of opposing chiralities has made it possible to control the size and shape of pores in POC crystals.[25, 26] The same approach also allowed 'gating POCs' to be combined with a second POC to exclude a competitive guest and to achieve high guest selectivity.[27] However, to our knowledge, this method has not been applied to control the solid state porosity of intrinsically porous molecules, other than POCs.

3.2.4 Separation of xylene isomers

Xylene isomers (ortho, meta and para, referred to as *o*X, *m*X and *p*X) are the important solvents and chemical feedstocks in industry and research. The separation of xylene isomers is one of the "seven chemical separations to change the world",[28] and is challenging because they have similar molecular structures and physical properties. As shown in Table 3.1, *p*X, *o*X and *m*X have similar boiling points. Although the difference in their freezing points allows separation by fractional crystallization, the energy cost of this technology is high due to the required temperature at about −53 °C.[29] Therefore, energy-efficient alternatives such as separation with microporous materials have been developed. However, due to the similar molecular sizes of the three isomers (Table 3.1), it is challenging to identify a suitable porous material for their separation. Recently, crystalline molecular materials such as pillar[*n*]arenes,[18] cucurbit[7]uril[30] and the polymorphic azobenzene cage[31] have been studied as adsorbents for the separation of xylene isomers based on their host-guest behaviour.

Table 3.1. Physical properties of *para*-xylene (*p*X), *meta*-xylene (*m*X), and *ortho*-xylene (*o*X)

Xylene isomer	Boiling point (°C)	Melting Point (°C)	Kinetic diameter (Å)	Molecular size (Å)[a]
*p*X	138.5	13.20	5.8	4.2*6.8
*m*X	139.1	–47.9	6.4	4.8
*o*X	144.4	–25.2	6.5	4.6

[a] The molecular size of the xylene isomers were calculated using the van der Waals Radii of the atoms.

3.3. Synthesis of isotrianglimine 1

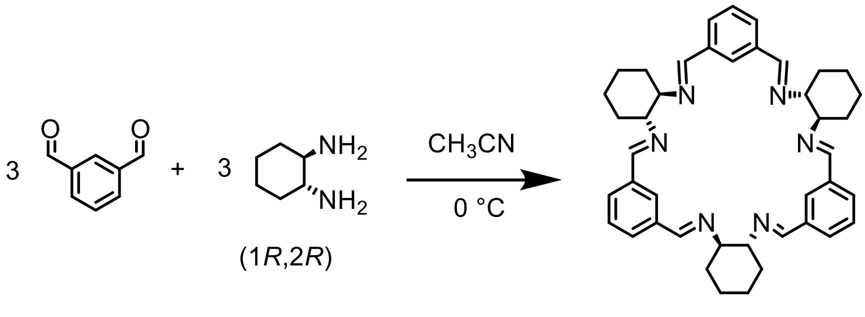

Figure 3.1. Scheme of the synthesis of isotrianglimine **1**.

Isotrianglimine [3+3] macrocycles, formed by reacting isophthaldehyde with aliphatic diamines, were first reported by Gawronski and co-workers in 2000.[32] Subsequently, a series of chiral isotrianglimines were developed, formed by the condensation of *trans*-1,2-cyclohexanediamine with substituted isophthaldehydes were reported,[33, 34] including **1**-*R* (Figure 3.1) that is synthesised by reacting *trans*-1,2-cyclohexanediamine with isophthalaldehyde.

3.4 Structural analysis of 1-*R* and 1-*rac*

As shown in Figure 3.2a, the structure of **1**-*R* is reminiscent of the window motif in the chiral POC **CC3**-*R*. And it has been reported to direct the crystal packing of POCs by generating energetically favourable heterochiral window-to-window packing motifs in racemic crystals.[26] Therefore, it is supposed that the macrocycle **1** would have similar behaviour to form racemic window-to-window packing dimers, which creates the 3-D intrinsic connected pores in racemic crystals. In order to confirm the suppose, the crystal structure of chiral and racemic macrocycle **1** were synthesised and analysed by single crystal x-ray diffraction (SC-XRD).

Firstly, solvated single crystals of **1**-*R* were obtained from methanol (MeOH@**1**-*R*, Figure 3.2b) that revealed the **1**-*R* molecules were stacked in an eclipsed fashion along the crystallographic *c*-axis. This motif gave rise to pillars of **1**-*R* that contained solvents in their intrinsic cavities. Residual electron density in the crystal structure that was within 3 Å of N6 was tentatively modelled as partially H_2O without riding H atoms. However, this electron density could indicate unresolved solvent disorder. (Table 3.2) In this structure, the neighbouring **1**-*R* pillars are linked by intermolecular hydrogen bonding interaction via the methanol solvent molecules. It was therefore unsurprising that the packing of **1**-*R* changed when the MeOH molecules were removed from the MeOH@**1**-*R* crystals (Figure 3.2c) to afford a polycrystalline **1**-*R*. It should be noted that a different guest-free polymorph of **1**-*R* can also be induced from ethyl acetate (EA). (Figure 3.2c)

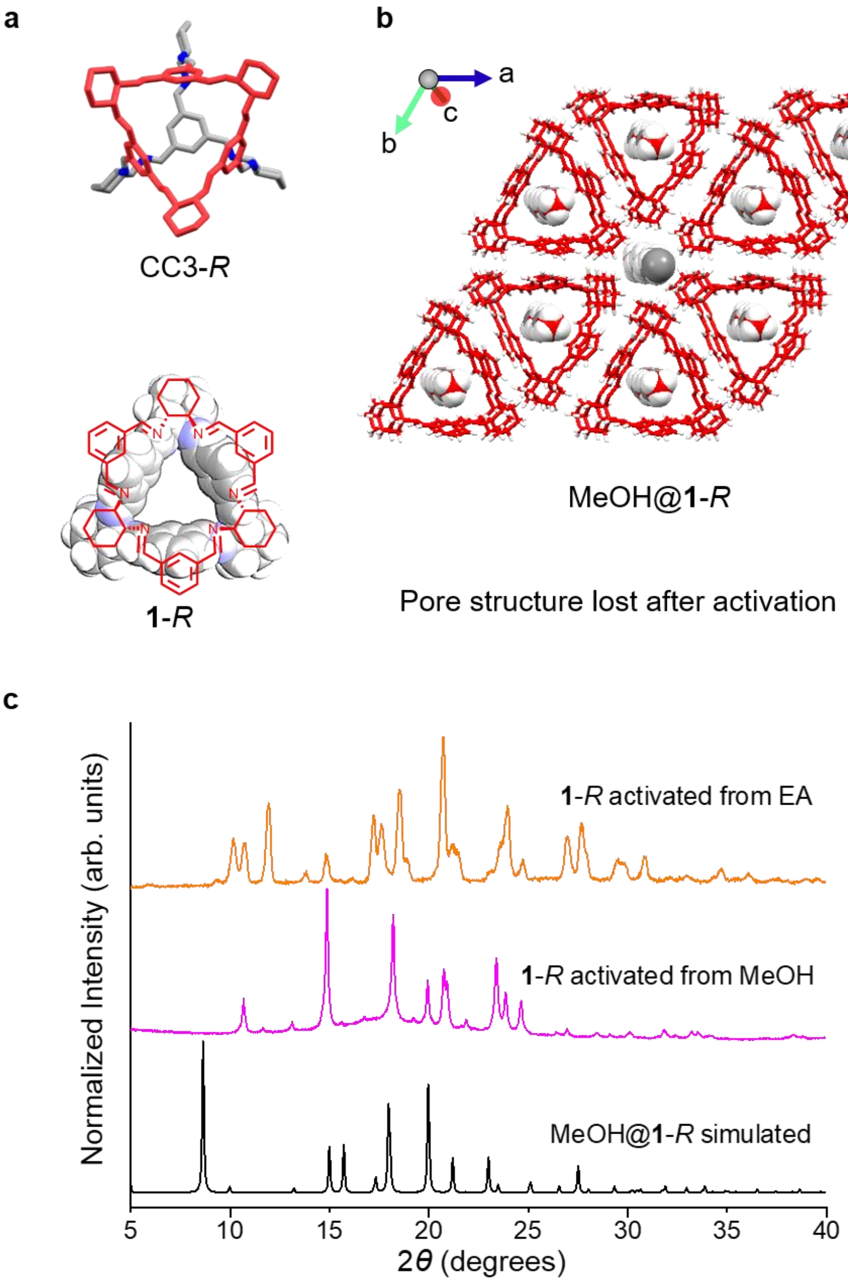

Figure 3.2. (a) Single crystal structures of the chiral POC CC3-*R* (above), which contains a structural fragment equivalent to **1**-*R*, and **1**-*R* (bottom) displayed in space filling mode. (b) Crystal packing in MeOH@**1**-*R*, MeOH guest displayed in space filling mode. (c) PXRD patterns of activated **1**-*R* recrystallised from EA and dried at 80 °C under vacuum (top), activated **1**-*R* recrystallised from MeOH and dried at 80 °C under vacuum (middle), and simulated PXRD pattern of solvated **1**-*R* recrystallised from MeOH (bottom).

Solvated racemic co-crystals of **1** (EA@**1**-*rac*) were obtained by recrystallising an equimolar ratio of **1**-*R* and **1**-*S* from ethyl acetate (EA, Figure 3.3a). The structure of EA@**1**-*rac* was refined as a 2-component twin with HKLF5 reflection file and BASF refined to 0.4661(12). Attempts were made to resolve all the disordered EA solvent molecules in the **1** cavities, but some residual electron density was modelled as disordered O atoms. (Table 3.2) The EA@**1**-*rac* was found to remain suitable for single crystal analysis after activation under a dynamic vacuum at 80 °C. In the activated structure, **1**-*rac*, the racemic window-to-window packing between macrocycles is stabilised by π-π stacking and C-H···π interactions, and this was retained after removing the EA solvent (Figure 3.3b-d and Table 3.2). The assembly of neighbouring **1**-*rac* heterochiral pairings along the *c* axis generates interconnected pores in the crystal structure that occupy 11.6 % of the unit cell, as calculated using *Platon* with a probe radii of 1.2 Å. The size of the interconnected pores could be represented with the largest free sphere (D_f) of 2.31 Å calculated by *Zeo++*.[35] This indicates that the porosity is generated in the racemic pairing motif of **1**-*rac*.

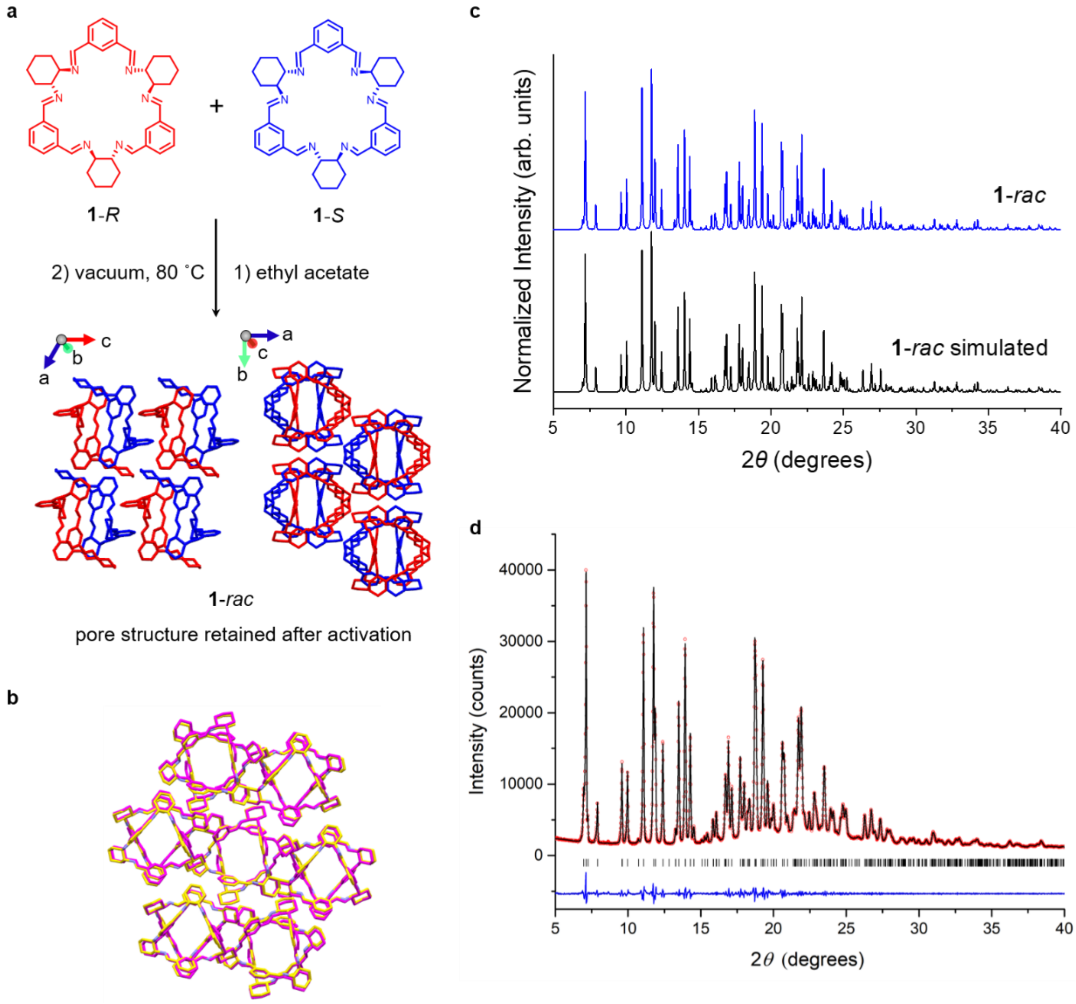

Figure 3.3. (a) Single crystal structure of **1**-*rac*. **1**-*R* (red) and **1**-*S* (blue); H atoms are omitted for clarity. (b) Crystal packing overlay for EA@**1**-*rac* (magenta) and activated **1**-*rac* (yellow), which was generated using the crystal packing similarity tool in Mercury. (c) PXRD patterns of activated **1**-*rac* recrystallised from EA and dried at 80 °C under vacuum (top), and simulated PXRD pattern of activated **1**-*rac* (bottom). (d) Pawley refinement of **1**-*rac* that was refined using the monoclinic *I* centred symmetry used to refine the single crystal structure. Final observed (red), calculated (black) and difference (blue) PXRD profiles for Pawley refinement (R_{wp} = 3.26%, R_p = 2.38%, χ^2 = 2.20, a = 24.8713(5) Å, b = 14.8879(3) Å, c = 22.8102(5) Å; β = 101.577(2)°; V = 8274.4(3) Å^3, $I2/a$).

Table 3.2. SC-XRD data for MeOH@**1**-*R* and activated **1**-*rac***.**

Molecule	MeOH@**1**-*R*	EA@**1**-*rac*	**1**-*rac*
Crystallisation Solvent	methanol	EA	EA
Space Group	$P6_3$	$P\bar{1}$	$I2/a$
Wavelength [Å]	Mo-Kα	Mo-Kα	Mo-Kα
Collection Temperature	100 K	100 K	100 K
Formula	$C_{42}H_{48}N_6$, $0.75(C_6H_{24}O_6)$	$2(C_{42}H_{48}N_6)$, $2(C_4H_8O_2)$, $2(H_2O)$	$C_{42}H_{48}N_6$
Mr	660.89	1481.93	636.86
Crystal Size (mm)	0.36×0.25× 0.14	0.25×0.19× 0.16	0.30×0.21× 0.11
Crystal System	hexagonal	triclinic	monoclinic
a [Å]	20.450(2)	14.3324(6)	24.7909(8)
b [Å]	= *a*	14.3555(6)	14.7339(4)
c [Å]	5.9423(5)	25.1851(9)	22.7185(8)
α [°]	90	89.815(3)	90
β [°]	90	77.839(4)	101.230(3)
γ [°]	120	60.849(4)	90
V [Å^3]	2152.2(5)	4393.8(3)	8139.4(5)
Z	2	2	8
D_{calcd} [g cm^{-3}]	1.020	1.120	1.039
μ [mm^{-1}]	0.062	0.071	0.062
$F(000)$	711	1592	2736
2θ range [°]	6.08 – 43.88	3.27 – 52.85	3.22 – 52.74
Reflections collected	19869		52053
Independent Obs. Data [$I > 2\sigma$]	1724, 0.1107 1504	27498 16482	8312, 5734
Data/restraints/ parameters	1724/3/154	27498 / 30 / 994	8312/0/433
Final R_1 values ($I > 2\sigma(I)$)	6.46%	8.21%	6.28%
Final R_1 values (all data)	7.57%	12.41%	10.02%
Final $wR(F^2)$ values (all data)	16.37%	22.77%	15.03%
Goodness-of-fit on F^2	1.078	1.203	1.042
Largest difference peak and hole [e.A^{-3}]	0.397/-0.173	0.710/-0.357	0.213/-0.196
CCDC	2073635	2073632	2073633

3.5 Gas isotherms

To evaluate the effects of the activation processes on the gas sorption properties of **1**-*R* and **1**-*rac*, the porosity using N_2, H_2, and CO_2 as the probe gases was investigated. The N_2 isotherms (Figure 3.4a) show that **1**-*rac* is porous to N_2, with an apparent SA_{BET} of 355 m^2 g^{-1}, and that it undergoes a low-pressure adsorption step at 0.66 mbar. By contrast, **1**-*R* activated from MeOH@**1**-*R* is essentially non-porous to N_2 and has a much lower calculated SA_{BET} of 4 m^2 g^{-1}.[36] **1**-*rac* also has a much higher H_2 uptake at 1 bar and 77 K (2.56 mmol g^{-1} for **1**-*rac* *vs*. 0.12 mmol g^{-1} for **1**-*R*) and no hysteresis was found in the H_2 adsorption isotherms for either sample (Figure 3.4b). The gas sorption isotherms confirm that we successfully created porosity in macrocycle **1** by using the heterochiral pairing strategy to stabilise a porous crystal packing.

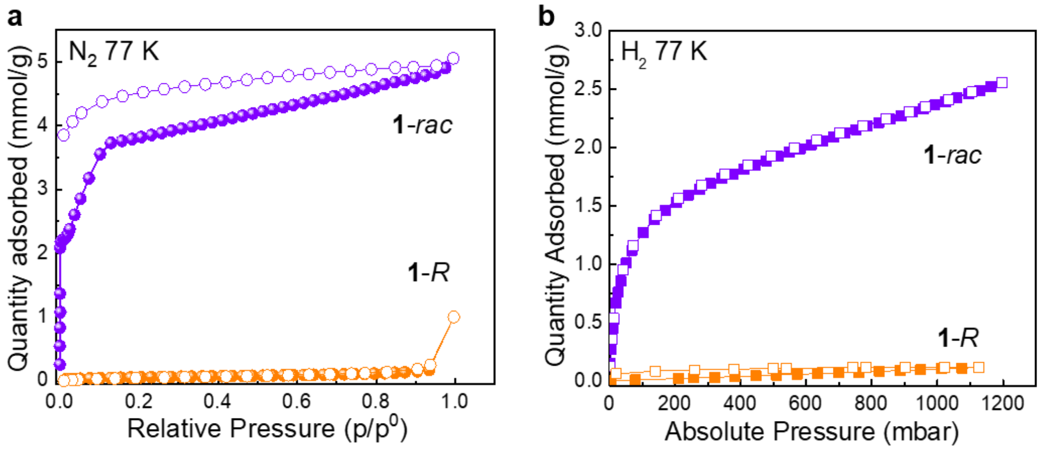

Figure 3.4. (a) N_2 sorption isotherms at 77 K for activated **1**-*R* (orange) and **1**-*rac* (purple). (b) H_2 sorption isotherms at 77 K for activated **1**-*R* and **1**-*rac*. Solid symbols: adsorption; hollow symbols: desorption.

As mentioned in Section 3.4, the **1**-*R* isolated from EA retained its crystallinity as a different guest-free polymorph. Similar to **1**-*R* activated from MeOH@**1**-*R*, the **1**-*R* structure isolated from EA was barely porous to N_2 and H_2 after activation. (Figure 3.5a,b)

For materials containing very small or disconnected pores, which N_2 molecules cannot access at cryogenic temperatures, CO_2 isotherms are often used to probe porosity.[37] For **1**-*R* isolated from EA, the rapid onset of CO_2 adsorption isotherm at very low pressure at 195 K indicates the presence of ultra-fine pores that cannot be accessed by N_2 molecules at 77 K (Figure 3.5c).[38] CO_2 uptake for **1**-*rac* shows a typical type - Ⅰ isotherm with no hysteresis loop at 195 K; at 1 bar, **1**-*rac* absorbed significantly more CO_2 than **1**-*R* (3.80 mmol *vs* 2.17 mmol) (Figure 3.5c). This result is consistent with the N_2 isotherms and confirms that substantial additional porosity has been created in **1**-*rac*.

The high-pressure CO_2 adsorption isotherm of **1**-*rac* at 273 K shows two successive 'plateaus' (Figure 3.5d), which corresponds to CO_2 accessing the different pores in the **1**-*rac* structure as it expands, and similar dynamic behaviour has been observed in other porous solids.[39] It is worth noting that the stepwise sorption isotherms highlight the structural flexibility of **1**-*rac*.[39] These different pores can be assigned to the cavity and the interconnected channels created by the heterochiral pairings in **1**-*rac*. In contrary to N_2 and H_2 isotherms, the uptake of CO_2 with chiral **1**-*R* is higher than the **1**-*rac* at a pressure range below 4 bar. As shown in 3.5e, at higher temperatures (273 K, 283 K, and 298 K), **1**-*R* also adsorbs more CO_2 than **1**-*rac* in the low relative pressure range (0–1 bar). Although it has been reported that introducing imine bonds into the porous polymer frame-works can improve CO_2 binding affinity. [40] It is unusual that **1**-*R* has more CO_2 uptake than that by **1**-*rac*, taking into account the nearly 24 times higher surface area than that of **1**-*rac* and their same amount of imine bonds per gram.

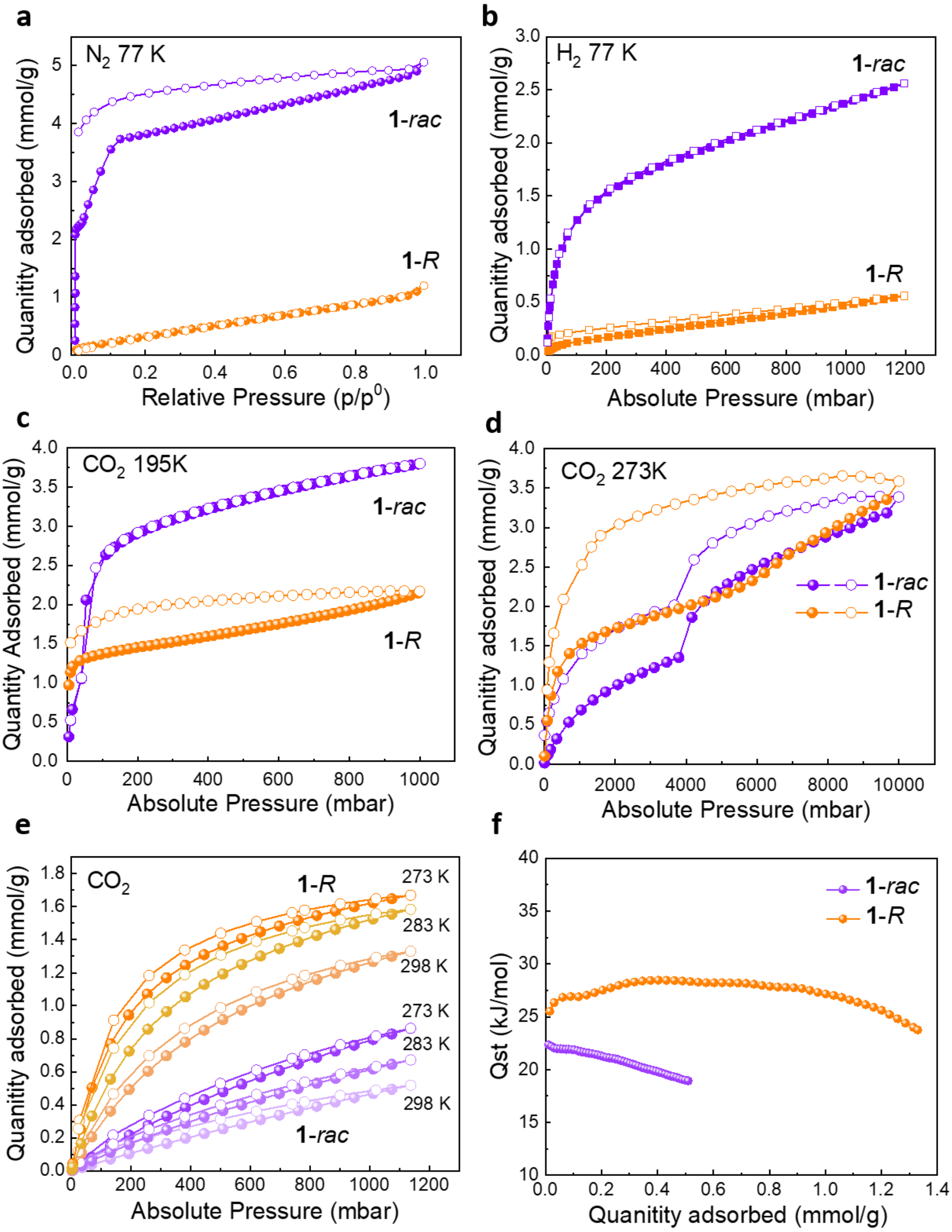

Figure 3.5. Gas sorption isotherms for **1**-*R* (orange) and **1**-*rac* (violet) samples that were activated from EA. (a) N_2 isotherms (77 K), (b) H_2 (77 K). (c) CO_2 isotherms at 195 K form 0 -1 bar. (d) CO_2 isotherms at 273K from 0 to 10 bar. (e) CO_2 isotherms at temperatures recorded between 273–298 K. (f) Isosteric heat of adsorption (Q_{st}) of CO_2 (273-298 K). Adsorption isotherms as closed symbols; desorption isotherms as open symbols.

To understand this initially counterintuitive phenomenon, the isosteric heats of adsorption (Q_{st}) were calculated from the CO_2 isotherms (273–298 K, 0–1 bar) for **1**-*rac* and **1**-*R*. As shown in 3.5f, the calculated isosteric heats of adsorption (Q_{st}) for **1**-*R* and **1**-*rac* were less than 30 kJ/mol, excluding the possibility of chemisorption by either adsorbent.[41] The Q_{st} for CO_2 on **1**-*R* remained constant over a larger adsorbate loading range (0–1 mmol/g), indicating an energetically homogeneous surface.[42] **1**-*rac* had a linear decrease in Q_{st} with CO_2 loading over the range of 0–0.5 mmol/g, indicating that **1**-*rac* is more energetically heterogeneous for the adsorption of CO_2.[42] The higher CO_2 uptake of **1**-*R* at lower pressures can be attributed to ultra-fine pores in **1**-*R* that can adsorb CO_2 as a monolayer. By contrast, the larger interconnected pores of **1**-*rac* lead to the multilayer adsorption of CO_2 but with lower uptakes at lower pressures.

3.6 Guest-host study of 1- *rac* with xylene isomers in solution

The largest included sphere along the free sphere path (D_{if}) calculated by *Zeo*++ [35, 43] in the activated **1**-*rac* structure is 4.26 Å, which is close to the molecular size of *para*-xylene (*p*X) (4.2×6.8 Å) (Section 3.2.4, Table 3.1). This close size match suggested that **1**-*rac* might be a good host for *p*X over its structural isomer, *meta*-xylene (*m*X, 4.8 Å). We initially crystallised **1**-*R* and **1**-*S* from *p*X and determined the crystal structure of the resulting inclusion complex, 1*p*X@**1**-*rac* (Figure 3.7a). The crystal structure of 1*p*X@**1**-*rac* revealed that one *p*X molecule crystallised in the centre of the cavity created between **1**-*R* and **1**-*S* molecules packed in a window-to-window arrangement. This showed that the encapsulation of *p*X does not interfere with the complementary interaction between the heterochiral **1** pairs. A second *p*X molecule in the structure was located in an extrinsic void created between four **1** molecules through C-H···π interactions. Compared with the guest-free structure of **1**-*rac*, the inclusion of *p*X does not significantly change the packing of **1** (Figure 3.6a,b), as confirmed by the crystal packing overlay shown in Figure 3.6e. However, **1**-*rac* does expand by around 8% to accommodate 1 mol/mol of *p*X in its structure.

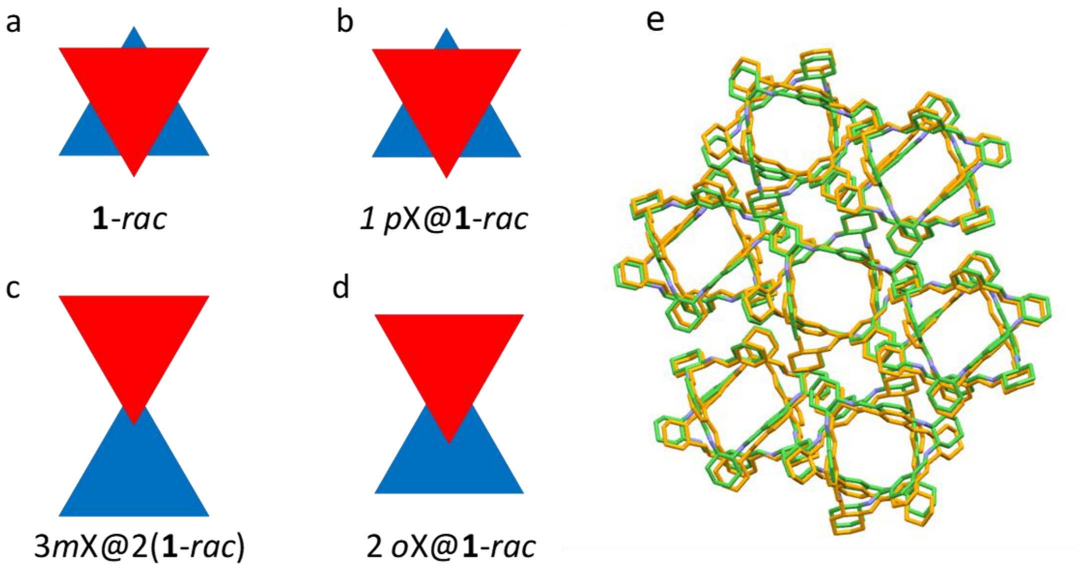

Figure 3.6. Schematic representation of the packing modes of the racemic **1** dimer in **1**-*rac* crystal structures. (a) **1**-*rac*, (b) 1*p*X@**1**-*rac*, (c) 3*m*X@2(**1**-*rac*), (d) 2*o*X@**1**-*rac*. **1**-*R* and **1**-*S* are coloured in red and blue, respectively. (e) Crystal packing overlay for 1*p*X@**1**-*rac* (green) and activated **1**-*rac* (yellow), which was generated using the crystal packing similarity tool in Mercury.

On the contrary, the host-guest structures with *m*X and *o*X have totally different packing mode compared with structures of **1**-*rac* and 1*p*X@**1**-*rac*. (Figure 3.6) Solvated single crystals of 3*m*X@2(**1**-*rac*) with monoclinic $P2_1/c$ space group are obtained from *m*X solvent. As shown in Figure 3.7b, in one unit cell, three *m*X molecules are included between two **1** molecules, one of the methyl ends of two *m*X sit inside the cavity of two **1**, respectively. And another *m*X is located in the space between two opposite chiral **1**, which interferes the complementary interaction between the heterochiral **1** pairs. 2*o*X@**1**-*rac* crystallised from *o*X with triclinic $P\bar{1}$ space group has closer packing along *a* and *c* axis compared with 1*p*X@**1**-*rac*. (Table 3.3) As shown in Figure 3.7c, the encapsulation of *o*X molecules rearranges significantly the packing of **1**-*rac* from window to window to angle to angle. *o*X molecules have two different inclusion positions in crystal, one is with methyl ends in the cavity of **1**, another is out of the cavity.

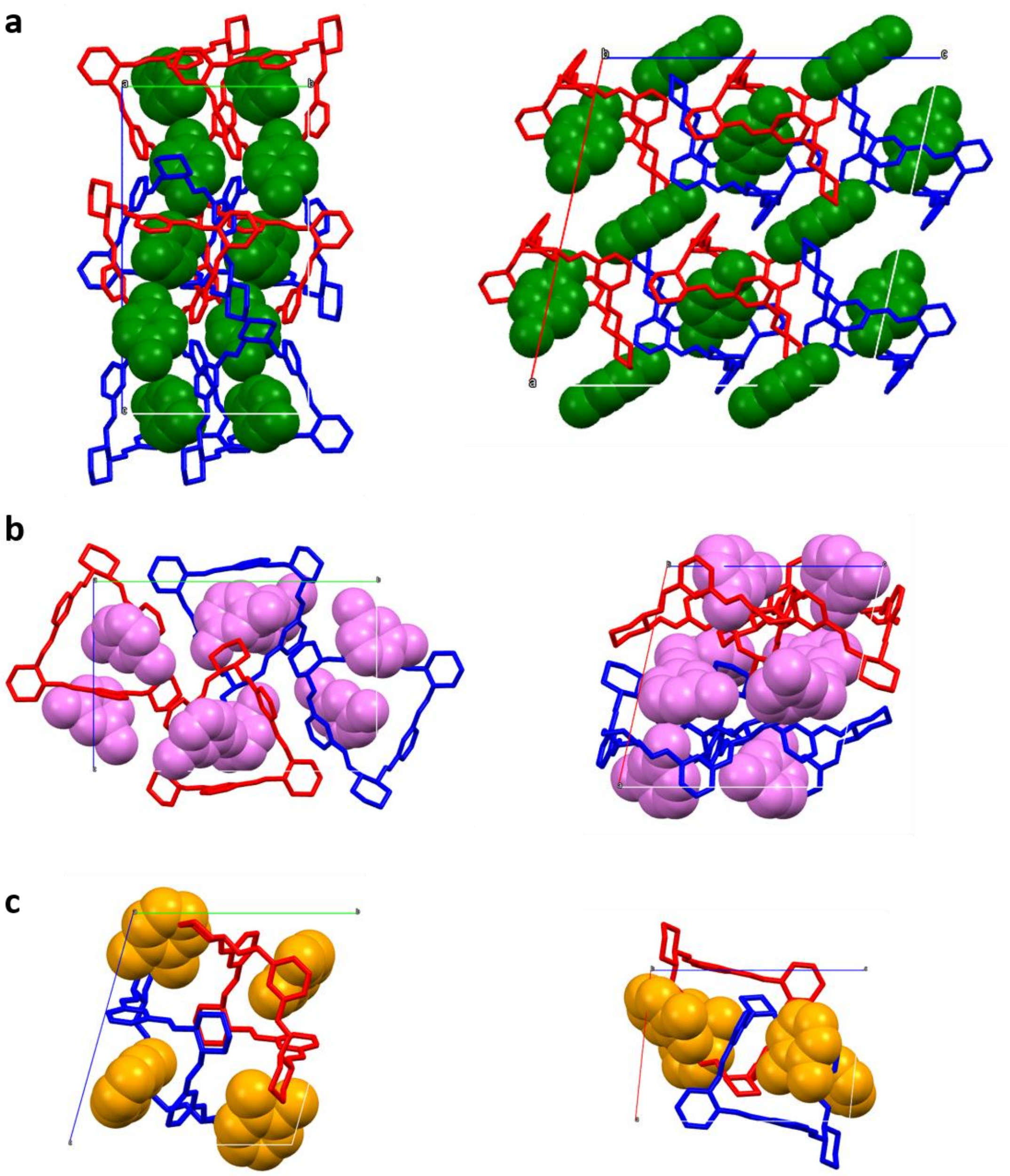

Figure 3.7. Crystal structure of (a) 1*p*X@**1**-*rac* viewed along the crystallographic *a*-axis (left) and *b*-axis(right); (b) 3*m*X@2(**1**-*rac*) viewed along the crystallographic *a*-axis (left) and *b*-axis (right); (c) 2*o*X@**1**-*rac* viewed along the crystallographic *a*-axis (left) and *b*-axis (right). **1**-*R* and **1**-*S* are coloured in red and blue, respectively. *p*X, *m*X and *o*X are coloured in green, pink and orange. H atoms are omitted for clarity.

Table 3.3. SC-XRD data for xylene loaded **1**-*rac* structures.

Molecule	1*p*X@**1**-*rac*	3*m*X@2(**1**-*rac*)	2*o*X@**1**-*rac*
Crystallisation Solvent	*p*X	*m*X	*o*X
Space Group	$C2/c$	$P2_1/c$	$P\bar{1}$
Wavelength [Å]	Mo-Kα	Mo-Kα	0.6889
Collection Temperature	100 K	100 K	100 K
Formula	$C_{42}H_{48}N_6$, $2(0.5(C_8 H_{10})$	$2(C_{42}H_{48}N_6)$, $3(C_8H_{10})$	$C_{42}H_{48}N_6$, $2(C_8H_{10})$
Mr	743.02	1594.0	849.18
Crystal Size (mm)	0.54×0.28×0.09	0.45×0.19×0.10	0.1×0.06×0.02
Crystal System	monoclinic	monoclinic	triclinic
a [Å]	25.2103(4)	29.9687(5)	11.19190(7)
b [Å]	14.0669(2)	22.3149(3)	15.18470(8)
c [Å]	25.3934(4)	14.6297(2)	15.73550(8)
α [°]	90	90	104.5050(4)
β [°]	102.506(2)	103.221(2)	91.5770(5)
γ [°]	90	90	105.6390(5)
V [$Å^3$]	8791.6(2)	9524.3(3)	2480.11(2)
Z	8	4	2
D_{calcd} [g cm^{-3}]	1.123	1.112	1.137
μ [mm^{-1}]	0.066	0.065	0.062
$F(000)$	3200	3436	916.0
2θ range [°]	3.56 – 66.15	3.65 – 52.78	2.60 – 51.69
Reflections collected	70247	133758	32622
Independent reflections, R_{int}	15555, 0.0536	19494, 0.0762	10349, 0.1264
Obs. Data [$I > 2\sigma$]	11060	13778	9404
Data/restraints/ parameters	15555/0/507	19494/160/1147	10349/112/632
Final R_1 values ($I > 2\sigma(I)$)	6.37%	6.68%	6.74%
Final R_1 values (all data)	9.63%	9.99%	7.41%
Final $wR(F^2)$ values (all data)	15.59%	14.81%	19.55%
Goodness-of-fit on F^2	1.015	1.065	1.077
Largest difference peak and hole [e.A^{-3}]	0.336/-0.369	0.387 / -0.198	0.521/-0.398
CCDC	2073634	2073637	2073636

3.7 Xylene isomers vapour-phase adsorption studies

In order to carry out xylene isomers vapour adsorption experiments for **1**-*rac*, an open 5 mL vial containing 3.5 mg of guest-free **1**-*rac* adsorbent was placed in a sealed 20 mL vial containing 0.5 mL pure *p*X, pure *m*X, pure *o*X for 5.5 h. Afterwards, the crystals were characterised by ^{1}H NMR after fully dissolving the sample in CD_2Cl_2. (Figure 3.8) These results suggested that **1**-*rac* can adsorb all three xylene isomers.

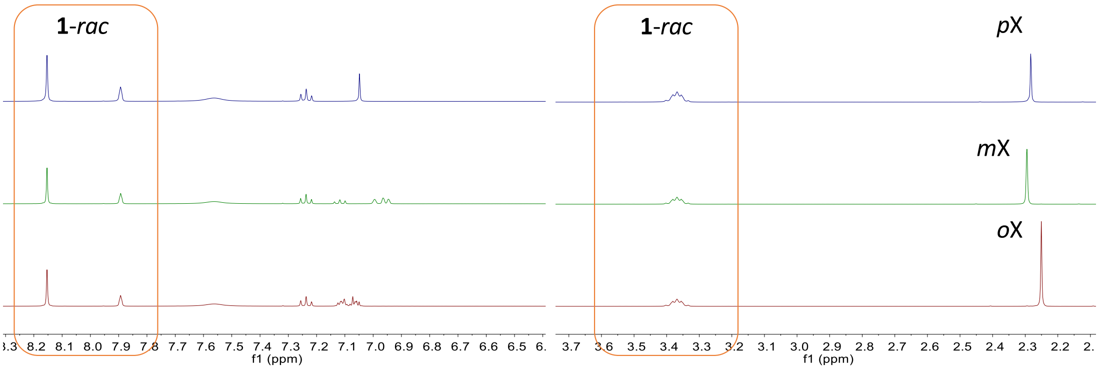

Figure 3.8 ^{1}H NMR spectrum (400 MHz, CD_2Cl_2) of **1**-*rac* after vapour adsorption of *p*X, *m*X, or *o*X for 5.5 h.

In addition, PXRD patterns for samples of **1**-*rac* after being exposed to xylene isomers vapour suggest that 1*p*X@**1**-*rac*, 3*m*X@2(**1**-*rac*) and 2*o*X@**1**-*rac* can be formed *in* *p*X, *m*X, and *o*X vapour, respectively. (Figure 3.9). This is further confirmed by their weight loss below the decomposition temperature of **1**-*rac* in the TGA curves, which is consistent with the xylene loading ratio of 1*p*X@**1**-*rac*, 3*m*X@2(**1**-*rac*) and 2*o*X@**1**-*rac*. (Figure 3.10)

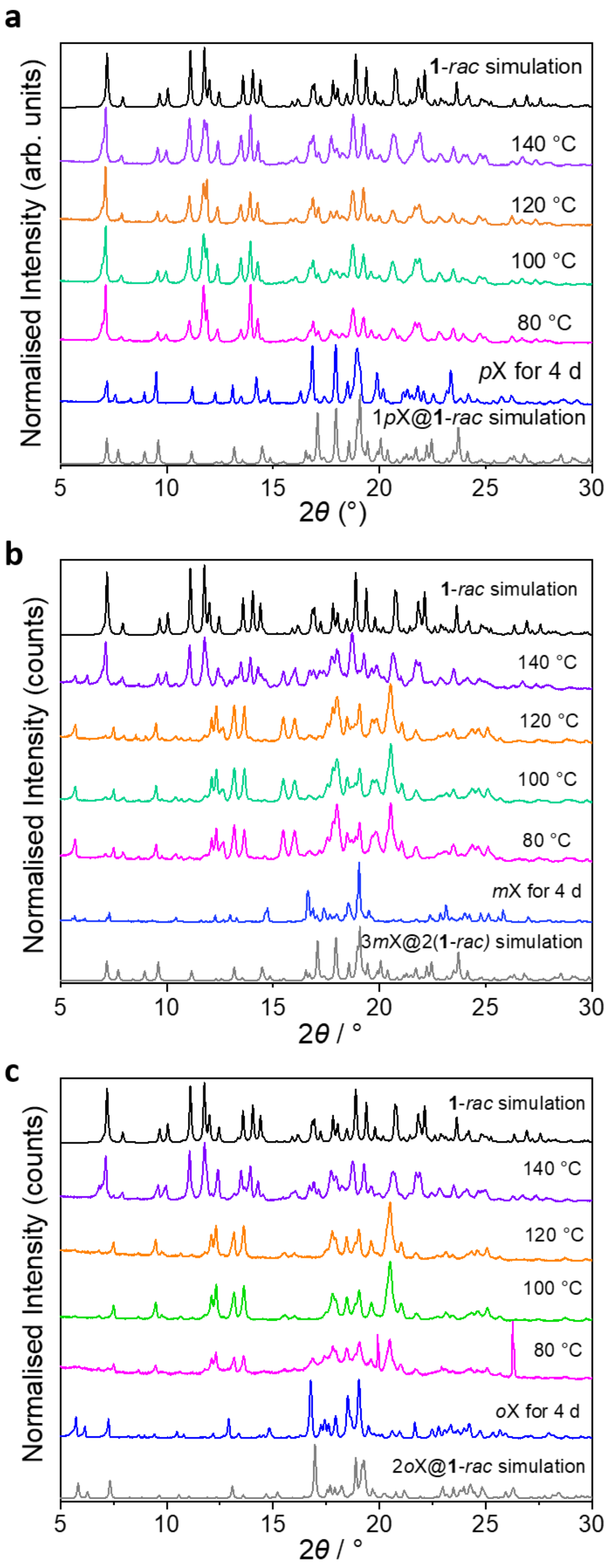

Figure 3.9. (a) PXRD patterns for samples of **1**-*rac* after being exposed to (a) *p*X, (b) *m*X and (c) *o*X vapour and then dried under vacuum at elevated temperatures.

When the xylene vapour exposed samples were activated under vacuum, they could be transformed into the activated **1**-*rac* structure at 140 °C (Figure 3.9), indicating that **1**-*rac* is the energetically most favourable phase. However, the lower transformation temperature at 80 °C (Figure 3.9) and lower activation starting temperature at 31 °C (Figure 3.10) for the *p*X loaded sample indicates that *p*X desorbs more easily from 1*p*X@**1**-*rac*. This is likely due to the more interconnected 1-D porosity in 1*p*X@**1**-*rac* and the narrower dimensions of *p*X. The result is consistent with that 1*p*X@**1**-*rac* has similar packing to **1**-*rac,* which suggests that *p*X can be more easily absorbed and desorbed through the window to window structure of **1**-*rac.*

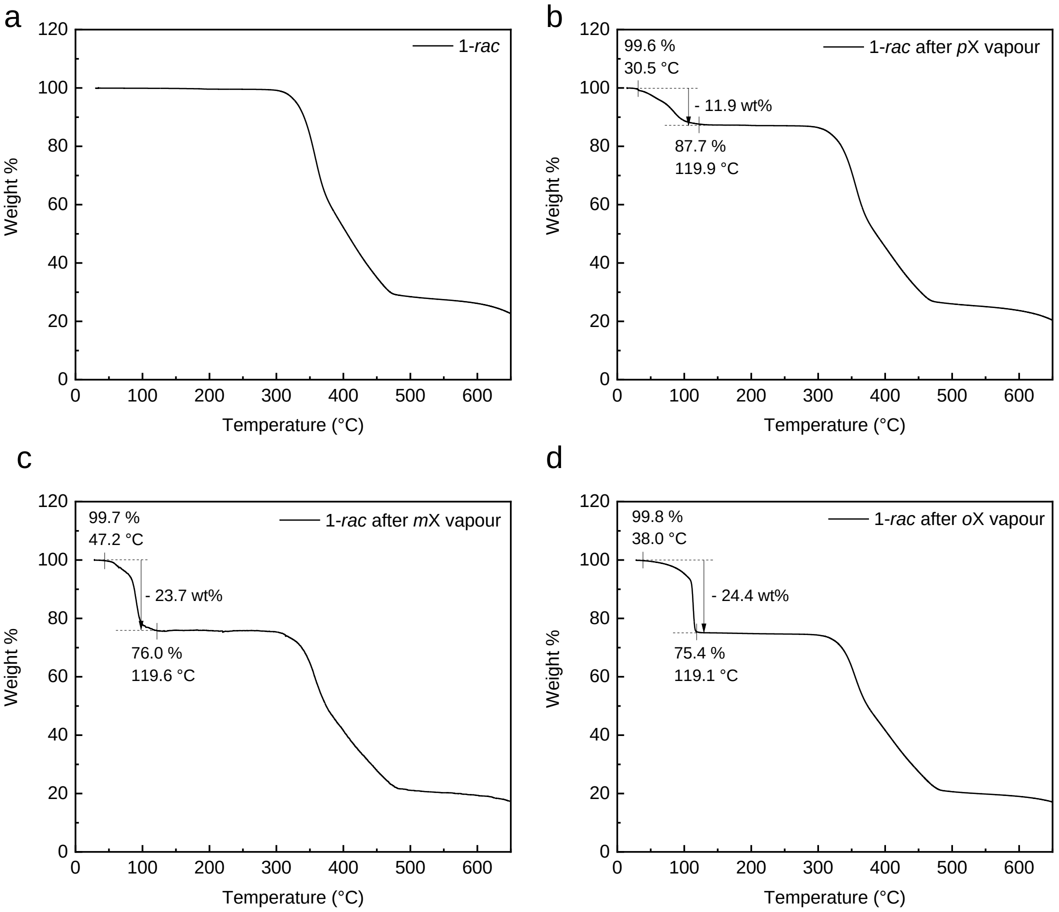

Figure 3.10. Thermogravimetric analysis of a) **1**-*rac*. b) **1**-*rac* after adsorption of *p*X. c) **1**-rac after adsorption of *m*X. c) **1**-*rac* after adsorption of *o*X. To generate the xylene loaded materials, **1**-*rac* was exposed to vapours of the pure xylene isomers for 14 hours at room temperature in a sealed vial.

3.8 The separation of xylene isomers with **1**-*rac*

Based on the guest-host study of *rac*-**1** with xylene isomers in solution, *rac*-**1** with the suitable pore size and structural flexibility for *p*X has potential for xylene isomers separations.

3.8.1 The separation of *para*-xylene from *meta*-xylene with **1**-*rac*

To determine if **1**-*rac* could separate *p*X from *m*X under a competitive adsorption environment, time-dependent solid–vapour sorption experiments were performed by using the vapours generated from a physical mixture of the two xylene isomers. An open 5 mL vial containing 3.5 mg of guest-free **1**-*rac* adsorbent was placed in a sealed 20 mL vial containing 0.5 mL of 1:1 (*vol*:*vol*) mixtures of *p*X, *m*X. Initially, the resultant crystals were evaporated at room temperature for 30-45 min. Afterwards, The relative uptake of guests adsorbed by the **1**-*rac* crystals was measured by completely dissolving the crystals in CD_2Cl_2 and measuring the ratio of xylene isomers to **1**-*rac* by ^{1}H NMR spectroscopy. As shown in Figure 3.11 and Figure 3.12a-b, porous **1**-*rac* captures *p*X selectively from a 1:1 (*vol*:*vol*) mixture of *p*X and *m*X. The maximum uptake of *p*X with **1**-*rac* was 0.83 mol/mol after 10 h, which is close to the ideal ratio of 1 in 1*p*X@**1**-*rac*.

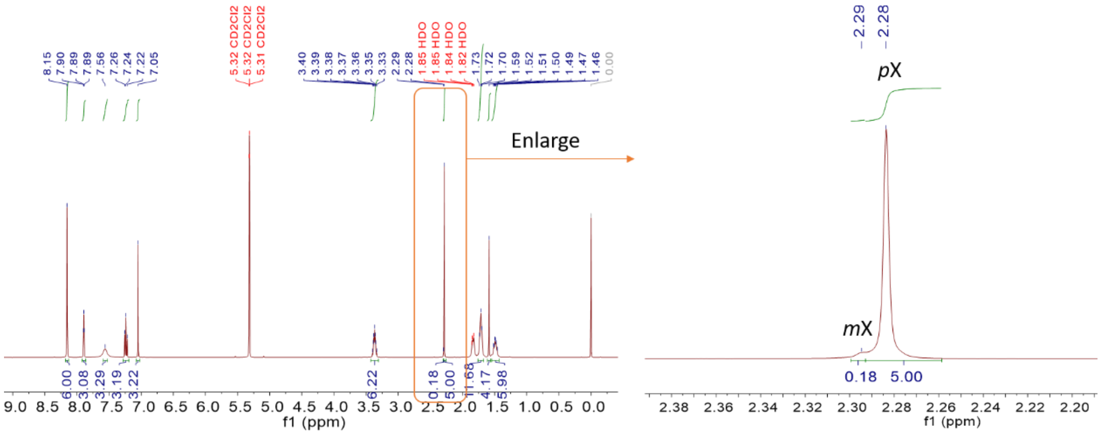

Figure 3.11. ^{1}H NMR spectrum (400 MHz, CD_2Cl_2) of **1**-*rac* after vapour adsorption of the *p*X:*m*X (1:1, *vol*:*vol*) mixture for 10 h. The relative uptake of *p*X and *m*X adsorbed by **1**-*rac* is plotted in Figure 4b.

Therefore, the 1*p*X@**1**-*rac* can also be formed in *p*X:*m*X (1:1, vol:vol) vapour mixture, as confirmed by the PXRD patterns shown in Figure 3.12c. In addition, the capacity of **1**-*rac* for *p*X in 1:1 *p*X-*m*X vapour mixture is about 1.5 times higher than for **1**-*R*, which we attribute to the increased porosity in **1**-*rac*. (Figure 3.12d)

$$K_{\mathrm{A:B}} = (K_{\mathrm{B:A}})^{-1} = Y_{\mathrm{A}}/Y_{\mathrm{B}} \cdot X_{\mathrm{B}}/X_{\mathrm{A}}\ (X_{\mathrm{B}} + X_{\mathrm{A}} = 1) \qquad (1)$$

A larger difference, however, is in the adsorption kinetics. For example, a formally non-porous pillar[6]arene macrocycle that adsorbs *p*X over *m*X with similar selectivity was found to reach saturation after 20 hours.[18] **1**-*rac* performs much better than this, reaching saturation after only 3 hours under the same conditions, with a selectivity coefficient of $K_{p\mathrm{X}:m\mathrm{X}}$ = 15.7.[44] $K_{p\mathrm{X}:m\mathrm{X}}$ was calculated according to equation 1, the selectivity of a host (H) for one guest (A) from a guest mixture can be described by the selectivity coefficient ($K_{\mathrm{A:B}}$),[44] where X_{A} and X_{B} represent the molar fractions of the two competing guests in the original solution mixture, and Y_{A} and Y_{B} represent the corresponding molar fractions of the same guests in the resulting inclusion complex.[44] The greatly improved adsorption kinetics of **1**-*rac* compared to the pillar[6]arene system is a direct result of its increased porosity, which results from the chiral pairing strategy. Furthermore, five adsorption-desorption cycles by using a 1:1 *p*X:*m*X vapour mixture indicates that **1**-*rac* has good stability for the separation of *p*X and *m*X.

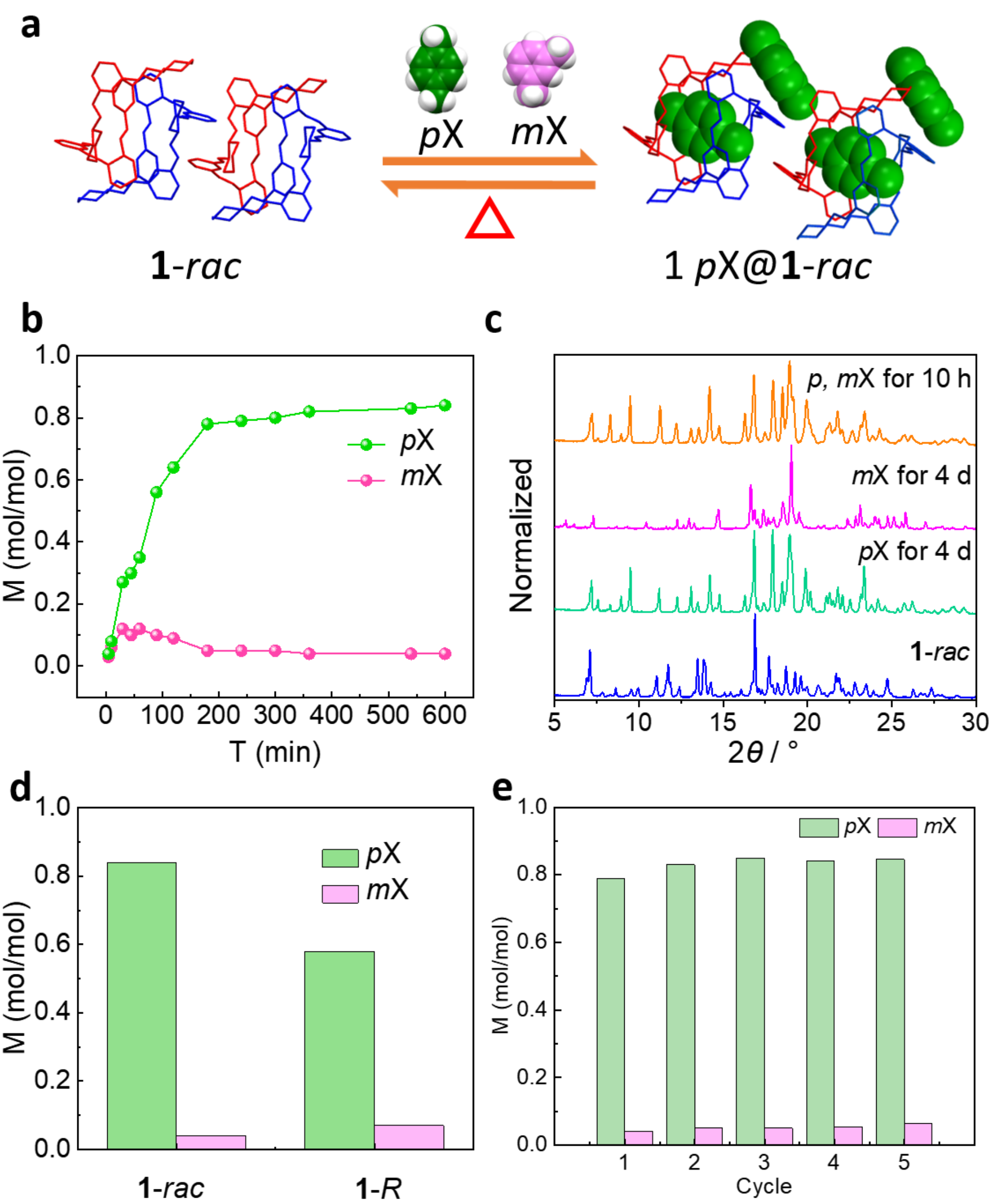

Figure 3.12. (a) Reversible capture of *p*X from 1:1 *p*X-*m*X vapour mixture illustrated by single-crystal structures for **1**-*rac* (left) and 1*p*X@**1**-*rac* (right). **1**-*R* and **1**-*S* are coloured red and blue, respectively; H atoms are omitted for clarity. (b) Time-dependent **1**-*rac* solid−vapour sorption plot for *p*X and *m*X equimolar vapour mixture. (c) PXRD patterns of **1**-*rac* after exposure to xylene vapours. (d) The capacity of **1**-*R* and **1**-*rac*, determined using a 1:1 *p*X-*m*X vapour mixture. (e) Adsorption–desorption cycles measured on a single sample of **1**-*rac* using a 1:1 *p*X:*m*X vapour mixture at room temperature. *p*X and *m*X uptakes in solid **1**-*rac* after 12 hours were calculated by ^{1}H NMR spectroscopy. Between the adsorption cycles, the material was thermally activated at 140 °C under a dynamic vacuum.

3.8.2 The separation of three xylene isomers with 1-*rac*

The time-dependent solid–vapour sorption experiments were also performed by using 1:1:1 (*vol*:*vol*:*vol*) mixture vapour of xylenes isomers. An open 5 mL vial containing 3.5 mg of guest-free **1**-*rac* adsorbent was placed in a sealed 20 mL vial containing 0.5 mL of 1:1:1 (*vol*:*vol*:*vol*) mixtures of *p*X, *m*X and *o*X. Initially, the resultant crystals were evaporated at room temperature for 30-45 min. Afterwards, The relative uptake of guests adsorbed by the **1**-*rac* crystals was measured by completely dissolving the crystals in CD_2Cl_2 and measuring the ratio of xylene isomers to **1**-*rac* by ^{1}H NMR spectroscopy. As shown in Figure 3.13, the **1**-*rac* can selectively capture *p*X from the mixture vapour of three xylenes isomers in the first 3 hours. The uptake shown in Figure 3.14a is 0.54 mol/mol *p*X, 0.15 mol/mol *m*X and 0.04 mol/mol *o*X. Then the uptake of *o*X and *m*X increases significantly to 0.72 mol/mol and 0.44 mol/mol, respectively with the decrease of *p*X uptake to 0.41 mol/mol after 10 h. (Figure 3.14b)

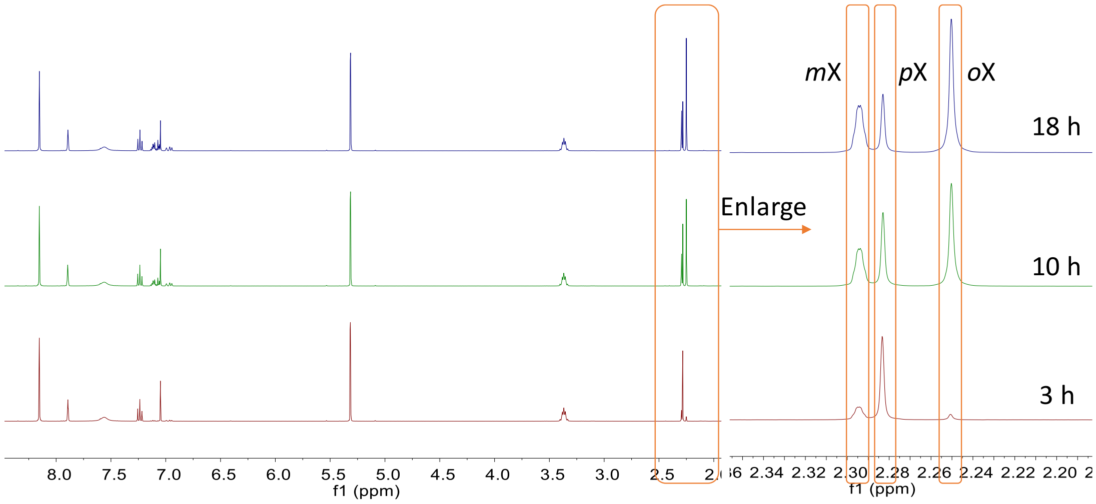

Figure 3.13. ^{1}H NMR spectra (400 MHz, CD_2Cl_2) from time-dependent vapour adsorption experiments for **1**-*rac* after exposure to the *p*X:*m*X:*o*X (1:1:1, *vol*:*vol*:*vol*) mixture. From bottom to top, the spectra were recorded at 3 h, 10 h, and 18 h.

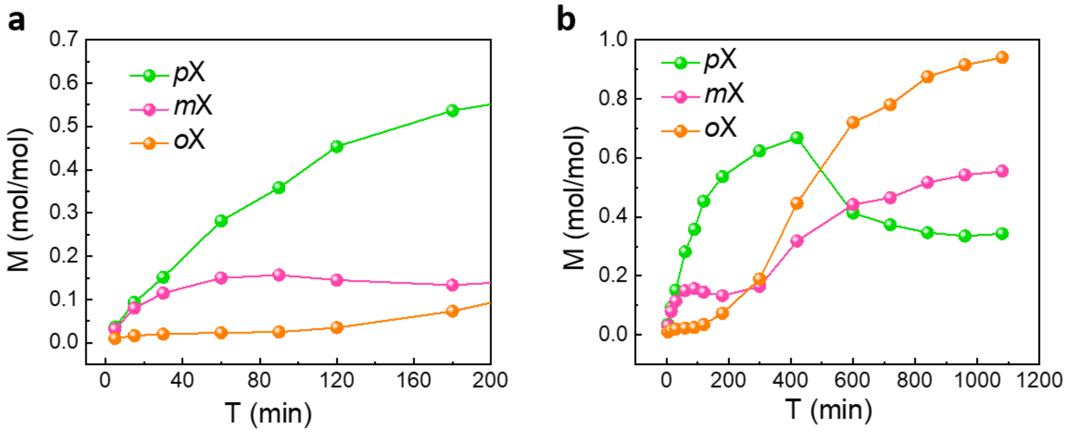

Figure 3.14. Time-dependent **1**-*rac* solid–vapour sorption plot for *p*X, *m*X, and *o*X from an equimolar vapour mixture, (a) over 3 hours, (b) over 18 hours.

In addition, it is observed that the PXRD pattern changed significantly after 10 h. (Figure 3.15) This may be due to the better stability of 2*o*X@**1**-*rac* indicated by the more closely-packed structure and the smaller lattice volume compared 1*p*X@**1**-*rac*, 3*m*X@2(**1**-*rac*) (Table 3.3).

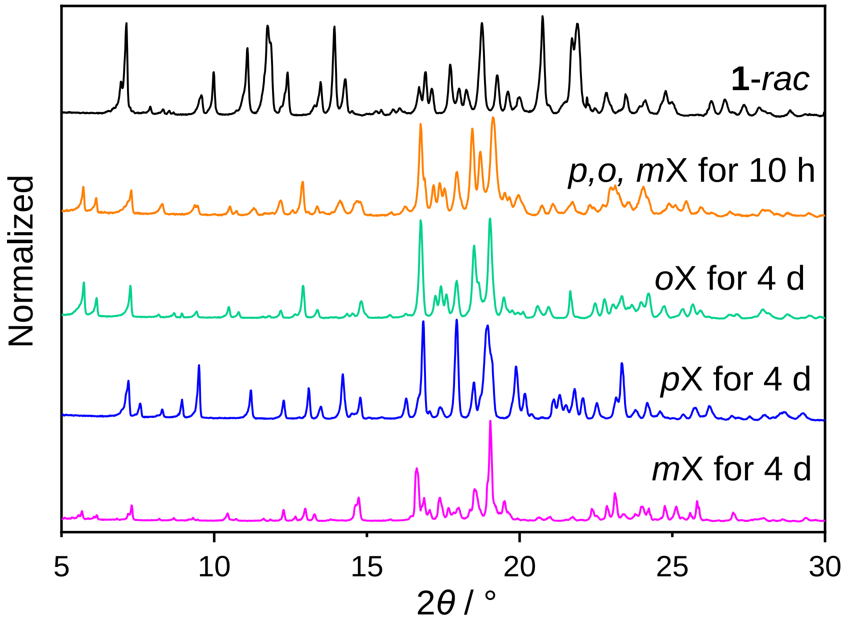

Figure 3.15. PXRD patterns of **1**-*rac* after exposure to xylene vapours. From bottom to top: **1**-*rac* after exposure to *m*X vapour for 4 d; **1**-*rac* after exposure to *p*X vapour for 4 d; **1**-*rac* after exposure to *o*X vapour for 4 d; **1**-*rac* after exposure to 1:1:1 pX:oX:*m*X mixture for 10 h; **1**-*rac* activated at 80 °C.

3.9 Conclusion

In conclusion, a heterochiral pairing strategy has been introduced to create porosity into a trianglimine macrocycle system. The porosity was created by co-crystallising two macrocycles with the opposing chiralities such that they pack in a window-to-window arrangement to connect the intrinsic macrocycles voids. This generates an interconnected pore network with an apparent SA_{BET} of 355 $m^2\ g^{-1}$. This is the highest reported surface area for the trianglimine macrocycle,[16, 23] which is usually barely porous in the solid state. Because of its increased porosity, the **1**-*rac* co-crystal has greatly improved adsorption kinetics and shows the potential to separate xylene isomers, exhibiting much higher selectivity toward *p*X, by a factor of 15.7 *vs.* *m*X, outperforming related macrocyclic systems for the same separation.[18] As well as introducing porosity, the heterochiral pairing strategy could also enrich the functionality of these macrocycle systems by enabling hybrid mixing of macrocycles with different functions that would otherwise not co-crystallise, as demonstrated with POCs for quantum sieving applications.[45] More broadly, this strategy could have practical importance in industrially relevant molecular separations in the future, where the slow kinetics of existing macrocycles is a key roadblock.

3.10 References

1. Christos Sapsanis, *et al.*, Insights on capacitive interdigitated electrodes coated with MOF thin films: Humidity and VOCs sensing as a case study. *Sensors* **2015,** *15* (8), 18153-18166.

2. Mohammad Gulam Rabbani; Hani M El-Kaderi, Synthesis and characterization of porous benzimidazole-linked polymers and their performance in small gas storage and selective uptake. *Chem. Mater.* **2012,** *24* (8), 1511-1517.

3. Jian-Rong Li, *et al.*, Selective gas adsorption and separation in metal–organic frameworks. *Chem. Soc. Rev.* **2009,** *38* (5), 1477-1504.

4. Malte Brutschy, *et al.*, Porous Organic Cage Compounds as Highly Potent Affinity Materials for Sensing by Quartz Crystal Microbalances. *Adv. Mater.* **2012,** *24* (45), 6049-6052.

5. Veselina M. Georgieva, *et al.*, Triggered Gate Opening and Breathing Effects during Selective CO_2 Adsorption by Merlinoite Zeolite. *J. Am. Chem. Soc.* **2019,** *141* (32), 12744-12759.

6. Shengqian Ma, *et al.*, A Coordinatively Linked Yb Metal–Organic Framework Demonstrates High Thermal Stability and Uncommon Gas-Adsorption Selectivity. *Angew. Chem. Int. Ed.* **2008,** *47* (22), 4130-4133.

7. Ren-Qi Wang, *et al.*, β-Cyclodextrin Covalent Organic Framework for Selective Molecular Adsorption. *Chem. Eur. J.* **2018,** *24* (43), 10979-10983.

8. T. Tozawa, *et al.*, Porous organic cages. *Nat. Mater.* **2009,** *8* (12), 973-8.

9. Tamoghna Mitra, *et al.*, Molecular shape sorting using molecular organic cages. *Nat. Chem.* **2013,** *5*, 276.

10. Anna G. Slater; Andrew I. Cooper, Function-led design of new porous materials. *Science* **2015,** *348* (6238), aaa8075.

11. J. R. Holst, *et al.*, Porous organic molecules. *Nat. Chem.* **2010,** *2* (11), 915-20.

12. Andrew I. Cooper, Porous Molecular Solids and Liquids. *ACS Cent. Sci.* **2017,** *3* (6), 544-553.

13. Fritz Vögtle; Edwin Weber, *Host Guest Complex Chemistry Macrocycles: Synthesis, Structures, Applications*. Springer Science & Business Media: 2012.

14. Agnieszka Janiak, *et al.*, From Cavities to Channels in Host:Guest Complexes of Bridged Trianglamine and Aliphatic Alcohols. *Cryst. Growth Des.* **2016,** *16* (5), 2779-2788.

15. Donglin He, *et al.*, Inherent Ethyl Acetate Selectivity in a Trianglimine Molecular Solid. *Chem. Eur. J.* **2021,** *27* (41), 10589-10594.

16. Arnaud Chaix, *et al.*, Trianglamine-Based Supramolecular Organic Framework with Permanent Intrinsic Porosity and Tunable Selectivity. *J. Am. Chem. Soc.* **2018,** *140* (44), 14571-14575.

17. Kecheng Jie, *et al.*, Styrene Purification by Guest-Induced Restructuring of Pillar[6]arene. *J. Am. Chem. Soc.* **2017,** *139* (8), 2908-2911.

18. Kecheng Jie, *et al.*, Near-Ideal Xylene Selectivity in Adaptive Molecular Pillar[n]arene Crystals. *J. Am. Chem. Soc.* **2018,** *140* (22), 6921-6930.

19. Michael Mastalerz, Porous Shape-Persistent Organic Cage Compounds of Different Size, Geometry, and Function. *Acc. Chem. Res.* **2018,** *51* (10), 2411-2422.

20. Gang Zhang, *et al.*, A Permanent Mesoporous Organic Cage with an Exceptionally High Surface Area. *Angew. Chem. Int. Ed.* **2014,** *53* (6), 1516-1520.

21. Neil B. McKeown, Nanoporous molecular crystals. *J. Mater. Chem.* **2010,** *20* (47), 10588-10597.

22. Marc A. Little; Andrew I. Cooper, The Chemistry of Porous Organic Molecular Materials. *Adv. Funct. Mater.* **2020,** *30* (41), 1909842.

23. Elena Sanna, *et al.*, A crystalline sponge based on dispersive forces suitable for X-ray structure determination of included molecular guests. *Chem. Sci.* **2015,** *6* (10), 5466-5472.

24. Michael J. Bojdys, *et al.*, Supramolecular Engineering of Intrinsic and Extrinsic Porosity in Covalent Organic Cages. *J. Am. Chem. Soc.* **2011,** *133* (41), 16566-16571.

25. James T. A. Jones, *et al.*, Modular and predictable assembly of porous organic molecular crystals. *Nature* **2011,** *474*, 367.

26. T. Hasell, *et al.*, Porous organic cage nanocrystals by solution mixing. *J. Am. Chem. Soc.* **2012,** *134* (1), 588-98.

27. Tom Hasell; Andrew I. Cooper, Porous organic cages: soluble, modular and molecular pores. *Nat. Rev. Mater.* **2016,** *1*, 16053.

28. David S Sholl; Ryan P Lively, Seven chemical separations to change the world. *Nature* **2016,** *532* (7600), 435-437.

29. Douglas M Ruthven, *Principles of adsorption and adsorption processes*. John Wiley & Sons: 1984.

30. Gengwu Zhang, *et al.*, Shape-Induced Selective Separation of Ortho-substituted Benzene Isomers Enabled by Cucurbit[7]uril Host Macrocycles. *Chem* **2020,** *6* (5), 1082-1096.

31. Basem Moosa, *et al.*, A Polymorphic Azobenzene Cage for Energy-Efficient and Highly Selective *p*-Xylene Separation. *Angew. Chem. Int. Ed.* **2020,** *59* (48), 21367-21371.

32. J. Gawroński, *et al.*, Designing Large Triangular Chiral Macrocycles: Efficient [3 + 3] Diamine−Dialdehyde Condensations Based on Conformational Bias. *J. Org. Chem.* **2000,** *65* (18), 5768-5773.

33. Nikolai Kuhnert, *et al.*, The synthesis of trianglimines: On the scope and limitations of the [3 + 3] cyclocondensation reaction between (1*R*,2*R*)-

diaminocyclohexane and aromatic dicarboxaldehydes. *Org. Biomol. Chem.* **2003,** *1* (7), 1157-1170.

34. Anna Troć, *et al.*, Specific Noncovalent Association of Chiral Large-Ring Hexaimines: Ion Mobility Mass Spectrometry and PM7 Study. *Chem. Eur. J.* **2016,** *22* (37), 13258-13264.

35. Thomas F. Willems, *et al.*, Algorithms and tools for high-throughput geometry-based analysis of crystalline porous materials. *Microporous Mesoporous Mater.* **2012,** *149* (1), 134-141.

36. Matthias Thommes, *et al.*, Physisorption of gases, with special reference to the evaluation of surface area and pore size distribution (IUPAC Technical Report). *Pure Appl. Chem.* **2015,** *87* (9-10), 1051-1069.

37. Peter I. Ravikovitch, *et al.*, Unified Approach to Pore Size Characterization of Microporous Carbonaceous Materials from N_2, Ar, and CO_2 Adsorption Isotherms. *Langmuir* **2000,** *16* (5), 2311-2320.

38. Brett D Chandler, *et al.*, Microporous metal− organic frameworks formed in a stepwise manner from luminescent building blocks. *J. Am. Chem. Soc.* **2006,** *128* (32), 10403-10412.

39. Bo Liu, *et al.*, Dynamic Zn-based metal–organic framework: stepwise adsorption, hysteretic desorption and selective carbon dioxide uptake. *J. Mater. Chem.* **2013,** *1* (22), 6535-6538.

40. Youlong Zhu, *et al.*, Imine-Linked Porous Polymer Frameworks with High Small Gas (H_2, CO_2, CH_4, C_2H_2) Uptake and CO_2/N_2 Selectivity. *Chem. Mater.* **2013,** *25* (9), 1630-1635.

41. Kai-Jie Chen, *et al.*, Tuning Pore Size in Square-Lattice Coordination Networks for Size-Selective Sieving of CO_2. *Angew. Chem. Int. Ed.* **2016,** *55* (35), 10268-10272.

42. S. Sircar; D. V. Cao, Heat of Adsorption. *Chem. Eng. Technol.* **2002,** *25* (10), 945-948.

43. M. D. Foster, *et al.*, A geometric solution to the largest-free-sphere problem in zeolite frameworks. *Microporous Mesoporous Mater.* **2006,** *90* (1), 32-38.

44. Adam M. Pivovar, *et al.*, Shape-Selective Separation of Molecular Isomers with Tunable Hydrogen-Bonded Host Frameworks. *Chem. Mater.* **2001,** *13* (9), 3018-3031.

45. Ming Liu, *et al.*, Barely porous organic cages for hydrogen isotope separation. *Science* **2019,** *366* (6465), 613.

Chapter 4:

Assembly of imine macrocycles by coordination with metal ions

4.1 Contributions to this chapter

The work reported about **MOC-1** in Chapter 4 is published in Donglin He‡; Linda Zhang‡*;Tao Liu; Rob Clowes; Marc A. Little*; Ming Liu*; Michael Hirscher; and Andrew I. Cooper*. *Angewandte Chemie International Edition*, 2022, e202202450. (‡ authors contributed equally)

Donglin He synthesised and characterised the compounds and conducted the structural study of the compounds. Dr Marc A. Little assisted with the refinement of the single crystal structures. Rob Clowes assisted with gas isotherms measurements. Dr Linda Zhang carried out the TDS measurement and cryogenic gas adsorption. Dr Tao Liu calculated the window diameter and pore diameter distribution histograms. Donglin He drafted the manuscript and all authors provided critical feedback and helped shape the manuscript.

4.2 Introduction

4.2.1 Metal-organic cages/polyhedrons

Metal-organic cages (MOCs),[1] also known as metal-organic polygons or polyhedrons (MOPs),[2] are discrete molecules with intrinsic cavities, formed through the self-assembly of metal cations (often as the vertices) and organic linkers (often as the edges and/or the faces). Like organic cages, many MOCs have good solubility in a range of solvents thus can be processed into different forms to optimise their structures and functions. Furthermore, as the discrete counterparts of MOFs, MOCs can also contain open metal sites, which can enhance their gas adsorption properties.[3-5] To date, MOCs have been demonstrated to selectively adsorb CO_2,[6] O_2,[7] CO,[8] NO,[9] and C_3H_8.[10] due to their specific pore sizes or open metal sites.

The solid-state porosity of MOCs is affected by guest accessibility to the intrinsic MOC cavity and extrinsic porosity in their structures.[11, 12] The intrinsic porosity of MOCs can be controlled by choosing appropriate organic linkers and metal centres,[13, 14] or by post-synthetic modification.[15] The extrinsic porosity in MOC solids can be controlled, to an extent, by using crystal engineering methods.[16, 17] An important consideration is that the organic units (or ligands) are key structural components of MOCs and significantly affect their molecular flexibility and porosity.[9, 18]. Although linear or planar organic linkers are the most common building units for MOCs, macrocycles with intrinsic voids or cavities, such as porphyrins,[19] calixarene,[9] and calixsalens[20] have recently emerged as MOCs building units. With their own intrinsic prefabricated cavities, macrocycles can enrich the functionality and structural diversity of MOCs. For example, calixarene-based macrocycles have been coordinated to tetranuclear clusters to form permanently porous MOCs,[21-23] with surface areas as high as 1239 m^2/g.[9]

4.2.2 Macrocycles for the assembly of metal-organic cages/ polyhedrons

Calixsalen macrocycles have a bowl-like shape and small intrinsic cavity (Figure 4.1a). They were first reported in 1999 by Jablonski *et al.*, who condensed 2-hydroxyisophthalaldehyde derivatives with chiral (*R*, *R*)-1,2-diaminocyclohexane.[24, 25] In 2018, Barbour *et al.* found that calixsalen macrocycles with Cl and Br substituents displayed remarkable sorption properties for ethylene and carbon dioxide, which suggested the potential of adjusting their sorption properties by introducing functional groups.[25] As shown in Figure 4.1 a, the enantiopure [3+3] calixsalen macrocycle, **M1**, has a rim and a tail. The rim consists of three cyclohexane rings and three hydroxy-substituted aromatic rings, while the tail consists of three bulky *tert*-butyl groups.[26] In the structure of **M1**, the three salen units have the same orientation,[26] and coordinating **M1** to metal ions, including zinc(II), has been used previously by Lisowski *et al.* to connect two **M1** macrocycles to form the trinuclear zinc **MOC-1** (Figure 4.1a).[20] The same group also reported that **MOC-1** has a SA_{BET} of 610 m^2/g after being activated at ambient temperature, and this material can enantioselectively bind chiral alcohols.[27] Most recently, **MOC-1** has been used for gas chromatographic separations,[28] and chiral separations.[29, 30]

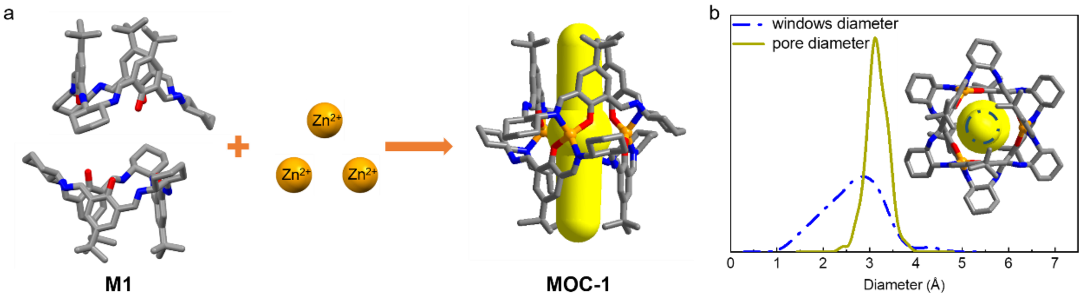

Figure 4.1. (a) The self-assembly of **MOC-1** from **M1** using zinc(II) ions. (b) Window diameter and pore diameter distribution histograms of **MOC-1** are shown in the right plot. The window diameter and pore diameter distribution histograms share the bottom X-axis. (orange, Zn; blue, N; red, O; grey, C)

The previously reported solvated single crystal structure of **MOC-1** shows that each MOC has a hollow cavity in a tubular shape with two narrow windows at both ends.[27] As shown in Figure 4.1b, the window diameter and pore diameter distribution histograms were calculated by py-window[31] based on xTB[32, 33] MD trajectory of **MOC-1** (see section 5.5.10, Chapter 5). The pore diameter of **MOC-1** is around 3.1 Å. In addition, the broad window diameter distribution below 2 Å is due to the rotation of the three *tert*-butyl groups.

Trianglimine macrocycles[34] were introduced in Chapter 1. Unlike calixsalen macrocycles, which are synthesised from isophthalaldehyde, terephthalaldehyde is used to synthesise trianglimine macrocycles. By using linearly connected bis-salicylaldehydes with two, three, or more aromatic rings, chiral large-ring triangular salen macrocycle with different cavities can be synthesised.[35] In addition, trianglsalens often have single or double OH groups substituting in each aromatic fragment of the macrocycle.[36, 37] With salen units similar to calixsalen macrocycles, trianglsalens have the potential for the synthesis of multicentre metal complexes, even for the assembly of MOPs. However, fewer reports use trianglsalens as building units for metal coordination.

4.2.3 Hydrogen isotopic separation

Deuterium (D_2) is a crucial fuel for future fusion power plants. D_2 is also used as a neutron moderator,[38, 39] in neutron scattering experiments,[40] and as a nonradiative isotope tracer.[41, 42] These applications require high purity D_2, which is non-trivial because of its low natural abundance of 0.0156 mol%. Typically, D_2 is purified industrially using the Girdler sulfide process[43] or by cryogenic distillation.[44] However, both methods are inefficient and energy-intensive.[38, 42] An attractive alternative to separate D_2 from its dominant isotope, hydrogen, is to adsorb D_2 on a microporous bed.

Kinetic quantum sieving (KQS), first proposed by Beenakker *et al.*,[45] describes the effect of lighter isotopes with larger de Broglie wavelengths encountering higher energy barriers as they diffuse through narrow pores at cryogenic temperatures. KQS effects lead to differences between the diffusion rates of isotopes, making it a potential process for the separation of D_2 from H_2. KQS requires adsorbents with ultrafine pore apertures; typically < 5 Å,[46] with pore apertures of 3.4 Å reported as the optimal size in rigid frameworks under cryogenic conditions.[47] Owing to their small pore sizes, several microporous materials have been investigated for KQS of hydrogen isotopes, including porous carbons[48], zeolites,[49, 50] metal-organic frameworks,[51, 52] and covalent organic frameworks.[47] Recently, a porous organic cage co-crystal has been reported that combined cages with narrow pores and cages with good capacities to achieve optimal separation performance in KQS.[53] However, despite some recent success, it remains challenging to precisely tune the pore size to the desired level required for KQS without compromising the adsorption capacity of the material. Also, the best selectivity tend to be achieved at very low temperatures (30–40 K), which is energetically costly.

MOCs/MOPs with the small pores that could be suitable for KQS and, potentially, open metal sites to enhance adsorption affinity, are interesting candidates for hydrogen isotope separation.[5, 54-57] Therefore, **MOC-1** with the window diameter around 2.8 Å has the optimal diameter for KQS.[53]

In this Chapter, calixsalen macrocycles and trianglimine macrocycles are investigated for the assembly of MOCs or MOPs. Their identity is confirmed by X-ray crystallography, NMR, elemental analyses and MS spectrum. In addition, gas isotherms and separations, including the D_2/H_2 separation by quantum sieving, are used to explore these assemblies potential applications.

4.3 M1 and MOC-1 synthesis and characterisation

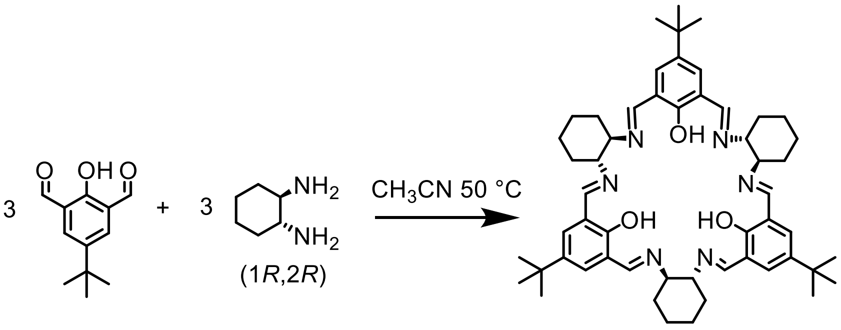

M1

Figure 4.2. Scheme of the synthesis of **M1.**

M1 was synthesised by the condensation of 4–*tert*–butyl–2,6–diformylphenol and (1*R*, 2*R*)–diaminocyclohexane as described previously.[20] (Figure 4.2) Using **M1** as building units, the **MOC-1** was synthesised by reacting **M1** with zinc(II) acetate in a 2:3 ratio in methanol as described previously.[20] (Figure 4.3).

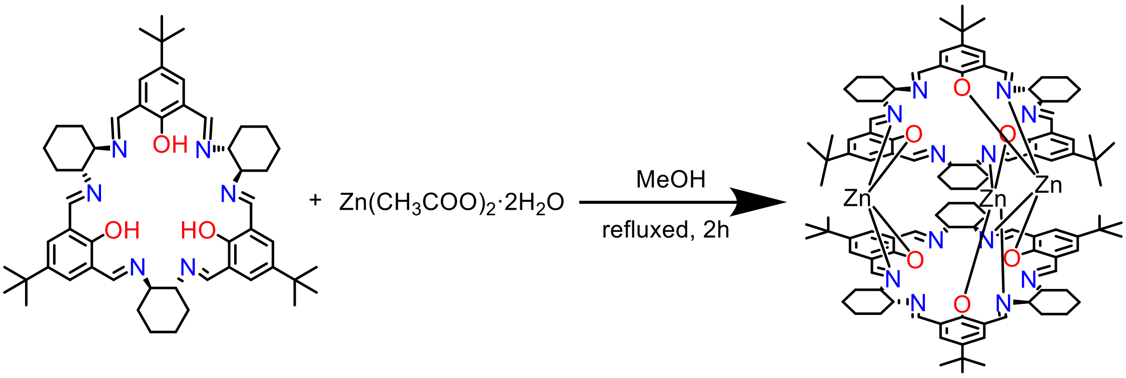

M1

MOC-1

Figure 4.3. Scheme of the synthesis of **MOC-1.**

Solvated single crystals of **MOC-1**, referred to as MeOH@**MOC-1**, were obtained as large yellow block crystals from the reaction solvent,[27, 58] and a previous study reported that activated crystals of **MOC-1** were unsuitable for single-crystal X-ray diffraction analysis.[27] However, in this study, two solvent-free single-crystal structures of **MOC-1** were successfully obtained after thermally activating high-quality crystals of MeOH@**MOC-1**, grown in the reaction solvent at room temperature over 12 hours. To activate MeOH@**MOC-1**, solvated crystals were collected by filtration and heated the sample under vacuum at 80 °C. After activation, the crystals transformed into a new phase referred to as, **MOC-1α**, which was confirmed by PXRD patterns shown in Figure 4.4a

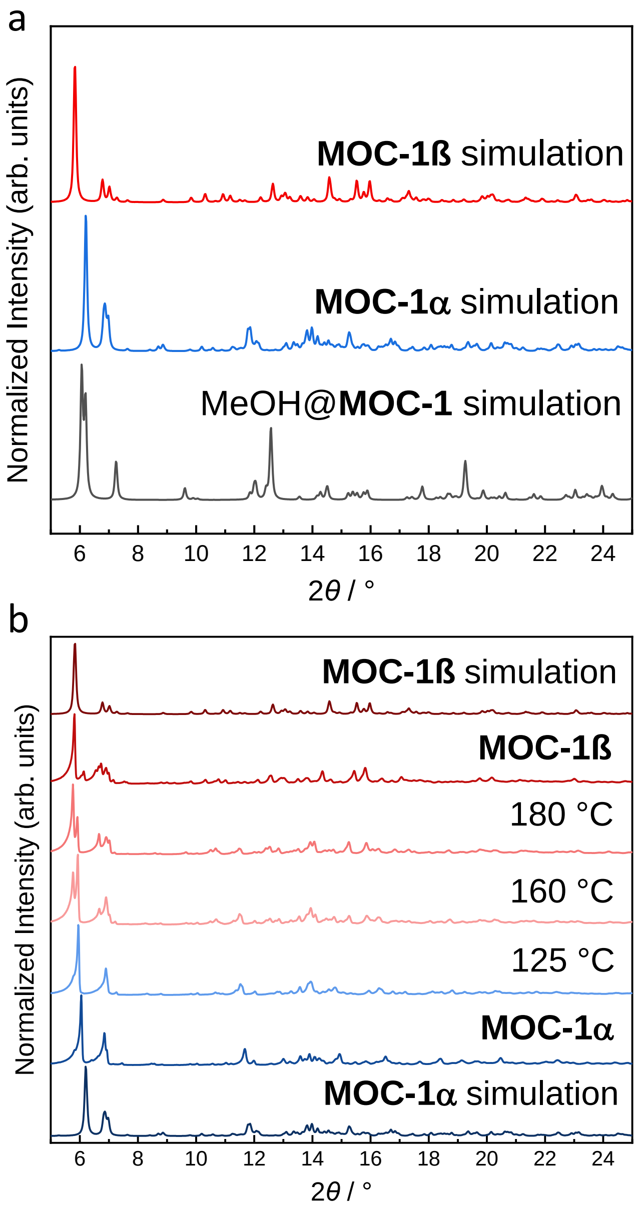

Figure 4.4. (a) Simulated PXRD pattern for MeOH@**MOC-1**, **MOC-1α** and **MOC-1β** using the single crystal structures. (b) PXRD patterns that were collected during in situ heating **MOC-1α** from 30 to 180 °C and simulated PXRD pattern for **MOC-1α** and **MOC-1β**.

Differential scanning calorimetry (DSC) curve (Figure 4.5) of **MOC-1α** shows an endotherm between 168 °C to 183 °C, which is attributed to the phase transformation. As shown in Figure 4.3b, a new activated phase **MOC-1β** can be obtained by heating

MOC-1α at 180 °C under vacuum. In addition, the DSC of **MOC-1β** did not show any endotherms over this temperature range, suggesting **MOC-1β** is the more thermostable phase.

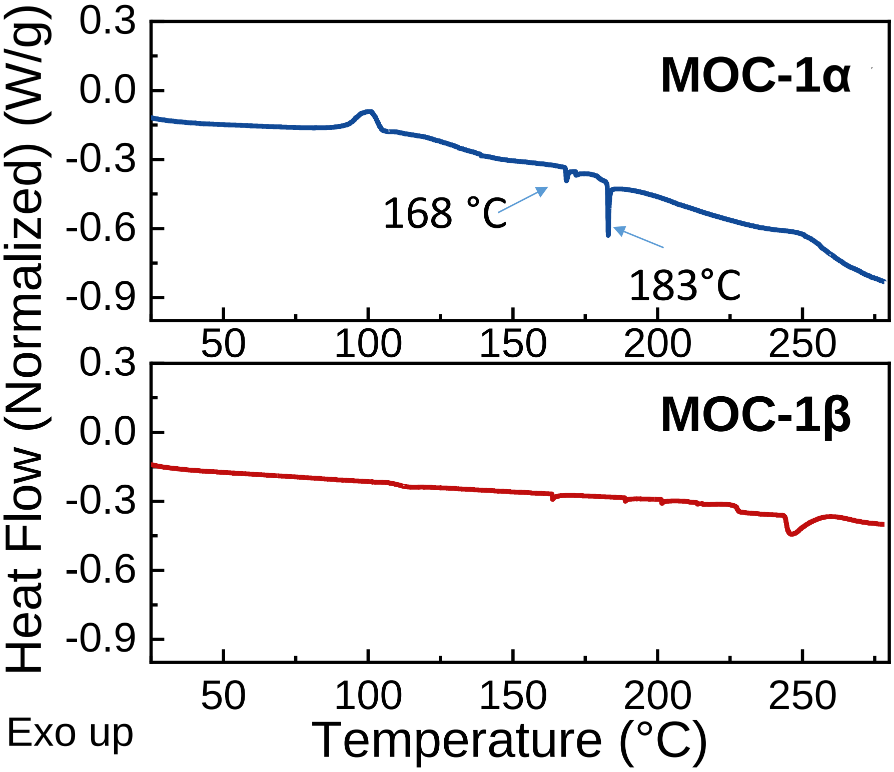

Figure 4.5. DSC curves of **MOC-1α** and **MOC-1β**. at 10 °C/min under an N_2 atmosphere.

Furthermore, thermogravimetric analysis (TGA) and NMR were used to confirm that the crystals were fully activated. There is a distinct solvent lost in MeOH@ **MOC-1** at 65.9 °C, as shown in Figure 4.6a, which is consistent with the boiling point of methanol (64.7 °C). By contrast, there is slight weight loss at 37.2 °C for may be due to the unbound water, which is consistent with the NMR result (Figure 4.7) that the methanol has been removed entirely in **MOC-1α**. In addition, there is no weight loss before the decomposition temperature for **MOC-1β**. Therefore, a temperature of ⩾ 80 °C can remove all of the methanol in **MOC-1**.

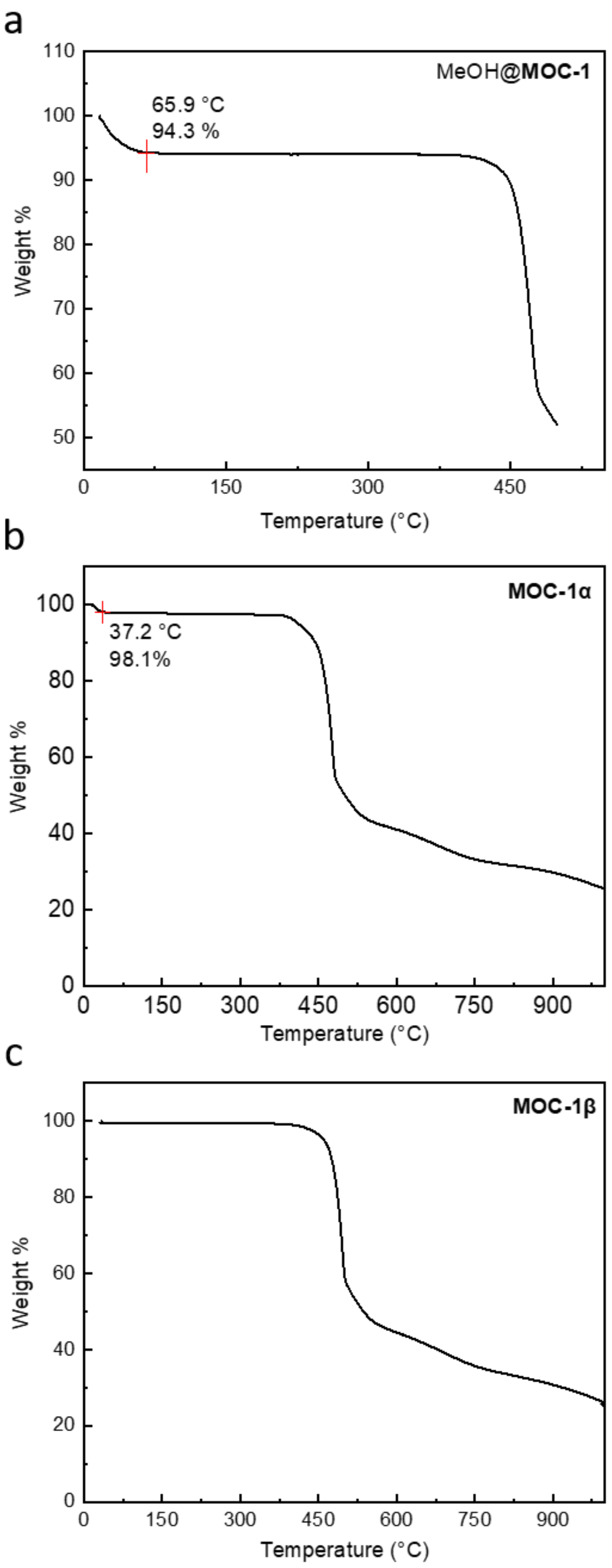

Figure 4.6. Thermogravimetric analyses of metal-organic cage **MOC-1**: (a) MeOH@ **MOC-1**, (b) **MOC-1α** activated at 80 °C, (c) **MOC-1β** activated at 180 °C.

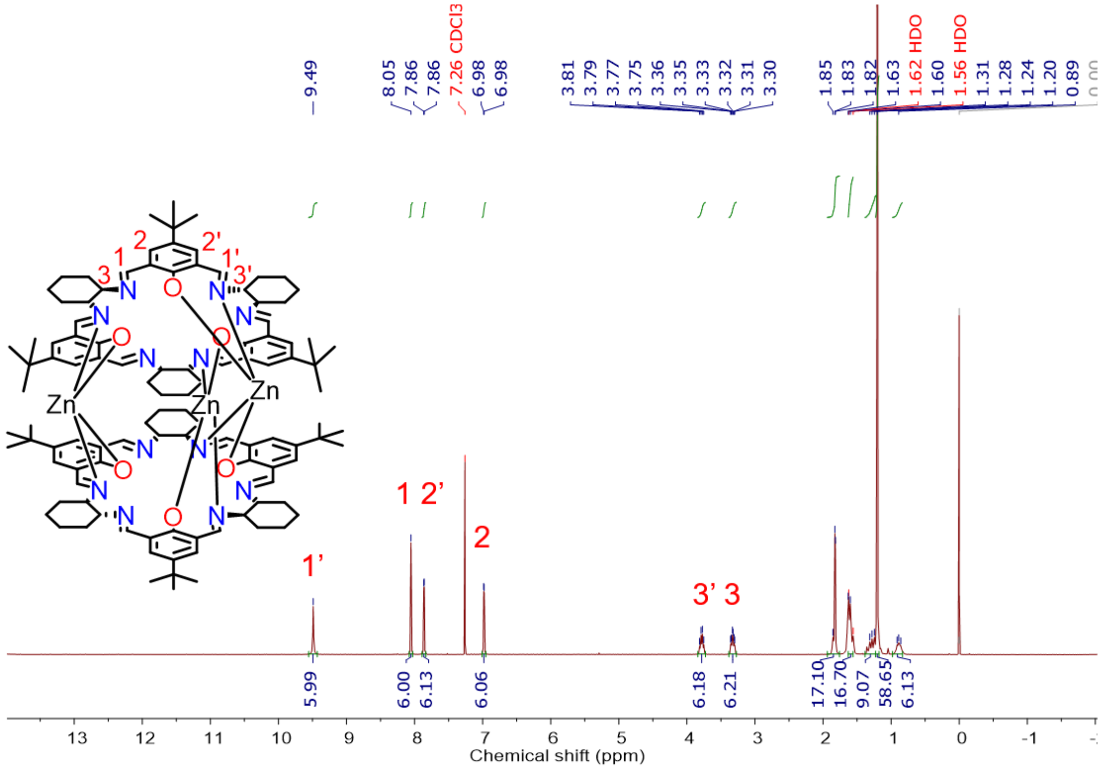

Figure 4.7. ^{1}H NMR spectrum (400 MHz, $CDCl_3$, 293 K) of **MOC-1α** activated at 80 °C.

4.4 Structural analysis of MOC-1

The crystal structures of **MOC-1** were determined by single-crystal X-ray diffraction. As shown in Table 4.1, solvated single crystals of MeOH@**MOC-1** have monoclinic *Cc* space group symmetry. While, as shown in Figure 4.8, **MOC-1** in MeOH@**MOC-1** has a tubular-shaped intrinsic cavity shape, highlighted using a yellow cylinder, with a broader cavity at the centre, highlighted using a yellow sphere. In MeOH@**MOC-1**, there are also large solvent-filled extrinsic voids. After solvent removal, the extrinsic pores shrink, and the structure transforms. Although two activated phases, **MOC-1α** and **MOC-1β**, both have *P1* space group symmetry and similar molecule structures (as confirmed by the molecules overlay in Figure 4.9). There is a difference in the crystal packing of MOC from the top view and side view of the crystal structures. (Figure 4.8) Compared with **MOC-1α, MOC-1β** shrinks more in crystal packing along the *b* axis. (Table 4.1, *b*: 18.076 Å for **MOC-1α** *vs* 14.415 Å for **MOC-1β**)

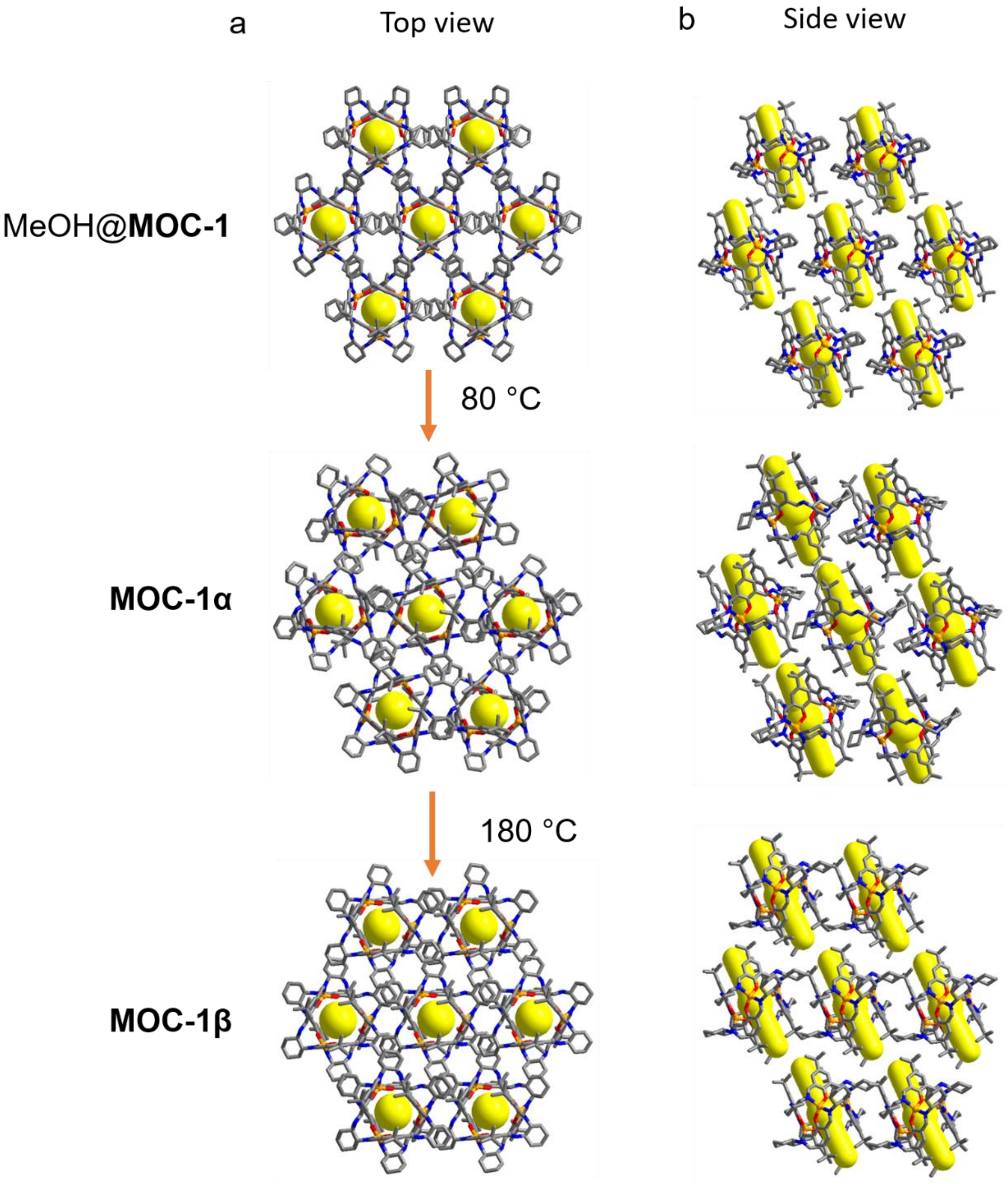

Figure 4.8. Crystal packing images of MeOH@**MOC-1** (top, methanol solvent is omitted for clarity), **MOC-1α** (middle) and **MOC-1β** (bottom) in (a) top view and (b) side view. H atoms are omitted for clarity (orange, Zn; blue, N; red, O; grey, C. The intrinsic cavity is highlighted by yellow.

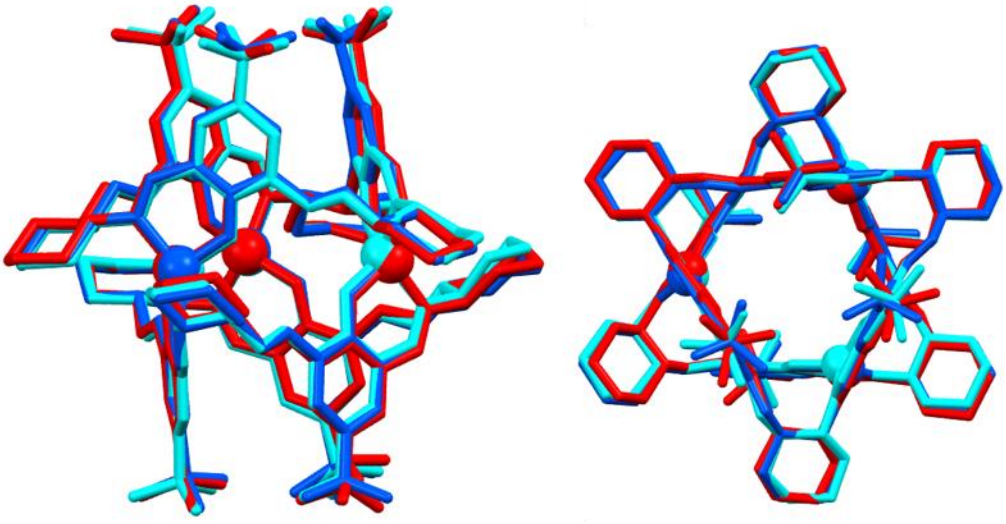

Figure 4.9. Molecules overlay for **MOC-1α** (blue and cyan) and **MOC-1β** (red), as generated using the Molecules Overlay tool in Mercury. H atoms are omitted for clarity.

Table 4.1. SC-XRD data for **MOC-1β**.

Molecule	MeOH@ **MOC-1**	**MOC-1α**	**MOC-1β**
Crystallisation Solvent	methanol	-	-
Space Group	*Cc*	*P1*	*P1*
Wavelength [Å]	Mo-Kα	Mo-Kα	Mo-Kα
Collection Temperature	100 K	100 K	100 K
Formula	$C_{108}H_{138}N_{12}O_7Zn_3$, 10.5($CH_3OH$), 3.25($H_2O$)	2($C_{108}H_{138}N_{12}O_6Zn_3$),3.25($H_2O$)	$C_{108}H_{138}N_{12}O_6Zn_3$, 0.5($H_2O$)
Mr	2307.40	3851.36	1905.94
Crystal Size (mm)	0.213×0.159×0.159	0.123×0.121×0.079	0.133×0.124×0.111
Crystal System	monoclinic	triclinic	triclinic
a [Å]	18.9478(9)	14.6670(10)	14.1697(11)
b [Å]	24.3539(9)	18.0763(12)	14.4152(13)
c [Å]	15.6901(11)	24.2155(14)	16.3546(16)
α [°]	90	78.958(5)	108.741(9)
β [°]	111.865(7)	73.662(5)	94.396(7)
γ [°]	90	68.325(6)	109.934(8)
V [Å^3]	6719.4(7)	5697.6(7)	2908.2(5)
Z	2	1	1
D_{calcd} [g cm^{-3}]	1.140	1.122	1.088
μ [mm^{-1}]	0.594	0.681	0.666
$F(000)$	2475	2048	1013
2θ range [°]	3.34 – 46.51	3.19 – 46.51	3.67 – 49.42
Reflections collected	36167	46181	38781
Independent reflections, R_{int}	9057, 0.0723	27140, 0.1176	17131, 0.1029
Obs. Data [$I > 2\sigma$]	7068	14768	10409
Data /restraints /parameters	9057/97/717	27140/2396/2412	17131/105/1150
Final R_1 values ($I > 2\sigma(I)$)	0.0745	0.0814	0.0836
Final R_1 values (all data)	0.0989	0.1733	0.1533
Final $wR(F^2)$ values (all data)	0.1975	0.1474	0.1620
Goodness-of-fit on F^2	1.039	1.001	1.028
Largest difference	0.563 /-0.374	0.689/-0.442	0.987/-0.510

In order to further investigate the difference in the pore structure of **MOC-1** due to the different packing, based on the crystal structures, the solvent-accessible volumes were calculated by Platon using a probe radii of 1.2 Å, and pore size distributions (PSD) were calculated by *Zeo*++.[59] After deleting the solvent from MeOH@**MOC-1**, the solvent-accessible volume accounts for about 36.9% of the unit cell volume. By contrast, the comparable void volume in **MOC-1α** is 17.3% of the unit cell volume. In **MOC-1β**, the void volume increased slightly to about 20.6% of unit cell volume. In addition, PSD histograms for MeOH@**MOC-1** (black), **MOC-1α** (blue) and **MOC-1β** (red) calculated by *Zeo*++ are shown in Figure 4.10. The PSD plot of MeOH@**MOC-1** shows three peaks at 3.4 Å, 4.3 Å and 4.6 Å (Figure 4.10a). In the PSD plots of **MOC-1α** and **MOC-1β**, there are also three peaks, but the centres vary from 3.6, 4.1, and 5.1 Å in **MOC-1α** to 3.0 Å, 3.8 Å and 4.1 Å in **MOC-1β**. The largest free spheres (D_f) in MeOH@**MOC-1**, **MOC-1α**, and **MOC-1β**, calculated by *Zeo*++ are 3.4, 2.0 and 2.6 Å, respectively, and these values represent their pore limiting diameters.[60] Therefore, the pore diameters of **MOC-1α** and **MOC-1β** are around 2.0 to 5.1 Å and 2.6 to 4.1 Å, respectively, satisfy the requirement of porous materials for KQS applications.

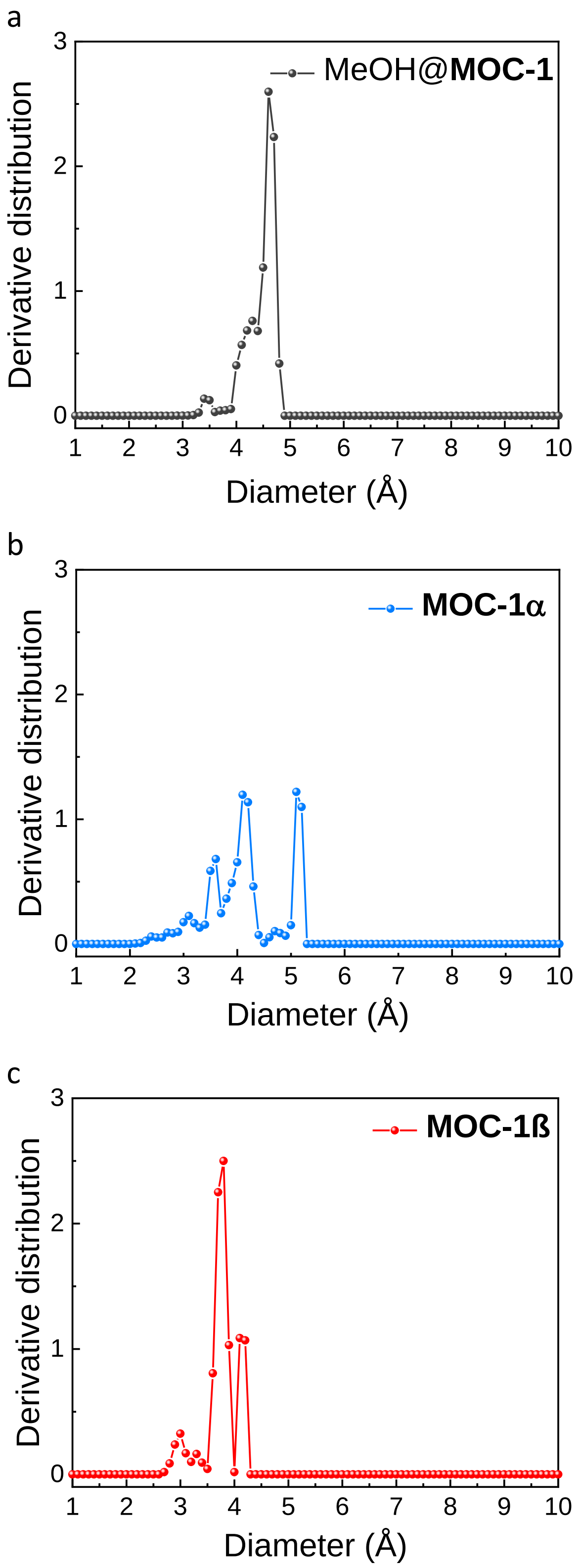

Figure 4.10. PSD histograms for MeOH@**MOC-1** (black), **MOC-1α** (blue,) and **MOC-1β** (red).

4.5 Gas isotherms of MOC-1

To quantify how the PSD of **MOC-1α** and **MOC-1β** affected their porosity, their N_2, Ar, CO_2 and H_2 gas adsorption isotherms were measured. As shown in Figure 4.11b, **MOC-1α** only adsorbed a small amount of N_2 (< 0.6 mmol/g) below $P/P_0 = 0.015$. However, after reaching a P/P_0 of 0.015, a step was observed in the adsorption isotherm, and the N_2 uptake increased sharply to > 5 mmol/g. This result is consistent with the pressure-induced gating effect previously reported for **MOC-1**.[27] By contrast, **MOC-1β** has a Type-I N_2 isotherm at 77 K (Figure 4.11), and in the absence of pressure-induced gating effect observed for **MOC-1α**, had the lower uptake at 1 bar (7.0 mmol/g for **MOC-1α** vs 4.2 mmol/g for **MOC-1β**) and calculated SA_{BET} (394 m^2/g for **MOC-1α** vs 270 m^2/g for **MOC-1β**). Hence, even though the calculated void volume in **MOC-1β** was higher than **MOC-1α** (17.3% for **MOC-1α** vs 20.6% for **MOC-1β**), the pressure-induced gating effect appears to have created additional porosity in **MOC-1α**.

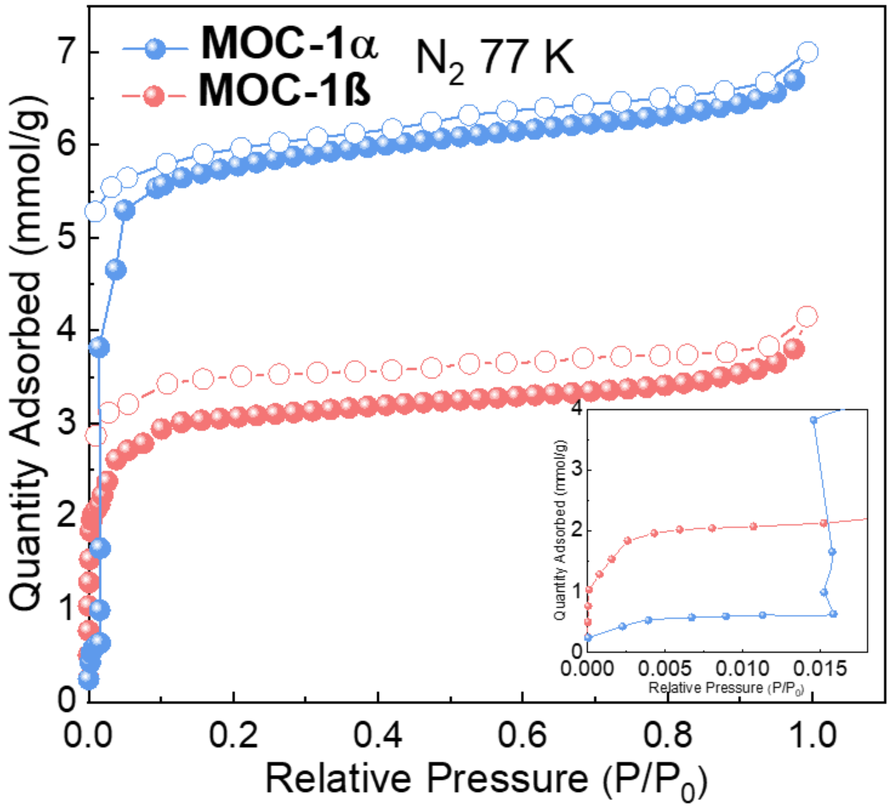

Figure 4.11. N_2 isotherms at 77 K for **MOC-1α** (blue colour) and **MOC-1β** (red colour). Solid symbols: adsorption; hollow symbols: desorption.

To further investigate the flexibility of the pore and the void volume for the gas sorption, higher pressure CO_2 and H_2 isotherms were measured for **MOC-1α** and **MOC-1β** from 0 to 10 bar. Two successive plateaus were observed in the high-pressure CO_2 isotherm of **MOC-1α** at 273 K, which indicates a pressure-induced gating effect.[61] (Figure 4.12a) By contrast, there is small loop for **MOC-1β** at 273 K. As for the CO_2 isotherm at 298 K, hysteresis was less extensive for **MOC-1α** and **MOC-1β** than the isotherm at 273 K. (Figure 4.12b)

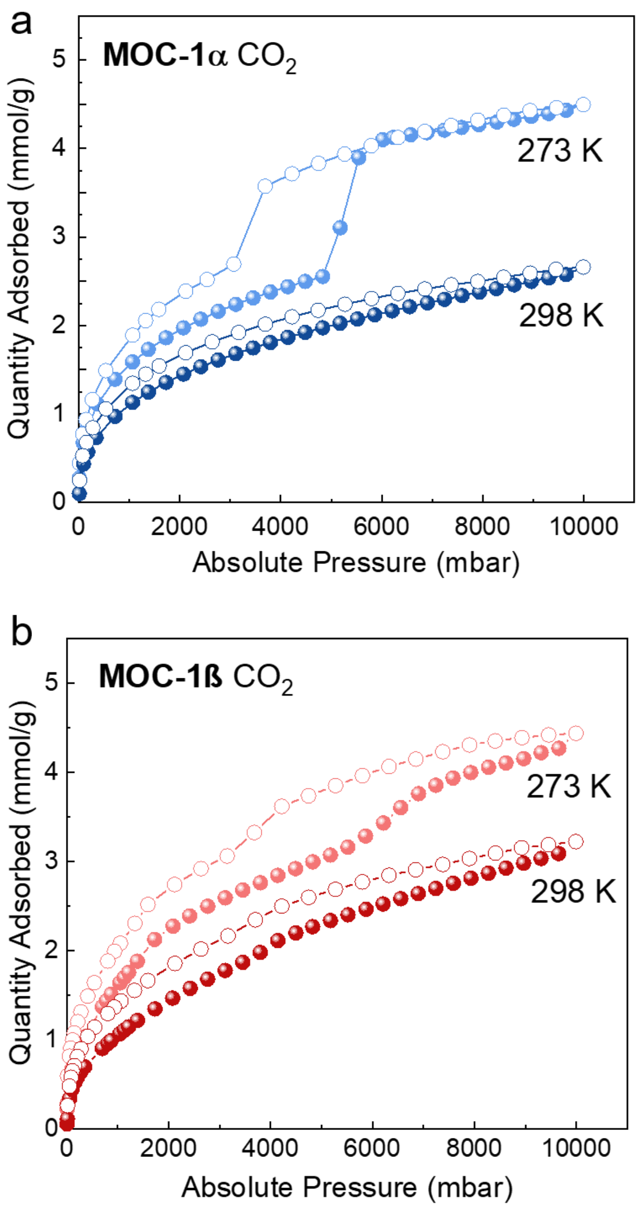

Figure 4.12. CO_2 sorption isotherms at 273 and 298 K for **MOC-1α**. (c) CO_2 sorption isotherms at 273 K and 298 K for **MOC-1β**. Solid symbols: adsorption; hollow symbols: desorption.

A pronounced hysteresis loop was found in the H_2 isotherms of **MOC-1α** at 77 K from 0 to 10 bar. By contrast, no distinct hysteresis loop was observed in the H_2 isotherms of **MOC-1β** (Figure 4.13). In combination, the higher-pressure isotherms are consistent with the N_2 isotherms, which suggest that **MOC-1α** is more structurally flexible than **MOC-1β** at 77 K.

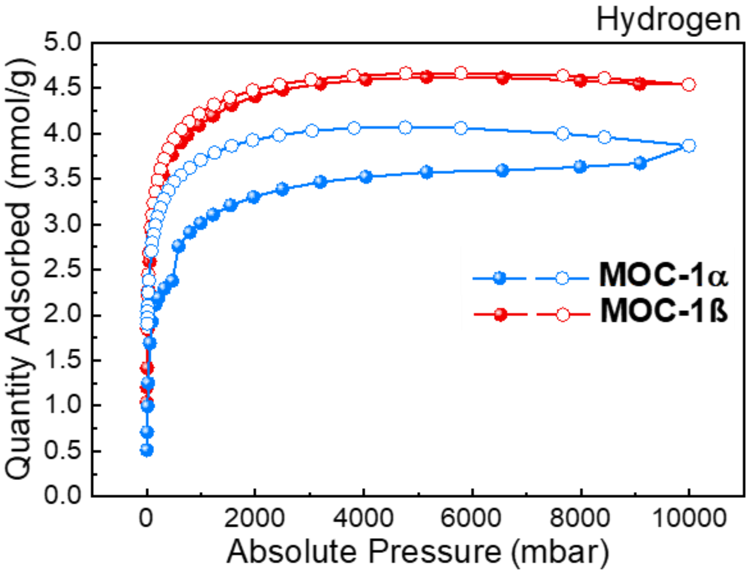

Figure 4.13. H_2 isotherms of **MOC-1α** (blue) and **MOC-1β** (red) at 77 K from 0 to 10 bar. Solid symbols: adsorption; hollow symbols: desorption.

H_2 and D_2 gas sorption isotherms for **MOC-1α** and **MOC-1β** recorded at various temperatures (30, 50, 77, and 100 K) are shown in Figure 4.14, **MOC-1α** has low D_2 and H_2 gas uptakes at 30 and 50 K (~ 1 mmol/g or lower at 1 bar), but much higher uptakes of 3.8 mmol/g for H_2 and 4.9 mmol/g for D_2 at 77 K and 1 bar. The increased H_2 and D_2 uptakes at the higher temperatures, where surface adsorption effects are also likely to be less profound, indicate that D_2 and H_2 can more easily penetrate the MOC cavities at 77 K. In addition, the **MOC-1α** isotherms exhibit hysteresis, which is less pronounced at 100 K, implying faster equilibration at higher temperatures. The stronger hysteresis at lower temperature, which decreases at higher temperatures, denotes a temperature-dependent diffusion limitation of gas molecules penetrating the cavities through different aperture sizes.

By contrast, the D_2 and H_2 adsorption isotherms for **MOC-1β** reached a maximum uptake of 7.5 mmol/g for D_2 and 5.9 mmol/g for H_2 at 30 K and 1 bar (Figure 4.14b), indicating that this MOC crystal is fully accessible to these gases even at lower temperatures. There was again strong hysteresis at 30 K, but again this hysteresis was reduced with increasing temperature, indicating better equilibrium. For **MOC-1α** and **MOC-1β**, higher D_2 uptakes than H_2 were observed at all measurement temperatures, which is attributed to higher diffusion rates and increased heats of adsorption for D_2.

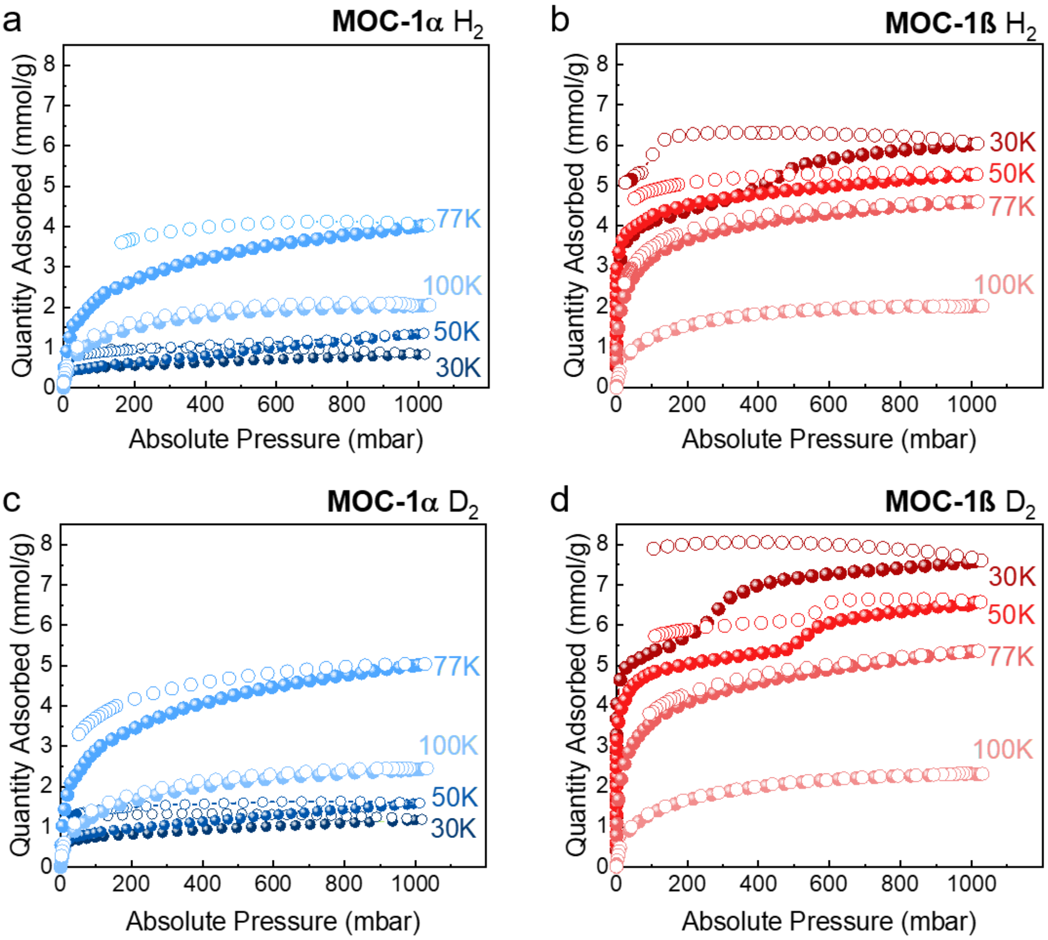

Figure 4.14. H_2 isotherms of (a) **MOC-1α** and (b) **MOC-1β**; D_2 isotherms of (c) **MOC-1α** and (d) **MOC-1β** recorded at 30 K, 50 K, 77 K and 100 K. Solid symbols: adsorption; hollow symbols: desorption.

4.6 Thermal desorption spectroscopy (TDS) of MOC-1

Encouraged by the apparent faster D_2 diffusion kinetics, we evaluated the ability of **MOC-1α** and **MOC-1β** to perform D_2 / H_2 separations using a laboratory-designed cryogenic thermal-desorption spectroscope (TDS). First, pure H_2 and D_2 atmospheres were used in the TDS experiments to determine the preferred H_2 and D_2 adsorption sites in **MOC-1α** and **MOC-1β**. In these TDS measurements, the **MOC-1α** and **MOC-1β** samples were exposed at room temperature to 10 and 200 mbar of pure H_2 and D_2, then cooled to 20 K under gas atmosphere, and finally, the sample chamber was evacuated at 20 K. The TDS spectra were recorded while heating the samples from 20 and 170 K (Figure 4.15).

The TDS spectra of **MOC-1α** (Figure 4.15a) collected after gas loading at 10 mbar shows little gas uptake. By contrast, the **MOC-1α** TDS spectra obtained from the 200 mbar gas loading shows one major peak for both isotopes, centred at about 102 K for D_2 and 106 K for H_2, with shoulders appearing at desorption temperatures below 70 K. The single peak with a shoulder shows there are at least two adsorption sites for H_2 and D_2 in **MOC-1α** with different adsorption potentials. The increase in gas uptake of both isotopes with higher pressure indicates the inner structure becomes more accessible at 200 mbar than 10 mbar.

The TDS spectra for **MOC-1β** after gas loading at 10 mbar of H_2 and D_2 (Figure 4.15b) show small peaks at around 25 K and more profound peaks at around 90 K. In addition, two shoulders were observed over the temperature range 40-80 K. The TDS spectra of **MOC-1β** after gas loading at 200 mbar have one major peak at lower desorption temperatures; 86 K for D_2 and 92 K for H_2, compared to values of 102 K for D_2 and 106 K for H_2 observed for **MOC-1α**. It is attributed that the first desorption peak at low temperature (approximately 25 K) to weakly adsorbed gas molecules on the outer surfaces of the crystals. For both **MOC-1α** and **MOC-1β**, the temperature of the maximum desorption peak is lower for D_2 than H_2, denoting a faster diffusion of D_2, which is in good agreement with H_2 and D_2 isotherms.

In the TDS spectra, the area under the desorption peak is proportional to the quantity of desorbed gas, which can be quantified by calibrating the mass spectrometer using a $Pd_{95}Ce_5$ alloy (see Section 5.5.9). At 200 mbar, the pure H_2 and D_2 uptakes for **MOC-1α** are 1.2 and 2.1 mmol/g, respectively. By contrast, the pure H_2 and D_2 uptakes 200 mbar for **MOC-1β** are higher and were 2.4 and 3.8 mmol/g, respectively, in good agreement with gas sorption isotherms.

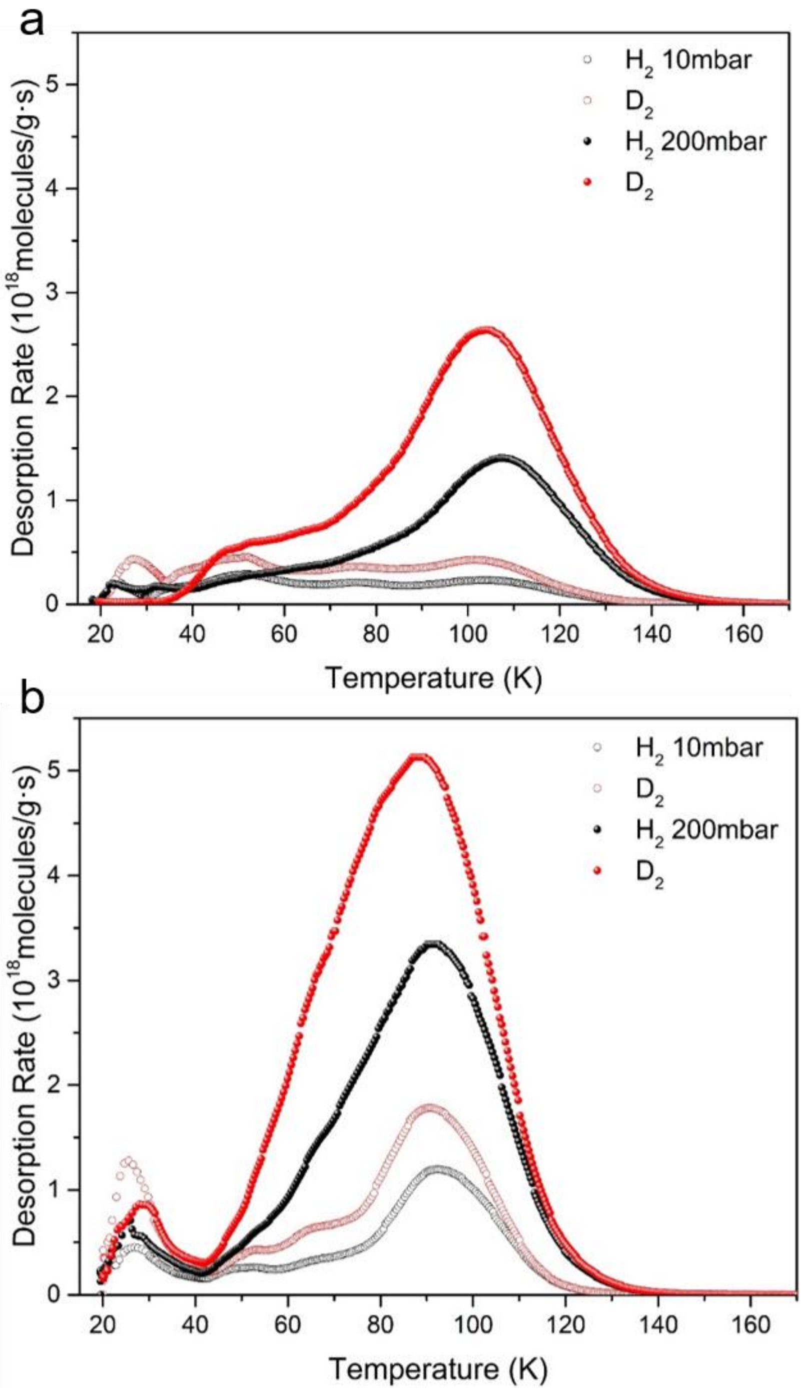

Figure 4.15. H_2 (Black) and D_2 (Red) thermal desorption spectra of H_2/D_2 single gas at 10 mbar and 200 mbar for (a) **MOC-1α** and (b) **MOC-1β**.

Then the TDS measurements were used to verify the competitive separation performances of **MOC-1α** and **MOC-1β**. These measurements were performed after directly exposing **MOC-1α** and **MOC-1β** to a 1:1 H_2:D_2 mixture (200 mbar) for 10 min at exposure temperatures (T_{exp}) between 30 and 100 K. The D_2 / H_2 selectivity can then be calculated from the ratio of the peak areas. The TDS spectra of **MOC-1α** are shown in Figure 4.16a, and Figure 4.16c shows the D_2 / H_2 selectivity alongside the corresponding D_2 uptake as a function of exposure temperature. The TDS spectra start from T_{exp} and measure the remaining free gas molecules released during the evacuation processes that are carried out at the same temperature. The gas uptakes increase with increasing temperatures, exhibiting a maximum of 100 K. Meanwhile, the selectivity decreases with increasing T_{exp}, exhibiting the highest $S_{D2/H2} = 9.1$ at 30 K. Generally, the strongest adsorption site, which corresponds to the highest desorption temperature, is occupied first and at very low loadings. The weaker sites are then occupied at higher gas loadings and this results in additional low-temperature desorption peaks. However, the H_2 and D_2 TDS spectra of **MOC-1α** vary in shape and magnitude depending on T_{exp}, which is contrary to the typical sequential filling behaviour of accessible sites with different binding strengths. No desorption peak can be observed above 60 K for $T_{exp} = 30$ K, implying no deep penetration into the structure at this temperature. With increasing exposure temperature, gases can penetrate deeper into the crystals, and the desorption peaks in TDS spectra shift to higher temperatures. The gas molecules can finally penetrate the MOC crystals at $T_{exp} = 100$ K. These temperature-dependent TDS spectra agree with the observation from pure gas isotherms, which is related to the temperature-dependent gate-opening behaviour.[52]

In contrast, **MOC-1β** shows different desorption spectra under identical conditions, as shown in Figure 4.16b. For **MOC-1β**, the desorption spectrum at 30 K shows no desorption of any isotopes occurring above 50 K, indicating the weak adsorption of gas molecules on top of the surface. However, the TDS spectra measured at 50 K exhibit two desorption maxima that last until 120 K, indicating the gas molecules can freely access the crystal pores at 50 K. The D_2 / H_2 selectivity and its corresponding D_2 uptake as a function of exposure temperature are shown in Figure 4.16d, in which the highest $S_{D2/H2}$ of 8.3 is observed at $T_{exp} = 30$ K. There is no considerable difference in the selectivity of **MOC-1α** and **MOC-1β** for D_2 / H_2 (Figure 4.16c, 4.16d) from 30 K to 100 K. However, the D_2 uptake for **MOC-1α** only slowly increases with increasing temperature, whereas the D_2 for **MOC-1β** is far higher at 1.1 mmol/g at 77 K. In addition, **MOC-1β** has a higher D_2 uptake maximum than **MOC-1α**. The increasing isotope uptake with decreasing selectivity is related to the opening of the aperture and the sufficient kinetic energy of the molecule, where the accessibility of both isotopes is enhanced. Despite low selectivity, after exposure at T_{exp} = 100 K to an isotope mixture, the desorption maxima are centred at 115 K for both **MOC-1α** and **MOC-1β**, which is an unusual case exhibiting such high desorption temperature without the presence of strong adsorption sites. Therefore, both **MOC-1α** ($S_{D2/H2}$ = 2.8) and **MOC-1β** ($S_{D2/H2}$ = 2.2) have reasonable selectivity for D_2 at 77 K compared with other porous materials without open metal sites. (Table 4.2)

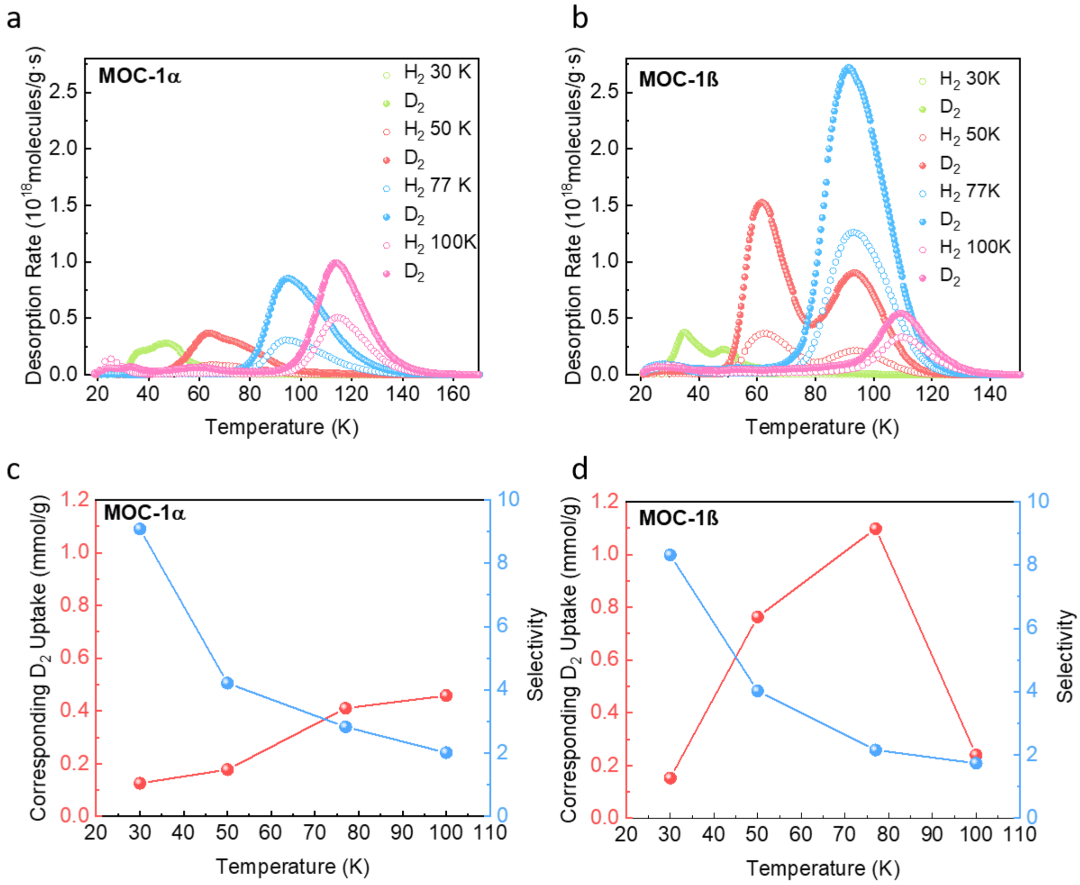

Figure 4.16. H_2 (open) and D_2 (close) thermal desorption spectra of 200 mbar 1:1 H_2/D_2 isotope mixture on (a) **MOC-1α** and (b) **MOC-1β** at different exposure temperatures, 30 K (magenta), 50 K (red), 77 K (blue), and 100 K (green). D_2/H_2 selectivity (blue) and the corresponding D_2 uptake (black) as function of exposure temperature for (c) **MOC-1α** and (d) **MOC-1β**.

Table 4.2. Summary of KQS selectivities above 77 K with various porous materials without open metal sites. (* D_2/H_2 mixture selectivity calculated by IAST)

Compound	Aperture (Å)	T (K)	P (mbar)	Selectivity (D_2/H_2) (1:1 Mixture)	Ratio (nD_2/nH_2) (Pure Gas Isotherms)	Ratio (kD_2/kH_2) (Rate constant)	Ref.
CMS	5-7/ 15-35	77	4000	1.53 (H_2:D_2=139:175)			62
Zeolite 5A	5	77		1.8 (H_2:D_2=99:1)			63
Zeolite 13X	8	77		1.9 (H_2:D_2=99:1)			
Zeolite Y	6-7	77	4000	Up to 1.52 (H_2:D_2=139:175)			64
CMS T3A	5.46	77	5-1000		1.063		65
		77	50-500		-	Up to 1.9	
PCS	5.66	77	5-1000		1.097	-	
		77	0-50			Up to 1.25	
3KT-172	4.9	77	20			1.86	48
1.5GN-H	4.6	77	100			5.83	
CNH	-	77	70-1000		1.09		66
HKUST-1	9/5	77	20		1.23		
SWCNT	13-14	77	10000		1.2		67
SG-SWCNT	28.5	77	0.1-10	Up to 3.8*			
LA-SWCNT	13.7	77	0.1-10	Up to 1.5*			
Zeolite 5A	5	77	0.01-10	Up to 3.26*			68
Zeolite NaX	7.4	77	139		1.18		69
			STP		1.33		
Zeolite 4A	4	77	150	2.09*			70
Zeolite 5A	5	77	150	2.48*			
Zeolite Y	6-7	77	150	1.32*			
Zeolite 10X	8	77	150	1.3*			
CMK-3	35	77	150	0.95*			
Zeolite 13X	8	77	0.1-1000	Up to 3.2*			71
			0.1-10	Up to 5.8*			
			50-1000		1.13		
M’MOF 1	5.6×12	77	5-1000		1.09		72
		87			1.11		
VSB-5	11	140	0-1000	Up to 4*			73
12-Connected MOFs	10	77	1000		1.1		74
Cu_2L_2	7.3	77	100		1.2		75
FMOFCu	2.5, 3.6	77	50	3-4			51
		87	50	3-4			
IFP-4	1.7	77	60	2.1			76
IFP-7	2.1	77	60	1.5			
ZIF-67	3.4	77	STP	1.29			77
ZIF-67 @NH_2-γ-Al_2O_3	3.4	77	STP	1.79			
ZIF-67 @NH_2–SiO_2	3.4	77		1.52			78
FJI-Y11	3.8, 8.4	77		1.76			79

Generally, desorption above liquid N_2 temperatures indicates the existence of strong binding sites, such as uncoordinated metals (Figure 4.17a).[54, 80] However, the lack of open metal sites in MOCs limits the interaction with hydrogen molecules. A similar phenomenon has been reported by Mondal *et al.*[76] in a series of 1-D channel ultra-microporous MOFs, called imidazolate framework potsdam (IFP), which possess a smaller pore size than the kinetic diameter of hydrogen molecules, which gets accessible to hydrogen by a temperature-dependent dynamic gate opening. IFP-4 and IFP-7 exhibit a selectivity around two above liquid nitrogen temperature, which can be ascribed to kinetic quantum sieving occurring only at the outermost pore aperture, since after penetrating the narrow pore channels, no passing of gas molecules is possible, and a single-file filling occurs (Figure 4.17b). Additionally, the gas uptake at 77 K in IFP only reaches 0.01 mmol/g in IFP-4 and 0.05 mmol/g in IFP-7, due to the narrow I-D channels. By contrast, the gas uptake is much larger for our MOCs (0.41 mmol/g in **MOC-1α** and 1.10 mmol/g in **MOC-1β** at 77 K). In contrast to the rigid 1-D channels in the IFP series, the narrow ultrafine pores in **MOC-1** allow single-file filling initially, but the flexible pores are adaptable and become more accessible to the target gas with increasing temperature. When the system is cooled down to low temperatures under a gas atmosphere, the gas molecules are captured on the additional inner surface and can be released by heating up to this temperature again (Figure 4.17c). Therefore, by introducing local flexibility into the MOC system, the practical temperature for hydrogen isotope separation can be increased dramatically and become comparable to the temperatures reached by MOFs possessing open metal sites.

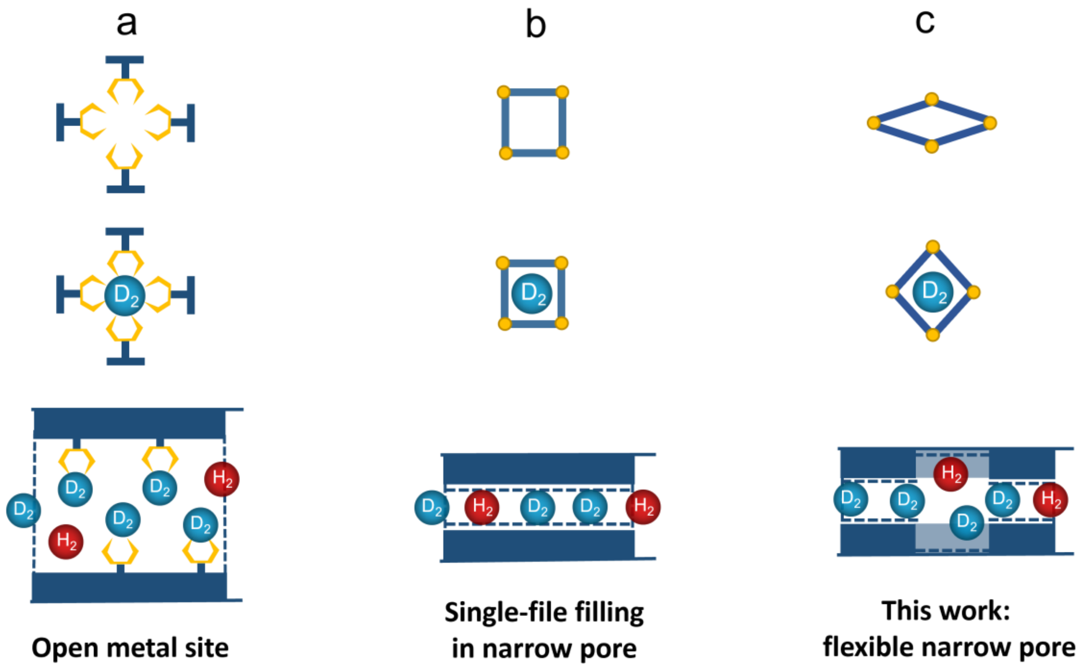

Figure 4.17. Three types of structures that could increase the practical temperature of hydrogen isotopes separation: (a) open metal sites[54]; (b) single-file filling in ultrafine 1D channels[76]; (c) this work: flexible narrow pores.

4.7 Stability of MOC-1

In order to confirm the local flexibility instead of phase transformation for hydrogen isotope separation. Firstly, the variable-temperature PXRD patterns of **MOC-1α** and **MOC-1β** were collected by heating from 30 to 298 K. As shown in Figure 4.18, the **MOC-1α** and **MOC-1β** remained the phase and was crystallinity between 30 to 100 K. This suggests that only temperature change from 30 to 298 K would not induce the structural transformation in **MOC-1α** and **MOC-1β.**

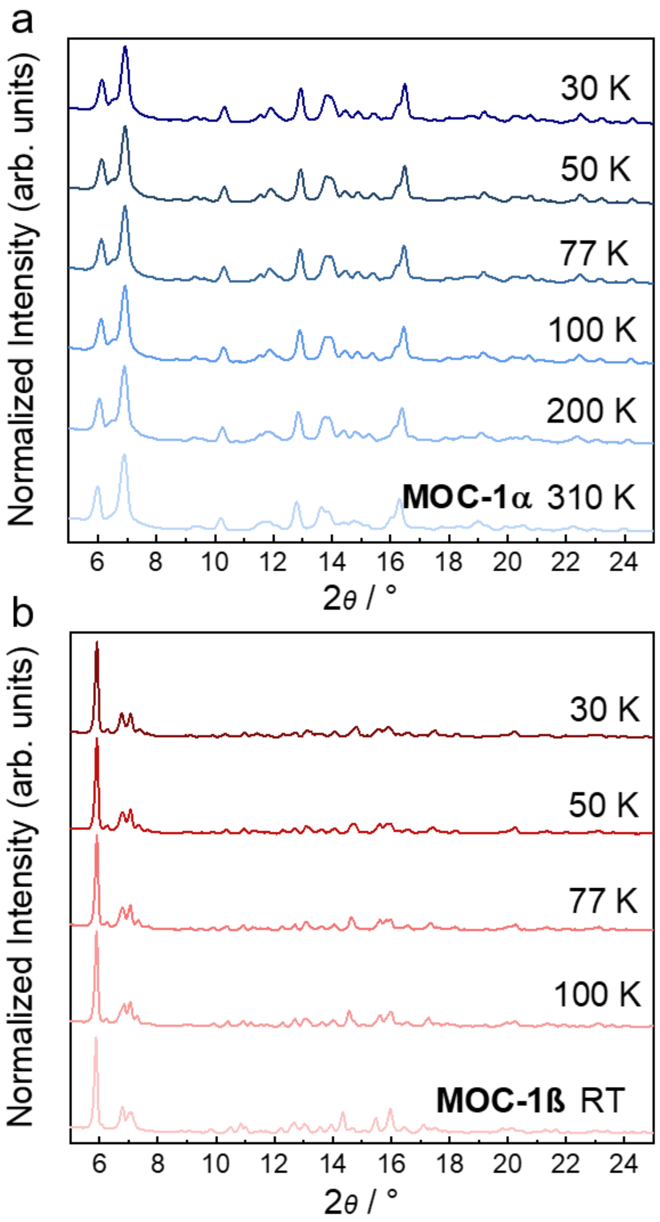

Figure 4.18. Variable-temperature PXRD patterns: (a) PXRD patterns of **MOC-1α** collected by heating from 30 to 310 K. (b) PXRD patterns of **MOC-1β** collected by heating from 30 to 298 K.

Then the PXRD patterns of **MOC-1α** and **MOC-1β** were collected after H_2 and D_2 isotherms. As shown in Figure 4.19, **MOC-1α** and **MOC-1β** were stable and remained the phase after H_2 and D_2 isotherms between 30 to 100 K. Hence, the stepped isotherms for H_2 and D_2 are due to local flexibility rather than more profound structural changes.

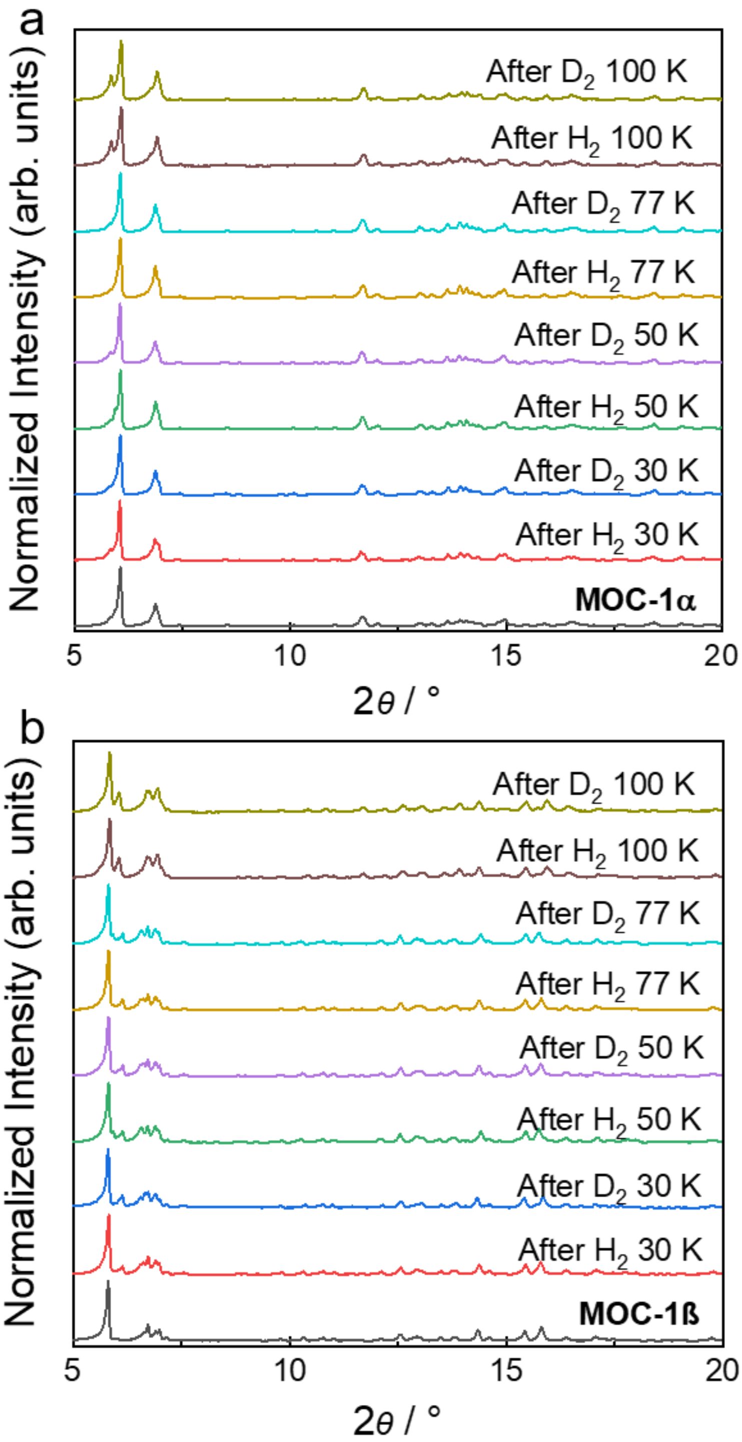

Figure 4.19. PXRD patterns of **MOC-1** after and before testing gas isotherms: (a) PXRD patterns of **MOC-1α** collected after and before testing H_2 and D_2 isotherms at 30 to 100 K. (b) PXRD patterns of **MOC-1β** collected after and before testing H_2 and D_2 isotherms at 30 to 100 K.

4.8 Synthesis of M2, M3, MOP-2, and MOP-3

Being inspired by the assembly **MOC-1** from the calixalen **M1**, more imine macrocycles with salen units were screened for forming hollow metal-organic molecules with metal ions. It is found that the cavity of calixalen macrocycles is difficult to be turned because the isophthalaldehyde used for the synthesis of macrocycles is hard to be extended in the length. Therefore, the trianglsalen macrocycle with modifiable cavity attracted my attention. The size of trianglsalen macrocycle can be controlled by varying the dialdehyde molecules length. Two target trianglsalen macrocycles were synthesised by adjusting the length of the dialdehydes. **M2** was synthesised as described previously by the condensation of 2,5-dihydroxyterephthalaldehyde with (1*R*,2*R*)-diaminocyclohexane.[36] Connecting one more aromatic ring in the dialdehyde via sp^2-sp^2, **M3** with larger cavity was synthesised in the 1:1 THF:EtOH solvent by the condensation of 3,3'-dihydroxy[1,1'-biphenyl]-4,4'-dicarboxaldehyde with trans-(1*R*,2*R*)-diaminocyclohexane.

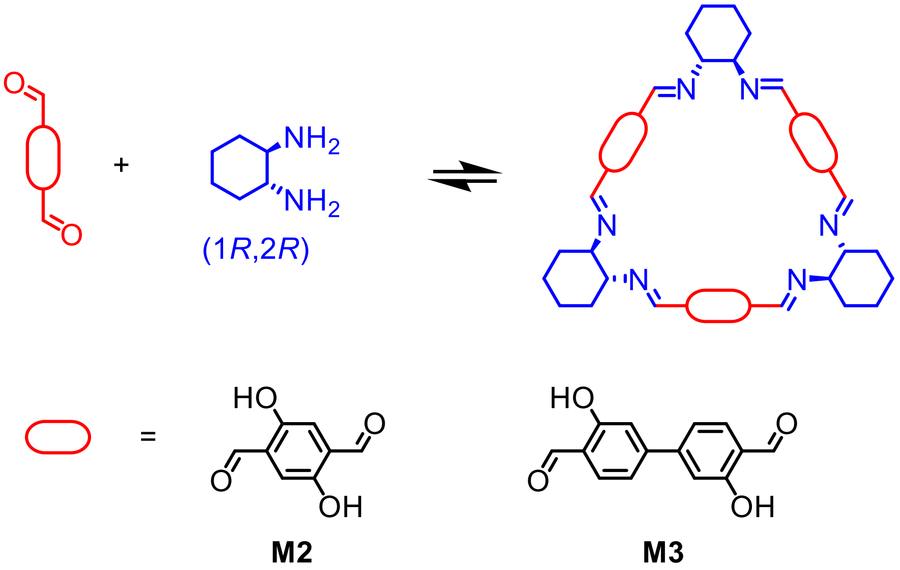

Figure 4.20. Scheme showing the synthesis of **M2** and **M3**.

To investigate what kind of metal-organic molecules can be formed from trianglsalen macrocycles, **M2** and **M3** were used for coordination with $Zn(CH_3COO)_2{\cdot}2H_2O$ in *N*,*N*-diethylformamide (DEF) at RT. As shown in Figure 4.21, neutral trianglsalen-based MOPs assembled from four deprotonated macrocycles and six Zn^{2+} in tetrahedral coordination with salen units (OH···N=C). **MOP-2** and **MOP-3** both exhibit octahedron shape and large intrinsic cavities with eight windows. The windows can be classified into two types. One is from the used trianglsalen macrocycles. Another is formed by the connection of three neighbouring macrocycles with Zn(II) ions. Compared with **MOP-2** in diameter of 2.6 nm, the diameter of **MOP-3** increases to 3.2 nm by using larger macrocycles.

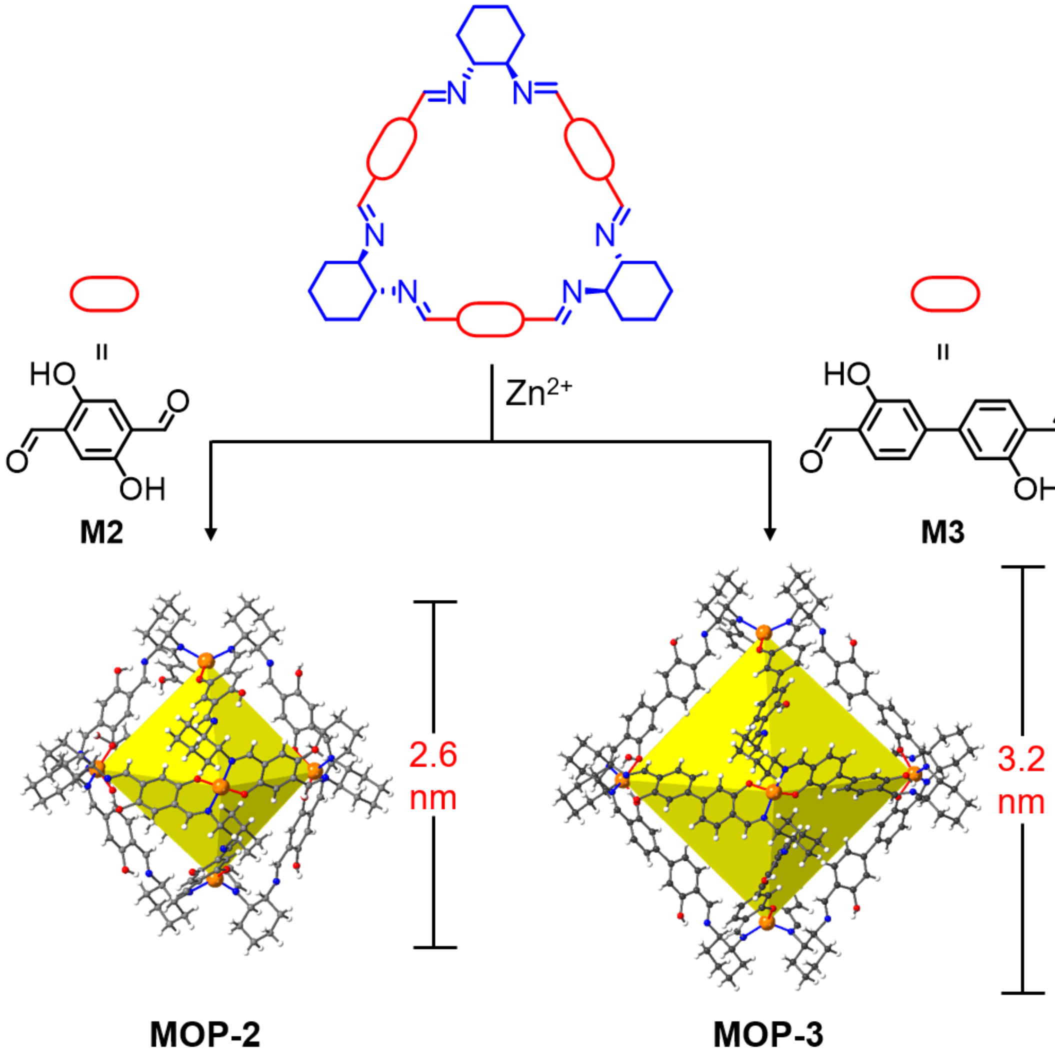

Figure 4.21. Synthetic strategy for **MOP-2** and **MOP-3** and their corresponding crystal structures.

MOP-2 and solvate **MOP-3** are slightly soluble in $CHCl_3$ and DCM. Their 1H NMR spectrums were recorded in CD_2Cl_2 and compared with free macrocyclic ligands. As shown in Figure 4.22, half of salen units in **M2** and **M3** are coordinated with Zn(II), which excludes the planar tetradentate coordination environment of Zn (II) with macrocyclic ligands in **MOP-2** and **MOP-3**.

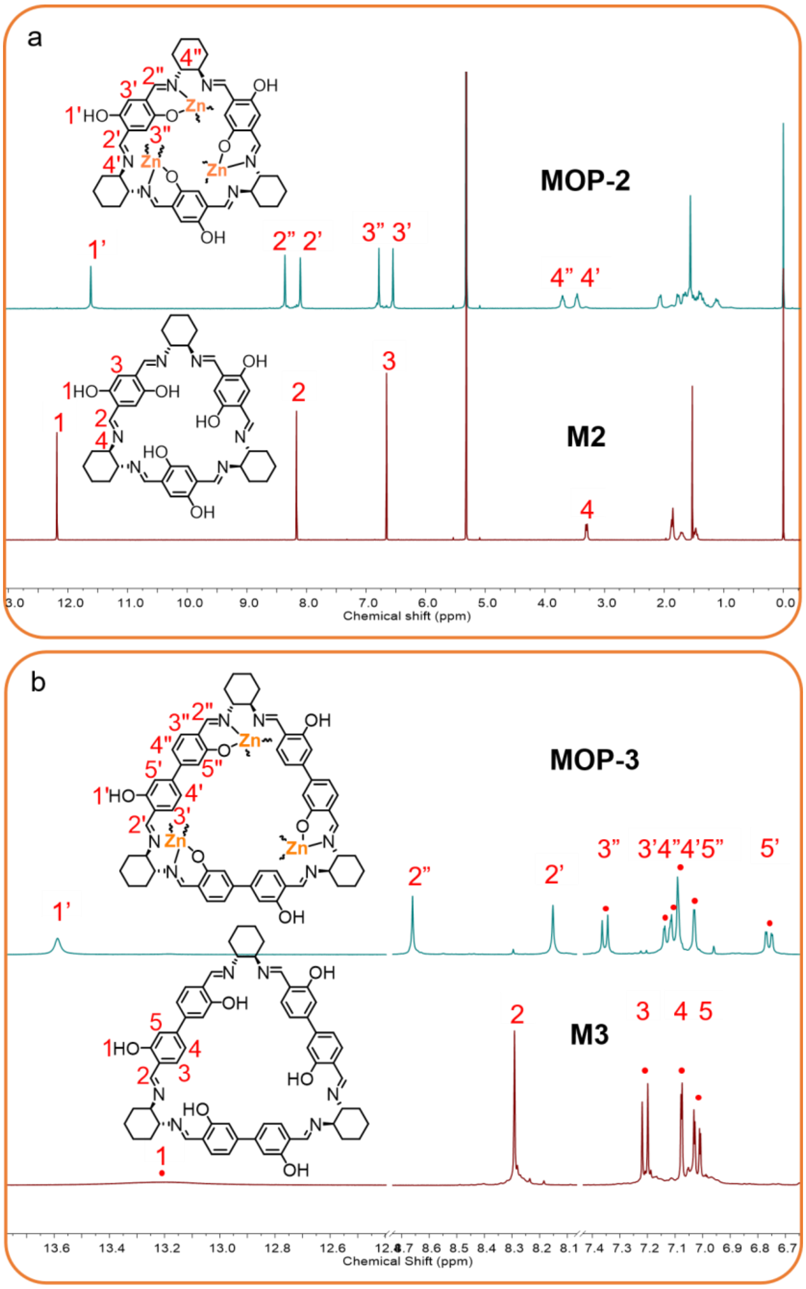

Figure 4.22. 1H NMR spectrum (400 MHz, CD_2Cl_2, 293 K) of (a) **M2** and **MOP-2**, (b) **M3** and **MOP-3**.

Compared with the imine signals (H2) of **M2**, **MOP-2** gave rise to two imine (H2', H2") and two aromatic signals (H3', H3"). The imine signals (H2") shifted downfield, which indicates the coordination of the nitrogen donors to the Zn(II) cations. The aromatic signals (H3") shifted downfield due to the close proximity of the deprotonated phenolic hydroxyl group. At the same time, the imine signals (H2') and aromatic signals (H3') shifted upfield. As shown in Figure 4.22b, similar signal shifts are found in **MOP-3** compared with **M3**, imine signals (H2) and aromatic signals (H3, H4, H5) of **M3** gave rise to two signals, shifted downfield to H2", H3", H4" and H5", and shifted upfield to H2', H3', H4' and H5'.

4.9 Structural analysis of MOP-2 and MOP-3

Single crystals of **MOP-2** that were suitable for single crystal X-ray diffraction were obtained by slowly diffusing of CH_3CN vapour into a *N*,*N*-diethylformamide (DEF) solution containing **M2** and $Zn(CH_3COO)_2{\cdot}2H_2O$. Solvated single crystals of **MOP-2** have trigonal *R3* space group symmetry. (Table 4.1) As shown in Figure 4.23, the yellow spheres highlight the intrinsic cavity of **MOP-2**. There are also large solvent-filled extrinsic voids highlighted by blue and cyan spheres. As shown in Figure 4.23a, the 3D porous supramolecular architecture is stabilised by solvents filled, and C–H···π interactions between aromatic rings and cyclohexane groups of **MOP-2** and hydrogen bonds between imine groups and hydroxyl groups of **MOP-2** along z axis. Perpendicular to the image in Figure 4.23b, there is the 1-D dumbbell-shaped channel. The blue and cyan spheres are two heads for 'dumbbell'.

By mixing **M3** and $Zn(CH_3COO)_2{\cdot}2H_2O$ in DEF at ambient temperature for 3 days without stirring afforded single crystals of **MOP-3**. As shown in Table 4.1, solvated single crystals of **MOP-3** also have trigonal *R3* space group symmetry. The crystal of **MOP-3** has a much larger cell volume of 36176 Å^3 than the **MOP-2 (**17527 Å^3**)**. In addition, due to sheer number of disordered, amorphous solvent molecules in the structure of **MOP-3**, solvent –mask was used for solving the structure. As shown in Figure 4.24, the intrinsic cavity of **MOP-3** highlighted by yellow spheres are larger than the **MOP-2**. Similar to **MOP-2**, **MOP-3** has large solvent-accessible extrinsic voids highlighted by cyan spheres, which forms 1-D channels perpendicular to the page. (Figure 4.24) The 3D porous supramolecular architecture of **MOP-3** is stabilised by solvents filled, and C–H···π interactions between aromatic rings and cyclohexane groups of **MOP-3** and hydrogen bonds between imine groups and hydroxyl groups of **MOP-3**. After deleting the solvent molecules in solvate structure, Platon calculations indicate the presence of approximately 43.0% and 64.7% solvent-accessible volumes in **MOP-2** and **MOP-3**, respectively.

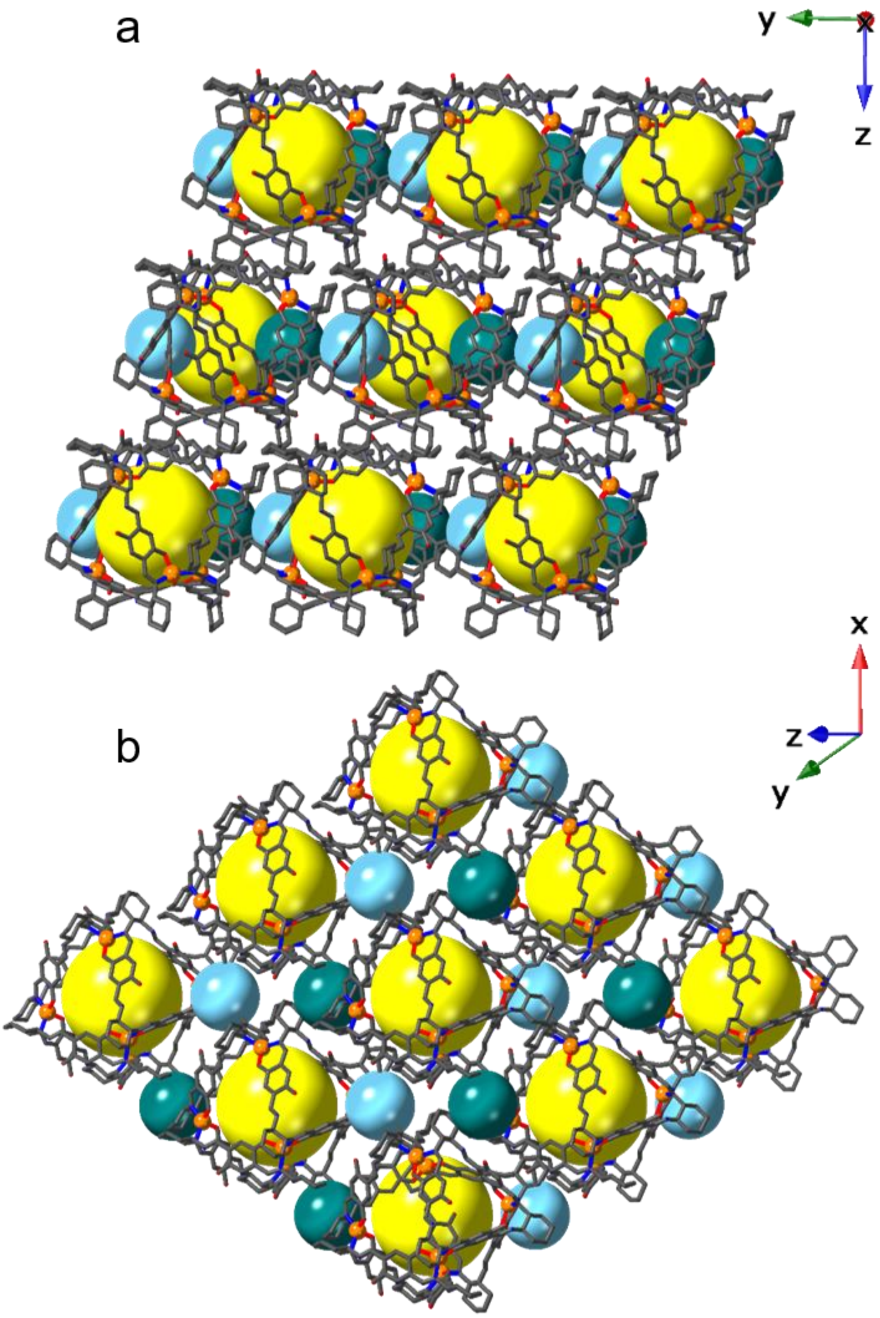

Figure 4.23. Crystal packing images of **MOP-2** (a) along x axis and (b) off y axis. (Orange, Zn; blue, N; red, O; grey, C, H atoms are omitted for clarity. The large yellow spheres represent the inner cavities of the MOPs, the small blue and cyan spheres represent external cavities created by the packing of the MOPs.)

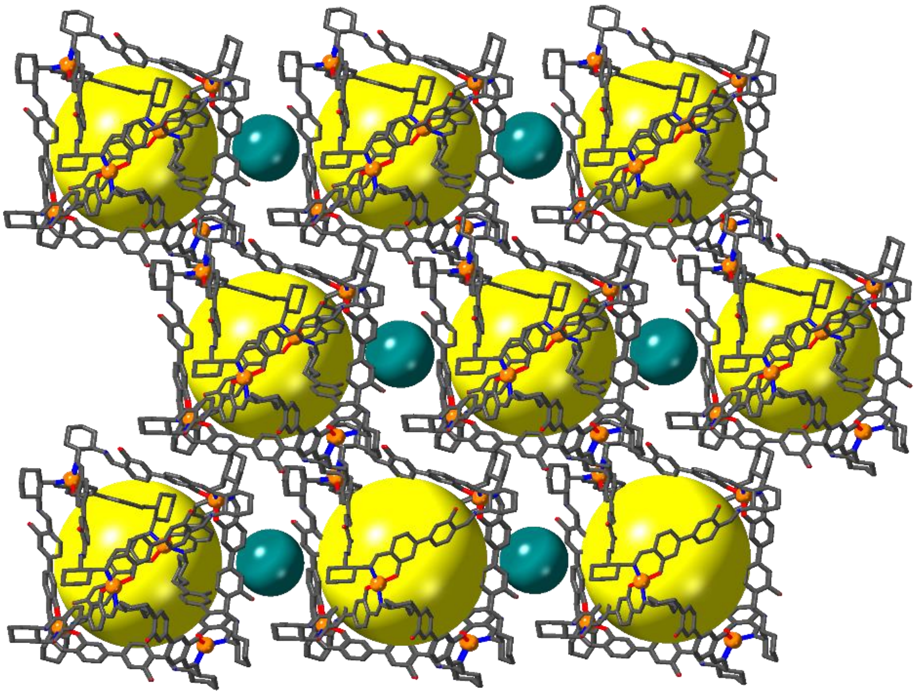

Figure 4.24. Crystal packing images of **MOP-3**. (Orange, Zn; blue, N; red, O; grey, C, H atoms are omitted for clarity. The large yellow spheres represent the inner cavities of the MOPs, the small cyan spheres represent external cavities created by the packing of the MOPs.)

Table 4.3. SC-XRD data for **MOP-2** and **MOP-3.**

Molecule	**MOP-2**	**MOP-3**
Crystallisation Solvent	DEF-CH_3CN	DEF
Space Group	*R3*	*R3*
Wavelength [Å]	Mo-Kα	Mo-Kα
Collection Temperature	100 K	100 K
Formula	$C_{168}H_{180}N_{24}O_{24}Zn_6$, $3(C_5H_{11}NO)$, CH_3CN, $6(H_2O)$, $3.25(H_2O)$	$C_{240}H_{228}N_{24}O_{24}Zn_6$
Mr	3764.07	4224.71
Crystal Size (mm)	0.304×0.089×0.031	0.030×0.020×0.020
Crystal System	trigonal	trigonal
a [Å]	20.2939(5)	39.3944(11)
b [Å]	20.2939(5)	39.3944(11)
c [Å]	49.1404(14)	26.9165(14)
α [°]	90	90
β [°]	90	90
γ [°]	120	120
V [Å^3]	17526.7(10)	36176(3)
Z	3	3
D_{calcd} [g cm^{-3}]	1.070	0.582
μ [mm^{-1}]	0.669	0.326
$F(000)$	5916	6624
2θ range [°]	2.007 – 26.521	1.627 – 20.812
Reflections collected	150243	152916
Independent reflections, R_{int}	16038, 0.0623	16845, 0.0964
Obs. Data [$I > 2\sigma$]	11766	13182
Data /restraints/ parameters	16038/37/ 764	16845/818/791
Final R_1 values ($I > 2\sigma(I)$)	0.0851	0.0369
Final R_1 values (all data)	0.1119	0.0550
Final $wR(F^2)$ values (all data)	0.2365	0.0891
Goodness-of-fit on F^2	1.057	1.016
Largest difference peak	1.085 / -0.514	0.157 / -0.196

4.10 Variable-temperature PXRD analysis and thermal analysis

The stability of **MOP-2** and **MOP-3** were measured by the variable-temperature PXRD analysis and TGA. As shown in Figure 4.25, PXRD data of **MOP-2** from synthesis solvent and exchanged by CH_3CN undergoes limited rearrangement. The PXRD patterns collected during in situ heating from 298 to 438 K show that the crystallinity of **MOP-2** reduces when the solvent is removed.

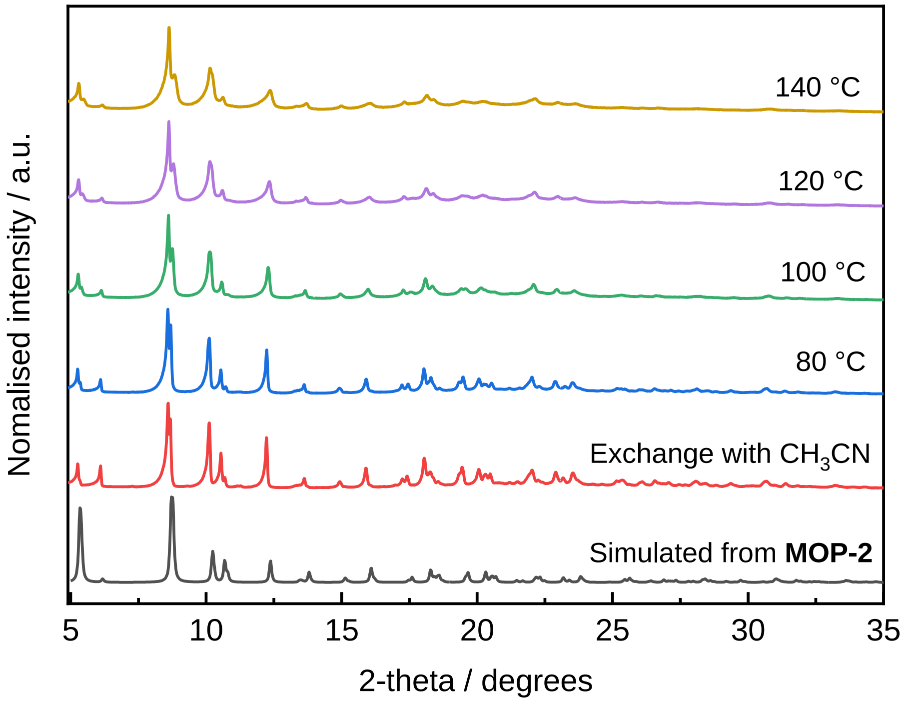

Figure 4.25. PXRD patterns were collected during in situ heating (298–438 K) for a sample of **MOP-2** from synthesis solvent and exchanged by CH_3CN. The samples were loaded in borosilicate glass capillaries (diameter = 0.5 mm).

After desolvation, the **MOP-2** tended to be less crystalline with peak broadening around 5.7 ° and multiple broad peaks around 9.3 to 10.8°, which indicates the structural transformation. (Figure 4.26) To explore the stability of the **MOP-2** crystals in aqueous solutions, including acid and base solutions, the crystal was immersed in boiling water, and in solutions with a pH of 1 or 10 for 24 h. The **MOP-2** crystals decomposed in the acid solution, most likely due to the poor stability of the imine coordination bonds in acid. By contrast, **MOP-2** showed no visible change in PXRD patterns when treated in boiling water and alkaline (pH 10) solutions for 24 h, as proven by the subsequently recorded PXRD patterns shown in Figure 4.26.

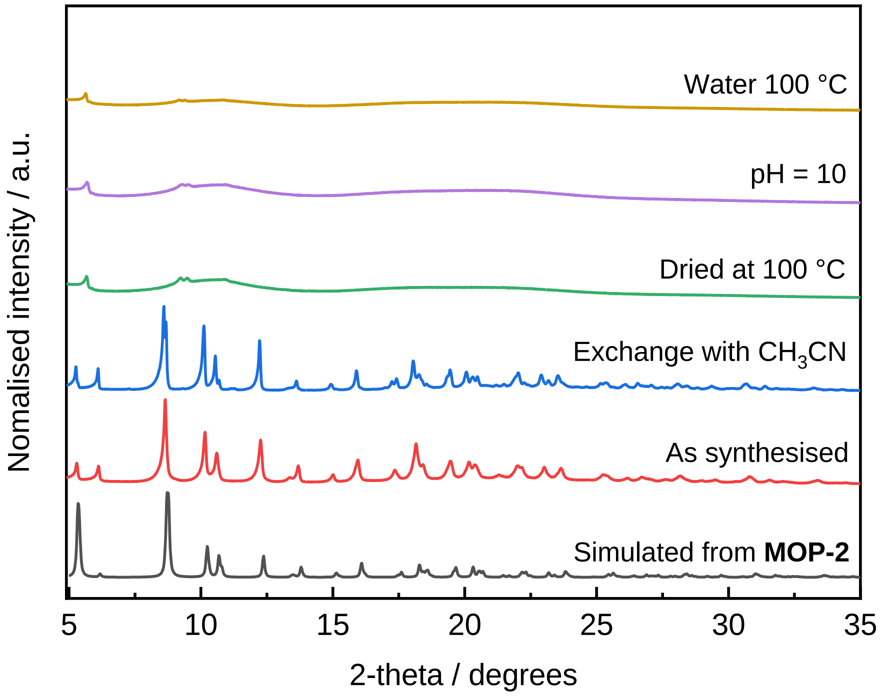

Figure 4.26. PXRD patterns under different conditions: dried at 100 °C in vacuum for 12 h, pH = 10 (24 h), boiling water (24 h).

As shown in Figure 4.27, TGA curves of **M2** and **M3** exhibits significant weight loss at near 350 °C due to the structure decomposition. As for their corresponding MOPs, desolvated **MOP-2** and **MOP-3** did not appear to exhibit sharp weight losses in their TGA curves below 300 °C, which indicates the complete desolvation of the crystal pores. Compared with the organic building unit **M2**, which exhibits decomposition temperatures around 359 °C, **MOP-2** shows a slowly weight loss around the similar temperature range. Similarly, **MOP-3** exhibits a more slowly weight-loss around the decomposition temperatures of **M3** around 353 °C. These results indicate the slight enhanced thermal stability after metal coordination.

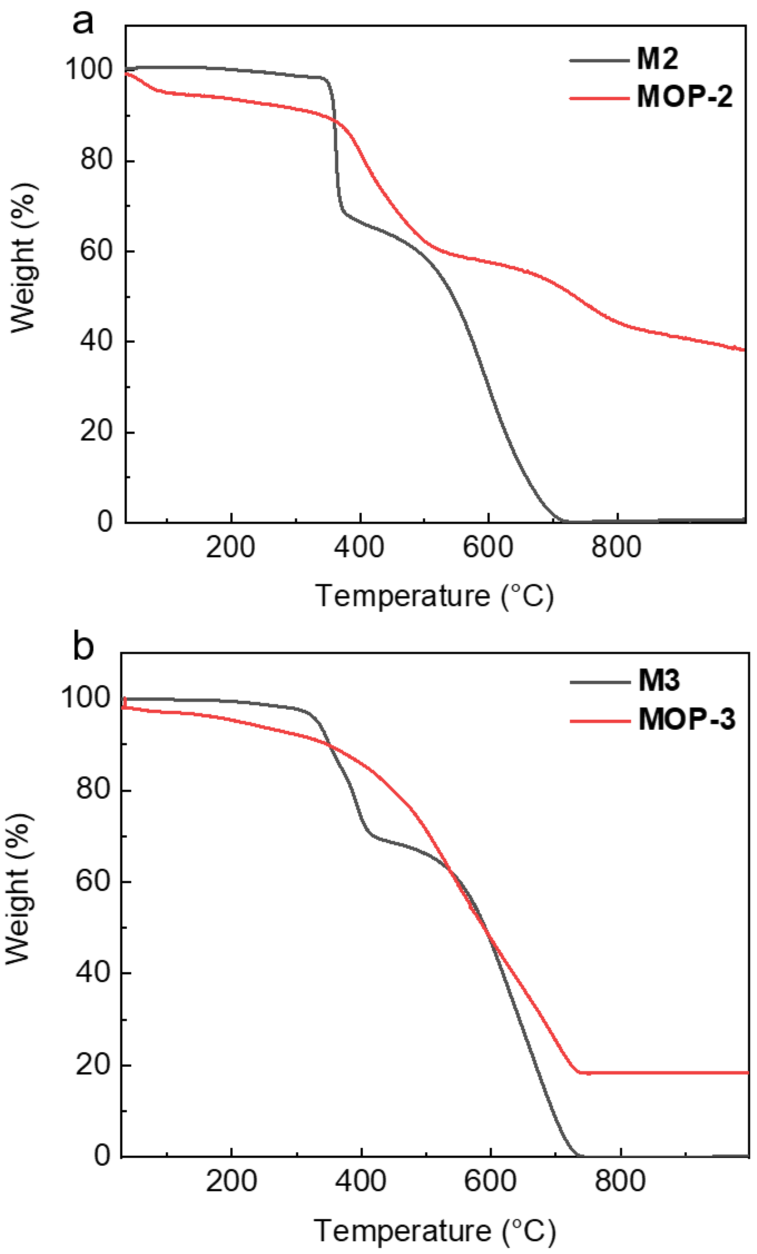

Figure 4.27. Thermogravimetric analysis of (a) **M2** (black line) and **MOP-2** (red line), (b) **M3** (black line) and **MOP-3** (red line).

4.11 Gas isotherms of MOP-2 and MOP-3

To desolvate the **MOP-2** crystals at a lower temperature to help maintain their high porosity, the crystalline samples were immersed and exchanged five times every 24 h in CH_3CN before drying at 100 °C under a high vacuum. After being transferred into a gas adsorption test tube, the **MOP-2** were degassed at 100 °C for 12 hours under a dynamic vacuum before gas analysis.

As for **MOP-3**, the crystalline samples were immersed in anhydrous acetone, and the solvent was exchanged with fresh acetone three times at intervals of 1 hour. The wet sample was then transferred to a Critical Point Drier (Quorum-E3100AG) and exchanged with liquid CO_2 3–4 times with the interval of 1.5 hours until all acetone in the material was successfully exchanged. After the final exchange, the system was heated to reach the critical point and the supercritical CO_2 was then released slowly over 1 hour. After the chamber pressure returned to ambient, samples were then transferred into a gas adsorption test tube and degassed at room temperature for 12 h. The desolvated **MOP-3** tended to be amorphous.

To investigate the permanent porosity of **MOP-2** and **MOP-3**, N_2 sorption isotherms were tested at 77 K. As shown in Figure 4.28, both **MOP-2** and **MOP-3** exhibited the composite of Types I and II that showed pronounced uptake at low pressures ($P/P_0 < 0.05$), being associated with the filling of micropores. The experimental SA_{BET} of **MOP-2** and **MOP-3** are 745 and 651 m^2/g, respectively. The calculated SA_{BET} by *Zeo++* based on solvate crystal structures are 634 and 3697 m^2/g with 1.82 Å probe (N_2 dynamic radius), respectively.[60] The experimental SA_{BET} of **MOP-2** is slightly higher than the calculated result. By contrast, the experimental SA_{BET} of **MOP-3** is much less than the calculated result. The difference between the experimental data and calculated data is due to the rearrangement of the structure after desolvation.

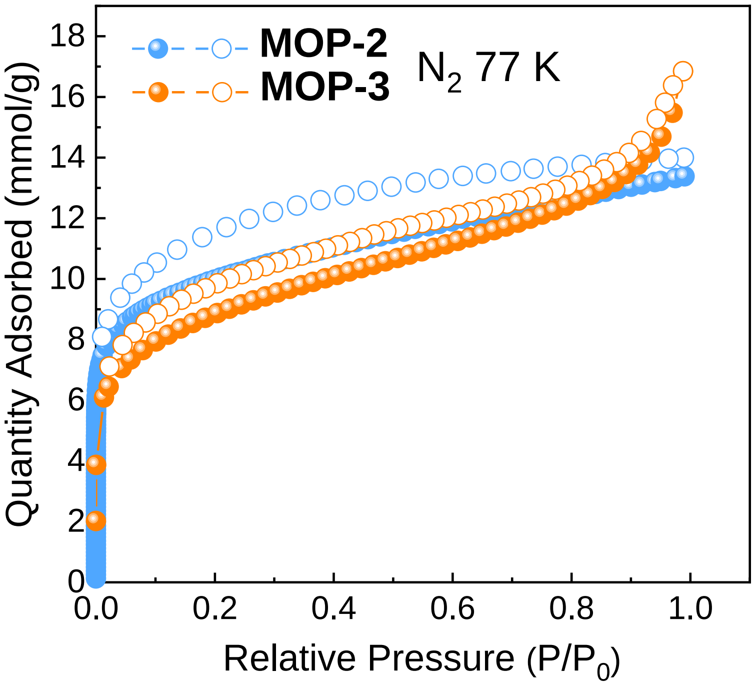

Figure 4.28. N_2 sorption isotherms at 77 K for **MOP-2** (blue) and **MOP-3** (orange).

To further investigate the gas sorption of **MOP-2** and **MOP-3**, H_2 and CO_2 isotherms were measured. As shown in Figure 4.29, the uptake of H_2 and CO_2 is consistent to their experimental SA_{BET}, and there is no stepwise in all the isotherms, which indicates the rigid pores in **MOP-2** and **MOP-3**. As shown in Figure 4.29a, around 1100 mbar, **MOP-2** has a capacity for H_2 about 6.6 mmol/g at 77 K compared with the **MOP-3** of 4.7 mmol/g. As for CO_2, shown in Figures 4.29b and 4.29c, **MOP-2** has a CO_2 capacity of about 3.7 and 2.4 mmol/g at 273 and 298 K, respectively. By contract, **MOP-3** has a CO_2 capacity of about 2.2 and 1.3 mmol/g at 273 and 298 K, respectively.

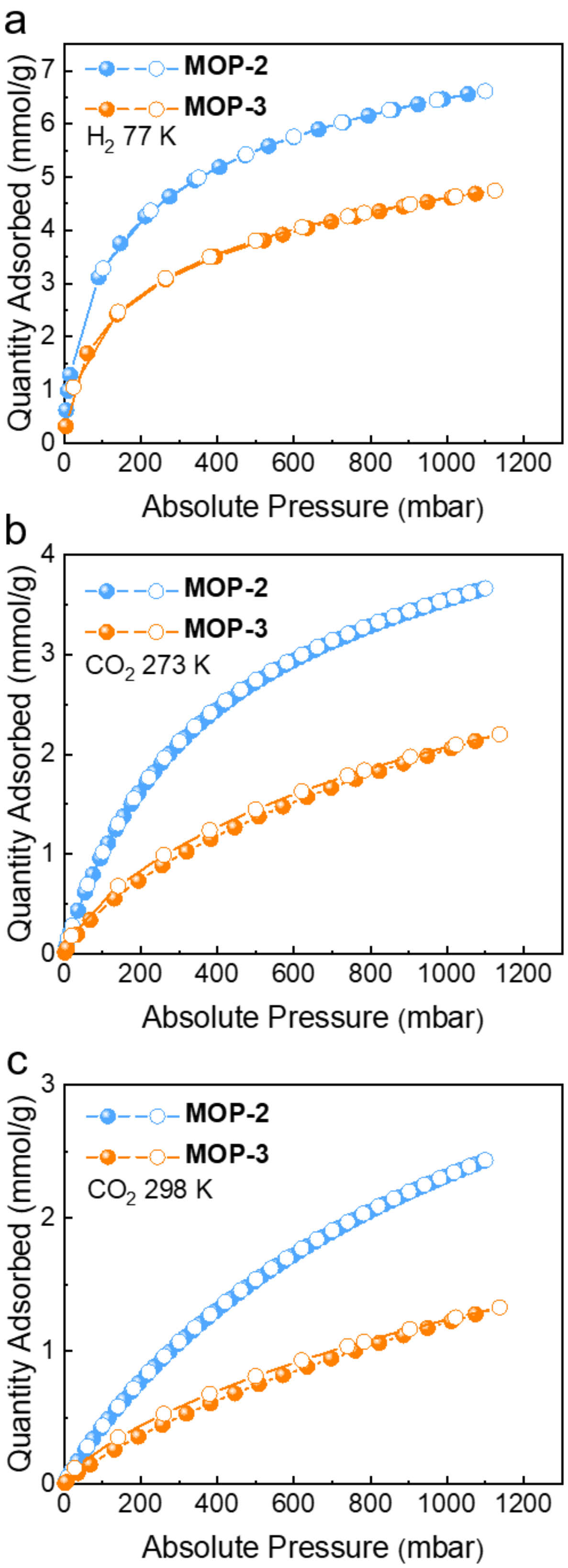

Figure 4.29. (a) H_2 sorption isotherms at 77 K, (b) CO_2 sorption isotherms at 273 K for, (c) CO_2 sorption isotherms at 298 K for **MOP-2** (blue) and **MOP-3** (orange).

The largest included sphere along the free sphere path (D_{if}) calculated by *Zeo*++ [60, 81] in **MOP-2** is 3.64 Å, which is close to the molecular size of the rare gas Kr (diameter = 3.69 Å).[82] Xe (4.10 Å) has a similar size and shape to Kr, which makes their separation technological challenging.[83] Therefore, the single-component Xe and Kr gas isotherms for **MOP-2** were measured at 273 K and 298 K. As shown in Figure 4.30a, around 1100 mbar, **MOP-2** has capacity for Xe about 3.0 mmol/g and Kr about 1.2 mmol/g at 273 K, which is close to the performance of CC3 (Xe about 2.5 mmol/g and Kr about 1.5 mmol/g) for these two gases.[83] CC3 is a porous organic cage that has been reported to have high selectivity for rare gas separations at low rare gas concentrations, and CC3 membranes have a high selectivity of about 4.8 for Kr/Xe.[84]

The Xe-Kr binary mixture adsorption selectivity was then predicted using ideal adsorption solution theory (IAST) based on the single-gas isotherms shown in Figure 4.30a.[85] The IAST-predicted selectivity is shown in Figure 4.30b for binary mixtures of Xe-Kr with compositions of 50:50 at 273K and 298 K. For equimolar mixtures, the initially predicted selectivity was 12.5, and then gradually decreased to 8.8 at 1000 mbar and 298 K. At 273 K, the predicted selectivity is from 11.1 to 8.9. These results indicate **MOP-2** has a great potential for rare gases separation, which will be investigated in future work.

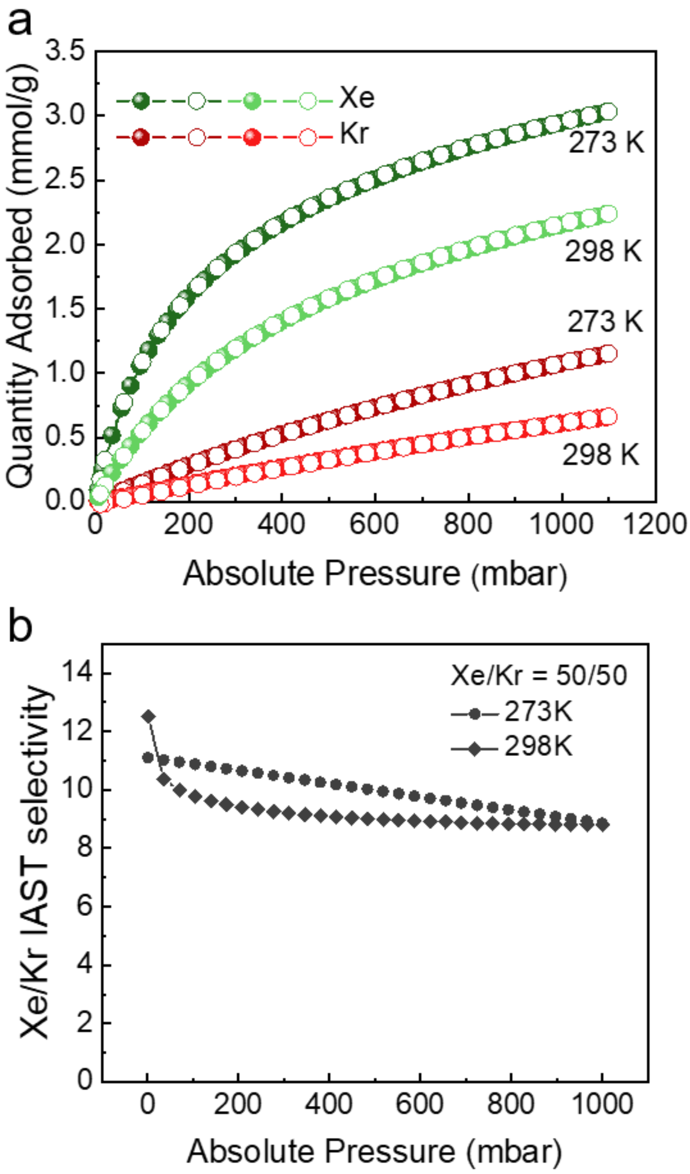

Figure 4.30. (a) Xe (green) and Kr (red) sorption isotherms for **MOP-2**, (b) IAST selectivity of Xe/Kr mixtures for **MOP-2** as calculated from these pure gas sorption isotherms.

4.12 Conclusion

Two new polymorphs of a trinuclear zinc MOC have been investigated for D_2 / H_2 separations. The two polymorphs were isolated by activating crystals of MeOH solvate of **MOC-1**, initially at 80 °C to afford **MOC-1α**, and then at 180 °C to transform **MOC-1α** into **MOC-1β**. Surprisingly, **MOC-1β** had a slightly larger extrinsic porosity than **MOC-1α**. There are other differences between the crystal structures, and

MOC-1α has a more extensive range of pore diameter sizes from about 2.0 Å to 5.1 Å and appeared more flexible in gas sorption measurements, which led to **MOC-1α** having a higher BET surface area of 393.8 m^2/g compared to **MOC-1β** (269.9 m^2/g). **MOC-1β** has a slightly higher unit cell void volume than **MOC-1α** (20.6% for **MOC-1β** *vs* 17.3% for **MOC-1α**), and **MOC-1β** thus has a higher pure D_2 capacity of 3.8 mmol/g than the **MOC-1α** (2.1mmol/g) at the exposing pressure of 200 mbar. In addition, TDS measurements confirm that the D_2 adsorption capacity with **MOC-1β** (1.10 mmol/g, $S_{D2/H2} = 2.2$) is higher than for **MOC-1α** (0.41 mmol/g, $S_{D2/H2} = 2.8$) at 77 K for 1:1 D_2–H_2 mixture. Furthermore, the local flexibility of MOC crystals provides the additional accessible inner surface to increase the adsorption and separation of hydrogen isotopes inside the crystals via kinetic quantum sieving. This leads to a desorption temperature of over 100 K even without existing strong adsorption sites. Hence, the selectivity and capacity of MOCs for hydrogen isotopes are sensitive to their pore size and flexibility. This study paves the way for hydrogen isotope separation above liquid nitrogen temperatures based on well-defined pore structures and the flexibility of molecular materials.

After that, a strategy for tuning the cavity size and window in MOPs by using trianglsalen macrocycles in different sizes was discovered. The size of trianglsalen macrocycles can be controlled by using bis-salicylaldehydes with one or more aromatic rings. Two trianglsalen macrocycles **M2** and **M3** were synthesised using bis-salicylaldehydes one and two aromatic rings, respectively. These macrocycles coordinated with Zn(II) ions to form two large zinc–organic polyhedral MOP-2 and MOP-3, which had molecular sizes of 2.3 and 2.9 nm, respectively. After desolvation, **MOP-2** and **MOP-3** were found to exhibit permanent porosity and had SA_{BET} of 745.04 and 651.38 m^2/g, respectively. Furthermore, **MOP-2** has a great potential for the rare gases separation with calculated selectivity up to 12.5 for Xe/Kr at 298 K, which highlights the broader scope of MOP in gas pair separation applications in the future.

4.13 References

1. O. Barreda, et al., Ligand-Based Phase Control in Porous Molecular Assemblies. *ACS Appl. Mater. Interfaces* **2018,** *10* (14), 11420-11424.

2. Mei Pan, et al., Chiral metal–organic cages/containers (MOCs): From structural and stereochemical design to applications. *Coord. Chem. Rev.* **2019,** *378,* 333-349.

3. M. Eddaoudi, et al., Porous Metal−Organic Polyhedra: 25 Å Cuboctahedron Constructed from 12 $Cu_2(CO_2)_4$ Paddle-Wheel Building Blocks. *J. Am. Chem. Soc.* **2001,** *123* (18), 4368-4369.

4. J. R. Li, et al., Selective gas adsorption and separation in metal-organic frameworks. *Chem. Soc. Rev.* **2009,** *38* (5), 1477-504.

5. J. M. Teo, et al., Hetero-bimetallic metal-organic polyhedra. *Chem. Commun. (Camb)* **2016,** *52* (2), 276-9.

6. A. W. Augustyniak, et al., A vanadium(IV) pyrazolate metal-organic polyhedron with permanent porosity and adsorption selectivity. *Chem. Commun. (Camb)* **2015,** *51* (79), 14724-7.

7. Gregory R. Lorzing, et al., Selective Gas Adsorption in Highly Porous Chromium(II)-Based Metal–Organic Polyhedra. *Chem. Mater.* **2017,** *29* (20), 8583-8587.

8. J. Park, et al., Chromium(II) Metal-Organic Polyhedra as Highly Porous Materials. *ACS Appl Mater Interfaces* **2017,** *9* (33), 28064-28068.

9. A. J. Gosselin, et al., Permanently Microporous Metal-Organic Polyhedra. *Chem. Rev.* **2020,** *120* (16), 8987-9014.

10. Xinxin Hang, et al., Discrete $\{Ni_{40}\}$ Coordination Cage: A Calixarene-Based Johnson-Type (J17) Hexadecahedron. *J. Am. Chem. Soc.* **2016,** *138* (9), 2969-2972.

11. S. P. Argent, et al., Porous Metal-Organic Polyhedra: Morphology, Porosity, and Guest Binding. *Inorg. Chem.* **2020,** *59* (21), 15646-15658.

12. Marc A. Little; Andrew I. Cooper, The Chemistry of Porous Organic Molecular Materials. *Adv. Funct. Mater.* **2020,** *30* (41), 1909842.

13. D. J. Tranchemontagne, et al., Reticular chemistry of metal-organic polyhedra. *Angew. Chem. Int. Ed. Engl.* **2008,** *47* (28), 5136-47.

14. Sara Pasquale, et al., Giant regular polyhedra from calixarene carboxylates and uranyl. *Nat. Commun.* **2012,** *3* (1), 785.

15. Guoliang Liu, et al., Process-Tracing Study on the Postassembly Modification of Highly Stable Zirconium Metal–Organic Cages. *J. Am. Chem. Soc.* **2018,** *140* (20), 6231-6234.

16. Feng-Rong Dai, et al., Synthetic Supercontainers Exhibit Distinct Solution versus Solid State Guest-Binding Behavior. *J. Am. Chem. Soc.* **2014,** *136* (20), 7480-7491.

17. Michael J. Bojdys, et al., Supramolecular Engineering of Intrinsic and Extrinsic Porosity in Covalent Organic Cages. *J. Am. Chem. Soc.* **2011,** *133* (41), 16566-16571.

18. A. E. Martin Diaz; J. E. M. Lewis, Structural Flexibility in Metal-Organic Cages. *Front Chem* **2021,** *9* (456), 706462.

19. Edmundo G. Percástegui; Vojtech Jancik, Coordination-driven assemblies based on meso-substituted porphyrins: Metal-organic cages and a new type of meso-metallaporphyrin macrocycles. *Coord. Chem. Rev.* **2020,** *407*, 213165.

20. A. Sarnicka, et al., Controlling the macrocycle size by the stoichiometry of the applied template ion. *Chem. Commun. (Camb)* **2012,** *48* (16), 2237-9.

21. Feng-Rong Dai; Zhenqiang Wang, Modular Assembly of Metal–Organic Supercontainers Incorporating Sulfonylcalixarenes. *J. Am. Chem. Soc.* **2012,** *134* (19), 8002-8005.

22. S. Du, et al., A giant coordination cage based on sulfonylcalix[4]arenes. *Chem. Commun. (Camb)* **2012,** *48* (73), 9177-9.

23. M. Liu, et al., Calixarene-based nanoscale coordination cages. *Angew. Chem. Int. Ed. Engl.* **2012,** *51* (7), 1585-8.

24. Zengmin Li; Chet Jablonski, Synthesis and characterization of ‘calixsalens’: a new class of macrocyclic chiral ligands. *Chem. Commun.* **1999,** (16), 1531-1532.

25. Agnieszka Janiak, et al., An unexpected relationship between solvent inclusion and gas sorption properties of chiral calixsalen solids. *Supramol. Chem.* **2018,** *30* (5-6), 479-487.

26. M. Kwit, et al., One-Step Construction of the Shape Persistent, Chiral But Symmetrical Polyimine Macrocycles. *Chem. Rec.* **2019,** *19* (2-3), 213-237.

27. J. Janczak, et al., Trinuclear Cage-Like Zn(II) Macrocyclic Complexes: Enantiomeric Recognition and Gas Adsorption Properties. *Chemistry* **2016,** *22* (2), 598-609.

28. Sheng-Ming Xie, et al., Homochiral Metal–Organic Cage for Gas Chromatographic Separations. *Anal. Chem.* **2018,** *90* (15), 9182-9188.

29. Zhentao Li, et al., Incorporation of homochiral metal-organic cage into ionic liquid based monolithic column for capillary electrochromatography. *Anal. Chim. Acta* **2020,** *1094*, 160-167.

30. Li-Xiao He, et al., Chiral metal-organic cages used as stationary phase for enantioseparations in capillary electrochromatography. *Electrophoresis* **2020,** *41* (1-2), 104-111.

31. Marcin Miklitz; Kim E. Jelfs, pywindow: Automated Structural Analysis of Molecular Pores. *J. Chem. Inf. Model.* **2018,** *58* (12), 2387-2391.

32. Christoph Bannwarth, et al., GFN2-xTB—An Accurate and Broadly Parametrized Self-Consistent Tight-Binding Quantum Chemical Method with

Multipole Electrostatics and Density-Dependent Dispersion Contributions. *J. Chem. Theory Comput.* **2019,** *15* (3), 1652-1671.

33. Christoph Bannwarth, et al., Extended tight-binding quantum chemistry methods. *WIREs Comput. Mol. Sci.* **2021,** *11* (2), e1493.

34. Marcin Kwit, et al., One-Step Construction of the Shape Persistent, Chiral But Symmetrical Polyimine Macrocycles. *Chem. Rec.* **2019,** *19* (2-3), 213-237.

35. Marcin Kwit, et al., Synthesis of chiral large-ring triangular salen ligands and structural characterization of their complexes. *Dalton Trans.* **2009,** (34), 6783-6789.

36. Joanna Szymkowiak; Marcin Kwit, Electronic and vibrational exciton coupling in oxidized trianglimines. *Chirality* **2018,** *30* (2), 117-130.

37. Joanna Szymkowiak, et al., Consistent supramolecular assembly arising from a mixture of components – self-sorting and solid solutions of chiral oxygenated trianglimines. *CrystEngComm* **2018,** *20* (35), 5200-5208.

38. P. Clark Souers, *Hydrogen Properties for Fusion Energy*. University of California Press: 1986.

39. M. Glugla, et al., The inner deuterium/tritium fuel cycle of ITER. *Fusion Eng. Des.* **2003,** *69* (1-4), 39-43.

40. Giuseppe Zaccai, How Soft Is a Protein? A Protein Dynamics Force Constant Measured by Neutron Scattering. *Science* **2000,** *288* (5471), 1604-1607.

41. Igor V. Stiopkin, et al., Hydrogen bonding at the water surface revealed by isotopic dilution spectroscopy. *Nature* **2011,** *474* (7350), 192-195.

42. Chaowei Shi, et al., Atomic-resolution structure of cytoskeletal bactofilin by solid-state NMR. *Sci. Adv.* **2015,** *1* (11), e1501087.

43. Howard K Rae *Separation of hydrogen isotopes*; American Chemical Society, Washington, DC: 1978.

44. GM Keyser, et al., Heavy water distillation. ACS Publications: 1978.

45. J. J. M. Beenakker, et al., Molecular transport in subnanometer pores: zero-point energy, reduced dimensionality and quantum sieving. *Chem. Phys. Lett.* **1995,** *232* (4), 379-382.

46. AV Anil Kumar; Suresh K Bhatia, Quantum effect induced reverse kinetic molecular sieving in microporous materials. *Phys. Rev. Lett.* **2005,** *95* (24), 245901.

47. Hyunchul Oh, et al., Quantum cryo-sieving for hydrogen isotope separation in microporous frameworks: an experimental study on the correlation between effective quantum sieving and pore size. *J. Mater. Chem.* **2013,** *1* (10), 3244-3248.

48. Yanlong Xing, et al., An exceptional kinetic quantum sieving separation effect of hydrogen isotopes on commercially available carbon molecular sieves. *Phys. Chem. Chem. Phys.* **2014,** *16* (30), 15800-15805.

49. Igor Bezverkhyy, et al., Enhancement of D_2/H_2 Selectivity in Zeolite A through Partial Na–K Exchange: Single-Gas and Coadsorption Studies at 45–77 K. *J. Phys. Chem. C* **2020,** *124* (45), 24756-24764.

50. Renjin Xiong, et al., Highly effective hydrogen isotope separation through dihydrogen bond on Cu(I)-exchanged zeolites well above liquid nitrogen temperature. *Chem. Eng. J.* **2020,** *391,* 123485.

51. Linda Zhang, et al., Exploiting Dynamic Opening of Apertures in a Partially Fluorinated MOF for Enhancing H_2 Desorption Temperature and Isotope Separation. *J. Am. Chem. Soc.* **2019,** *141* (50), 19850-19858.

52. Raeesh Muhammad, et al., Exploiting the Specific Isotope-Selective Adsorption of Metal–Organic Framework for Hydrogen Isotope Separation. *J. Am. Chem. Soc.* **2021,** *143* (22), 8232-8236.

53. Ming Liu, et al., Barely porous organic cages for hydrogen isotope separation. *Science* **2019,** *366* (6465), 613-620.

54. H. Oh, et al., Highly effective hydrogen isotope separation in nanoporous metal-organic frameworks with open metal sites: direct measurement and theoretical analysis. *ACS Nano* **2014,** *8* (1), 761-70.

55. X. Liu, et al., Molecular-Scale Hybrid Membranes Derived from Metal-Organic Polyhedra for Gas Separation. *ACS Appl. Mater. Interfaces* **2018,** *10* (25), 21381-21389.

56. M. A. Andres, et al., Ultrathin Films of Porous Metal-Organic Polyhedra for Gas Separation. *Chemistry* **2020,** *26* (1), 143-147.

57. G. A. Craig, et al., Hysteresis in the gas sorption isotherms of metal-organic cages accompanied by subtle changes in molecular packing. *Chem. Commun. (Camb)* **2020,** *56* (25), 3689-3692.

58. Agnieszka Janiak, et al., Readily prepared inclusion forming chiral calixsalens. *Org. Biomol. Chem.* **2016,** *14* (2), 669-673.

59. Marielle Pinheiro, et al., Characterization and comparison of pore landscapes in crystalline porous materials. *J. Mol. Graphics Modell.* **2013,** *44*, 208-219.

60. Thomas F. Willems, et al., Algorithms and tools for high-throughput geometry-based analysis of crystalline porous materials. *Microporous Mesoporous Mater.* **2012,** *149* (1), 134-141.

61. Bo Liu, et al., Dynamic Zn-based metal–organic framework: stepwise adsorption, hysteretic desorption and selective carbon dioxide uptake. *J. Mater. Chem.* **2013,** *1* (22), 6535-6538.

62. Xiao-Zhong Chu, et al., Adsorption dynamics of hydrogen and deuterium in a carbon molecular sieve bed at 77 K. *Sep. Purif. Technol.* **2015,** *146*, 168-175.

63. A. J. Arvai; C. Nielsen *ADSC Quantum-210 ADX Program*, Area Detectir System Corporation: Poway, CA, USA, 1983.

64. Xiao-Zhong Chu, et al., Dynamic experiments and model of hydrogen and deuterium separation with micropore molecular sieve Y at 77 K. *Chem. Eng. J.* **2009,** *152* (2-3), 428-433.

65. Xuebo Zhao, et al., Kinetic isotope effect for H_2 and D_2 quantum molecular sieving in adsorption/desorption on porous carbon materials. *J. Phys. Chem. B* **2006,** *110* (20), 9947-9955.

66. Hideki Tanaka, et al., Quantum effects on hydrogen isotope adsorption on single-wall carbon nanohorns. *J. Am. Chem. Soc.* **2005,** *127* (20), 7511-7516.

67. Daisuke Noguchi, et al., Storage function of carbon nanospaces for molecules and ions. *ECS Transactions* **2007,** *11* (8), 63-75.

68. Kenji Kotoh, et al., Multi-component adsorption characteristics of hydrogen isotopes on synthetic zeolite 5A-type at 77.4 K. *J. Nucl. Sci. Technol.* **2002,** *39* (4), 435-441.

69. JM Salazar, et al., Adsorption of hydrogen isotopes in the zeolite NaX: Experiments and simulations. *Int. J. Hydrogen Energy* **2017,** *42* (18), 13099-13110.

70. Xiao-Zhong Chu, et al., Adsorption of hydrogen isotopes on micro-and mesoporous adsorbents with orderly structure. *J. Phys. Chem. B* **2006,** *110* (45), 22596-22600.

71. Kenji Kotoh; Kazuhiko Kudo, Multi-component adsorption behavior of hydrogen isotopes on zeolite 5A and 13X at 77.4 K. *Fusion Sci, Technol.* **2005,** *48* (1), 148-151.

72. Banglin Chen, et al., Surface interactions and quantum kinetic molecular sieving for H_2 and D_2 adsorption on a mixed metal − organic framework material. *J. Am. Chem. Soc.* **2008,** *130* (20), 6411-6423.

73. Amit Sharma, et al., Hydrogen Uptake on Coordinatively Unsaturated Metal Sites in VSB-5: Strong Binding Affinity Leading to High-Temperature D_2/H_2 Selectivity. *Langmuir* **2017,** *33* (51), 14586-14591.

74. J. Jia, et al., Twelve-connected porous metal-organic frameworks with high H_2 adsorption. *Chem. Commun. (Camb)* **2007,** (8), 840-842.

75. X. Lin, et al., High H_2 adsorption by coordination-framework materials. *Angew. Chem. Int. Ed. Engl.* **2006,** *45* (44), 7358-7364.

76. S. S. Mondal, et al., Systematic Experimental Study on Quantum Sieving of Hydrogen Isotopes in Metal-Amide-Imidazolate Frameworks with narrow 1-D Channels. *Chemphyschem* **2019,** *20* (10), 1311-1315.

77. Enming Ping, et al., Kinetic and Chemical Affinity Quantum Sieving Effects of ZIF-67 for H_2 and D_2 and Gas Chromatographic Separation of Hydrogen Isotopes on Columns Packed with ZIF-67@ NH2-γ-Al_2O_3. *ACS Applied Energy Materials* **2021,** *4* (10), 10857-10866.

78. Xiaoxiao Chen, et al., New gas chromatographic packing ZIF-67@ NH_2–SiO_2 for separation of hydrogen isotope H_2/D_2. *Int. J. Hydrogen Energy* **2021,** *46* (24), 13029-13037.

79. Yanan Si, et al., Highly effective H_2/D_2 separation in a stable Cu-based metal-organic framework. *Nano Res.* **2021,** *14* (2), 518-525.

80. Hyunchul Oh, et al., Highly effective hydrogen isotope separation in nanoporous metal–organic frameworks with open metal sites: direct measurement and theoretical analysis. *ACS nano* **2014,** *8* (1), 761-770.

81. M. D. Foster, et al., A geometric solution to the largest-free-sphere problem in zeolite frameworks. *Microporous Mesoporous Mater.* **2006,** *90* (1), 32-38.

82. Timothy Van Heest, et al., Identification of Metal–Organic Framework Materials for Adsorption Separation of Rare Gases: Applicability of Ideal Adsorbed Solution Theory (IAST) and Effects of Inaccessible Framework Regions. *J. Phys. Chem. C* **2012,** *116* (24), 13183-13195.

83. Linjiang Chen, et al., Separation of rare gases and chiral molecules by selective binding in porous organic cages. *Nat. Mater.* **2014,** *13* (10), 954-960.

84. Jolie M. Lucero; Moises A. Carreon, Separation of Light Gases from Xenon over Porous Organic Cage Membranes. *ACS Appl. Mater. Interfaces* **2020,** *12* (28), 32182-32188.

85. David W. Hand, et al., Prediction of multicomponent adsorption equilibria using ideal adsorbed solution theory. *Environ. Sci. Technol.* **1985,** *19* (11), 1037-1043.

Chapter 5:

Experimental methods and characterisation data

5.1 Materials

All chemicals and solvents were obtained from Sigma-Aldrich, Acros Organics, Fischer Scientific, Alfa Aesar, TCI UK, Manchester Organics (UK) and Shanghai Sunway Corporation Ltd. All chemicals and solvents were used as received. All gases for sorption analysis were supplied by BOC at a purity of $\geqslant$99.999%.

5.2 General methods

Nuclear magnetic resonance (NMR): ^{1}H NMR spectra were recorded using an internal deuterium lock for the residual protons in $CDCl_3$ (δ = 7.26 ppm) or CD_2Cl_2 (δ = 5.32 ppm) at ambient probe temperature on either a Bruker Avance 400 (400MHz). Data are presented as follows: chemical shift, integration, peak multiplicity (s = singlet, d = doublet, t = triplet, q = quartet, quint = quintet, m = multiplet, br = broad), coupling constants (J / Hz), and assignment. Chemical shifts are expressed in ppm on a δ scale relative to δ TMS (0 ppm), δ CD_2Cl_2 (5.32 ppm), or δ $CDCl_3$ (7.26 ppm). Assignments were determined either based on unambiguous chemical shifts or coupling patterns or by analogy to fully interpreted spectra for structurally related compounds.

^{13}C NMR spectra were recorded and referenced against the residual ^{13}C signal of the solvent at ambient probe temperatures on the following instruments: Bruker Avance 400 (101 MHz).

High resolution mass spectrometry (HRMS): HRMS was carried out using an Agilent Technologies 6530B accurate-mass QTOF Dual ESI mass spectrometer (capillary voltage 4000 V, fragmentor 225 V) in positive-ion detection mode. The mobile phase was MeOH + 0.1% formic acid at a flow rate of 0.25 mL/min.

Matrix-assisted laser desorption/ionisation time of flight mass spectrometry (MALDI-TOF MS): MALDI-TOF MS was conducted using an AXIMA Confidence MALDI MS (Shimadzu Biotech) fitted with a 50 Hz N_2 laser. A 10:1 -5-1 ratio of matrix/sample was dissolved in tetrahydrofuran (THF, 10 mg mL^{-1}) and this was drop-coated onto the microtitre plate before analysis. The matrix used was trans-2-[3-(4-tert-butylphenyl)-2-methyl-2-propenylidene]malononitrile (DCTB).

Fourier-transform infrared (FTIR) spectra: IR spectra were recorded using a Bruker Tensor 27 FT-IR spectrometer with Quest ATR (diamond crystal puck) attachment running Opus 6.5 software. Samples were analysed as dry powders for 32 scans with a resolution of 4 cm^{-1}. Spectra were recorded in transmission mode. FTIR spectroscopy was used to characterise vibrational frequencies of the chemical bonds constituting the sample to analyse its chemical structure.

Elemental analysis: CHN analysis was performed on a Thermo EA1112 Flash CHNS-O Analyser using standard microanalytical procedures.

Powder X-ray diffraction (PXRD): Laboratory PXRD data were collected in transmission mode on samples held thin Mylar film in aluminium well plates on a Panalytical Empyrean diffractometer, equipped with a high throughput screening XYZ stage, X ray focusing mirror, and PIXcel detector, using Cu Kα (λ = 1.541 Å) radiation. Data were measured over the range 5–30° in ~0.013° steps over 15 minutes. Unless stated, PXRD patterns were recorded at room temperature.

High resolution variable temperature PXRD for EA@**TAMC** was collected using the I11 beamline at Diamond Light Source (λ =0.82446 Å), using the Mythen II position sensitive detector. The finely ground sample was loaded into a 0.5 mm diameter borosilicate glass capillary and exposed to ethyl acetate vapour for 48 hours at room temperature. A capillary spinner was used to improve powder averaging during data acquisition. The temperature was controlled using an Oxford Cryosystems Cryostream Plus. The sample was cooled to 223 K to record a reference profile of the solvated structure, then heated from 273 – 393 K, with data collections at 5 K steps. The sample temperature was maintained above 363 K for approximately 1.5 hours to effect desolvation. The sample was then cooled to 295 K to acquire the final diffraction profile. Indexing and Le Bail refinements were performed by using *TOPAS* - Academic.[1, 2]

For variable temperature PXRD in-*situ* experiments for **MOP-2**, samples were loaded into borosilicate glass capillaries which were spun during data collections to improve powder averaging. PXRD data for these samples were recorded in transmission mode on a Panalytical Empyrean diffractometer, equipped with a sample spinner, X-ray focusing mirror, and PIXcel detector, using Cu-K*α* (λ = 1.541 Å) radiation.

Thermogravimetric analysis (TGA): TGA was carried out using a Q5000IR analyzer (TA instruments) with an automated vertical overhead thermobalance. The samples were heated at the rate of 10 °C /min using dry N_2 as the protective gas.

Differential scanning calorimetry (DSC): Performed on a TA Instruments Q200 DSC, under nitrogen flow, and with heating and cooling rates of 5 °C/min.

Single crystal X-ray crystallography (SC-XRD): SC-XRD data sets were measured on a Rigaku MicroMax-007 HF rotating anode diffractometer (Mo-Kα radiation, λ = 0.71073 Å, Kappa 4-circle goniometer, Rigaku Saturn724+ detector); or at beamline I19, Diamond Light Source, Didcot, UK using silicon double crystal monochromated synchrotron radiation (λ = 0.6889 Å, Pilatus 2M detector). Absorption corrections, using the multi-scan method, were performed with the program CrysAlisPro 1.171.40.45a. For synchrotron X-ray data, collected at Diamond Light Source, data reduction and absorption corrections were performed with xia2.[3] Structures were solved with *SHELXT*,[4] and refined by full-matrix least-squares on $|F|^2$ by *SHELXL*,[5] interfaced through the program *OLEX2*.[6] H atom positions for the C-H groups were refined using the riding model.

Gas sorption: Unless stated, N_2 adsorption and desorption isotherms were collected at 77 K using an ASAP2020 volumetric adsorption analyser (Micrometrics Instrument Corporation). CO_2, CH_4 and H_2 isotherms were collected up to a pressure of 1200 mbar on a Micromeritics ASAP2020 at 77 K for H_2, or at 273 and 298 K for CO_2 and CH_4.

The details of the cryogenic hydrogen adsorption and TDS experiments for **MOC-1α** and **MOC-1β** are in the Section 5.5.8 and 5.5.9, respectively.

Isotherm measurements of **MOP-2** were performed using a Micromeritics 3flex surface characterisation analyser, equipped with a Cold-Edge technologies liquid helium cryostat chiller unit for temperature control. N_2 and H_2 isotherms for **MOP-2** were collected at 77 K. CO_2, CH_4, Kr and Xe isotherms for **MOP-2** were collected at 273 and 298 K.

TAMC was degassed at 70 °C for 15 hours under dynamic vacuum prior to gas analysis. **1**-*R*, **1**-*rac*, **MOC-1α** and **MOC-1β** were degassed at 80 °C for 15 hours under dynamic vacuum before gas analysis. **MOP-2** and **MOP-3** were degassed at 100 °C and RT, respectively for 12 hours under dynamic vacuum before gas analysis.

Brunauer-Emmett-Teller (BET) measurement: BET theory is applied to quantify specific surface area of the particles by using probing gas that does not react chemically with the particles. Nitrogen is the most commonly probing gas used for BET measurement. It is assumed that the gas condenses onto the surface in multilayers; gas molecules only interact with adjacent layers; the Langmuir theory can be applied to each layer; the enthalpy of adsorption for the first layer is constant and greater than the second (and higher); the enthalpy of adsorption for the second (and higher) layers is the same as the enthalpy of liquefaction.[7] It should be noted that the isotherm is only valid in the range $P/P_0 = 0.05 – 0.3$, as outside of this range, it is not linear.

5.3 Chapter 2 experimental method and data

5.3.1 Synthesis of TAMC

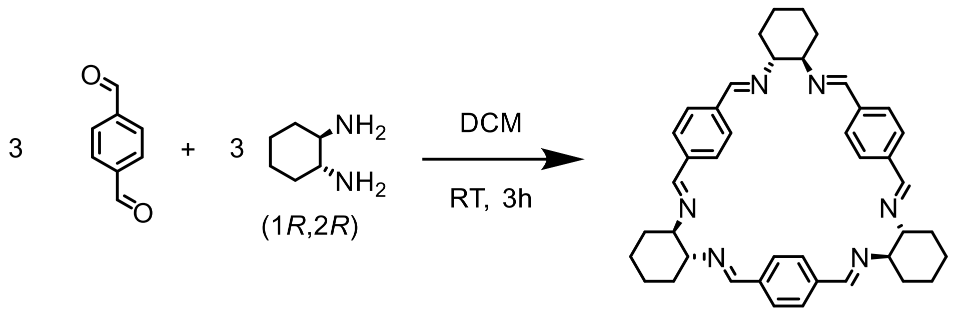

TAMC

TAMC was synthesised as described previously.[8] Terephthaldehyde (1.34 g, 10 mmol) in dichloromethane (8.3 mL) was added to a solution of (1*R*,2*R*)-diaminocyclohexane (1.14 g, 10 mmol) in dichloromethane (5 mL). The mixture was stirred at room temperature for 3 h. The solvent was evaporated under vacuum to afford the crude compound as a white powder. The crude product was recrystallised from ethyl acetate (EA) at 80 °C to afford needle-shaped crystals of product. Yield: 0.89 g (42.0%).

^{1}H NMR (400 MHz, $CDCl_3$) δ_H 8.14 (6H, s, N=CH), 7.52 (12H, s, Ar-H), 3.37 (6H, m, CH-N), 1.84 -1.45 (24H, m, cyclohexyl CH_2); ^{13}C NMR (101 MHz, $CDCl_3$) δ_C 160.23 (N=CH), 137.72 (ArC-), 128.01 (ArCH), 74.40 (CH-N), 32.72 (CH_2), 24.45 (CH_2); HRMS (ESI+): [$C_{42}H_{48}N_6$] calcd at: 636.3974 . Found $[M+H]^+$ at 637.4012. Elemental analysis calculated for $C_{42}H_{48}N_6$ (%): C 79.21 H 7.60 N 13.20, found at C 78.95 H 7.76 N 13.26. (See Figure 5.1 and 5.2 for NMR spectra and Figure 5.3 for MS). Elemental Analysis: C, 78.95; H 7.76; N 13.26 (C, 79.21; H 7.60; N 13.20 calculated for $C_{42}H_{48}N_6$). Data in accordance with literature values.[8, 9]

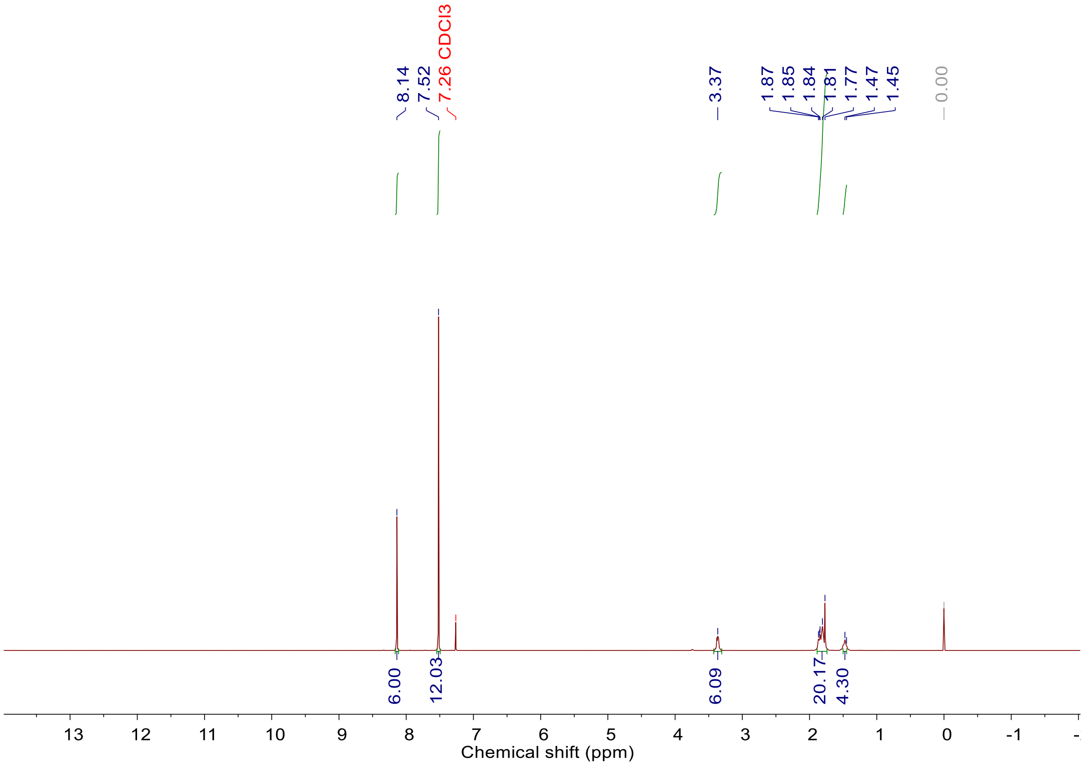

Figure 5.1. ^{1}H NMR spectrum (400 MHz, $CDCl_3$, 293 K) of **TAMC.**

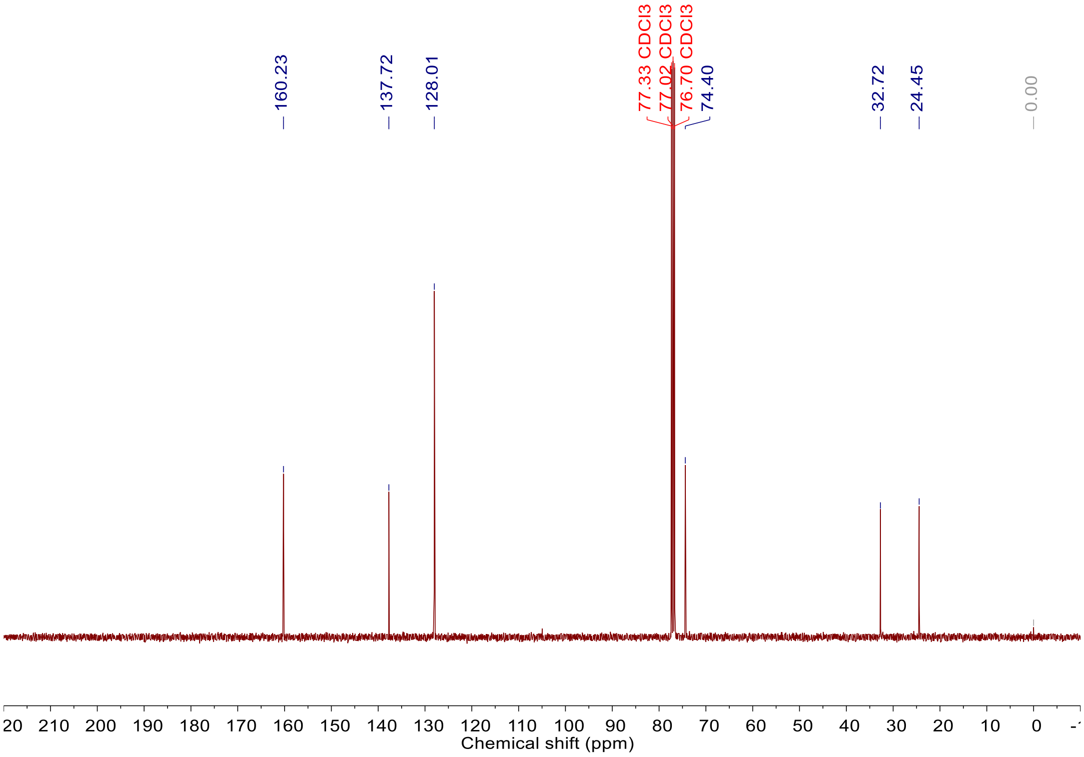

Figure 5.2. ^{13}C NMR spectrum (101 MHz, $CDCl_3$, 293 K) of **TAMC**.

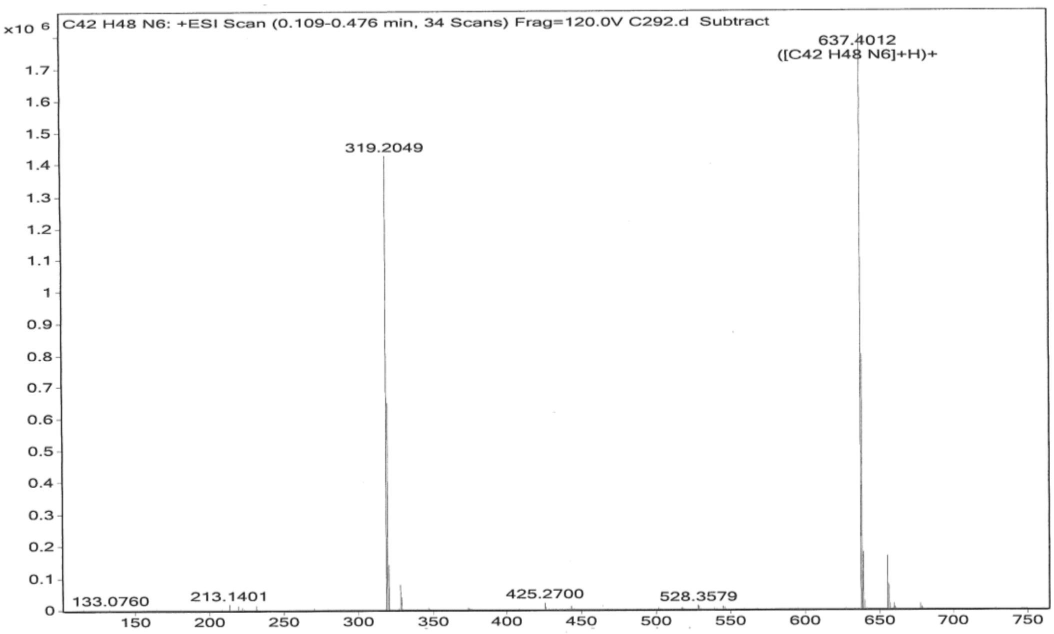

Figure 5.3 MS $[M+H]^+$ of **TAMC**.

5.3.2 Vapour phase isotherm adsorption (gravimetric apparatus)

Vapour sorption was measured using an IGA-002 gravimetric sorption analyser (*Hiden Isochema*, Warrington, UK) with a weight measurement resolution of 0.2 μg and long term stability of +/- 1 μg. Approximately 25 mg of **TAMC** was loaded in a gas permeable stainless steel mesh pan and degassed in situ at 343 K under high vacuum ($1x10^{-6}$ mbar) for a minimum of 4 hours until the sample mass was stable. Isotherms were measured from 0 to 0.9 P/P_0, with initial steps at 0.01 P/P_0 increments. The sample temperature was regulated using a water bath at 298 +/- 0.02 K throughout the isotherm measurements. The equilibration time for each isotherm point was determined automatically by the IGA-002 software, based on real-time analysis of the asymptotic sorption kinetic curve. The vapour pressure was held constant at each isotherm point with a typical regulation accuracy of +/- 0.02 mbar. Liquid solvents (ethyl acetate and ethanol) used to generate pure vapour were degassed fully in the IGA-002 by repeated evacuation and vapour expansion cycles prior to the measurements.

5.3.3 Breakthrough experiments

Breakthrough curves were measured for a fixed bed of *α*-**TAMC** at 298 K using an ABR automated breakthrough analyser (manufactured by *Hiden Isochema*, Warrington, U.K.). The α-**TAMC** powder activated at 70 °C was packed in a column made of stainless steel (20 mL) between two layers of quartz wool and two layers of spherical inert glass beads (d = 2–3 mm) to improve the distribution of the inlet fluid. The gases were introduced through the bottom inlet of the adsorption bed. Frit gaskets installed at both the top and bottom ends of the adsorption bed were used to further prevent any potential powder contamination of the pipelines. All gases used were high purity. The gas lines were purged with the correct gas mixture before each experiment.

The EA-EtOH vapour mixture was produced by adding liquid mixture with a ratio of 50:50 v/v into the vapour generator and letting them reach gas-liquid equilibrium at 273 K and one bar pressure. The carrier gas for the vapours was N_2. The flow rate of each gas was controlled by individual mass flow controllers. The system was controlled by the software *HIsorp* supplied by *Hiden Isochema*.

The m/z values used for detecting the gases were 28 for N_2 and 4 for He, the vapour were 31 for EtOH and 61 for EA. The reason for not using the base peak of EA is that m/z 43 overlapped signal of EtOH. It is known that the relative ratios of m/z 61 for EA is 14.9 % and the m/z 31 for EtOH is base peak with relative ratios of 100%. Therefore, the normalisation and smoothing process were used in analysing raw signal of EA and EtOH because the intensity of EtOH signal will be much higher than EA signal with the same concentration.

The samples are activated in situ by heating and flowing helium through the column. This involved heating **TAMC** to 343 K for 12 hours. The vapours of interest were desorbed from the column by flowing helium through at the same rate as the vapours in the corresponding breakthrough experiment. The effluents were measured by an in-line mass spectrometer (Hiden DSMS, integrated with the breakthrough analyser).

5.3.4 Vapour-phase adsorption measurements

5.3.4.1 Time-dependent TAMC solid−vapour sorption for EA/EtOH vapour based on NMR

For each single-component EA/EtOH (1/1, v/v) adsorption experiment, an open 5 mL vial containing 5.5 mg of guest-free **TAMC** adsorbent was placed in a sealed 20 mL vial containing 1 mL of EA or EtOH. Uptake in the **TAMC** crystals was measured by completely dissolving the crystals in $CDCl_3$ and measuring the ratio of EA or EtOH to **TAMC** (mol/mol) by ^{1}H NMR, respectively.

For each mixture vapour-phase experiment, an open 5 mL vial containing 5.5 mg of guest-free **TAMC** adsorbent was placed in a sealed 20 mL vial containing 0.5 mL of EA and EtOH, respectively. Uptake in the **TAMC** crystals was measured by completely dissolving the crystals in $CDCl_3$ and measuring the ratio of EA or EtOH to **TAMC** (mol/mol) by ^{1}H NMR, respectively.

5.3.4.2 Selective uptake from an EA-EtOH azeotropic vapour mixture in TAMC

For the azeotropic mixture vapour phase experiment, an atmospheric distillation apparatus was used to generate EA-EtOH azeotropic mixture vapour with 10 mL 30%/70% (w/w) EtOH-EA solvent. A cap of NMR tube containing 10 mg of guest-free **TAMC** adsorbent was placed below the arm of the distillation head by a long needle. Solvent uptake in the **TAMC** crystals was measured by completely dissolving the crystals in $CDCl_3$ and measuring the ratio of EA or EtOH to **TAMC** (mol/mol) by ^{1}H NMR, respectively.

5.3.5 Computational methods

5.3.5.1 Conformational search

Conformers were generated using the mixed torsional/low-mode searching method implemented in the Maestro [10] software with a maximum of 10000 steps allowed. Energies during the initial search were calculated using the OPLS2005 force field[11] For identification of duplicates, conformers with an RMSD of greater than 0.3 Å were retained and all unique conformers with an energy less than 50 kJ mol^{-1} above the lowest energy structure were kept. Each unique conformer was re-optimised using density functional theory (DFT) with the B3LYP[12, 13] functional and 6-311G** basis set with the D3 version of Grimme's dispersion correction with Becke-Johnson damping (GD3BJ)[14]; these calculations were performed using Gaussian09.[15] Redundant conformers after re-optimisation with an all-atom RMSD < 0.3 Å were eliminated.

Eight unique conformers were located over a final energy range of 44 kJ/mol (Figure 2.18d). The lowest energy conformer was separated from the rest by 18 kJ/mol, so this lowest energy conformer was used as a starting point for crystal structure prediction. The others were deemed to high in energy to be likely to produce low energy crystal structures.

5.3.5.2 CSP method

In the first stages of crystal structure prediction (CSP), molecules are held rigid. Crystal structures were generated starting with the lowest energy DFT-optimised conformer (Section 5.3.5.1) and, to examine the effect of molecular geometry, CSP for EA:**TAMC** was also performed using the molecular geometries taken from the experimental crystal structures. Trial crystal structures were generated with one formula unit (**TAMC** for CSP of the host, and 1 EA + 1 **TAMC** for the solvate) in the asymmetric unit in the most commonly observed Sohncke space groups for organic molecules. Calculations for 1:1 EA:**TAMC** were performed in 6 space groups (P1, $P2_12_12_1$, $P2_12_12$, $P2_1$, C2 and $P4_12_12$) and extended to 13 space groups (P1; $P3_1$; $P3_2$; $P6_1$; $P6_5$; $P2_12_12_1$; $P2_12_12$; $P2_1$; C2; $P4_1$; $P4_3$; $P4_12_12$; $P4_32_12$) for the gas phase molecular geometry. CSP for pure (unsolvated) **TAMC** were performed using the gas phase optimised molecular geometry in 13 space groups (P1; $P3_1$; $P3_2$; $P6_1$; $P6_5$; $P2_12_12_1$; $P2_12_12$; $P2_1$; C2; $P4_1$; $P4_3$; $P4_12_12$; $P4_32_12$).

CSP was performed using a quasi-random sampling procedure, as implemented in the Global Lattice Energy Explorer software.[16] The generation of structures involves a low-discrepancy sampling of all structural variables within each space group: unit cell lengths and angles; molecular positions and orientations within the asymmetric unit. Space group symmetry was then applied and a geometric test was performed for overlap between molecules, which was removed by lattice expansion. The lattice energy minimisation for each individual candidate crystal structure was performed using DMACRYS.[17] Intermolecular interactions were modelled using an empirically parametrised exp-6 repulsion-dispersion model and electrostatics described using atomic multipoles. The multipoles (up to hexadecapole on all atoms) were derived using GDMA[18] based on molecular charge densities obtained from B3LYP/6-311G** calculations on the single molecules, including multipoles up to hexadecapole on all atoms. Atom–atom repulsion and dispersion interactions were modelled using the

FIT[19] intermolecular potential. charge–charge, charge–dipole and dipole–dipole interactions were calculated using Ewald summation; all other intermolecular interactions were summed to a 25-Å cut-off between molecular centres-of-mass. All accepted trial structures were lattice energy minimised and the search was run until a set total number of lattice energy minimisations had been performed in each space group. For calculations performed with the gas phase optimised molecular geometry, 10,000 lattice energy minimisations were performed in each space group for pure **TAMC** and 20,000 lattice energy minimisations were performed per space group for 1:1 EA:**TAMC**. For EA:**TAMC** calculations using molecular geometries from the experimentally determined crystal structures, these numbers were halved (10,000 minimisations per space group).

5.3.5.3 Periodic DFT re-optimisation

Low energy crystal structures from CSP were re-optimised using solid state DFT to allow for relaxation of the molecular geometry in each predicted crystal structure. For pure **TAMC** crystal structures, we re-optimised all predicted crystal structures found within 20 kJ/mol of the global energy minimum from the rigid-molecule, force field predictions. For 1:1 EA:**TAMC**, we found that the position of EA within the crystal structures was very sensitive to the initial geometry of **TAMC**. Therefore, DFT re-optimisation was performed on the low energy CSP structures from both sets of predictions (using the gas phase optimised **TAMC** geometry and the **TAMC** geometry taken from the experimental EA:**TAMC** crystal structure).

Re-optimisation was performed in three steps. First, an optimisation was performed with the unit cell parameters held fixed at those from the force field CSP structure, allowing atom positions in the unit cell to vary. This was followed by optimisation including the unit cell parameters and a correction for the finite plane wave basis set. These first two steps used the PBE functional with pairwise TS dispersion correction,[20] ultrasoft pseudopotentials and a 500 eV plane wave cutoff on the basis set.

The final energies were calculated with a single point energy evaluation with the basis set increased to a 750 eV energy cutoff and the TS dispersion correction replaced by the many-body MBD@ rsSCS dispersion model.[21] A maximum k-point separation of 0.04 Å^{-1} was used in all calculations.

These calculations were performed using CASTEP version 17.21.[22]

5.3.5.4 Substructure search

For each predicted crystal structure, the corresponding position of **EA** and **TAMC** are identified using the CSD Python Application Programming Interface, together with in-house scripts. If the distance between the carbon atom on the methyl/ethyl and the centroid of **TAMC** are less than 2.0 Å, the methyl/ethyl end of **EA** is considered as inside the **TAMC** cavity. Note that, for efficiency, the centroid of six nitrogen atoms on the **TAMC** molecule is used to represent the centroid of the whole **TAMC** molecule.

5.3.5.5 Ideal adsorbed solution theory (IAST)

Mixture adsorption equilibria were predicted by ideal adsorbed solution theory (IAST)[23] using single-component adsorption data, measured experimentally. A detailed description of the approach used to obtain the results reported here can be found in the literature.[24] To apply IAST, single-component adsorption isotherms were specified by fitting an isotherm equation to the discrete, experimental adsorption measurements.

5.3.5.6 ESP and NCI analysis

The analysis of ESP and NCI are undertaken by the Multiwfn program,[25] employing the wave functions generated with B3LYP/6-311g(d,p) and visualised through the VMD package.[26] The NCI is based on single point calculate at the experiment geometry of EA@**TAMC**. The geometry of EA and EtOH for ESP analyse are optimised by Gaussian16.

5.3.5.7 Interaction energy calculation

Periodic DFT calculations were carried out with the Vienna ab initio Simulation Package (VASP) version 5.4.4.[27, 28] The projector augmented-wave (PAW) method was applied to describe the electron-ion interactions.[29] Generalised gradient approximation (GGA) with the Perdew–Burke–Ernzerhof (PBE) exchange-correlation functional was adopted to treat electron interaction energy.[30, 31] Grimme's semi-empirical DFT-D3[32] scheme was used here to give a better description of long range interactions; the latest Becke–Johnson damping functions[14, 33] for the DFT-D3 method were adopted. A kinetic-energy cutoff of 500 eV was used to define the plane-wave basis set. During geometry optimisations, the Hellmann–Feynman force convergence criterion on each atom was set to smaller than 0.01 eV/Å Convergence threshold of self-consistency was set to 10^{-5} eV in total energy. Gamma-centered K-point meshes were calculated by VASP for each structure using a gamma-centered k-spacing of 0.2 $Å^{-1}$. The geometry of all structures used here are after optimised. The interaction energy are evaluated via the fllowing equation:

$$E_{int} = (E_{X@\mathbf{TAMC}} - E_{alpha\text{-}\mathbf{TAMC}} - 2*E_X)/2 \qquad (1)$$

Where X represent the EA or EtOH.

5.4. Chapter 3 experimental methods and characterisation data

5.4.1 Synthesis of 1-*R*

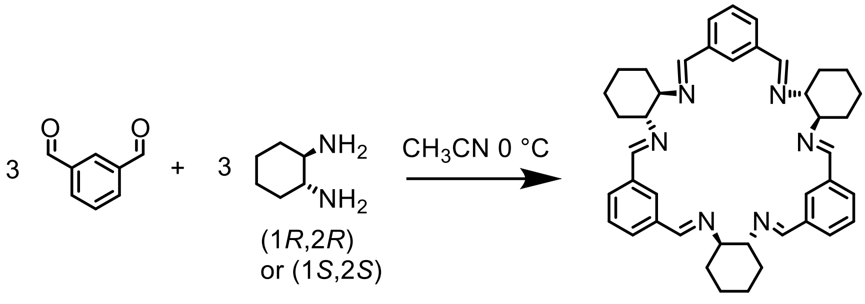

1-*R*
or **1**-*S*

1-*R*: (1*R*,2*R*)-1,2-diaminocyclohexane or (1*S*,2*S*)-1,2-diaminocyclohexane (1.243 g, 10.89 mmol) was dissolved in acetonitrile (18 mL) and cooled to 0 °C. Isophthalaldehyde (1.460 g, 10.89 mmol) and a catalytic amount of trifluoroacetic acid (1 drop) were dissolved in acetonitrile (30 mL) and then added to the reaction. A white precipitate formed during the addition, and after being stirred at 0 °C for 30 minutes, the white precipitate was removed by filtration and washed three times with acetonitrile. Needle-shaped crystals of the pure product were isolated by recrystallizing the crude product three times from ethyl acetate (EA) at 80 °C. Yield: 1.30 g (56.3%)

^{1}H NMR (400 MHz, CD_2Cl_2) δ_H 8.15 (6H, s,N=CH), 7.89 (3H, s, ArH),7.56 (6H, broad s, Ar-H), 7.24(3H, t, ArH), 3.33-3.40 (6H, m, CH-N), 1.46-1.85 (24H, m, cyclohexyl CH_2); ^{13}C NMR (101 MHz, CD_2Cl_2) δ_C 159.66 (N=CH), 137.02 (ArC-), 128.79 (ArCH), 127.92 (ArCH), 75.01 (CH-N), 33.47 (CH_2), 24.87 (CH_2); HRMS (ESI+): [$C_{42}H_{48}N_6$] calcd at: 636.3974. Found $[M+H]^+$ at 637.4021. Elemental analysis calculated for $C_{42}H_{48}N_6$ (%): C 79.21 H 7.60 N 13.20, found at C 78.71 H 7.70 N 13.23. (See Figure 5.4 and 5.5 for NMR spectra and 5.6 for MS). Elemental Analysis: C, 78.71; H 7.70; N 13.23 (C, 79.21; H 7.60; N 13.20 calculated for $C_{42}H_{48}N_6$). Data in accordance with literature values.[9]

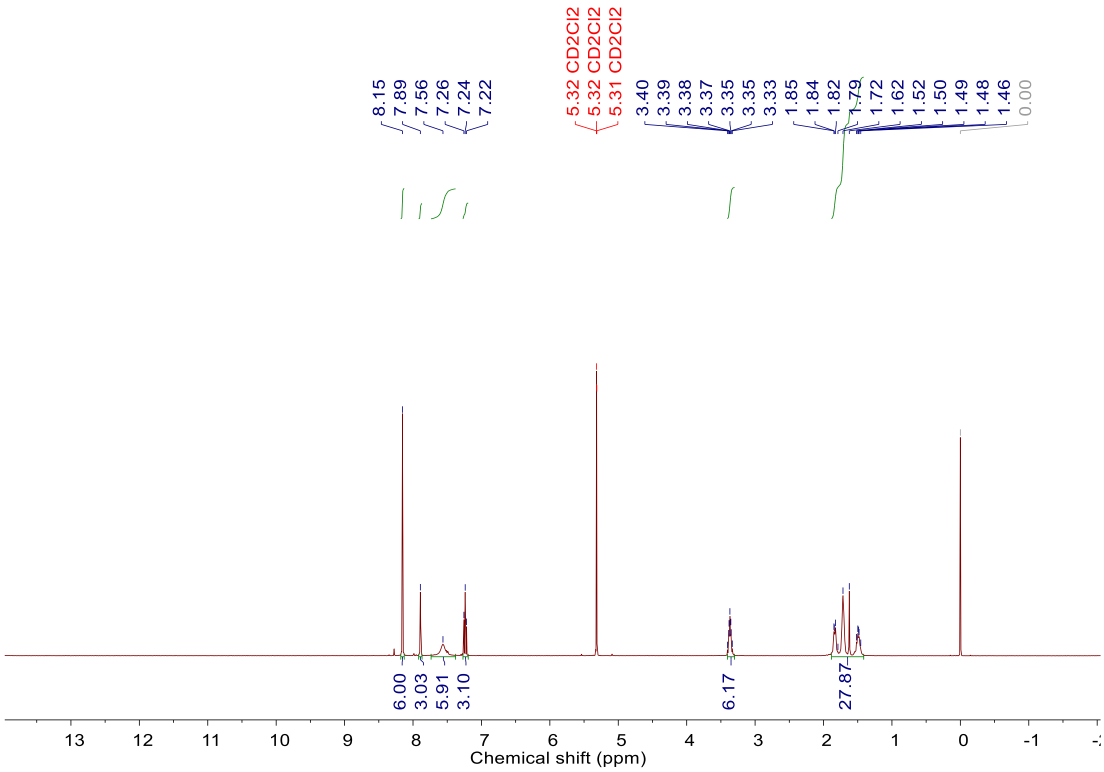

Figure 5.4. ^{1}H NMR spectrum (400 MHz, CD_2Cl_2, 293 K) of **1**-*R*.

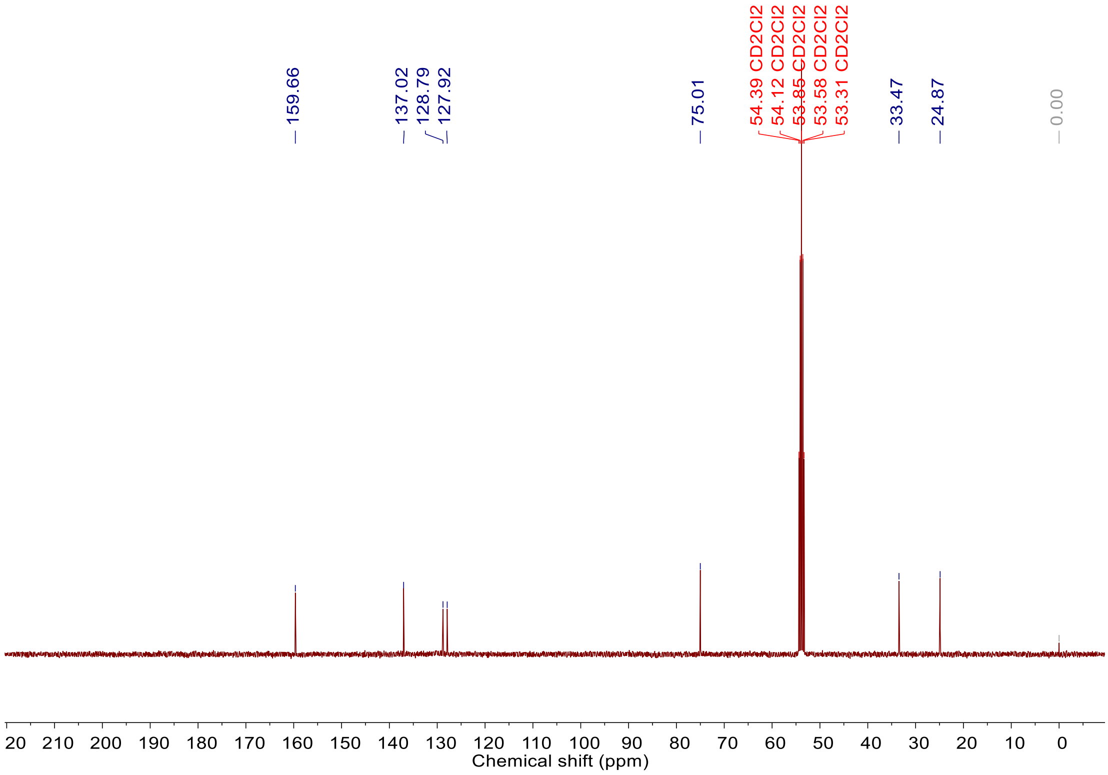

Figure 5.5. ^{13}C NMR spectrum (101 MHz, CD_2Cl_2, 293 K) of **1**-*R*.

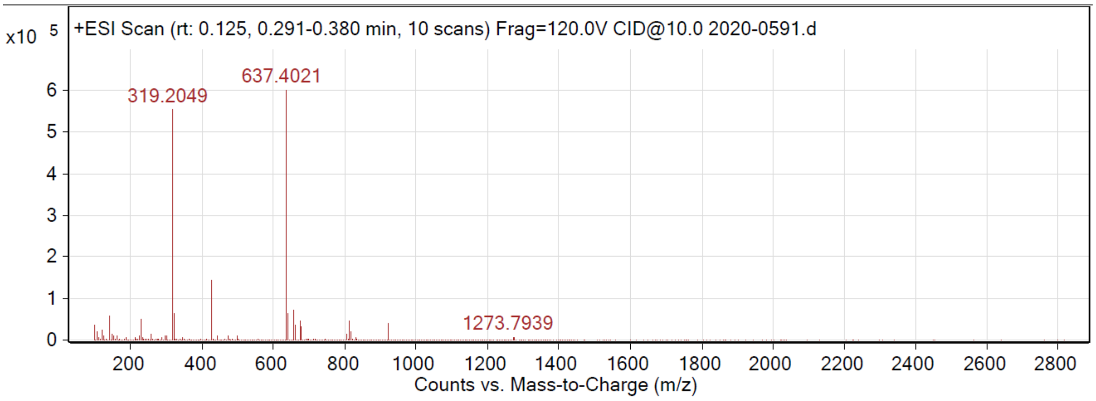

Figure 5.6. MS $[M+H]^+$ of **1**-*R*.

5.4.2 Cocrystallisation of 1-*R* and 1-*S*

1-*rac*: equivalent molar amounts of **1**-*R* (50 mg, 0.079 mmol) and **1**-*S* (50 mg, 0.079 mmol) were dissolved in EA (50 mL) at 80 °C. The EA solution was then cooled down to room temperature and left to stand. Colourless block-shaped crystals of racemic **1**-*rac* were obtained after 1–2 days. To generate the activated crystals of **1**-*rac*, the colourless block-shaped crystals were removed by filtration from EA. The crystals rapidly lost EA solvent in the air to afford a polycrystalline white powder, which was then activated after heating at 80 °C under vacuum for 12 h. The single crystal of guest-free, **1**-*rac*, was obtained using this procedure.

5.4.3 Single crystal growth

Table 5.1. Methods of obtaining **1**-*R* and **1**-*rac* structures.

Crystal structures	Methods		
	Solution growth	Vapour diffusion	Desolvation
MeOH@**1**-*R*[a]	MeOH	n. r.	n. r.
1-*rac*[b]	EA	n. r.	Removal of EA at 80 °C
1*p*X@**1**-*rac*[c]	*p*X solution	*p*X or *p*X – *m*X mixture	n. r.
2*m*X@**1**-*rac*[d]	*m*X solution	n. r.	n. r.
3*o*X@**1**-*rac*[e]	*o*X solution	*o*X vapour	n. r.

[a] 5 mg dry **1**-*R* was dissolved in 2 mL of MeOH and then transferred into small glass sample vials by filtration. The resultant homogenous solution was allowed to slowly evaporate at room temperature over 3 to 5 days to afford colourless crystals.

[b] Experimental details are included in Section 5.4.2.

[c]-[e] 5 mg dry **1**-*rac* was dissolved in 2 mL of *p*X, *m*X, *o*X and then transferred into small glass sample vials by filtration. The resultant homogenous solutions were then allowed to slowly evaporate at room temperature over 5 to 12 days to afford colourless crystals.

5.4.4 Isosteric heat of adsorption

The isosteric heat (*Qst*) for CO_2 adsorption with **1**-*rac and* **1**-*R* were calculated using their CO_2 isotherms measured at 273, 283, and 298 K and the Clausius-Clapyron equation:

$\ln(P)/m = Qst / R * 1/T$

where *P* is the pressure described in bar, *m* (mmol/g) is constant quantity adsorbed, *Qst* (kJ/mol) is the isosteric heat, R [J/(mol·K)] is the gas the constant and *T* (K) is the adsorption temperature. A plot of the ln(*P*) versus 1/*T* at constant quantity adsorbed can provide a linear relationship. The slope of that line is *Qst* /R, then the *Qst* can be calculated.[34]

5.4.5 Selective uptake from a xylene isomers vapour mixture in 1-*rac*

For each mixture vapour-phase experiment, an open 5 mL vial containing 3.5 mg of **1**-*rac* that was activated at 80 °C was placed in a sealed 20 mL vial containing 1 mL of *p*X:*m*X (1:1 *vol*:*vol*) or *p*X:*m*X:*o*X (1:1:1 *vol*:*vol*:*vol*). The relative uptake of guests adsorbed by the **1**-*rac* crystals was measured by completely dissolving the crystals in CD_2Cl_2 and measuring the ratio of xylene isomers to **1**-*rac* by ^1H NMR spectroscopy.

5.5 Chapter 4 experimental method and data

5.5.1 The derived salicylaldehyde

2,6-Diformyl-4-*tert*-butylphenol as a precursor for **M1** was purchased from Sigma-Aldrich.

2,5-Dihydroxy-1,4-benzenedicarboxaldehyde as a precursor for **M2** and 3,3'-Dihydroxy[1,1'-biphenyl]-4,4'-dicarboxaldehyde as a precursor for **M3** were purchased from Shanghai Sunway Corporation Ltd.

5.5.2 Synthesis of M1

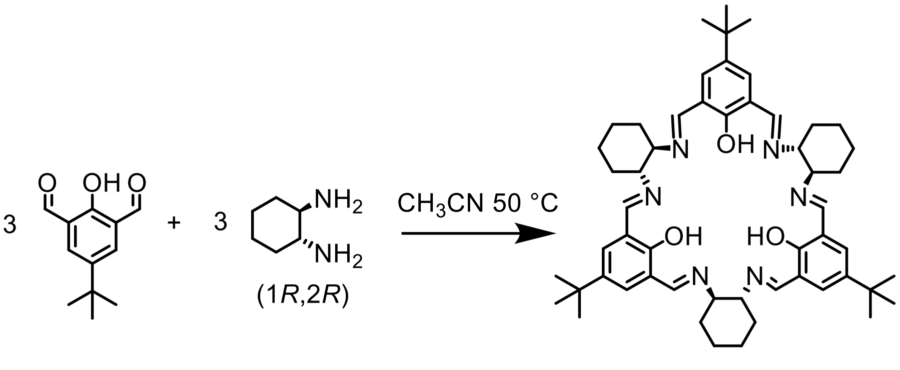

M1

M1 was synthesised as described previously.[35] A solution of 4–tert–butyl–2,6–diformylphenol 2.062 g (10 mmol) in 20 mL of acetonitrile was added to the stirred solution of 1.142 g (10 mmol) (1*R*, 2*R*)–diaminocyclohexane in 15 mL of acetonitrile. The resulted yellow suspensions was stirred at 50 °C for 16 h, filtered out, washed with acetonitrile three times and dried to give 2.451 g of light yellow product (86%).

^{1}H NMR (400 MHz, $CDCl_3$) δ_H 13.92 (3H, s, O*H*), 8.68 (3H, s, N=C*H*), 8.25 (3H, s, N=C*H*), 7.82 (3H, s, Ar*H*), 7.08 (3H, s, Ar*H*), 3.29-3.46 (6H, m, C*H*-N), 1.46-1.87 (24H, m, cyclohexyl C*H*$_2$), 1.15 (27H, s, C*H*$_3$). ^{13}C NMR (400 MHz, $CDCl_3$) δ_C 163.88 (N=CH), 159.39 (ArC-O), 156.15 (ArC-O), 140.16 (ArC-*t-Bu*), 130.52 (ArCH), 126.11 (ArCH), 122.89 (ArC-), 118.52 (ArC-), 75.58 (CH-N), 73.10 (CH-N), 33.89 (C-*t-Bu*), 33.59 (CH_3), 33.24 (CH_3), 31.30 (CH_3), 24.49 (CH_2), 24.39 (CH_2). HRMS: [$C_{54}H_{72}N_6O_3$] calcd at: 852.5666. Found $[M+H]^+$ at 853.5739. (See Figure 5.7 and 5.8 for NMR spectra and 5.9 for MS). Elemental Analysis: C, 74.24; H 8.58; N 9.77 (C, 76.02; H 8.51; N 9.85 calculated for $C_{54}H_{72}N_6O_3$). Data in accordance with literature values.[36]

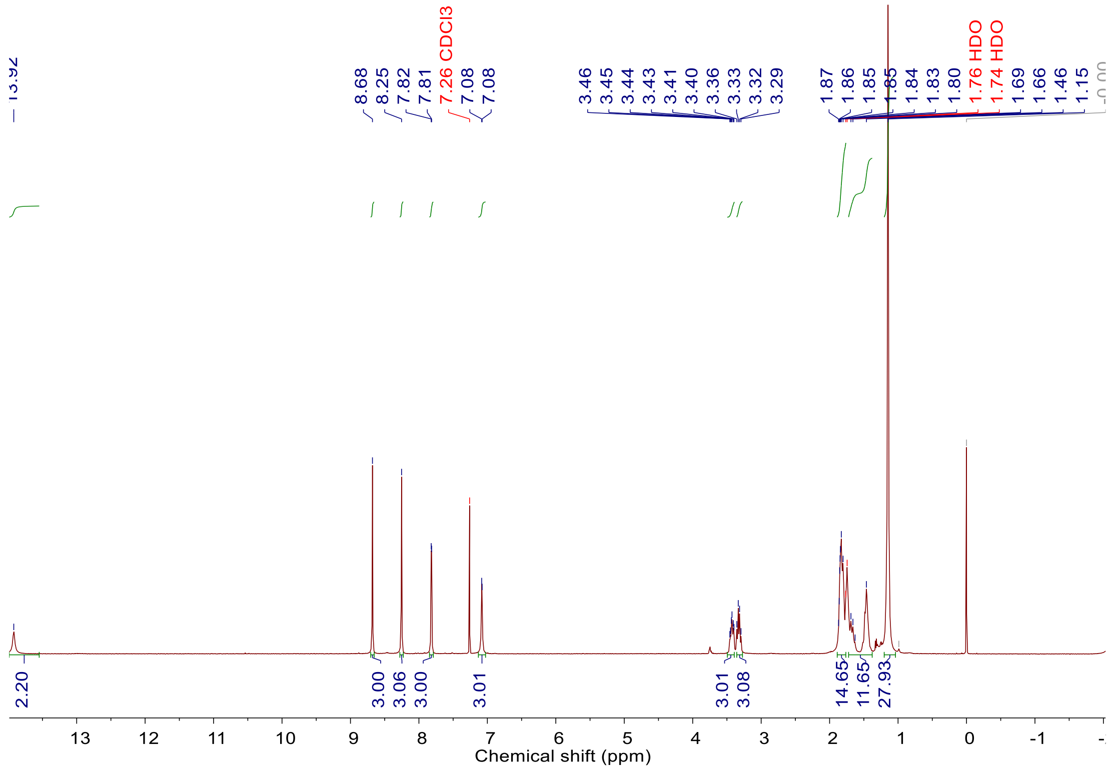

Figure 5.7. ^{1}H NMR spectrum (400 MHz, CDCl$_3$, 293 K) of **M1**.

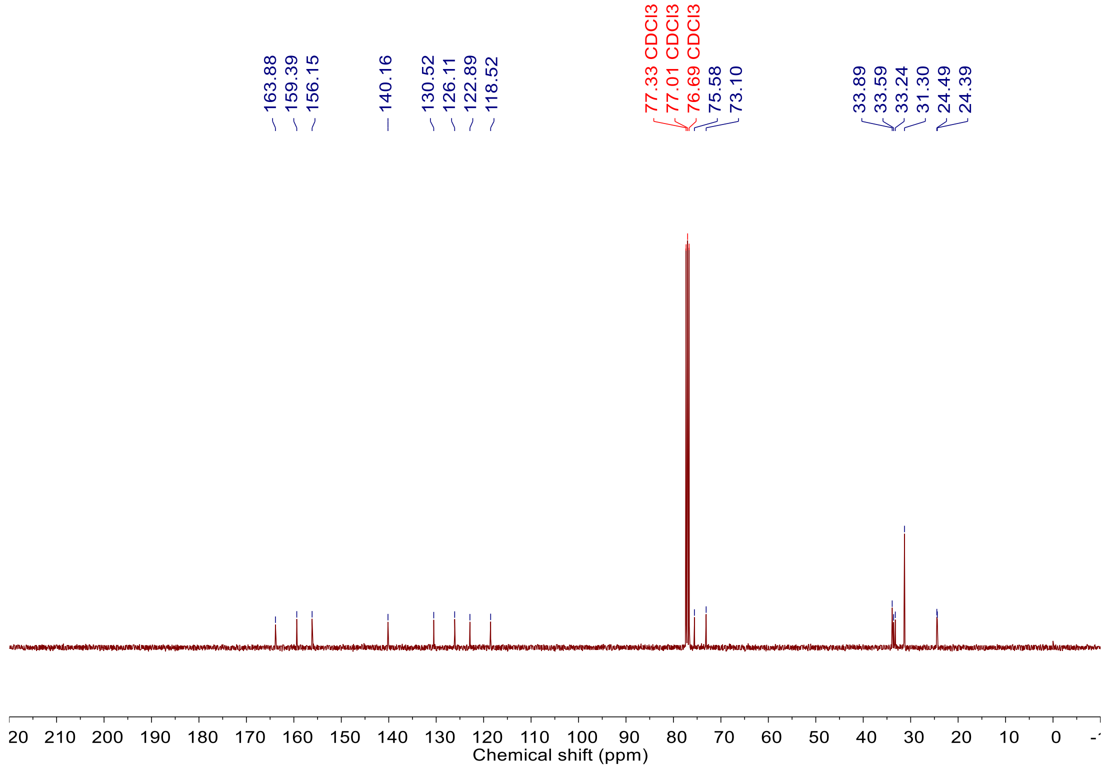

Figure 5.8. ^{13}C NMR spectrum (101 MHz, CDCl$_3$, 293 K) of **M1**.

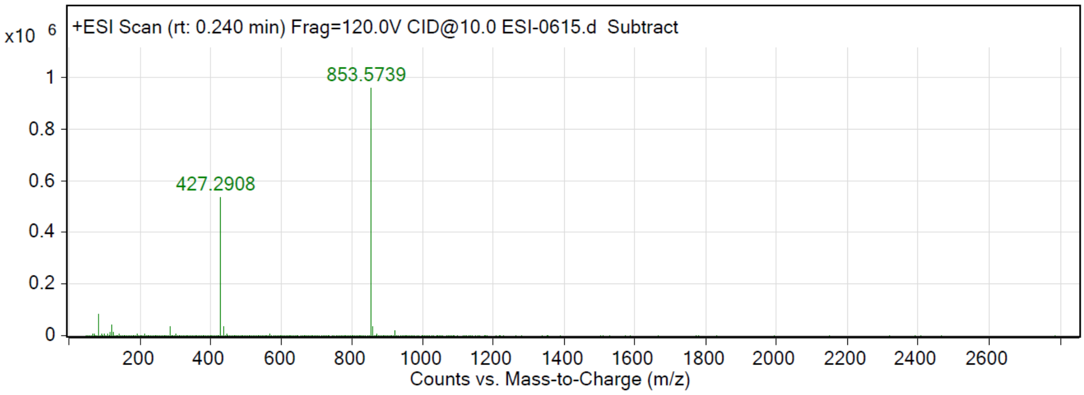

Figure 5.9. MS $[M+H]^+$ of **M1**.

5.5.3 Synthesis of M2

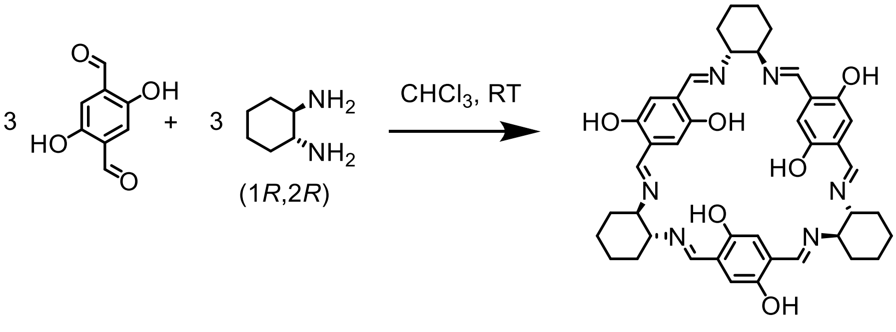

M2

M2 was synthesised as described previously with the slight adjustment.[37] The solution of trans-(1*R*,2*R*)-diaminocyclohexane (560 mg, 5 mmol) in 100 ml was added into 150 ml solution of 2,5- dihydroxyterephthalaldehyde (815 mg, 5 mmol) in $CHCl_3$. The mixture solution was stirred under nitrogen atmosphere at room temperature for 7 days. After that time, to the mixture was added ethanol (100 mL). The product crystallised as yellow-orange solid with almost quantitatively yield.

^1H NMR (400 MHz, $CDCl_3$) δ_H 12.26 (6H, s, O*H*), 8.16 (6H, s, N=C*H*), 6.68 (6H, s, Ar*H*), 3.31 - 3.28 (6H, m, C*H*-N), 1.71 - 1.43 (24H, m, cyclohexyl C*H*$_2$). ^{13}C NMR (101 MHz, $CDCl_3$) δ = 163.92 (N=CH), 152.50, 121.01, 118.38, 73.83, 32.97, 24.19. HRMS: [$C_{42}H_{48}N_6O_6$] calcd at 732.3635, $[M+H]^+$, m/z found 733.3718. Elemental Analysis: C, 67.86; H 6.60; N 11.40 (C, 68.83; H 6.60; N 11.47 calculated for $C_{42}H_{48}N_6O_6$). IR (V_{max}/ cm^{-1}): 770.58, 785.85, 800.15, 854.13, 1038.99, 1093.06, 1155.29, 1215.06, 1309.79, 1346.58, 1448.06, 1505.05, 1621.68, 2858.13, 2923.82. (See Figure 5.10 and 5.11 for NMR spectra, Figure 5.12 for MS and Figure 5.26 for FT-IR spectra) Data in accordance with literature values.[37]

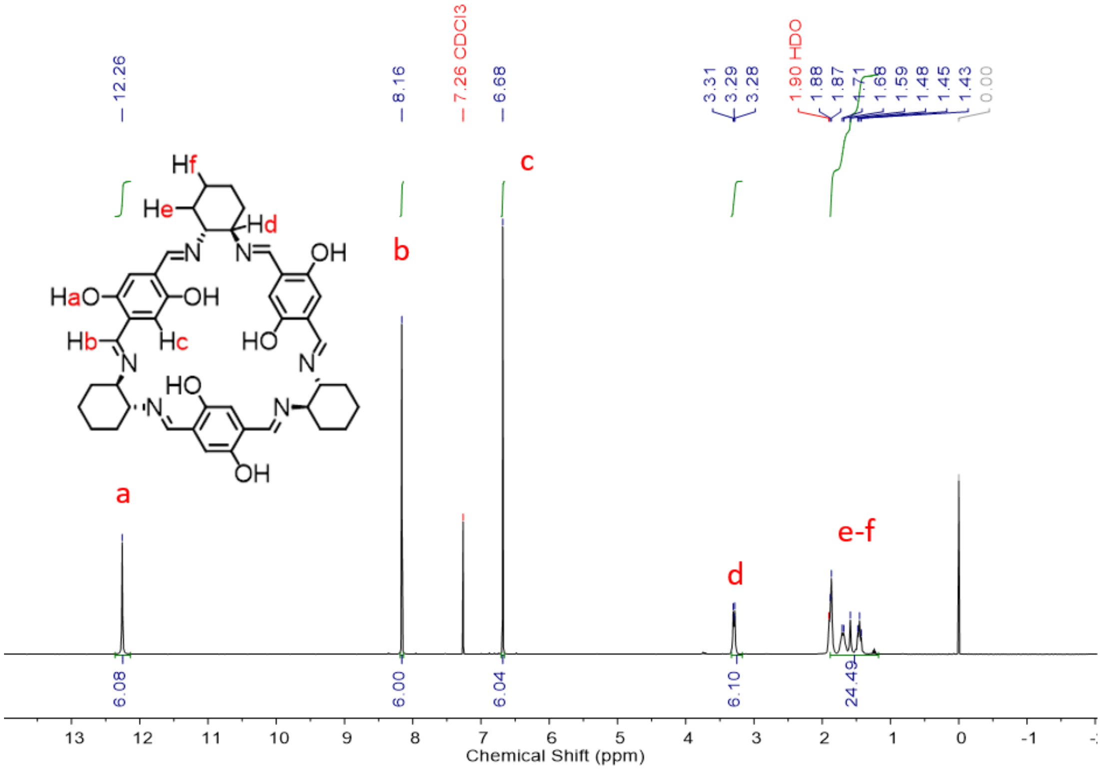

Figure 5.10. ^{1}H NMR spectrum (400 MHz, $CDCl_3$, 293 K) of **M2**.

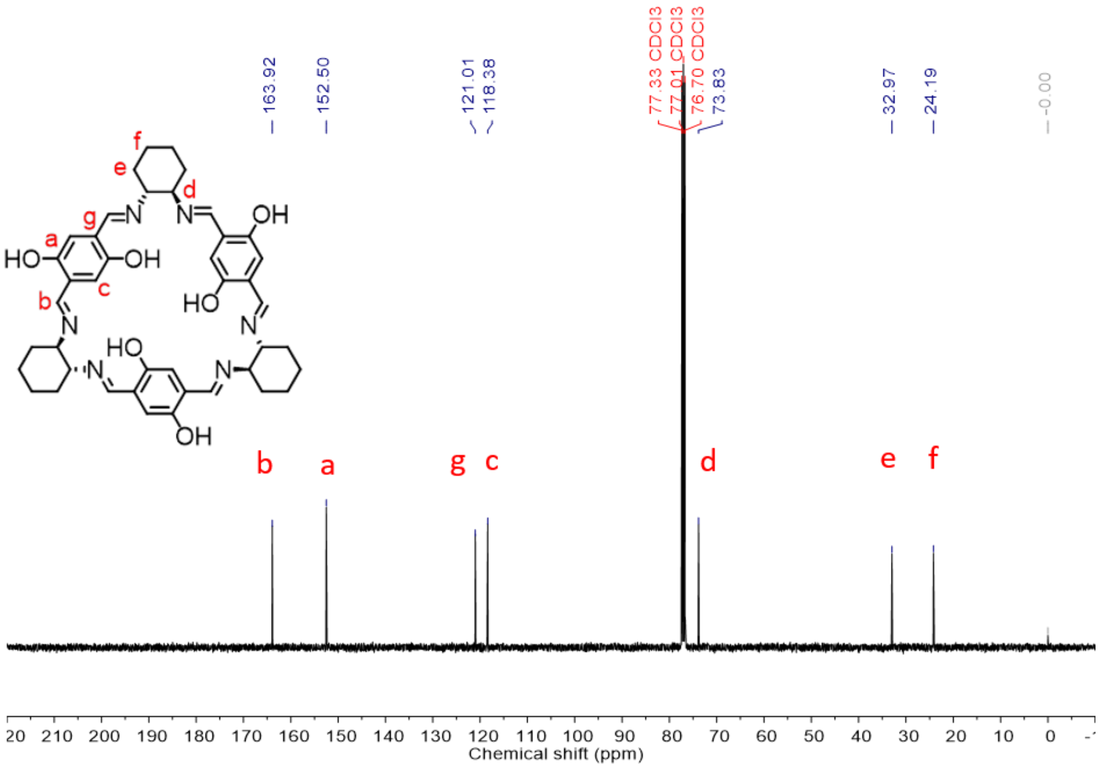

Figure 5.11. ^{13}C NMR spectrum (101 MHz, $CDCl_3$, 293 K) of **M2**.

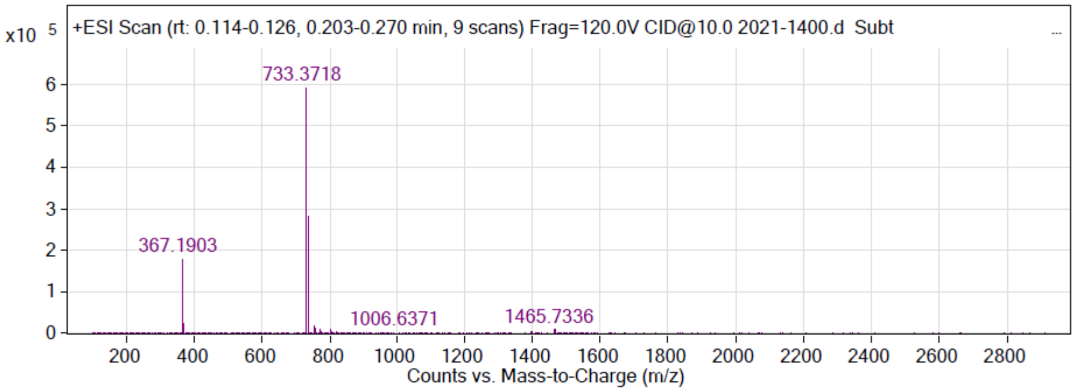

Figure 5.12. MS $[M+H]^+$ of **M2**.

5.5.4 Synthesis of M3

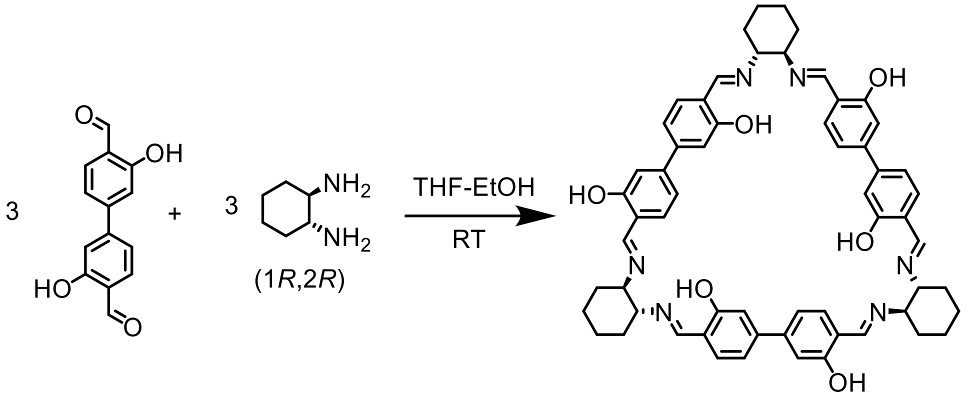

M3

3,3'-Dihydroxy[1,1'-biphenyl]-4,4'-dicarboxaldehyde (121 mg 0.5 mmol) was dissolved in tetrahydrofuran (25 mL). Then, 25 mL (1*R*,2*R*)-1,2-diaminocyclohexane (57 mg, 0.5 mmol) dissolved in ethanol added to the reaction slowly. The mixture was stirred at room temperature for 12 h, then the solvent was evaporated at room temperature. The yellow solid product was obtained by filtering and washing with ethanol. Yield: 107.6 mg (67.3%).

^{1}H NMR (400 MHz, $CDCl_3$) δ_H 13.27 (6H, , s, O*H*), 8.22 (6H, s, N=C*H*), 7.14 (6H, d, *J* = 8 Hz, N=C*H*), 7.06 (6H, s, Ar*H*), 6.96 (6H, dd, *J*= 4 Hz, *J*= 8, Ar*H*), 3.27-3.49 (6H, m, C*H*-N), 1.48-1.77 (24H, m, cyclohexyl C*H*$_2$). ^{13}C NMR (400 MHz, $CDCl_3$) δ_C 164.44 (N=CH), 160.96 (ArC-O), 143.69 (ArC-Ar), 131.78 (ArCH), 117.92 (ArC-), 117.65 (ArCH), 114.95 (ArCH), 73.06 (CH-N), 32.82 (CH_2), 24.29 (CH_2). HRMS: [$C_{60}H_{60}N_6O_6$] calcd at: 960.4574. Found $[M+H]^+$ at 961.4654. Elemental Analysis: C, 73.64; H 6.29; N 8.62 (C, 74.98; H 6.29; N 8.74 calculated for $C_{60}H_{60}N_6O_6$). IR (V_{max}/ cm^{-1}): 794.85, 883.81, 1146.11, 1202.85, 1250.99, 1357.79, 1550.13, 1619.75, 2855.22, 2926.02. (See Figure 5.13 - 15 for NMR spectra, Figure 5.17 for MS and Figure 5.29 for FT-IR spectra)

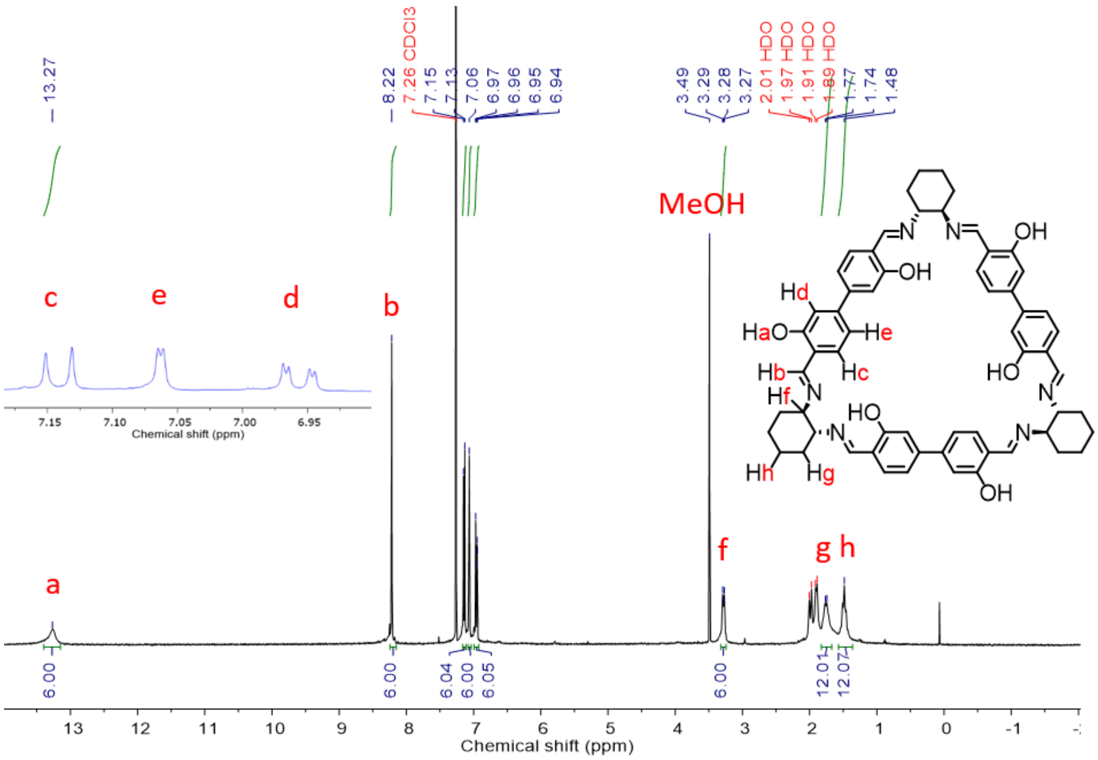

Figure 5.13. ^{1}H NMR spectrum (400 MHz, $CDCl_3$, 293 K) of **M3**.

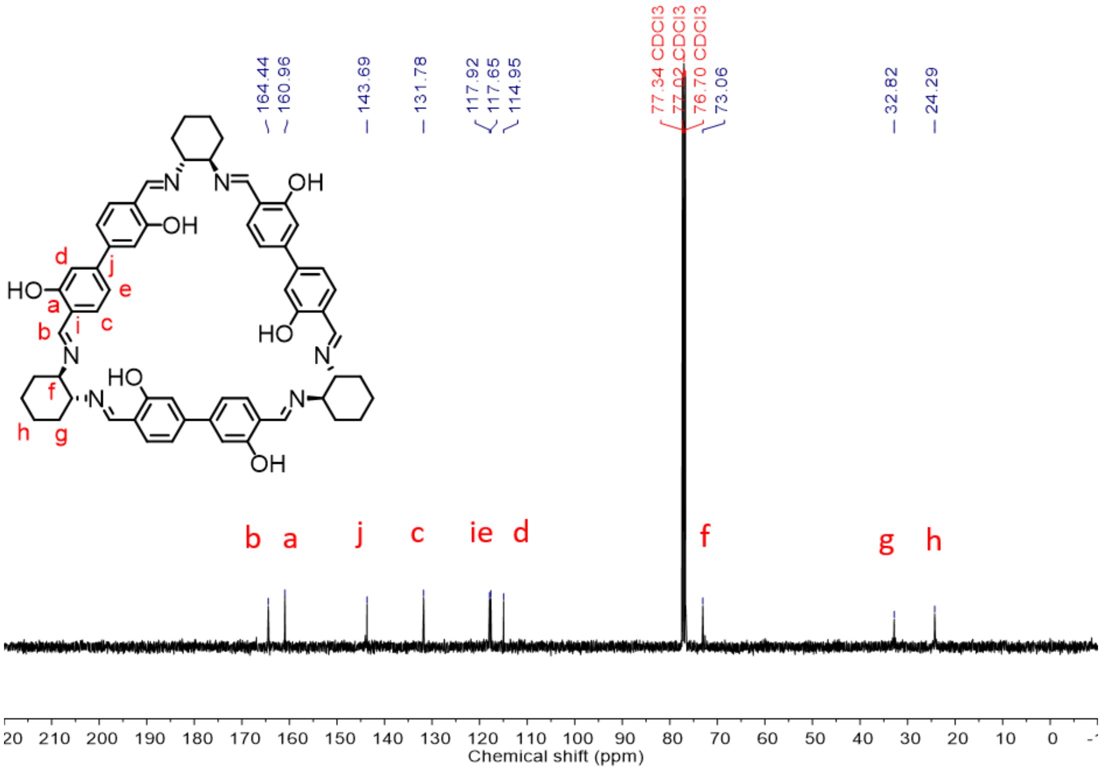

Figure 5.14. ^{13}C NMR spectrum (101 MHz, $CDCl_3$, 293 K) of **M3**.

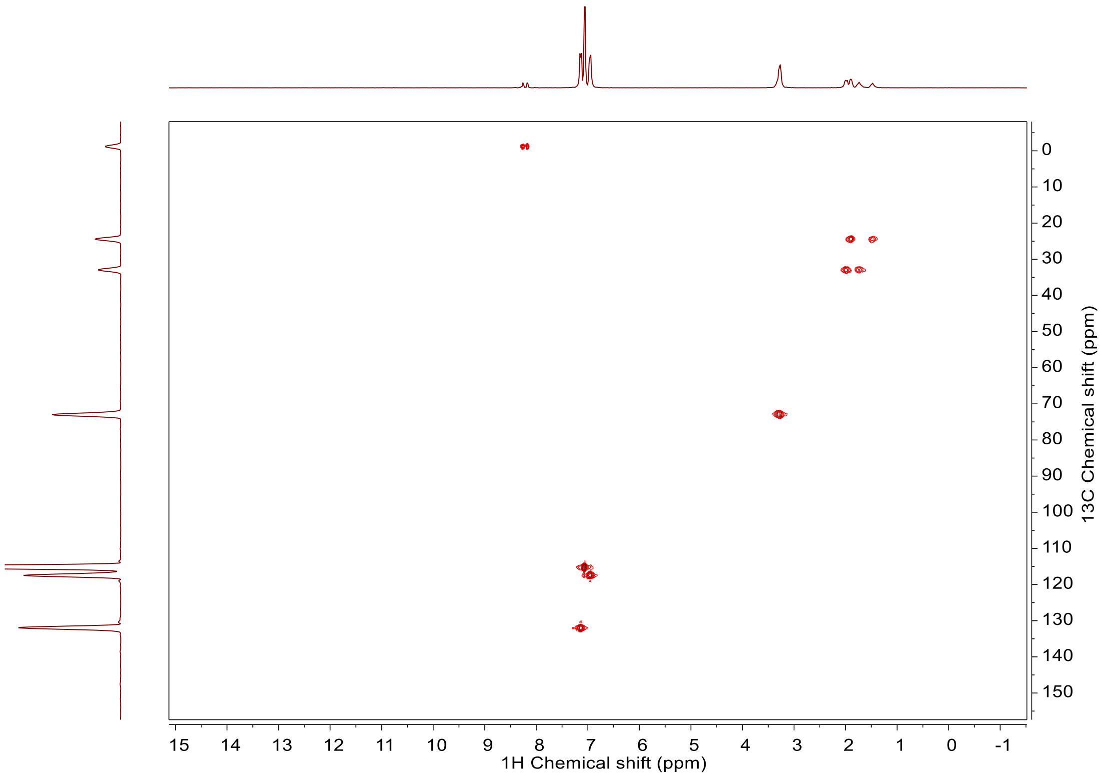

Figure 5.15. HSQC ($CDCl_3$) spectrum of **M3**.

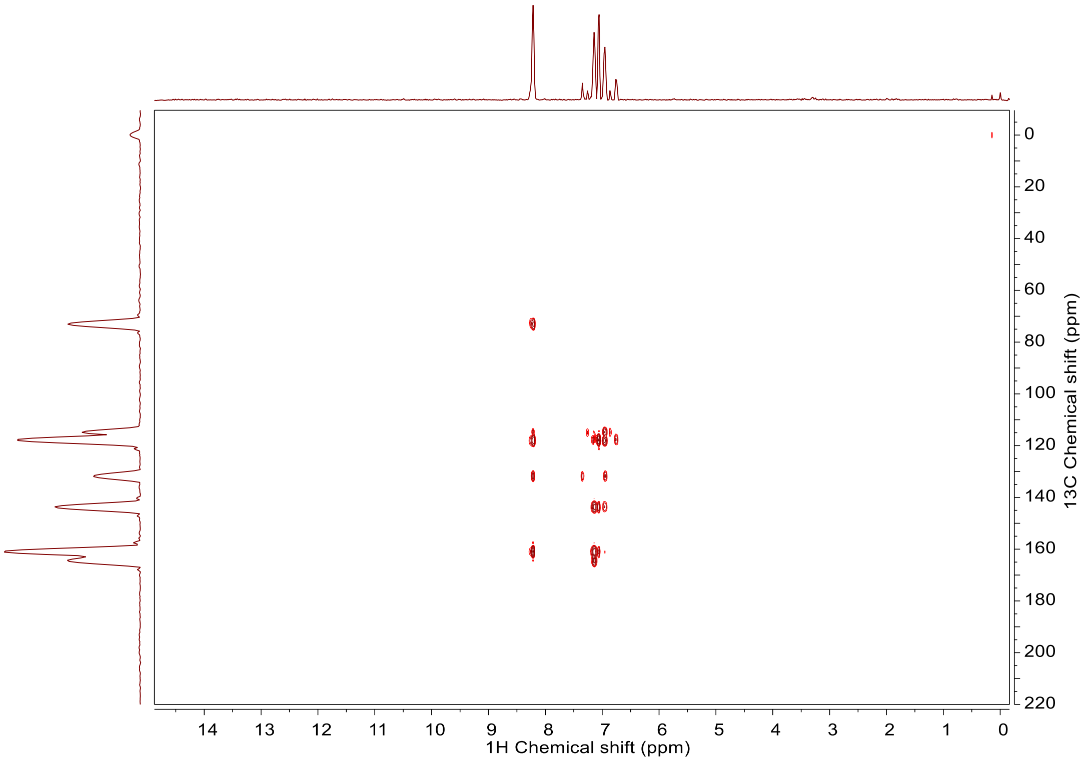

Figure 5.16. HMBC ($CDCl_3$) spectrum of macrocycle **M3**.

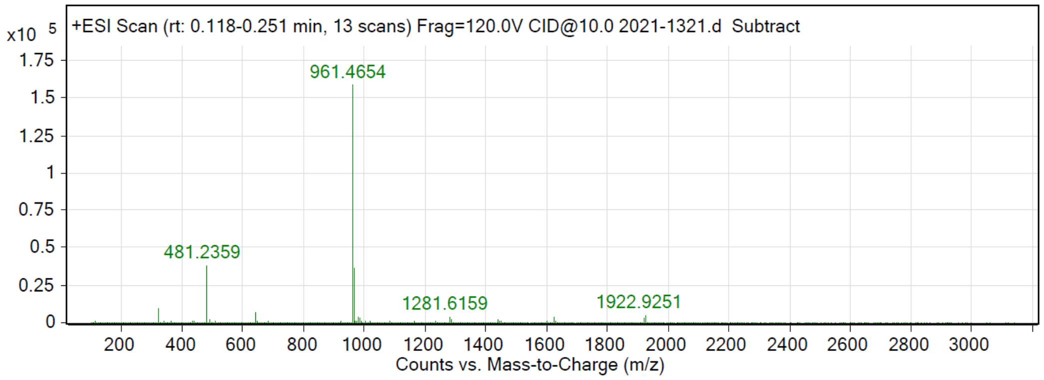

Figure 5.17. MS $[M+H]^+$ of macrocycle **M3**.

5.5.5 Synthesis of MOC-1

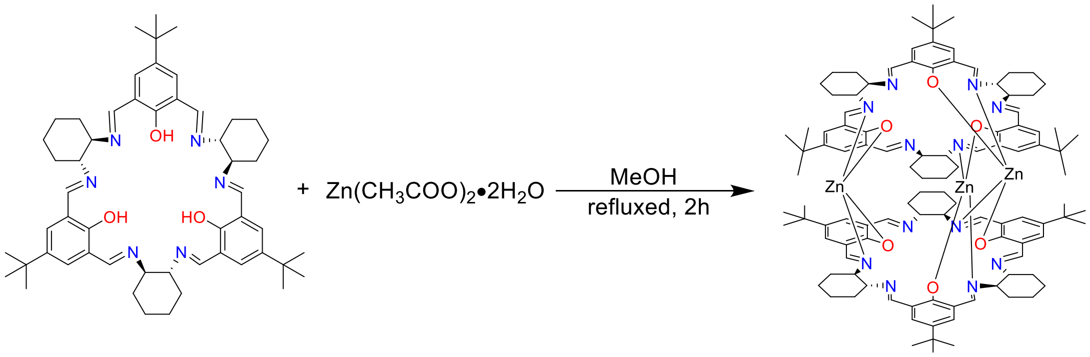

M1 **MOC-1**

MOC-1 was synthesised as described previously.[35]. A solution of 0.199 g (9 mmol) $Zn(CH3COO)_2\cdot 2H_2O$ dissolved in 30 mL of methanol was added to the stirred suspension of the 3+3 macrocycle **M1** (0.516 g, 6 mmol) in 70 mL of methanol. The mixture was refluxed for 2 h, cooled down and left to stand at room temperature overnight to give 0.315 g (55%) of yellow product.

^{1}H NMR (400 MHz, $CDCl_3$) δ_H 9.49 (6H, s,N=C*H*), 8.06 (6H, s,N=C*H*), 7.87 (6H, d, *J* = 4 Hz, Ar*H*), 6.99 (6H, d, *J* = 4 Hz, Ar*H*), 3.77 (6H, m, C*H*-N), 3.34 (6H, m, C*H*-N),1.24-1.89 (42H, m, cyclohexyl C*H*$_2$), 1.21 (54H, s, C*H*$_3$), 0.88 (6H, m, C*H*$_2$); δ_C 171.06, 168.02, 163.02, 135.46, 135.26, 129.06, 127.12, 118.00, 75.87, 71.97, 33.62, 33.46, 31.46, 24.60, 24.41; HRMS: $[C_{108}H_{138}N_{12}O_6Zn_3]$ calcd at 1893.8739. Found $[M+H]^+$ at 1895.8818. (See Figure 5.18 and 5.19 for NMR spectra and Figure 5.20 for MS). Data in accordance with literature values.[35]

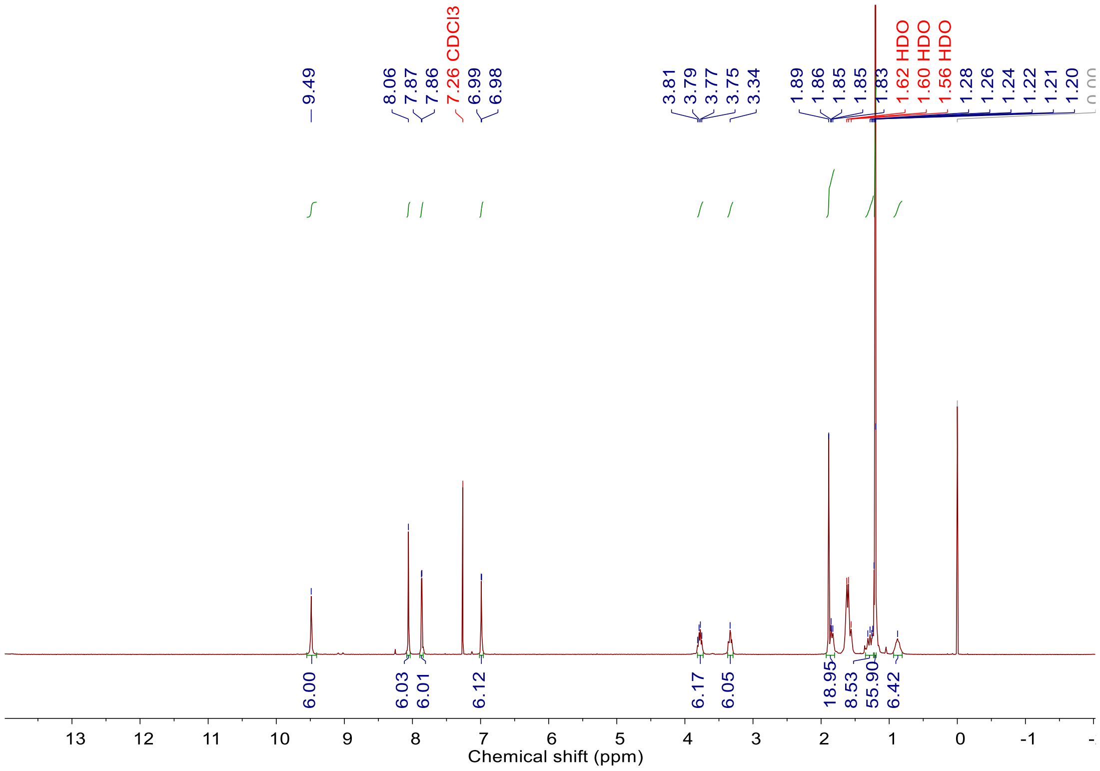

Figure 5.18. ^{1}H NMR spectrum (400 MHz, $CDCl_3$, 293 K) of **MOC-1**.

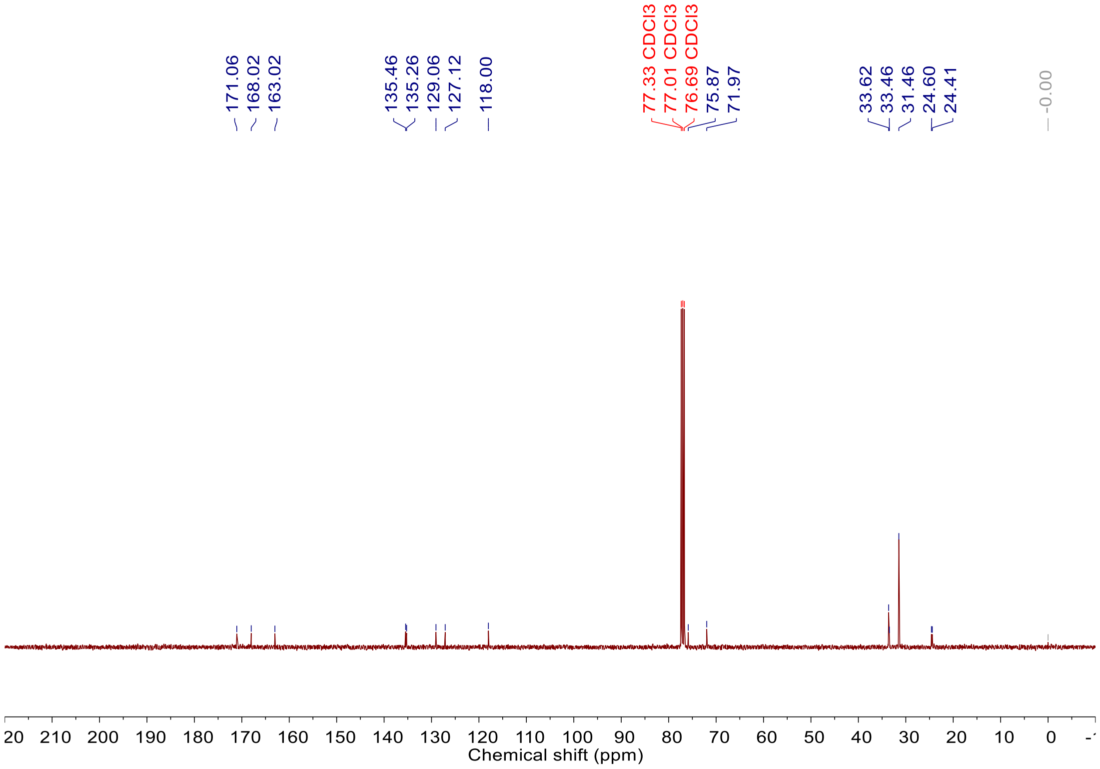

Figure 5.19. ^{13}C NMR spectrum (101 MHz, $CDCl_3$, 293 K) of **MOC-1**.

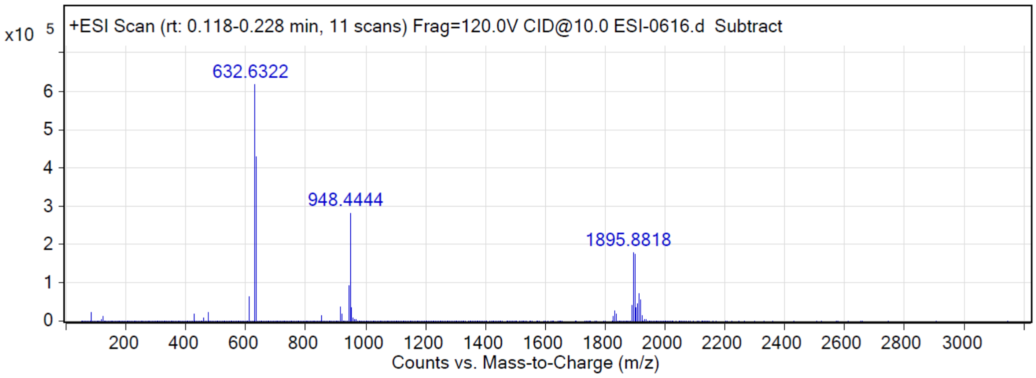

Figure 5.20. MS $[M+H]^+$ of macrocycle **MOC-1**.

5.5.6 Synthesis of MOP-2

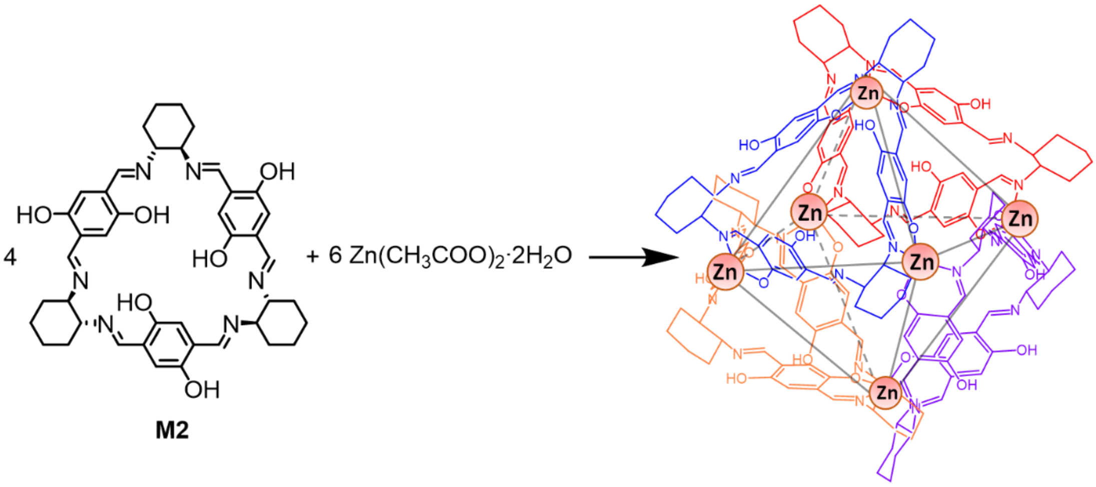

MOP-2: A solution of 66 mg (0.30 mmol) $Zn(CH_3COO)_2·2H_2O$ dissolved in 15 mL of DEF was added to the stirred solution of the 3+3 macrocycle **M2** (146 mg, 0.20 mmol) in 15 mL of DEF. Then the mixed solution was put into small vials. The vial was loaded into a larger vial that contains CH_3CN. After 7 days, orange crystal had formed in the small glass vial and the residual solvent was removed via syringe. CH_3CN was added to fully immerse the crystals and the CH_3CN solvent was exchanged every 24 hours for 5 days. After that, the desolvated **MOP-2** (105 mg, 64.2 %) was obtained by filtering and drying at 100 °C in vacuum for 12 h.

^{1}H NMR (400 MHz, $CDCl_3$) δ_H 11.62 (3H, , s, O*H*), 8.36 (3H, s,N=C*H*), 8.10 (3H, s,N=C*H*), 6.78 (3H, s, Ar*H*), 6.55 (3H, s, Ar*H*), 3.71 (3H, m, C*H*-N), 3.46 (3H, m, C*H*-N),1.35-1.78 (24H, m, cyclohexyl C*H*$_2$); δ_C 170.63, 167.13, 163.92, 148.26, 126.25, 126.13, 120.29, 119.14, 76.78, 71.25, 24.47; MALDI-TOF MS:

[$C_{168}H_{180}N_{24}O_{24}Zn_6$] calcd at 3311.712. Found $[M+H]^+$ at 3312.146. Elemental Analysis: C, 58.00; H, 5.46; N, 9.59 (C, 60.93; H 5.48; N 10.15 calculated for $C_{168}H_{180}N_{24}O_{24}Zn_6$). IR ($V_{max}$/ cm^{-1}): 818.72, 865.27, 1135.53, 1153.40, 1218.24, 1311.03, 1371.01, 1471.97, 1603.01, 2856.88, 2927.36. (See Figure 5.21 - 24 for NMR spectra, Figure 5.25 for MS and Figure 5.26 for FT-IR spectra)

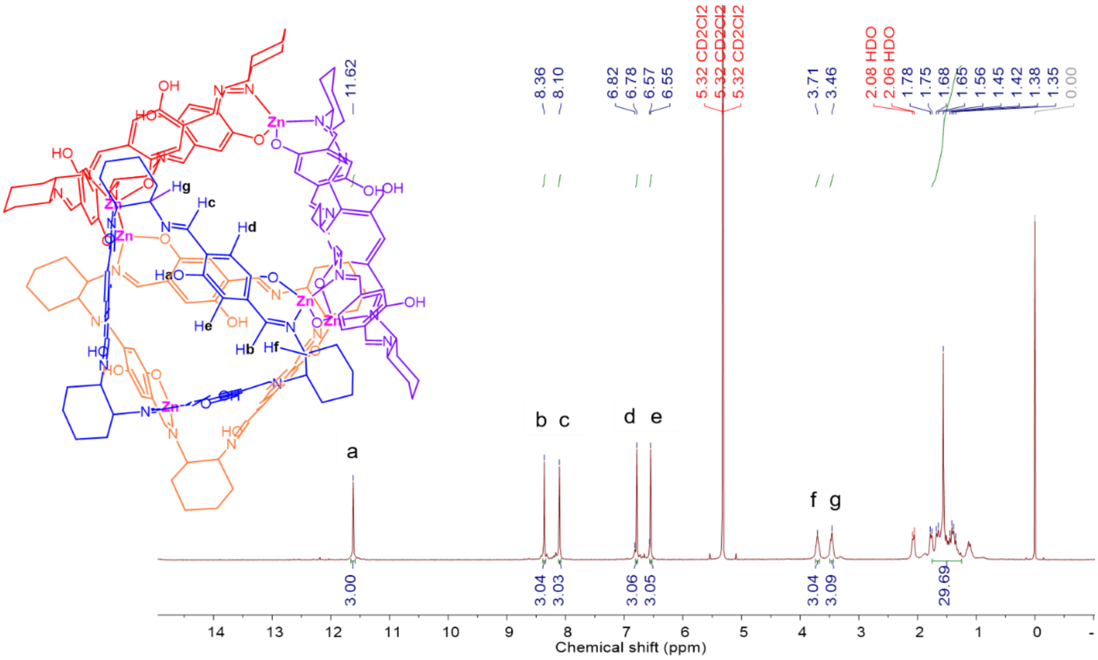

Figure 5.21. ^1H NMR spectrum (400 MHz, $CDCl_3$, 293 K) of **MOP-2**.

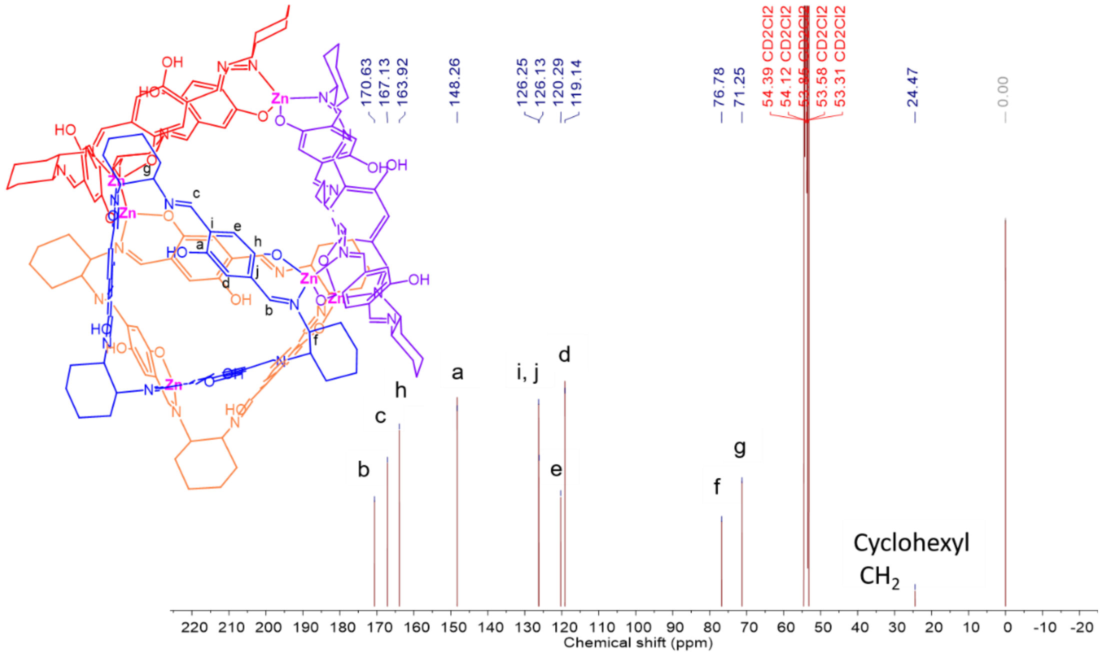

Figure 5.22. ^{13}C NMR spectrum (101 MHz, CD_2Cl_2, 293 K) of **MOP-2**.

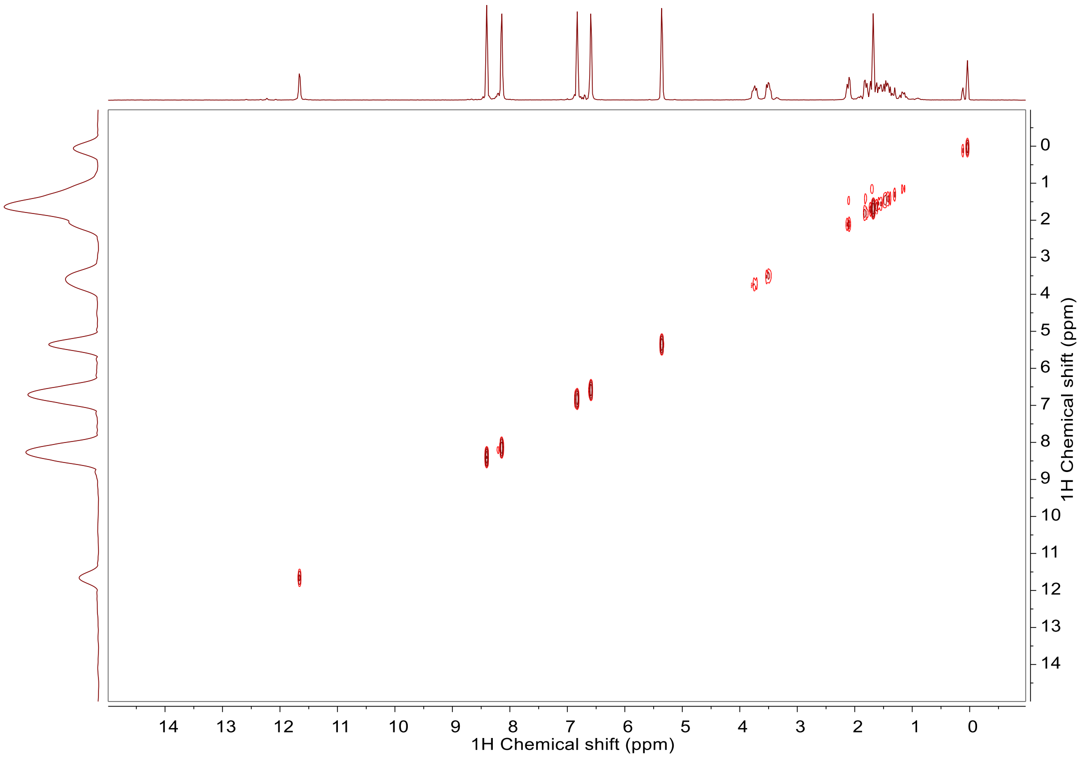

Figure 5.24. COSY (CD_2Cl_2) spectrum of **MOP-2**.

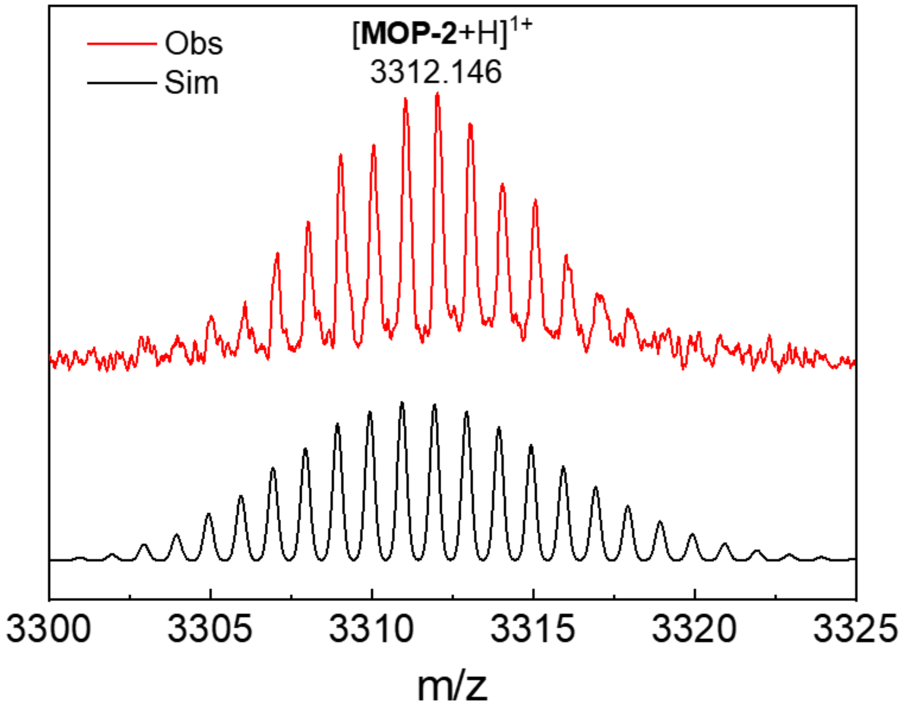

Figure 5.25. MALDI-TOF MS $[M+H]^+$ of **MOP-2**.

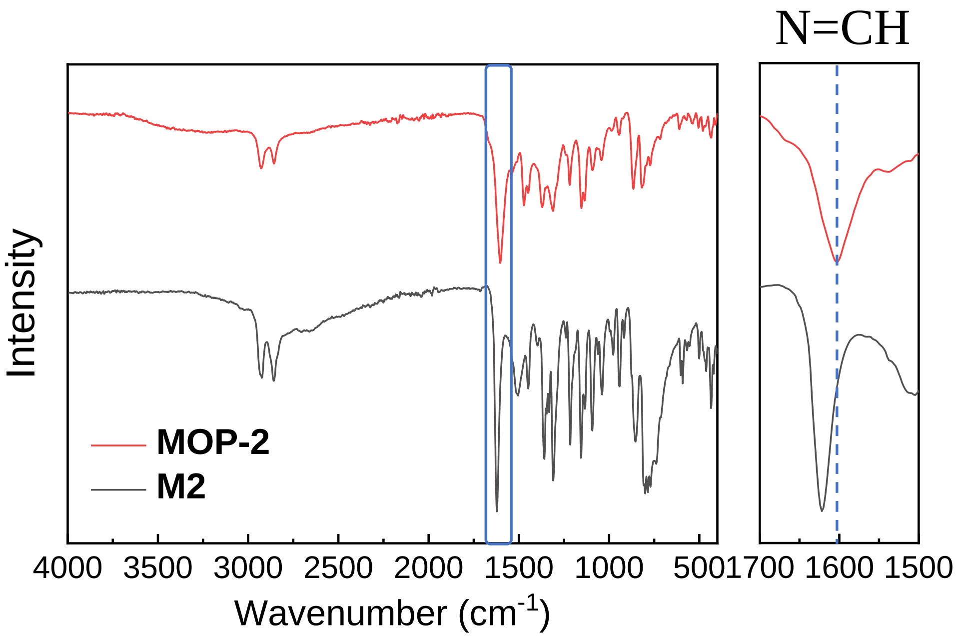

Figure 5.26. FT-IR spectra of **M2** and **MOP-2**.

5.5.7 Synthesis of MOP-3

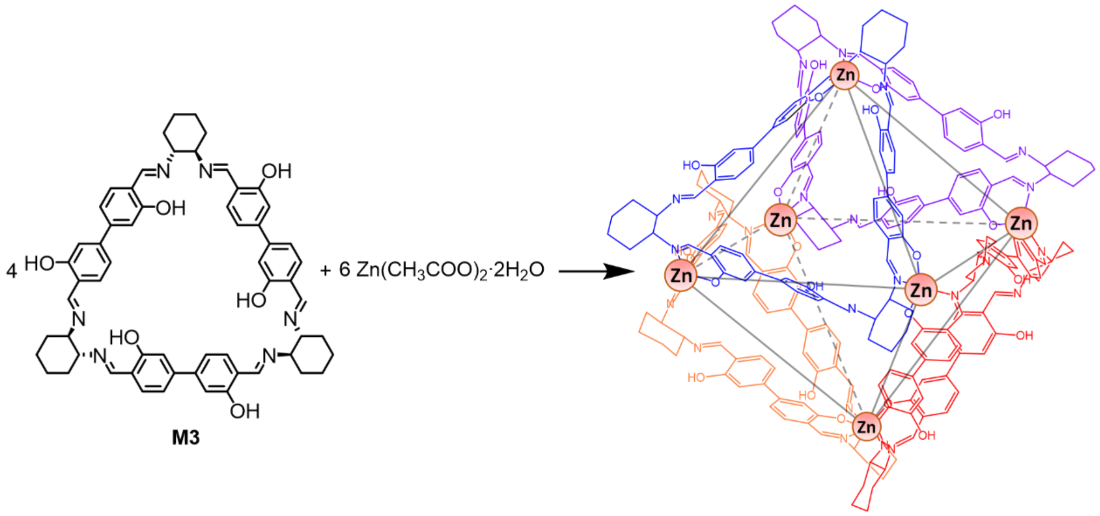

MOP-3: A solution of 27 mg (0.012 mmol) $Zn(CH_3COO)_2·2H_2O$ dissolved in 20 mL of DEF was added to the stirred solution of the 3+3 macrocycle **M3** (78 mg, 0.08 mmol) in 40 mL of DEF. The mixture was stirred at room temperature for 10 min. Then the solution was filtered, put into a flask and left to stand at room temperature. After 3 days, yellow block crystal had formed in the flask, and the residual solvent was removed via syringe. CH_3CN was added to immerse the crystals fully, and the CH_3CN solvent was exchanged every 24 hours for 5 days. After that, the desolvated **MOP-3** (53 mg, 62.7%) was obtained by filtering and drying at 100 °C under a vacuum for 12 h.

^{1}H NMR (400 MHz, $CDCl_3$) δ_H 13.59 (3H, , s, O*H*), 8.66 (3H, s,N=C*H*), 8.15 (3H, s,N=C*H*), 7.35 (3H, d, *J* = 8 Hz, Ar*H*), 7.13 (3H, d, *J* = 8 Hz, Ar*H*), 7.11 (3H, s, Ar*H*), 7.09 (3H, s, Ar*H*), 7.03 (3H, s, Ar*H*), 6.74 (3H, dd, *J*= 8 Hz, *J*= 8, Ar*H*), 3.46 (3H, m, C*H*-N), 2.20 (3H, m, C*H*-N), 1.41-1.73 (24H, m, cyclohexyl C*H*$_2$); MALDI-TOF MS: [$C_{240}H_{228}N_{24}O_{24}Zn_6$] calcd at 4224.888. Found [Zn_4(**M3**)$_2$]$^{1+}$ at 2179.570, [Zn_5(**M3**)$_2$]$^{1+}$ at 2242.915. Elemental Analysis: C, 67.13; H, 5.39; N, 7.85 (C, 68.23; H 5.44; N 7.96 calculated for $C_{240}H_{228}N_{24}O_{24}Zn_6$). IR ($V_{max}$/ cm^{-1}): 788.99, 865.28, 888.86, 1190.18, 1371.47, 1506.62, 1594.57, 2855.66, 2925.64. (See Figure 5.27 for NMR spectra, Figure 5.28 for MS and Figure 5.29 for FT-IR spectra)

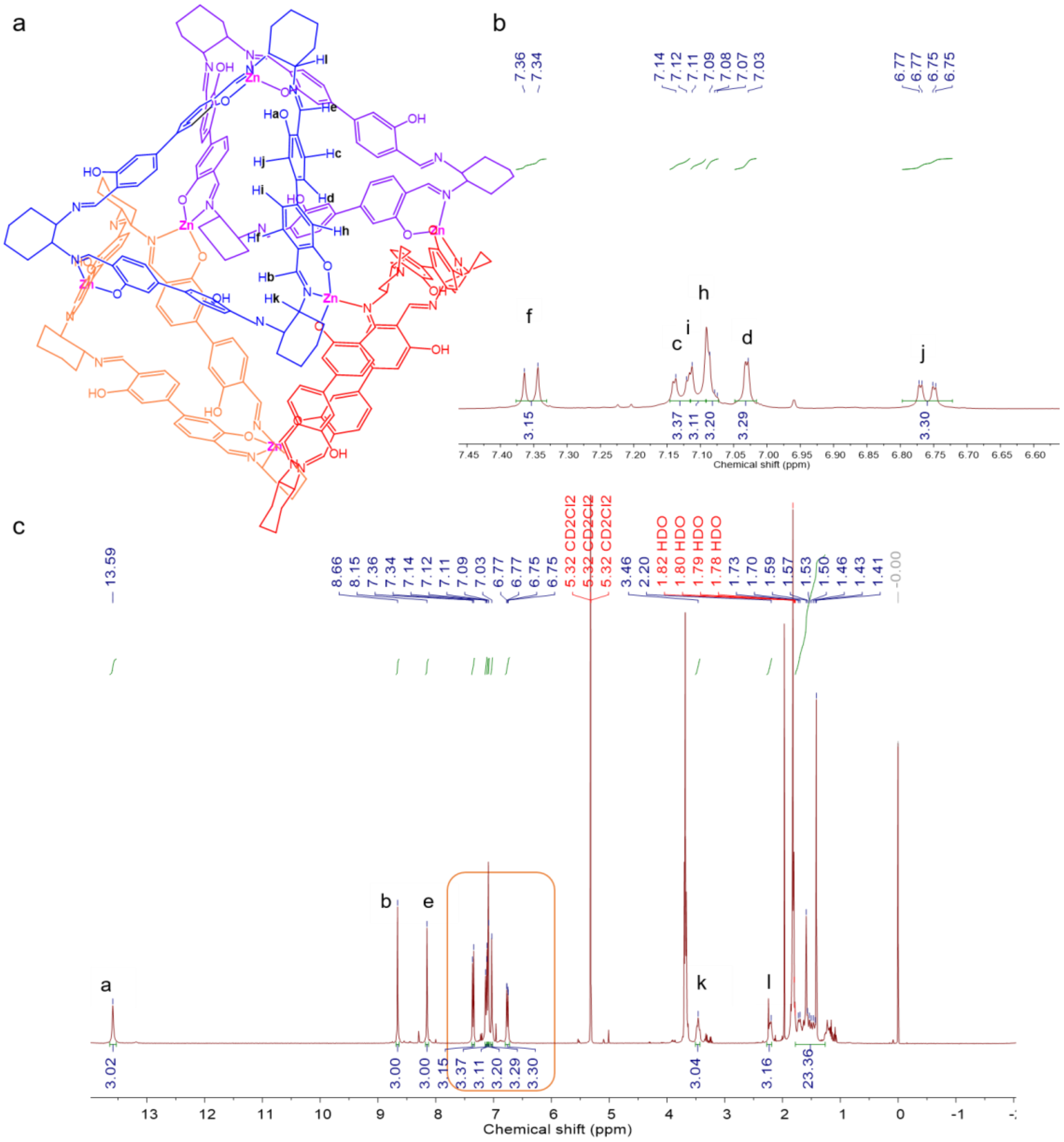

Figure 5.27. ^{1}H NMR spectrum (400 MHz, $CDCl_3$, 293 K) of **MOP-3**.

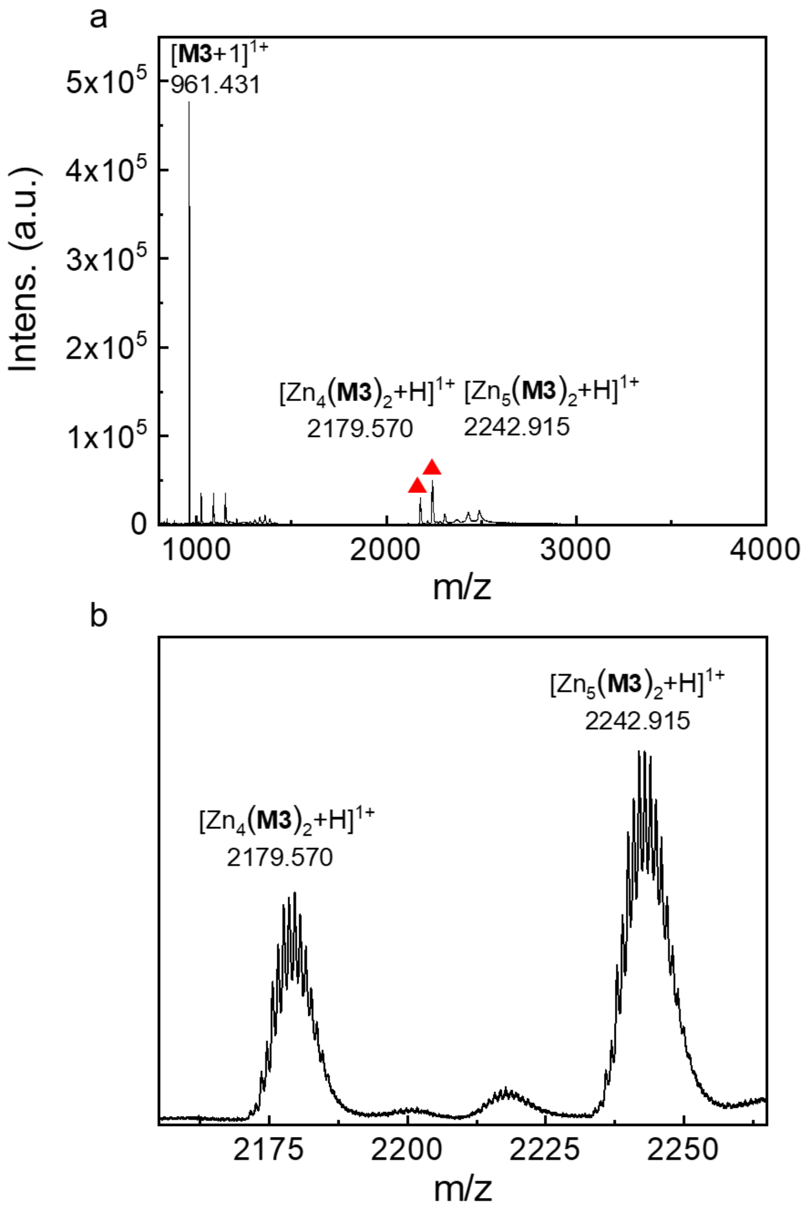

Figure 5.28. MALDI-TOF MS $[M+H]^+$ of **MOP-3** (**MOP-3** = Zn_6(**M3**)$_4$) for (a) whole spectrum and (b). partial enlarged spectrum.

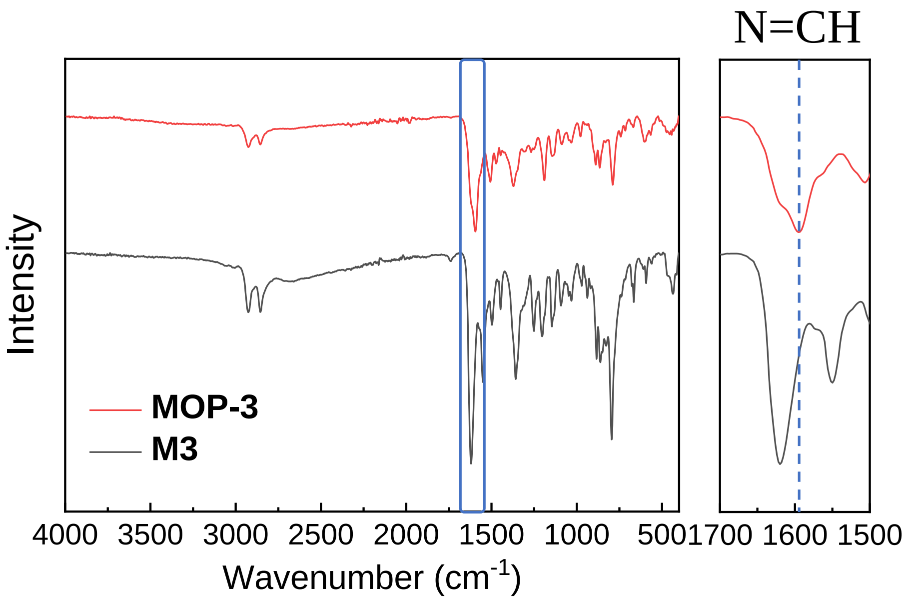

Figure 5.29. FT-IR spectra of **M3** and **MOP-3**.

5.5.8 Gas sorption

All samples were degassed at 80 °C for 15 hours under a dynamic vacuum before gas sorption analysis.

The cryogenic hydrogen adsorption experiments were carried out on a fully automated Sieverts apparatus (Autosorb-iQ2, Quantachrome Instruments). The calibration cell was an empty analysis carried out at the same temperature and pressure range of each experiment; corrections relating to the sample volume and the nonlinearity of the adsorbate were made. Around 50 mg of each sample was activated at 80 °C for **MOC-1α** and at 180 °C for **MOC-1β** under vacuum for 12 h in order to remove any solvent molecules. A coupled cryocooler based on the Gifford−McMahon cycle was used to control the sample temperature. The cooling system permitted us to measure temperatures from 20 to 300 K with temperature stability of <0.05 K.

5.5.9 Thermal desorption spectroscopy (TDS)

TDS experiments were carried out on an in-house device with about 2 mg of each sample. The sample holder is screwed tightly to a Cu block, which is surrounded by a heating spiral in the high vacuum chamber. The Cu block is connected to a flowing helium cryostat, allowing cooling below 20 K. All the samples were first loaded in the sample holder and activated under vacuum for 2 h at the temperature of 353 K for **MOC-1α** and at 453 K for **MOC-1β**. Then, the sample was exposed to a 10/200 mbar equimolar D_2/H_2 isotope mixture at different exposure temperatures (30, 50, 77, and 100 K) for 10 min. The remaining gas molecules were removed at the corresponding exposure temperatures until a high vacuum was reached again. Afterwards, the sample was rapidly cooled down below 20 K. Then, a linear heating ramp (0.1 K/s) was applied, the desorbing gas was continuously detected using a mass spectrometer (QMS), recognizing a pressure increase in the sample chamber when gas desorbs. The area under the desorption peak was proportional to the desorbing amount of gas, which can be quantified after careful calibration of the TDS apparatus.

Calibration of the mass spectrometer signal

A solid piece of a diluted Pd alloy $Pd_{95}Ce_5$ (~0.5 g) was used for calibration. Before the calibration, the oxide layer of the alloy was removed by etching with aqua regia. Then the alloy was heated up to 600 K under a high vacuum to remove any hydrogen that might be absorbed during the etching procedure. Afterwards, it was exposed to 40 mbar pure H_2 or pure D_2 for 1.5–2.5 h at 350 K. As H and D were bound preferentially to the Cerium atoms at low exposure pressures, the alloy could be handled under ambient conditions for a short time. The alloy was weighed after being cooled down to room temperature. The mass difference between the unloaded state and loaded state was equal to the mass uptake of hydrogen or deuterium, respectively. After weighing, the alloy was loaded in the chamber again, and then a 0.1 K/s heating ramp (RT to 600 K) was applied for a subsequent desorption spectrum. The obtained mass of gas directly corresponds to the area under the desorption peak.

5.5.10 Computational details

An isolated molecule, extracted from the experimental crystal structure of **MOC-1α**, was optimised by GFN2-XTB method with D4 dispersion[38] model in gas phase with defaults for convergence. The optimised geometry was confirmed as a true minimum by numerical harmonic frequency calculation without imaginary frequency.[39-41] Based on that, MD simulation was performed for 200 ps, in which 100 ps for equilibration and 100 ps for production with a time step of 2 fs, along with SHAKE restraints on all bonds,[42] in the NVT ensemble using the Berendsen thermostat[43] to maintain a temperature of 298 K. Structures were dumped every 1 ps. The results will be very similar by using isolated molecules from **MOC-1β**.

Pywindow[44] was used to calculate the pore diameter and widow diameter of the molecular dynamics trajectories, including 100 geometries obtained from xTB calculations.

Pore size distribution (PSD) histogram was calculated by *Zeo++*[45], it is advised to use probe radius similar to atomic radii for which one should expect the said 0.1 Å accuracy in peak positions. Therefore, we chose the probe radii below the half of the largest free sphere (D_f) of the crystal's pore structure. As for the MeOH@**MOC-1**, **MOC-1α** and **MOC-1β**, the D_f is 3.4, 2.0 and 2.6 Å, respectively. The probe radii chosen for MeOH@**2** and **MOC-1β** is 1.2 Å, and 0.97 Å is for **MOC-1α**.

Ideal adsorbed solution theory (IAST): Xe/Kr mixture adsorption equilibria with **MOP-2** were predicted by ideal adsorbed solution theory (IAST)[23] using single-component adsorption data, measured experimentally. A detailed description of the approach used to obtain the results reported here can be found in the literature.[24] To apply IAST, single-component adsorption isotherms were specified by fitting an isotherm equation to the discrete, experimental adsorption measurements.

5.6 References

1. A. A. Coelho, *TOPAS* and *TOPAS*-Academic: an optimization program integrating computer algebra and crystallographic objects written in C plus. *J. Appl. Crystallogr.* **2018,** *51* (1), 210-218.

2. A Coelho, *TOPAS*-Academic, v5, Coelho Software: Brisbane, Australia, 2012.

3. G. Winter, *et al.*, DIALS: implementation and evaluation of a new integration package. *Acta Crystallogr., D Struct. Biol.* **2018,** *74* (Pt 2), 85-97.

4. George M Sheldrick, *SHELXT*–Integrated space-group and crystal-structure determination. *Acta Crystallogr., Sect. A: Found. Adv.* **2015,** *71* (1), 3-8.

5. G. M. Sheldrick, Crystal structure refinement with *SHELXL*. *Acta Crystallogr., C Struct. Chem.* **2015,** *71* (Pt 1), 3-8.

6. O. V. Dolomanov, *et al., OLEX2*: a complete structure solution, refinement and analysis program. *J. Appl. Crystallogr.* **2009,** *42* (2), 339-341.

7. Stephen Brunauer, *et al.*, Adsorption of Gases in Multimolecular Layers. *J. Am. Chem. Soc.* **1938,** *60* (2), 309-319.

8. Nikolai Kuhnert, *et al.*, The application of quasi-enantiomeric trianglamine macrocycles as chiral probes for anion recognition in ion trap ESI mass spectrometry. *Tetrahedron: Asymmetry* **2007,** *18* (14), 1648-1654.

9. J. Gawroński, *et al.*, Designing Large Triangular Chiral Macrocycles: Efficient [3 + 3] Diamine−Dialdehyde Condensations Based on Conformational Bias. *J. Org. Chem.* **2000,** *65* (18), 5768-5773.

10. Schrödinger, LLC. Release 2018-1. ConfGen. *Schrödinger: New York, NY* **2018**.

11. Jay L. Banks, *et al.*, Integrated Modeling Program, Applied Chemical Theory (IMPACT). *J. Comput. Chem.* **2005,** *26* (16), 1752-1780.

12. Axel D. Becke, Density‐functional thermochemistry. III. The role of exact exchange. *J. Chem. Phys.* **1993,** *98* (7), 5648-5652.

13. C. T. Lee, *et al.*, Development of the Colle-Salvetti Correlation-Energy Formula into a Functional of the Electron-Density. *Phys. Rev. B* **1988,** *37* (2), 785-789.

14. Stefan Grimme, *et al.*, Effect of the damping function in dispersion corrected density functional theory. *J. Comput. Chem.* **2011,** *32* (7), 1456-1465.

15. MJ Frisch, *et al.*, Gaussian 09, Revision D. 01. 2016; Gaussian Inc. *Wallingford CT*.

16. David H Case, *et al.*, Convergence properties of crystal structure prediction by quasi-random sampling. *J. Chem. Theory Comput.* **2016,** *12* (2), 910-924.

17. Sarah L Price, *et al.*, Modelling organic crystal structures using distributed multipole and polarizability-based model intermolecular potentials. *Phys. Chem. Chem. Phys.* **2010,** *12* (30), 8478-8490.

18. AJ Stone, GDMA: A program for performing distributed multipole analysis of wave functions calculated using the Gaussian program system. *University of Cambridge* **2010**.

19. David S Coombes, *et al.*, Role of electrostatic interactions in determining the crystal structures of polar organic molecules. A distributed multipole study. *J. Phys. Chem.* **1996,** *100* (18), 7352-7360.

20. A. Tkatchenko; M. Scheffler, Accurate molecular van der Waals interactions from ground-state electron density and free-atom reference data. *Phys. Rev. Lett.* **2009,** *102* (7), 073005.

21. A. Ambrosetti, *et al.*, Long-range correlation energy calculated from coupled atomic response functions. *J. Chem. Phys.* **2014,** *140* (18), 18A508.

22. Stewart J Clark, *et al.*, First principles methods using CASTEP. *Z. Kristallogr. Cryst. Mater.* **2005,** *220* (5-6), 567-570.

23. David W. Hand, *et al.*, Prediction of multicomponent adsorption equilibria using ideal adsorbed solution theory. *Environ. Sci. Technol.* **1985,** *19* (11), 1037-1043.

24. Naomi F. Cessford, *et al.*, Evaluation of Ideal Adsorbed Solution Theory as a Tool for the Design of Metal–Organic Framework Materials. *Ind. Eng. Chem. Res.* **2012,** *51* (13), 4911-4921.

25. Tian Lu; Feiwu Chen, Multiwfn: a multifunctional wavefunction analyzer. *J. Comput. Chem.* **2012,** *33* (5), 580-592.

26. William Humphrey, *et al.*, VMD: visual molecular dynamics. *J. Mol. Graph.* **1996,** *14* (1), 33-38.

27. Georg Kresse; Jürgen Furthmüller, Efficient iterative schemes for ab initio total-energy calculations using a plane-wave basis set. *Phys. Rev. B* **1996,** *54* (16), 11169.

28. Georg Kresse; Jürgen Furthmüller, Efficiency of ab-initio total energy calculations for metals and semiconductors using a plane-wave basis set. *Comput. Mater. Sci.* **1996,** *6* (1), 15-50.

29. Georg Kresse; D Joubert, From ultrasoft pseudopotentials to the projector augmented-wave method. *Phys. Rev. B* **1999,** *59* (3), 1758.

30. John P Perdew, *et al.*, Generalized gradient approximation made simple. *Phys. Rev. Lett.* **1996,** *77* (18), 3865.

31. Yingkai Zhang; Weitao Yang, Comment on "Generalized gradient approximation made simple". *Phys. Rev. Lett.* **1998,** *80* (4), 890.

32. Stefan Grimme, *et al.*, A consistent and accurate ab initio parametrization of density functional dispersion correction (DFT-D) for the 94 elements H-Pu. *J. Chem. Phys.* **2010,** *132* (15), 154104.

33. Axel D Becke; Erin R Johnson, Exchange-hole dipole moment and the dispersion interaction. *J. Chem. Phys.* **2005,** *122* (15), 154104.

34. Sidney John Gregg, *The adsorption of gases by solids*. Methuen & co. ltd.: 1934.

35. Aleksandra Sarnicka, *et al.*, Controlling the macrocycle size by the stoichiometry of the applied template ion. *Chem. Commun.* **2012,** *48* (16), 2237-2239.

36. Yong Fu, *et al.*, A novel calixsalen macrocycle: metal sensing behavior for Zn^{2+} and intracellular imaging application. *Tetrahedron Lett.* **2012,** *53* (7), 804-807.

37. Joanna Szymkowiak; Marcin Kwit, Electronic and vibrational exciton coupling in oxidized trianglimines. *Chirality* **2018,** *30* (2), 117-130.

38. Eike Caldeweyher, *et al.*, A generally applicable atomic-charge dependent London dispersion correction. *J. Chem. Phys.* **2019,** *150* (15), 154122.

39. Christoph Bannwarth, *et al.*, Extended tight-binding quantum chemistry methods. *WIREs Comput. Mol. Sci.* **2021,** *11* (2), e1493.

40. Stefan Grimme, *et al.*, A robust and accurate tight-binding quantum chemical method for structures, vibrational frequencies, and noncovalent interactions of large molecular systems parametrized for all spd-block elements (Z= 1–86). *J. Chem. Theory Comput.* **2017,** *13* (5), 1989-2009.

41. C Bannwarth, *et al.*, Quantum Chemical Method with Multipole Electrostatics and Density-Dependent Dispersion Contributions. *J. Chem. Theory Comput* **2019,** *15*, 1652-71.

42. Jean-Paul Ryckaert, *et al.*, Numerical integration of the cartesian equations of motion of a system with constraints: molecular dynamics of n-alkanes. *J. Comput. Phys.* **1977,** *23* (3), 327-341.

43. H. J. C. Berendsen, *et al.*, Molecular dynamics with coupling to an external bath. *J. Chem. Phys.* **1984,** *81* (8), 3684-3690.

44. Marcin Miklitz; Kim E. Jelfs, pywindow: Automated Structural Analysis of Molecular Pores. *J. Chem. Inf. Model.* **2018,** *58* (12), 2387-2391.

45. Marielle Pinheiro, *et al.*, Characterization and comparison of pore landscapes in crystalline porous materials. *J. Mol. Graphics Modell.* **2013,** *44*, 208-219.

Chapter 6:

Conclusions and future work

6.1 Conclusions

The work presented in this thesis has attempted to develop an understanding of the design of imine macrocycles based crystalline solids for gas and vapour separation. One primary aim was to discover novel adsorbent materials with high selectivity and capacity at ambient temperatures and pressure. Another was to use imine macrocycles as good molecular hosts and building blocks to construct higher-level assemblies via non-covalent bonding. Based on different structure and function groups in imine macrocycles, the solvent direction via hydrogen bond and C−H···π interaction, chiral recognition by co-crystallising macrocycles with the opposing chiralities, and metal coordination with salen units were developed for the synthesis of imine macrocycles based crystalline solids. The structures and properties were investigated by using a combination of diffraction techniques, spectrum analysis, gas and vapour sorption analysis, thermal analysis, and calorimetry.

In order to construct selective binding sites in a trianglimine, guided by CSP, solvent templating was applied to the formation of stable EA@**TAMC** crystals from ethyl acetate. The flexible structure of the guest-free *α*-**TAMC** solid allows the formation of perfect complementary voids for ethyl acetate, leading to selective EA adsorption. As a result of this inherently high selectivity, *α*-**TAMC** shows great promise for the dynamic separation of EA from EA-EtOH mixtures, as confirmed by breakthrough experiments. **TAMC** is easily synthesised, shows good reliability after multiple adsorption cycles, and holds strong promise for practical separation or detection applications in the future. More generally, the concept of solvent-templated molecular crystals, stabilised because they occupy deep energy basins on their structure landscapes, might be extended to other molecular separations in the future.

Macrocycles are usually non-porous or barely porous in the solid-state because of their small intrinsic cavity sizes and tendency to close pack, which limits their application in gas and vapour separations. Hence, a heterochiral pairing strategy was developed to introduce porosity in an isotrianglimine macrocycles. Porosity was created by co-crystallising two macrocycles with the opposing chiralities such that they pack in a window-to-window arrangement to connect the intrinsic macrocycle voids. This strategy generates an interconnected pore network with an apparent SA_{BET} of 355

m^2g^{-1}, which is the highest reported surface area for the trianglimine macrocycle,[1, 2] Due to its increased porosity, the **1**-*rac* co-crystal has greatly improved adsorption kinetics and exhibits much higher selectivity toward *p*X, by a factor of 15.7 *vs.* *m*X, outperforming related macrocyclic systems for the same separation.[3] As well as introducing porosity, the heterochiral pairing strategy could also enrich the functionality of these macrocycle systems by enabling hybrid mixing of macrocycles with different functions that would otherwise not co-crystallise, as demonstrated with POCs for quantum sieving applications.[4]

The salen units (OH···N=C) in imine macrocycles make them ideals candidates for coordination with metal ions to form metal complexes. This strategy was used to construct hollow metal-organic molecules with permanent porosity for gas and vapour separation. The calixsalen macrocycle (**M1**) and trianglsalen macrocycles (**M2** and **M3**) were coordinated with znic(II) ions for the construction of MOCs/MOPs with tuneable cavities and windows. A sandwich-like **MOC-1** was assembled from two calixsalen macrocycles with three zinc(II) ions for hydrogen isotope separations. The two polymorphs of **MOC-1** were isolated by activating crystals of the MeOH solvate, initially at 80 °C to afford **MOC-1α**, and then at 180 °C to transform **MOC-1α** into **MOC-1β**. **MOC-1α** has a more extensive range of pore diameter sizes from about 2.0 Å to 5.1 Å and appeared more flexible in gas sorption measurements, which led to **MOC-1α** having a higher BET surface area of 393.8 m^2/g compared to **MOC-1β** (269.9 m^2/g). Surprisingly, **MOC-1β** had a slightly larger extrinsic porosity and higher unit cell void volume than **MOC-1α** (20.6% for **MOC-1β** vs 17.3% for **MOC-1α)**. **MOC-1β** thus has a higher pure D_2 capacity of 3.8 mmol/g than the **MOC-1α** (2.1mmol/g) at the exposing pressure of 200 mbar. In addition, TDS measurements confirm that the D_2 adsorption capacity with **MOC-1β** (1.10 mmol/g, $S_{D2/H2} = 2.2$) is higher than for **MOC-1α** (0.41 mmol/g, $S_{D2/H2} = 2.8$) at 77 K for 1:1 D_2–H_2 mixture. The local flexibility of **MOC-1** crystals provides the additional accessible inner surface to increase the adsorption and separation of hydrogen isotopes inside the crystals via kinetic quantum sieving. This leads to a desorption temperature of over 100 K even without existing strong adsorption sites. Furthermore, the assembly of four trianglsalen macrocycles with six zinc ions afforded neutral octahedral MOPs. Using the larger **M3**, the resulting **MOP-3** has a larger size of 2.9 nm than the **MOP-2** (2.3 nm). After activation, **MOP-2** and **MOP-3** tended to be amorphous but remained with permanent porosities of 745.04 and 651.38 m²/g, respectively. **MOP-2** exhibited great potential for the Xe/Kr separation, which will be a good candidate for rare gases separation in the future.

6.2 Future work

Overall, this thesis has demonstrated the significant role of imine macrocycles in the assembly of novel adsorbent materials with high selectivity and capacity at ambient temperatures and pressure. However, the area of imine macrocycles based crystalline solids for gas and vapour separation remains underdeveloped.

One challenge is on constructing selective binding sites in imine macrocycles. Although, in this thesis, solvent templating has been successfully introduced to create selective binding sites in trianglimine for ethyl acetate, and CSP has been used for guiding the discovery and mechanism explanation. The examples for using this method is not common, and it is challenging to use CSP to predict the structure of flexible systems, especially for solvate systems. Therefore, in the future, more attention will be paid to selective binding sites via hydrogen bond, C−H···π interaction and (open) metal sites that have stronger interactions and are easy to predict. **MOC-1** is a good example of the metal site binding of guest molecules and the metal site in **MOP-1** has been reported to bind alcohol molecules. Forming coordination bonds between the OH oxygen atom in alcohol molecules and tetradentate coordinated zinc(II) atoms in the **MOC-1** that became five-coordinated.[5]

Another challenge is to increase the capacity for gas and vapour separation. Balancing the selectivity and capacity is always a significant consideration in the design of adsorbent materials. Researchers are trying to increase the capacity without reducing the selectivity, which will increase the kinetic and efficiency of separation processes. However, it is still challenging because the narrow pore in gas and vapour molecular size can achieve high selectivity but may have low capacity without a high surface area and larger accessible channel. Therefore, developing a strategy to control the pore structure is key to solving this problem. Although, in this thesis, chiral recognition has been applied in the formation of hollow organic dimers with higher surface areas than the used macrocycles, and metal coordination has been used to construct hollow metal-organic molecules with a tuneable cavity for gas separation. More attempts can be made to design and synthesise novel imine macrocycles for the assembly of porous materials with specific pores and good surface areas for the separation process. In this thesis, more attention is focused on the [3+3] imine macrocycles based materials. However, [2+2] and [4+4] imine macrocycles are also synthesisable.[6, 7] In addition, the diversity of imine macrocycles can be expanded by using different dialdehydes with different substitution patterns and different diamines. Therefore, the dynamic library of imine macrocycles is needed to be built for the development of functional assemblies in the future. Considering the predictable products of imine macrocycles based on certain start materials, using a combination of predictive computational chemistry methods and robotic platforms will accelerate their discovery. Furthermore, these state-of-the-art strategies can be expanded in the design and synthesis of imine macrocycles based crystalline solids for gas and vapour separations, which will be an important step forward in this field.

6.3 References

1. Elena Sanna, *et al.*, A crystalline sponge based on dispersive forces suitable for X-ray structure determination of included molecular guests. *Chem. Sci.* **2015,** *6* (10), 5466-5472.

2. Arnaud Chaix, *et al.*, Trianglamine-Based Supramolecular Organic Framework with Permanent Intrinsic Porosity and Tunable Selectivity. *J. Am. Chem. Soc.* **2018,** *140* (44), 14571-14575.

3. Kecheng Jie, *et al.*, Near-Ideal Xylene Selectivity in Adaptive Molecular Pillar[n]arene Crystals. *J. Am. Chem. Soc.* **2018,** *140* (22), 6921-6930.

4. Ming Liu, *et al.*, Barely porous organic cages for hydrogen isotope separation. *Science* **2019,** *366* (6465), 613.

5. Jan Janczak, *et al.*, Trinuclear Cage-Like ZnII Macrocyclic Complexes: Enantiomeric Recognition and Gas Adsorption Properties. *Chem. Eur. J.* **2016,** *22* (2), 598-609.

6. Almudena González-Álvarez, *et al.*, Selective Host Amplification from a Dynamic Combinatorial Library of Oligoimines for the Syntheses of Different Optically Active Polyazamacrocycles. *Eur. J. Org. Chem.* **2004,** *2004* (5), 1117-1127.

7. Nikolai Kuhnert, *et al.*, The synthesis and conformation of oxygenated trianglimine macrocycles. *Org. Biomol. Chem.* **2005,** *3* (3), 524-537.